# Uniform Finishing of Complex Profiles using Rotational Magnetorheological Fluid-based Finishing (R-MRFF) Process

**A thesis submitted**
**in partial fulfillment of the requirements**
**for the degree of**

**Doctor of Philosophy**

**By**


## Manjesh Kumar
**Roll No.-176103021**




**Department of Mechanical Engineering**

**Indian Institute of Technology Guwahati**

**Guwahati, India**


**March, 2022**

Department of Mechanical Engineering
Indian Institute of Technology Guwahati
Guwahati-781039
INDIA

# CERTIFICATE

It is certified that the work contained in the thesis entitled "**Uniform Finishing of Complex Profiles using Rotational Magnetorheological Fluid-based Finishing (R-MRFF) Process**", submitted by **Manjesh Kumar**, Roll No. 176103021 to the Indian Institute of Technology Guwahati for the degree of Doctor of Philosophy has been carried out under my supervision in the Department of Mechanical Engineering, Indian Institute of Technology Guwahati. This work has not been submitted elsewhere for the award of any other degree or diploma.

Manas Das

Dr. Manas Das

Date: 31.11.2021

Department of Mechanical Engineering
Indian Institute of Technology Guwahati
Guwahati-781039, Assam, India

# Declaration

I declare that this written submission represents my ideas in my own words and where others' ideas or words have been included, I have adequately cited and referenced the original sources. I also declare that I have adhered to all principles of academic honesty and integrity and have not misrepresented or fabricated or falsified any idea/data/fact/source in my submission. I understand that any violation of the above will be cause for disciplinary action by the Institute and can also evoke penal action from the sources which have thus not been properly cited or from whom proper permission has not been taken when needed.

Manjesh Kumar

Date: 31.11.2021

Manjesh Kumar
Roll No. 176103021

***Dedicated to***

My father

# ACKNOWLEDGEMENT

I would like to take this opportunity to pay my deep sense of respect and sincere gratitude to my supervisor, Dr. Manas Das, Department of Mechanical Engineering, Indian Institute of Technology Guwahati, Assam-781039 for his invaluable advice, resourceful guidance, inspiring instructions, active supervision and constant encouragement without which it would not have been possible for me to reach to this point.

I also wish to thank to my doctoral committee members, Dr. R. G Narayanan, Dr. Swarup Bag and Dr. Sandip Das for their guidance, moral support and encouragement to my ideas in the subject as well as other areas of innovations. I must not miss the opportunity to thank all the Professors of Mechanical Engineering Department, Indian Institute of Technology Guwahati, whose motivation and timely help molded me in all possible forms.

I would also like to thank Mr. Jiten Basumatary for his support in carrying out my work in advanced manufacturing lab. I am very much thankful to workshop superintendent Mr. N. K. Das and workshop technicians, Mr. Upen Gohain and Mr. Dhaneswar Khaklary for their help to fabricate my experimental setup and workpieces. I would like to acknowledge central instrument facility (CIF) of IIT Guwahati for kind assistance to carry out my research work.

I thankfully acknowledge Science & Engineering Research Board (SERB), New Delhi, India, for their financial support for project No. EEQ/2017/000597 entitled "Fabrication of Prosthetic Im-plants and further Nanofinishing using Magnetic Field Assisted Finishing (MFAF) Process".

Last, but not least, I am deeply indebted to my parents for the sacrifices they have borne to ensure the fulfillment of my dreams. I would like to thank my family for their support and motivation during my PhD.

The time I spent with all my friends and seniors at IIT Guwahati, Abhinav Kumar, Niranjan Kumar Chaudhary, Mukesh Kumar, Ambrish Singh, Vikash Kumar, Hari Narayan Singh Yadav, Ranajit Mahanti, Anand Mohan Pandey, Atul Singh Rajput, Keili Durgaprasad, Dr. Anupam Alok, Dr. Chandan Kumar, Dr. Anwesa Barman, who made my life enjoyable and memorable on the campus.

---

MANJESH KUMAR

# Abstract

The surface roughness of any component is a major concern in the medical, automotive, aerospace, military, and other industries. The performance and life of the components depend primarily on their surface quality. The components explored in the current study for finishing purposes are miniature gear and poppet valve. The poppet valve accurately regulates the perfect air/fuel mixture into the combustion chamber of a gas propulsion engine or internal combustion (IC) engine to reduce hydrocarbon emissions. Miniature gears are used in biomedical devices for pumping, cutting, and various other works, also in small servo motors, which are widely used in the UAVs, automotive, and aerospace industries. Previous finishing methods (mentioned in the literature) generate defects like burrs, pits, scratches, dents, etc. The uniform nano-scale finishing on such components is tough to achieve due to constraints related to the fixture design and fixture material. The surface roughness requirement of these complex components is at the nanometer level and should be uniform over the entire surface. The rotational magnetorheological fluid-based finishing (R-MRFF) process is proposed in the present study to counteract the problems faced during finishing miniature gear and poppet valve profiles while providing the required uniform surface finish and surface characteristics. A novel flow restrictor and workpiece fixture are designed and developed to uniformly nano-finish SS316L miniature gear teeth profiles. Also, a novel magnet fixture is designed and developed to nano-finish Nickel-Al-Bronze alloy (AB2 grade) based poppet valve ridge profiles uniformly. Magnetorheological polishing (MRP) fluid is used in the R-MRFF process to finish both components.

For designing the proposed uniform flow restrictor, first of all, uniform magnetic flux density, normal and shear stress distributions are calculated along the gear teeth profiles. For this purpose, magnetostatic fluid-flow analysis is carried out using a finite element (FE) based Comsol® Multiphysics software package. Further, based on FE analysis results, the optimum uniform flow restrictor and workpiece fixture model is designed among different proposed geometries of uniform flow restrictors. Three types of MR polishing media with varying sizes of iron particles and different abrasives concentrations have been prepared. After finishing with the novel workpiece fixture and Type-III MRP media, the minimum surface roughness ($R_a$) of the gear-tooth involute profile was decreased to 34.3 nm and 24.5 nm (without and with using a uniform flow restrictor, respectively) from its initial value of 265 nm. No recast layer, pits, or dents were observed on the finished surface. While finishing with the uniform flow

restrictor, almost the same surface roughness values are achieved at each gear tooth profile. From the analysis of variance (ANOVA), each process parameter's influence on % ΔRa and MRR are analyzed, and significant process parameters are selected. The value of the optimized process parameters, i.e., a volumetric proportion of IPs/SiC abrasives, extrusion pressure, and rotational speed of magnets, are 1.5, 35 bar, and 109 rpm, respectively, obtaining 90.75% improvement in Ra and 0.00118 g/min MRR. After comparing the predicted and experimental (validation experiments) results of % ΔRa and MRR, the maximum error is found to be less than 10 %, which depicts the feasibility of the proposed model. Surface roughness simulation and material removal model are also performed using finishing force analysis and FEA findings. The maximum percentage error of 11.5% and 8.69% between experimental and simulated MRR and surface roughness, respectively, was observed for miniature gear teeth profiles using a flow restrictor, which is also within a feasible limit.

Magnetostatic simulation is conducted using FEA based Ansys® software package to optimize the size, location, and the number of permanent magnets for poppet valve profile polishing. Three MRP fluids are prepared in an acid-based medium having carbonyl iron particles (CIPs) and SiC abrasives. Type-3 MRP media generates more oxide layer on poppet valve profiles, which improves its chemical inertness and corrosion resistance capability. After finishing the poppet valve, the achieved final surface roughness value is 20.1 nm from its initial value of 320 nm. Also, an ANOVA study is carried out to develop the statistical model. The quadratic regression equation predicts 93.25% improvement in Ra, at optimum process parameter conditions of 900 rpm rotational speed, 0.01 mm/min feed rate of poppet, 35% CIPs concentration, and 7% abrasives concentration. The predicted results are validated with experiments. A magnetostatic fluid-solid-interaction simulation of the R-MRFF process is conducted to study normal and shear stress distribution on poppet valve profiles during finishing. Surface roughness simulation and material removal modelling are also performed using finishing force analysis and FEA findings. The maximum percentage error of 12.87% and 11.5% between experimental and simulated MRR and surface roughness, respectively, was observed within a feasible limit for poppet valve profiles. The R-MRFF process will enhance the sealing effectiveness between super-finished poppet valve and its seat to reduce hydrocarbon emissions at elevated pressures and temperatures during its use.

# Table of Contents

# List of Figures

# List of Tables

# NOMENCLATURES

| | |
|---|---|
| $A$ | Magnetic vector potential (Tm or Wb/m) |
| $A_c$ | Cross-sectional area of spherical abrasive ($m^2$) |
| $A_f$ | Area of cube face ($m^2$) |
| $A_p$ | Normal projected area of gear working surfaces ($m^2$) |
| $B$ | Magnetic flux density (T or $Wb/m^2$) |
| $B(x)$ | Magnetic flux density (T) variations in working gap(x) |
| $D_i$ | Indentation diameter (m) |
| $D_g$ | Abrasive particle diameter in (m) |
| $F$ | Force per unit volume ($N/m^3$) |
| $F_m$ | Normal magnetic force (N) |
| $F_n$ | Normal force (N) |
| $F_s$ | Shear force (N) |
| $F_t$ | Tangential force (N) |
| $F_{cen}$ | Centrifugal force acting on active abrasives (N) |
| $(F_{indentation})_i$ | Normal indentation force on active abrasive along tooth top, involute and in between surface of gear (N) |
| $(F_{indentation})_f$ | Normal indentation force on active abrasive along tooth face surface of gear (N) |
| $(F_c)_i$ | Cutting force acting on active abrasive along tooth top, involute and in-between surface of gear (N) |
| $(F_c)_f$ | Cutting force acting on active abrasive along tooth face surface of gear (N) |
| $F_R$ | Resistance force (N) |
| $H$ | Magnetic field strength (A/m) |
| $H_{BHN}$ | Brinell hardness number |
| $H_0$ | Saturation magnetic field strength (A/m) |
| $h_i$ | Initial roughness peak height (μm) |
| $h_{i,max}$ | Highest peak height (μm) |
| $m$ | Consistency index |
| $M$ | Iron particles magnetization ($A\text{-}m^2/kg$) |
| $M_m$ | Mass magnetization (emu/g) |
| $M_s$ | Saturation magnetization (A/m) |

| | |
|---|---|
| $m_{ip}$ | Mass of an iron particle (kg) |
| $m_{AP}$ | Mass of an abrasive particle (kg) |
| $N_m$ | Rotational speed of magnet fixture (rpm) |
| $N_p$ | Poppet valve rotational speed (rpm) |
| $N_g$ | Total number of active abrasive particles |
| $n$ | Number of data points |
| $p$ | Pressure exerted on gear profiles by MRP media ($N/m^2$) |
| $r$ | Radial distance (m) |
| $R_a$ | Centre-line-average (CLA) surface roughness (nm) |
| $r_p$ | Radius of poppet ridge profiles (m) |
| $t$ | Depth of indentation of an active abrasive into workpiece surfaces (μm) |
| $u$ | Velocity of MRP media (m/s) |
| $v$ | MRPF radial velocity (m/s) |
| $V$ | Volume fraction of each constituent of MRP media |
| $V_A$ | Abrsives volume fraction |
| $w$ | Width of ridge profiles (m) |
| $\chi_m$ | Mass of magnetic susceptibility of IPs ($m^3/kg$) |
| $\varepsilon_c$ | Average compressive strain |
| $\phi$ | Volume fraction of IPs |
| $\dot{\gamma}$ | Shear rate (/s) |
| $\eta$ | Non-Newtonian viscosity (kg/ (m.s)) |
| $\mu$ | Newtonian viscosity (Pa.s) |
| $\mu_0$ | Relative permeability of free space (Wb/A.m) |
| $\rho$ | Density of each constituent of MRP media |
| $\rho_{MRP}$ | Density of MRP media ($kg/m^3$) |
| $\sigma_n$ | Normal stress (Pa) |
| $\sigma_y$ | Yield stress of workpiece in shear (MPa) |
| $\tau$ | Shear stress (kPa) |
| $\tau_y$ | Avg. MRP fluid shear yield stress (kPa) |
| $\omega$ | Angular velocity (rad/s) |

# Acronym

| | |
|---|---|
| AFM | Abrasive flow machining |
| $Al_2O_3$ | Aluminium oxide |
| ANOVA | Analysis of variance |
| BEMRF | Ball end magnetorheological finishing |
| CIPs | Carbonyl iron particles |
| CMP | Chemo-mechanical polishing |
| CMG | Chemo-mechanical grinding |
| CeO2 | Cerium oxide |
| $CuF_2$ | Copper (II) fluoride |
| $CuNO_3$ | Copper (II) nitrate |
| DP | Diamond powder |
| DI | Deionized water |
| DOE | Design of experiment |
| EIPs | Electrolytic iron particles |
| FESEM | Field emission scanning electron microscope |
| FEA | Finite element analysis |
| HF | Hydrofluoric acid |
| $HNO_3$ | Nitric acid |
| $H_2O_2$ | Hydrogen peroxide |
| IPs | Iron particles |
| MAAFM | Magnetically assisted abrasive flow machining |
| MAF | Magnetic abrasive finishing |
| MFAF | Magnetic field assisted finishing |
| MFD | Magnetic flux density |
| MFP | Magnetic float polishing |
| MRF | Magnetorheological finishing |
| MRPF | Magnetorheological polishing fluid |
| MRJF | Magnetorheological jet finishing |
| MRAFF | Magnetorheological abrasive flow finishing |
| MRFF | Magnetorheological fluid based finishing |
| R-MRAFF | Rotational magnetorheological abrasive flow finishing |

| | |
|---|---|
| R-MRFF | Rotational magnetorheological fluid based finishing |
| RSM | Response surface methodology |
| SiC | Silicon carbide |
| $SiO_2$ | Silica |
| SAGW | Soft abrasive grinding wheel |

# Chapter 1 Introduction and Literature Survey

## 1.1 Introduction

The functional requirement of the components and safety and aesthetic compulsion makes it necessary to improve the surface characteristics before putting it into useful applications. Therefore, it is crucial to achieve a superior surface finish very close to dimensional precision. Also, 3D complex components are being found more useful in today's industries, leading to an increased demand for nano-finishing. The abrasives trapped within carbonyl iron particles (CIPs) chains of magnetorheological polishing (MRP) fluid are mainly responsible for surface finishing. The traditional finishing methods are comparatively less valuable in the case of 3D complex surface finishing due to the lack of better controllable finishing forces and constraints in tool movement. Magnetorheological fluid based finishing processes have better control over the finishing forces and more flexibility in tool movement over various surfaces. MRP fluids are a class of new intelligent material whose rheological characteristics change rapidly and can be controlled easily in the presence of an applied magnetic field. The devices based on MRP fluids are dampers, brakes, clutches, polishing devices and hydraulic valves, etc. These devices have a very promising potential future. Some have been commercially used in engineering applications such as automobiles, polishing machines, exercise equipment, aerospace and even biomedical, etc.

The MRP fluid based finishing processes include magnetorheological finishing (MRF), magnetorheological jet finishing (MRJF), magnetorheological abrasive flow finishing (MRAFF), rotational-magnetorheological abrasive flow finishing (R-MRAFF) and ball end magnetorheological finishing (BEMRF), etc. Most of these processes have been developed in the recent past. They have been employed to produce optical, mechanical, and electronic components with a micrometre or sub-micrometre form accuracy and surface roughness within nanometre range with hardly any surface defects. These polishing methods have been widely used to ultra-finish the complex components of many industrial and aerospace equipment. Some complex components are gears, bearings, brakes, clutches, control valves (poppet, spool, and rotary), moulds, tubes, barrels, cylinders, pump-rotors, injector-nozzles, and spring collets, etc.

## 1.2 Complex Surface Finishing Processes

Different complex surface finishing processes are described in the present section.

### 1.2.1 Overview of Finishing Processes

Surface finish is a combination of three factors on which it is dependent: surface roughness, surface waviness, and lay. The schematic of surface roughness, waviness and lay is shown in Fig. 1.1.

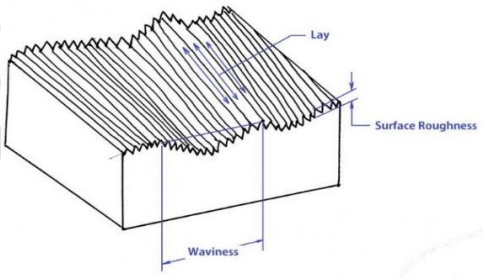


**Fig. 1.1** Representation of surface roughness, waviness, and lay [1]

Surface roughness is defined as surface irregularities that are finely and uniformly spaced. In the field of manufacturing, only surface roughness is known as surface finish. Roughness, waviness and lay together are called Surface texture instead of surface finish. Surface waviness is surface irregularities that are irregularly spaced. Lay is the pattern that is formed due to machining operations on the surface like planning, shaping, grinding, etc.

The products with high surface roughness will have little life span because of corrosion and wear. No one would expect such a life span from their purchased product after spending their earned money. To achieve a better life span of products, whether it is huge or miniature size, only one solution is there: proper finishing of products. Surface finish is performed by these three processes, i.e., machine finishing, surface treatment, and surface coating. Our scope is only machine finishing. The surface finishing procedure is shown in Fig. 1.2. The surface finishing processes are classified into various traditional, non-traditional (advanced) and hybrid processes. The various classifications of machine surface finishing processes are shown in Fig. 1.3.


**Fig. 1.2** Processing of surface finish

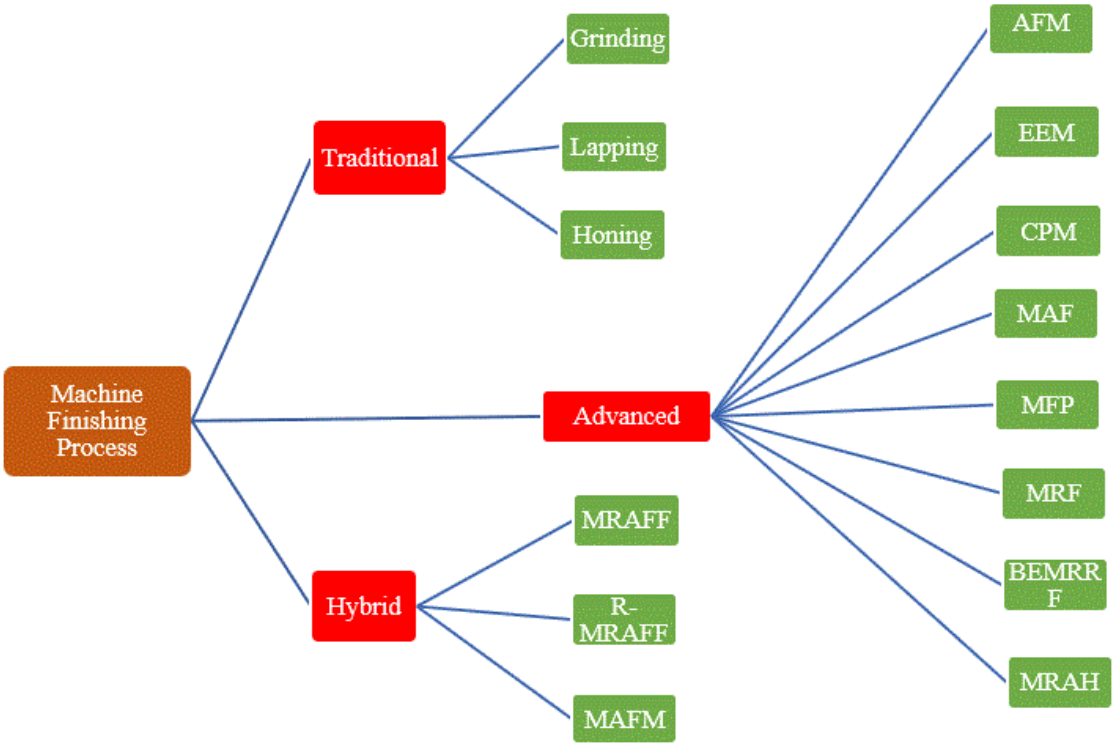


**Fig. 1.3** Classification of surface finishing processes

## 1.2.2 Traditional Finishing Processes

In the traditional finishing process, friction between the abrasive/abrasive tool and the workpiece is responsible for material removal and producing a good surface finish with close tolerance. This process is simple and does not require hefty machine knowledge.

### 1.2.2.1 Grinding

Grinding, an abrasive machining process, is widely used as a finishing process. In this process, a grinding wheel laced with the abrasive particle is used to finish the surface of the workpiece. This process gives more material removal rate compared to other traditional finishing processes. Here abrasion is the reason for material removal. Mizugaki et al. [2] attached an elastic grinding wheel with felt buff to the end effector of an industrial robot. It can easily follow the profile path of the complex surface due to its higher degree of freedom incorporated with the industrial robot. Huang et al. [3] reported the finishing of turbine-vane overhaul using sand belt grinding wheel. Shiou et al. [4] used a spherical grinding tool to finish complex surfaces of a plastic injection mould steel on a CNC machining centre. They developed the

spherical grinding tool and its alignment components. The Schematic diagram of the spherical grinding process is shown in Fig. 1.4 (a).

### 1.2.2.2 Honing

Honing is performed by a honing tool or honing stone which is actually an abrasive stick or abrasive stone. After applying pressure, the honing tool abrades the workpiece surface along a predefined path. Weulu and Timmermann [5] used honing stone to finish the complex surface of dies and moulds. The honing stone is attached to the six-axis robot for better flexibility. Nowicki and Szafarczyk [6] attached abrasive sticks having two or four degrees of freedom with the machining head of an NC milling machine. The abrasive sticks rotate with the machine head, and feed is given to the workpiece in X, Y and Z directions. A non-conventional honing is also used to achieve low surface roughness on complex surfaces made of alloy steel [7].

### 1.2.2.3 Lapping

The lapping process provides a high degree of surface flatness by pressing a lap over the workpiece with abrasive media in between them. It ensures proper match of surfaces. A conditional ring or retaining ring maintains uniform slurry distribution. Jack and Mohsen [8] studied the lapping and superfinishing effects on hypoid gears for transmission errors. Lapping improves surface finish drastically; however, during gear rolling, surface quality considerably decreases. Fulmali and chadge [9] discuss the role of the lapping process in valve industries. It is used for different types of valves and their seats. The size and type of abrasives used for valve lapping depend upon the finishing requirements. The basic lapping process is shown in Fig. 1.4(b).

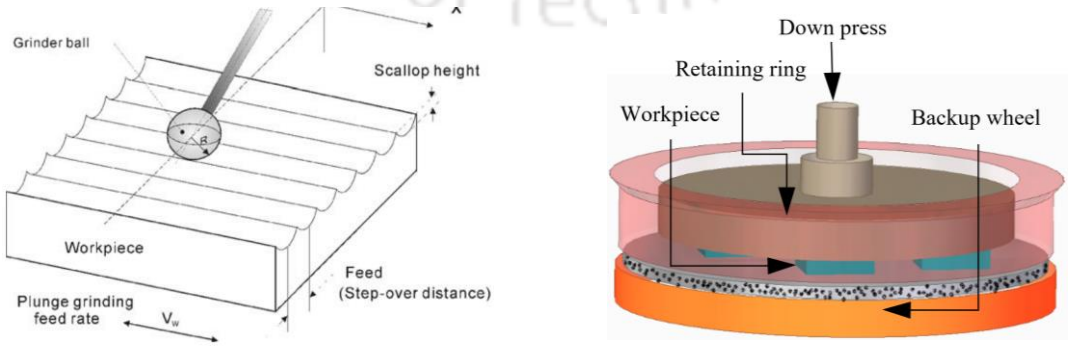


(a) (b)

**Fig. 1.4** (a) Schematic diagram of the spherical grinding process [4] and (b) lapping process

## 1.2.3 Advanced Finishing Processes

### 1.2.3.1 Abrasive Flow Machining

Extrude Hone first developed the AFM technology in the 1960s to finish complex internal shapes and targeted surfaces. Even in the most restricted locations, AFM may process more holes, gaps or sides in one activity [10]. AFM was earlier employed to polish stereolithography models [11]. The AFM could effectively polish components from mild aluminium to robust nickel alloys, ceramics, and carbides [12]. There are three types of AFM that have been developed so far, i.e., one way AFM, two way AFM, and orbital AFM (Fig. 1.5). In the case of one way AFM, the piston exerts force from one side only. The abrasive medium passes over the component and leaves from the other area of the system. In the case of two way AFM, a semi-solid media laden with abrasives is moving in an upward and downward direction through a path constricted by the component, with the help of two vertically opposite cylinders connected to a hydraulic unit. In general, two way AFM is mostly used in AFM technology. In the orbital AFM process, fast, lower amplitude fluctuations of the component against a self-shaping elastoplastic abrasive system help to achieve the desired surface and edge finish. The various developments in the AFM process have been in use for a wide range of finishing applications.

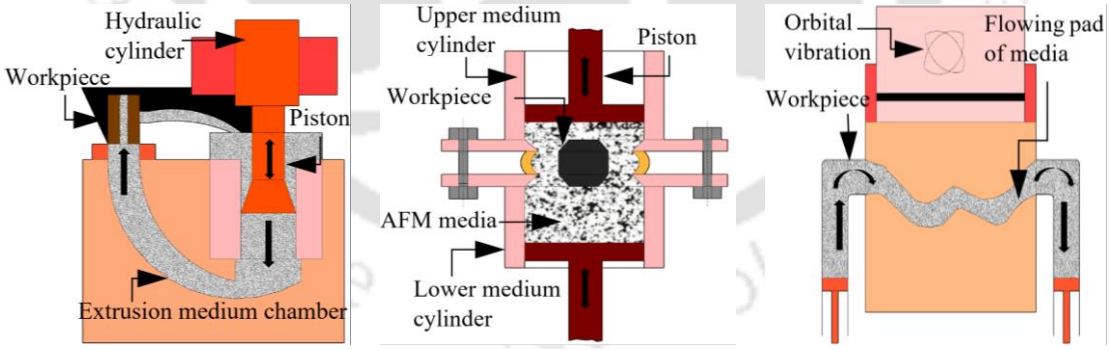


(a) (b) (c)

**Fig. 1.5** Different kinds of AFM process: (a) one way, (b) two way, and (c) orbital AFM

The AFM media that is used for finishing cannot be re-used; hence, the whole process becomes costly. Also, the viscosity increases in those portions at which the flow passage is constrained and thus, abrasion occurs. Also, the viscosity of the AFM process cannot be controlled externally [13].

### 1.2.3.2 Magnetic Abrasive Finishing (MAF)

In the traditional AFM method, a magnetic field was introduced all over the test specimen to establish a new innovative technique called magnetically assisted AFM (MAAFM) [14]. In this process, usually ferromagnetic particles are sintered with fine abrasive particles ($Al_2O_3$, $ZrO_2$, $CeO_2$, $SiO_2$ (silica), SiC, CBN, boron carbide ($B_4C$), natural diamond, synthetic diamond, or their combinations). Such particles are called ferromagnetic abrasive particles (or magnetic abrasive particles, MAPs). Under a magnetic field, a sideways pull is experienced by the abrasive media, which mainly consists of ferromagnetic particles. These particles impinged on the workpiece, causing the phenomena of micro-chipping [15]. The magnetic field improves MRR for non-magnetic products, though magnetic components identified insulating impact [16]. There has been no noticeable change in mean roughness (Ra) and material removal rate (MRR) post MAAFM method relative to the AFM method. In magnetic abrasive finishing (MAF) or MAAFM process, polishing operation is performed using magnetic field throughout the working zone between base specimen surface and revolving magnet-poles head, as shown in Fig. 1.6 (a). The magnetic field provides rigidity and preserves ferromagnetic abrasives in the working zone [17].

### 1.2.3.3 Magnetic Float Polishing (MFP)

The finishing methods described in the previous sections were designed for ground structures, tubular structures, or their variants, resulting in complicated 3D shapes which do not qualify for the finishing of spherical structures. To satisfy this need, the magnetic float polishing (MFP) method was proposed [18]. The polishing technique involves mechanical brushing and chemo-mechanical cleaning. The spherical ceramic balls are polished underneath, under the control of magnetic transmutation (buoyant) force through relative movement between balls and abrasive particles [19]. Description of the experimental setup utilized in polishing silicon nitride ($Si_3N_4$) ceramic balls with the help of a limited loading MFP system is shown in Fig. 1.6(b).

### 1.2.3.4 Chemo-mechanical Polishing (CMP)

In the CMP method, both chemical and mechanical processes are used together for material removal. Generally, it is used to finish semiconductor material. A new soft abrasive grinding wheel (SAGW) used in chemo-mechanical grinding (CMG) was developed for machining

silicon wafers. The wheel consisted of magnesia (MgO) soft abrasives, calcium carbonate ($CaCO_3$) additives, and magnesium oxychloride bond. The grinding with the new SAGW produced a surface roughness (Ra) of about 0.5 nm and a subsurface damage layer thickness of about 10 nm. This study also revealed that the chemical reactions between MgO abrasive, $CaCO_3$ additives, and silicon material did occur during grinding, thereby generating a soft reactant layer on the ground surface. The reactant layer was easily removed during the grinding process [20]. The mechanism of chemo-mechanical polishing is shown in Fig. 1.6(c).

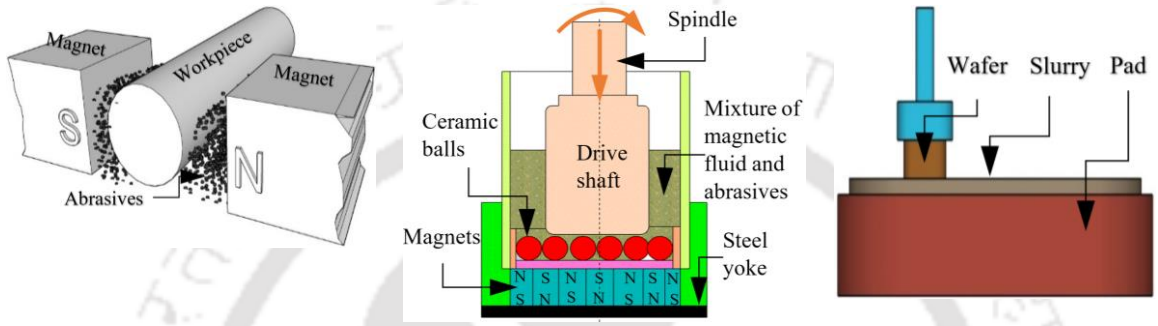


(a) (b) (c)

**Fig. 1.6** (a) Mechanism of MAF process, (b) schematic of MFP, and (c) CMP setup

### 1.2.3.5 Magnetorheological Finishing (MRF)

Initially, MR fluid was used as working media in dampers, actuators, breaks, clutches, seals, valves, or composite structures. Later MR fluid has proved its capability in producing complex aspheric optics used for aerial surveillance with an accuracy somewhere around 50 nm, surface roughness below 1 nm [21]. Besides glass, zinc, gallium, quartz, sapphire, silicon nitride, arsenide, and selenide can also be finished by MR fluid [22], [23]. The MRF process primarily consists of a workpiece, a rotating wheel or a rotating fixture, a delivery nozzle, a suction pump, and a magnet. Three primary methodologies mentioned in most MRF-related literature are (a) rotating wheel method, (b) rotating tool method, and (c) rotating disk method.

In the rotating wheel method, a magnetic carrying wheel revolves. MR fluid applied on the wheel became stiffened on magnetic field processing. Owing to the magnetic field gradient, CIPs migrate toward the wheel, and abrasives move toward the specimen. It pulls MR fluid to the colliding distance between the specimen and the wheel. Whenever the carrier wheel rotates, material removal occurs. The principle of the rotating wheel method of MRF is displayed in Fig. 1.7(a). This kind of polishing method is often employed to polish the asphere optical specimen [24]. In the rotating tool, MR fluid sticks to the edge of a magnetic polishing tool and creates a versatile end form polishing device [25]. The rotating polishing tool is subjected to

the magnetic field; thus, MR fluid stiffens at the edge of this versatile tool. The abrasive particles come nearer to the specimen surface, and material dislodgement occurs. This rotating polishing device, also recognized as ball end MRF (BEMRF). This process could polish various complicated structures like concave, convex, asphere and freeform structures as it can move in 3 or 5-axis CNC machines [26]. The principle of the rotating tool method is shown in Fig. 1.7(b). The continuous replenishment of MR fluid takes away heat and debris, and thus wearing of the cutting tool can be avoided. An MR fluid-loaded disk is often employed in the MRF process, where the test specimen is immersed in the vessel [27]. The magnet's north and south pole lift up the disk, and a spinning spindle carries the specimen [28]. In this method, the disk revolves at a lesser speed than the rotating spindle to create a relative movement. MR fluid in the disk becomes stiffened under magnetic field. The specimen can be either rotating or static during the process, which relies on the polishing system. The principle of the rotating disk method is shown in Fig. 1.7(c).

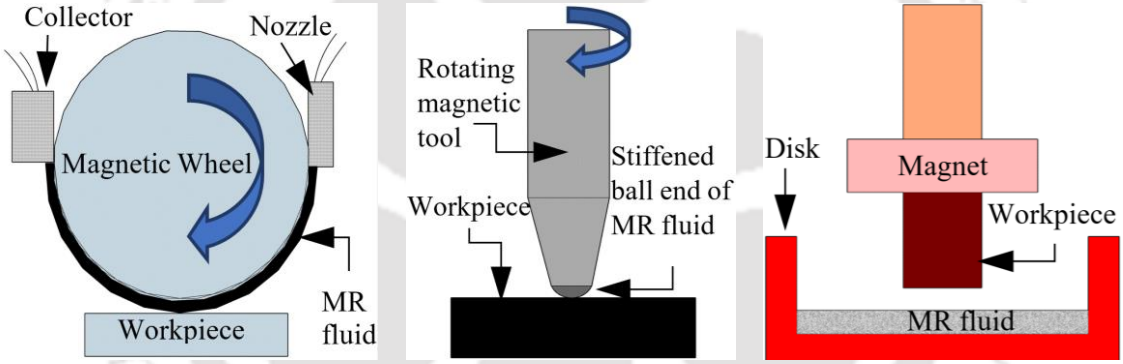


**Fig. 1.7** Principle of rotating (a) wheel, (b) tool, and (c) disk MRF methods

## 1.2.4 Hybrid Processes

### 1.2.4.1 Magnetorheological Abrasive Flow Finishing (MRAFF)

MR fluid containing iron and abrasive particles is utilized in AFM to establish the magnetorheological abrasive flow finishing (MRAFF) process [29]. In the MRAFF process, the advantages of both AFM and MRF technology were combined. A magnetic field is applied for the stiffening of MR fluid. In the MRAFF process, a similar AFM setup (Fig. 1.5(b)) is used. The AFM media is replaced with MR fluid along with an external magnetic field. Finishing occurs only on the portions wherever the magnetic field is applied. The abrasives

added in MR fluid, shear the peak of the surface that comes in their flow path, thus polishing the surface. The mechanism of the MRAFF process is shown in Fig. 1.8(a).

### 1.2.4.2 Rotational Magnetorheological Abrasive Flow Finishing (R-MRAFF)

Rotational motion of magnet or workpiece is added in MRAFF process to develop Rotational-MRAFF (R-MRAFF) process. Due to the movement of the magnet fixture, MR fluid also moves along with the fixture to generate a relative movement between the specimen and MR fluid to polish the surfaces uniformly. The working principle of the R-MRAFF process is demonstrated in Fig. 1.8(b). R-MRAFF process can improve the overall accuracy of ground channels, long tunnels and blind holes. This method can also do highly precise polishing of different freeform surfaces, commonly made up of complex materials like stainless steel (SS), titanium, nickel-chromium steel and cemented carbide [30], [31].

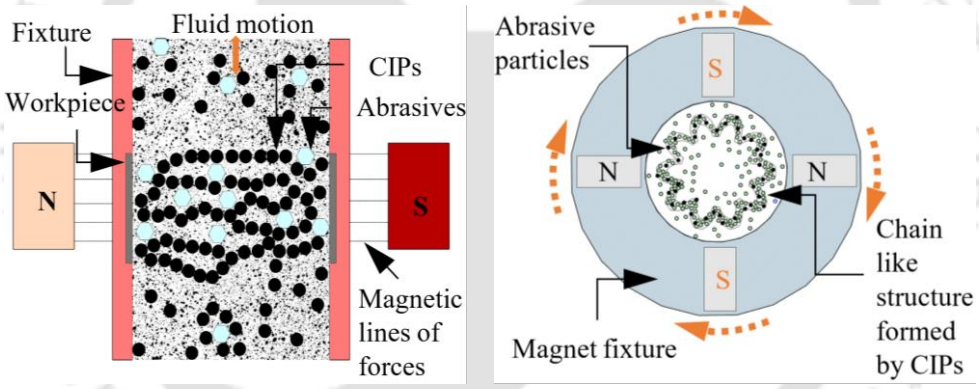


(a) (b)

**Fig. 1.8** Mechanism of (a) MRAFF and (b) R-MRAFF process

## 1.3 Literature Survey

Magnetorheological fluid-based finishing (MRFF) processes are precise finishing processes where a magnetic field is used to control the forces involved during finishing. Using these processes, deterministic finishing can be easily achieved. The following subsections describe the work reported in the area of MRFF processes. In subsection 1.3.1, a literature review about MR fluid is presented. In subsection 1.3.2, a relevant literature survey on gear components (manufacturing defects) and their finishing processes related to the present work is discussed. In subsection 1.3.3, a literature survey on poppet valves used in various applications and their

finishing method is described. In subsection 1.3.4, a theoretical investigation into the MRFF process, i.e. mathematical modelling, force and stress analysis, is presented.

## 1.3.1 Magnetorheological (MR) Fluid

Different MR fluid formulations are required for the various materials [32]. The most suitable option is water-based MR fluid for metallic surfaces and oil-based MR fluid for ceramic-based surfaces. In general, MR fluids should have large saturation magnetization and small coercivity or remnant magnetization. MR fluid should also be able to maintain its rheological properties over a wide range of temperatures. MR fluids are required to be stable against settling and oxidation. The iron particles (IPs) used in MR fluids are very small in diameter of approximately 3–10 μm, dispersed in a non-magnetic carrier fluid. The magnetizable particles used are mainly iron particles. The IPs widely used are carbonyl iron particles (CIPs) formed by the thermal decomposition of iron particles [33]. CIP is basically iron pentacarbonyl, ($Fe(CO)_5$) powder. CIPs have high saturation magnetization as well as higher oxidation stability. High permeability and low magnetic residue of CIPs are preferable for fine surface finish [34]. For diamagnetic materials such as copper and its alloys, electrolytic iron particles (EIPs) are used for a better surface finishing. EIP is bigger in size than CIPs and gives higher finishing forces. Fig. 1.9(a) and (b) demonstrate the field emission scanning electron microscopic (FESEM) photograph of CIPs and EIPs, respectively. The circular shape and softness of CIPs give the minimum contribution in MRR relative to MR fluid having abrasives because they are irregular in shape [35]. Abrasives that are mostly used are $Al_2O_3$, $ZrO_2$, $CeO_2$, $SiO_2$ (silica), SiC, CBN, boron carbide ($B_4C$), natural diamond, synthetic diamond, or their combinations [36]–[38]. All are just high-hard ceramic particles [32].

Generally used carrier media are water, mineral oils, polyethers, synthetic hydrocarbons and silicone oil [39]. Depending upon the applications, water-based or oil-based carrier media could be implemented. Water-based carrier media are generally used to finish metal components when a higher MRR and finishing performance are required [21]. In comparison, oil-based carrier media are more generally used in finishing ceramic-based surfaces [40]. Oil as a base material eliminates abrasive contact to the workpiece surface. Water-based fluid produces greater friction due to lack of lubrication relative to the oil-based fluid, resulting in higher polishing efficiency [39], [41]. Apart from carrier fluids, additives are also added to discourage the accumulation and settling of CIPs. Apart from this, additives supply necessary lubrication and resistance to corrosion and wear [42], [43]. The corrosion-resistant agent is

critical as water is a carrier media in most MR fluids. Commonly added additives are polymers, grease, thixotropic agents, glycerol and surfactants [25], [44]. Acid additives have also been used for the synthesis of stable MR fluids [33]. The behaviour of MR fluid changes with the change in particle size. Jain et al. [45] used 5% abrasives ($CeO_2$), 47% carrier fluid, 8% stabilizer and 40 % magnetic particles for polishing a copper workpiece. They observed a 71.51 % improvement in surface roughness value. For polishing of copper workpiece, Jha and Khan [25] used 14% $Al_2O_3$ as abrasive, 23% magnetic particle, and 63 % carrier fluid. They observed a 42.34% improvement in surface roughness value. Chen et al. [46] used 6% Al2O3, 57% carrier fluid, 1% stabilizer, and 36% magnetic particles for polishing a stainless steel workpiece. After polishing, 97.83% improvement in surface roughness value was observed. The compositions of MR fluid depend on the workpiece material and the required surface finish.

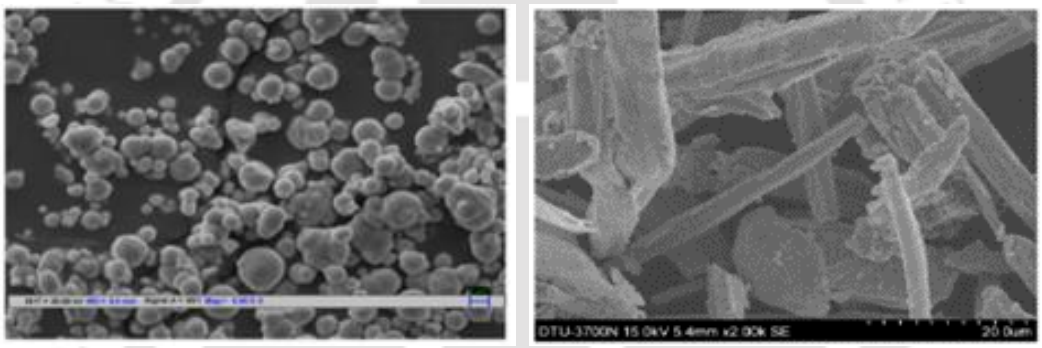

(a) (b)

**Fig. 1.9** SEM images of (a) CIPs and (b) EIPs [47], [48]

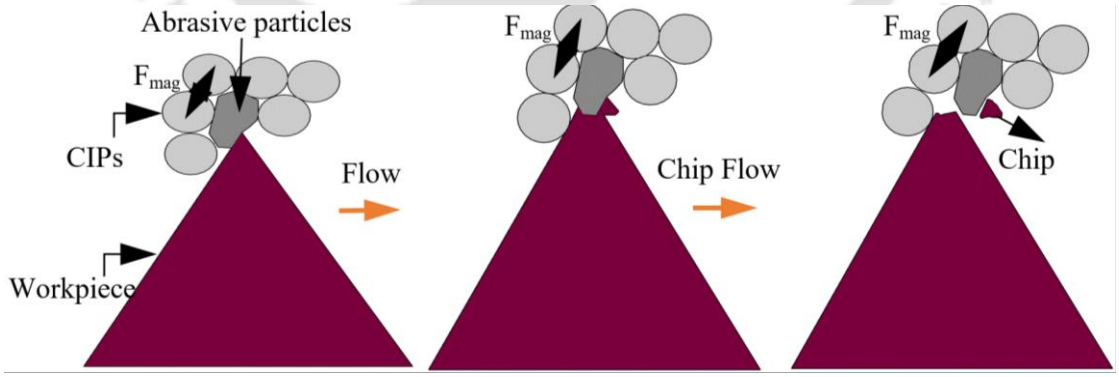


(a) (b) (c)

**Fig. 1.10** Abrasive particle (a) approaching, (b) taking a small cut, and (c) crossing the roughness peak after microchip elimination during cutting operation [29]

In MR fluid, CIPs forms a chain-like structure along the magnetic field lines. It makes the MR fluid thick [44]. Abrasives stuck in-between CIPs chains dislodge the materials from the

workpiece surfaces [29]. In the MR fluid-based finishing method, normal and tangential forces are responsible for indenting and cutting higher roughness peaks. The working principle of MR fluid is shown in Fig. 1.10. As shown in Fig. 1.10 (a), CIPs are bound by attractive magnetic force under the effect of a magnetic field. In-between these CIPs, abrasive particle is stuck. As the MR fluid flows across the roughness peak, the stuck abrasive takes a slight cut on the roughness peak (Fig. 1.10(b)). Finally, the cut mico-chip is flown away from the surface roughness peaks to give a flat smooth surface.

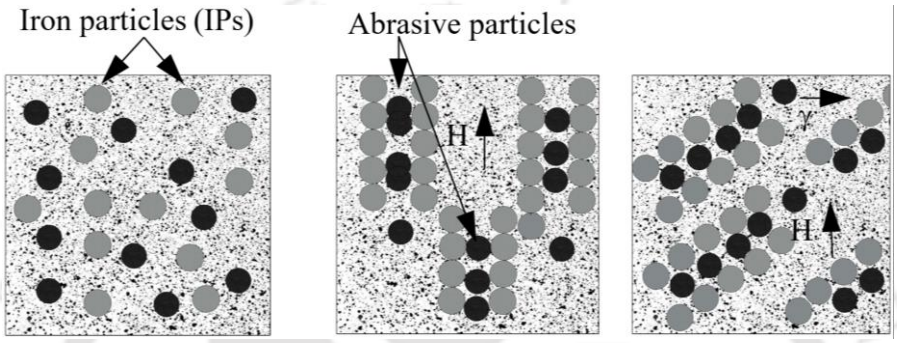


**Fig. 1.11** Magnetorheological effect: MR fluid (a) under no magnetic field, (b) using magnetic field strength (H), and (c) using magnetic field strength (H) and shear strain (γ) [49]

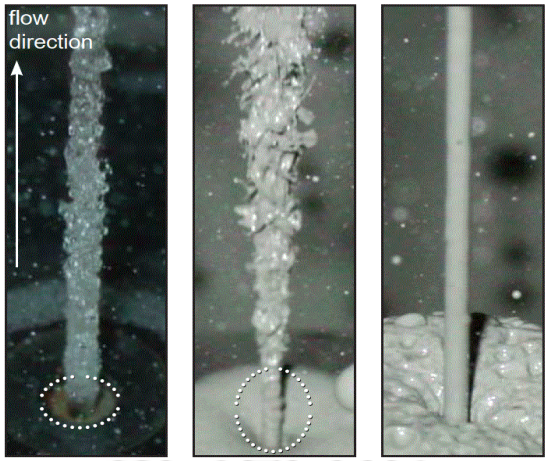


**Fig. 1.12** (a) Water jet and MR fluid (b) without and (c) with the magnetic field at a velocity of 30 m/s from a 2 mm diameter nozzle [50], [51]

Without a magnetic field, MR fluid behaves like a Newtonian fluid [52]. The magnetorheological fluid thickens and acts as a viscoelastic fluid in an external magnetic field. The magnitude of viscoelasticity largely depends upon the applied magnetic field. As CIPs form a chain-like structure across magnetic field lines, the energy that is required to overcome and break the chains is responsible for starting wide, restricted yield stress [53], [54]. The yield

stress is more resilient to an emitted shear strain (Fig. 1.11(c)). CIPs organize in an ordered fashion around magnetic field lines (Fig. 1.11(b)). After removing the magnetic field, CIPs stay in random order within the carrier fluid (Fig. 1.11(a)). Without a magnetic field, MR fluid functions as a dispersed jet (Fig. 1.12(b)) and using a magnetic field, MR fluid works as a directed jet (Fig. 1.12(c)), showing the same behaviour as the water jet having speed of 30 m/s (Fig. 1.12(a)).

### 1.3.1.1 Viscosity Models of MR Fluid

The relation between shear stress and shear rate must be evaluated depending on the application of MR fluid [55]. In order to ascertain this relationship, various model has been proposed, and their validity is checked using regression analysis. Bingham plastic, Casson fluid and Herschel-Bulkley models are widely used mathematical models depicting the behaviour of MR fluid with a relation between shear rate and shear stress. Herschel-Bulkley model is well known for shear thinning or shear thickening behaviour of the MR fluid [32]. The simplest model that depicts the behaviour of MR fluid is the Bingham plastic model [56]–[58]. The yield stress of MR fluid relies on both the concentration and size of the CIPs. Yield stress rises mostly by the increment in the percentage amount of the CIPs. The fluid prepared by finer CIPs exhibits comparatively lower yield stress compared to fluid prepared by coarser CIPs [42].

The plot of shear stress ($\tau$) against shear rate ($\dot{\gamma}$), is called 'flow curve'. For a Newtonian fluid, the flow curve is a straight line. The slope of the curve is, $\eta$ and it passes through the origin as shown in Fig. 1.13 (a) [59]. The flow curve is non-linear in the case of non-Newtonian fluid. And it does not pass through the origin, i.e., where the apparent viscosity (shear stress divided by shear rate) is not constant at a given temperature and pressure but is dependent on flow conditions such as flow geometry, shear rate, etc. The most common type of non-Newtonian fluid behaviour observed is pseudoplastic or shear-thinning. It is characterized by apparent viscosity, which decreases with increasing shear rate. Common pseudoplastic fluids are lava, ketchup, blood, paint and nail polish, etc. Most MR fluids show significant shear thinning behaviour because of the suspension agent and changes in CIPs structure during shear [60]. A dilatant fluid (also called shear thickening fluid) is a non-Newtonian fluid in which apparent viscosity increases with increasing shear rate. An example of shear thickening fluid is a suspension of corn starch and sand in water.

MR fluid is visco-plastic in nature. The existence of yield stress ($\tau_y$) characterizes this visco-plastic fluid behaviour. Before the fluid starts flowing, this yield stress must be

surpassed. Such kind of fluid deform elastically when externally applied stress ($\tau$) is smaller than the yield stress ($\tau_y$). Once the magnitude of generated shear stress has exceeded the value of yield stress, the flow curve may become linear (Bingham plastic fluid) or non-linear (Herschel-Bulkley fluid and Casson fluid ) but will not pass through origin [59]. A common example of visco-plastic fluid behaviour includes particulate suspension, emulsion, foodstuffs, blood and shrilling mud etc.

A fluid that behaves linearly for $|\tau| > |\tau_y|$ is called Bingham plastic fluid and is characterized by a constant plastic viscosity and yield stress. On the other hand, a fluid possessing yield stress as well as a non-linear flow curve on linear coordinate (for $|\tau| > |\tau_y|$) , is called a 'yield pseudoplastic' fluid (Herschel-Bulkley fluid and Casson fluid).

The study of rheological properties of MR fluids, such as shear yield stress and viscosity, is crucial as they are the key design factors in the applications of MR fluids. A rheometer is used to obtain the shear stress and shear rate data. By using the data, the constitutive models are proposed to interpret the important parameters. Herschel-Bulkley and Casson Fluid models (Fig. 1.13(b)) indicates shear-thinning nature. Over the years, many empirical expressions have been proposed. The commonly used models for visco-plastic fluids are briefly described in the following subsections.

***Bingham Plastic Model***

This model assumes that the MR fluid behaves like a solid substance before reaching critical shear stress. This yield stress is called yield point, and beyond this yield point, it behaves like a Newtonian fluid [61]. Beyond yield stress ($\tau_y$), the properties change from a rigid solid to a viscous liquid. The yield stress obtained using this model is the dynamic yield stress, which is the intercept of the high shear rate asymptote with the shear stress axis. The shear stress ($\tau$) versus shear rate ( $\dot{\gamma}$ ) relationship followed by such a fluid is as follows

$$\tau = \tau_y + \eta\dot{\gamma} \tag{1.1}$$

where, $\eta$ is the viscosity of the MR fluid.

***Herschel-Bulkley Model***

The Herschel-Bulkley model is considered to characterize MR fluid's rheological behaviour, which is non-Newtonian with pseudoplastic properties [61].

$$\tau = \tau_y + K\dot{\gamma}^n \text{ for } \tau > \tau_y \quad (1.2)$$

Where, $K$ is the consistency index, and $n$ is the power-law index. Here $\tau_y$ is a function of the magnetic field. The Herschel-Bulkley model is a modification of the power-law model. This model also assumes that the suspension behaves like a solid below the critical value of shear stress. The Bingham plastic model can be considered a special case of the Herschel-Bulkley model for $n = 1$. The parameter $K$ resembles the viscosity. The flow curve for Herschel-Bulkley models for different values of the power-law index ($n$) is shown in Fig. 1.13(c). Power-law index ($n > 1$), indicates a shear thickening fluid and $n < 1$ indicates a shear-thinning fluid (Fig. 1.13 (a)).

***Casson Fluid Model***

In describing the time-independent viscosity, the most widely used empirical model was developed by Casson. In this fluid model, it is considered that rigid primary particles flocculate into rod-like structures, and an expression is developed for the tension in rods under flow. The rods break when the tension exceeds a critical value. With increasing shear rate, the length of the rods will progressively be reduced until the rods are completely broken down into primary particles at very high shear rates. Based on this reasoning, the relationship between the shear stress (τ) and shear rate ($\dot{\gamma}$) becomes [61].

$$\sqrt{\tau} = \sqrt{\tau_y} + \sqrt{\eta_\infty \dot{\gamma}} \text{ for } \tau > \tau_y \quad (1.3)$$

Where, $\eta_\infty$ is the suspension viscosity at infinite shear rate. The Casson fluid model represents the fluid's continuous shear thinning behaviour, decreasing viscosity from infinity at zero shear rate to zero at the infinite shear rate [61]. The above-mentioned models are inconsistent and have computational difficulties. Hence, apart from the models mentioned above, some new combined models have been proposed as described below.

***Bingham-Papanastasiou Model***

Owing to the discontinuous nature of the Bingham plastic model, it is challenging to implement in numerical schemes. To solve this, Papanastasiou proposed one equation that is valid for the whole range of shear stress (both the yielded and unyielded zones) and is given as [62]

$$\eta = \mu + \frac{\tau_y}{|\dot{\gamma}|}\left[1 - e^{(-m|\dot{\gamma}|)}\right] \tag{1.4}$$

where, $m$ is regularizing parameter (consistency index), which regulates the exponential increment of stress. $\eta$ is the non-linear (non-Newtonian) viscosity. $\mu$ is the Newtonian viscosity (no outside magnetic field is present and fluid yield stress is zero), $\tau_y$ is critical shear stress (yield stress) that disrupts the magnetic chain structure (Fig. 1.11). Higher yield stress suggests a greater MR impact of the MR fluid. Here $\eta$ is a function of the magnetic field (H).

***Herschel-Bulkley-Papanastasiou Model***

For the same reason as mentioned earlier, a combination of Herchel-Bulkley [63] and Papanastasiou [64] models was proposed, and the modified equation is given below

$$\eta = K|\dot{\gamma}|^{n-1} + \frac{\tau_y}{|\dot{\gamma}|}\left[1 - e^{(-m|\dot{\gamma}|)}\right] \tag{1.5}$$

***Casson-Papanastasiou Model***

Combined Casson-Papanastasiou model is given below [65],

$$\eta = \sqrt{\mu} + \sqrt{\frac{\tau_y}{|\dot{\gamma}|}}\left[1 - e^{(-m|\dot{\gamma}|)}\right] \tag{1.6}$$

Ginder and Davis [66], [67] calculated the inter particles forces and resulting shear stresses in MR fluid. The effects of magnetic nonlinearity and saturation on the shear stresses of MR fluids have been studied using a finite-element technique and analytical approximation. They reported that, at the lowest applied magnetic field ($H_0$), the yield stress varies as $H_0^2$. For intermediate applied fields, the polar and contact region of each particle are saturated; in this region, the yield stress is predicted to increase as $H_0^{1.5}$ as,

$$\tau_y = \sqrt{6}\phi\mu_0 M_s^{0.5} H_0^{1.5} \tag{1.7}$$

where, "$\phi$" is the volume fraction of CIPs, "$H_0$" is applied magnetic field strength (A/m), $\mu_0$ is the magnetic permeability of free space ($4\pi\times10^{-7}$ N/A$^2$). The particles can be treated as dipoles for fields high enough to achieve complete saturation; the stress is then independent of the magnetic field and scale as $M_s^2$. The yield stress in this region is given as,

$$\tau_y^{sat} = \frac{4}{5^{2.5}}\xi(3)\phi\mu_0 M_s^2 \tag{1.8}$$

where, $M_s$ is saturation magnetization and $\xi(3)$ is Riemann zeta function.

Ginder [68] also observed the shear-thinning behaviour of MR-fluid (i.e., it possess an apparent decreasing viscosity with increasing strain rate) at all applied fields. They found that the yield stress depends upon magnetic flux density as $\tau_y \propto B^{1.5}$.

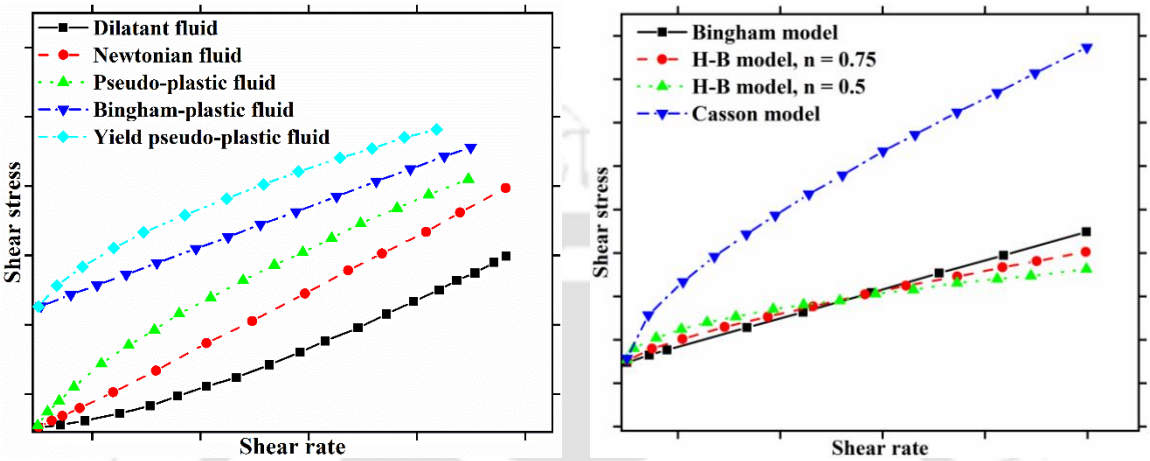


**Fig. 1.13** Different time-independent flow behaviour [59], (b) flow characterization of MRP fluid [61], [69]

## 1.3.2 Gear

The gear tooth profiles require finishing at nano-level to achieve smooth transmission of power, noiseless operation, reliability and longer service life. The gear tooth profiles suffer a considerable amount of damage due to manufacturing defects and repetitive operations. Utilizing the conventional tool for gears finishing at high MRR may increase tooth profile error due to the transverse grinding lines, burns, fine cracks, uneven stress, and thermal distortion. The rough surface and shape inaccuracy of a gear tooth profile occurs because of the high speed of the material removal mechanism, which leads to undesirable effects such as noise and vibration in the gearbox.

For a small gear, the finishing process on a tooth profile is much more complicated than a conventional shaped gear. Very few finishing processes can be applied to small gears due to the narrow spacing between their teeth. Due to the small space between the gear teeth, the conventional method cannot achieve the desired result. An ultra-precision MRFF method has been developed to perform nano-finishing on the small gear tooth profiles.

Miniature gears are used in biomedical devices for pumping, cutting, and various other works, also used in small servo motors, which are widely used in the automotive and aerospace

industry. Spur gears are used for mechanical transmission by two parallel shafts. The effect of surface finish on gear tooth plays a major role [70]. To improve the efficiency of gear, proper finishing is required. Generally, lapping, grinding, honing, electrochemical honing etc., are used to finish the gears [71]. For the modern mechanical transmission's high-speed, heavy-duty, low noise and higher fatigue life, a better surface finish on the gear surface is required [72]. The life span of gears is increased by better finishing of the gear surfaces [52].

Generally, small gears are fabricated by the hobbing process. The hobbed gears mainly have two types of defects, namely burrs and pits. These are typically found at the edge of the gear teeth. In the case of small gears, even if the burrs and pits of the size of 0.01 mm, are quite large compared to small gears. Apart from these, there are also many scratches and dents on the gear tooth surfaces and between gear teeth. Gillespie [73] reported that the burrs deteriorate the quality of the gear. Burrs can be defined as the excess unwanted material which remains at the edge of the gear or any workpiece after processing. Gillespie and blotter [74] have defined four types of burrs, i.e., poison burr, rollover burr, tear burr and cut-off burr. Poisson burr is derived from Poisson's ratio. When the material is compressed, it has a tendency to bulge at the sides of the material. This is known as Poisson's burr. In the case of Poisson's burr, the material is compressed until permanent deformation occurs. By tearing of the materials, some burrs are formed on the surface, known as tear burr.

Rollover burrs are generally formed at the side of the tooth in case of hobbing. Generally, rollover burrs are removed by using a disk-shaped whetstone or by a deburring tool. The rollover burr in the gear and process of deburring for rollover burr is shown in Fig. 1.14 (a) and (b), respectively. Miyake et al. [75] defined two types of burrs in their study. One is the primary burr, and the other is the secondary burr. They described the rollover burrs as the primary burrs. A new burr is generated when the deburring tool or whetstone is used to remove the rollover burr. This type of burr is defined as secondary burrs. The secondary burrs are protruded towards the tooth groove, which is difficult to remove using deburring tools.

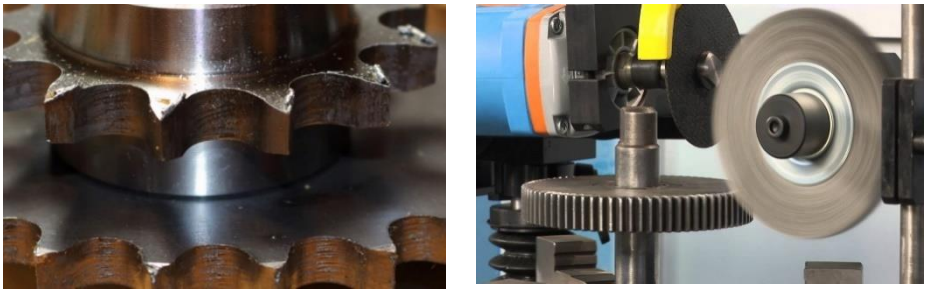

(a) (b)

**Fig. 1.14** Rollover burr in gear, and (b) gear deburring tool for rollover burr [76]

Even though the secondary burrs are sometimes removed using nylon/abrasive filament brush, most of the time, burrs remain at the root of the gear because the tooth groove is narrow (in between teeth). Pits are also found in small gears along with the primary and secondary burrs. The different burrs and pits formed on different surfaces of a small gear, is shown in Fig. 1.15.

Tazakawa and Kitajima [77] described that a pit is composed of a dent and projection due to plastic deformation that is generated when striking another object. Kawasaki et al. [78] devised a method for crushing pits; it did not experiment on small gears. The need for high and precise finishing has become so necessary for meeting the demands of nanotechnology. With a target to meet the exigency of nanotechnology in mind, a new high precision technique using a smart material, i.e. MR fluid, have been introduced here. Small gears can be manufactured by a wire-EDM (WEDM) process. During the wire-EDM cutting process recast layer might form on the machined surface of the gear workpiece. Due to the spark produced during the EDM process on the material surface, the melted metal undergoes rapid quenching, resulting in a layer of this metal forming on the workpiece surface. This unwanted layer of metal produced during the EDM process is known as the Recast layer (Fig. 1.16). Depending on the material of different workpieces, the effect of this recast layer also varies. Those materials which have more thermal conductivity are subjected to a thinner layer.

On the contrary, the materials which have less thermal conductivity are subjected to a thicker layer. For the higher conductive material, the energy dissipation is more than the lower conductive material. In the current study, steel gear is fabricated by the WEDM process. A material with low thermal conductivity like steel can be expected to have a thicker affected layer with more cracking. The reason is, in the case of steel material while machining by EDM process, the spark intensity in the spark area remains longer before the material can dissipate the energy to the surrounding areas.

In the white layer of the recast layer, the microcracking phenomenon is extremely prominent. If the white layer becomes too thick or is not removed properly using finer EDM polishing, the effect of this microcracking may cause premature failure to the machined workpiece. Characterization of different parts of the recast layer is shown in Fig. 1.16. The depth of the white layer increases proportionally with the spark intensity during the EDM process. Various layers of the workpiece material get affected due to the EDM process. These affected zones are known as altered metal zone. Beneath the white layer, there is a zone known as the heat-affected zone (Fig. 1.16). The heat-affected zone retains the properties of the parent

material. The parent material of the workpiece is below this heat affected zone which is not affected by thermal treatment during EDM process.

Karpuschewski and Knoche [79] found that AFM is the best alternative method for the traditional finishing of gears. Xu et al. [80] also proposed that AFM is an effective way to deburring, polishing or radiusing, etc. They have investigated the effect of the AFM process on the surface of the helical gear.

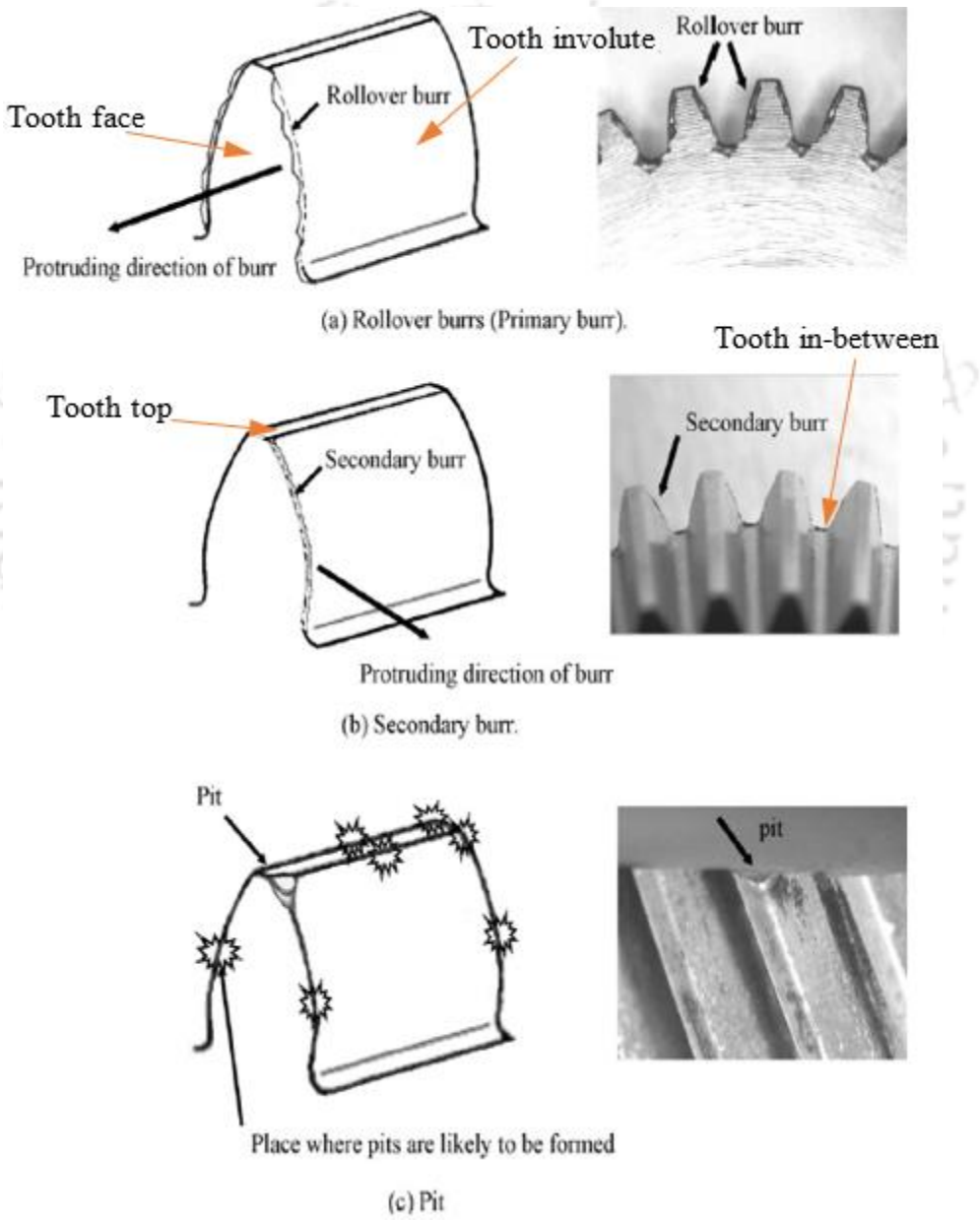


**Fig. 1.15** (a) Rollover burrs, (b) secondary burrs, and (c) pits formed on different surfaces of a small gear [77]

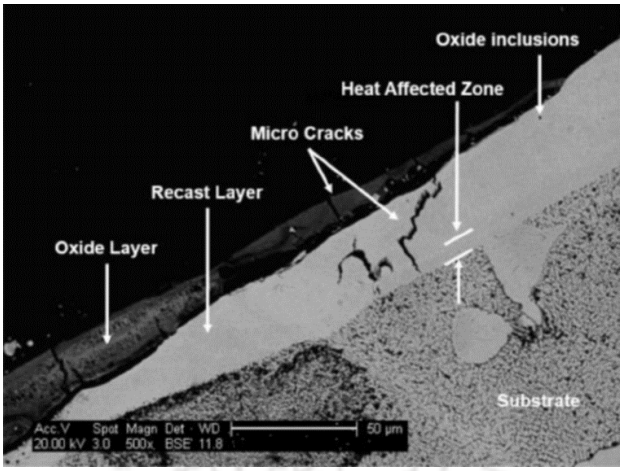


**Fig. 1.16** Characterization of different parts of recast layer [81]

Experimental results indicated that the surface roughness (Ra) of the left tooth surface, right tooth surface and addendum surface before processing (1.429 µm, 1.108 µm and 2.732 µm, respectively) dropped after processing (0.228 µm, 0.216 µm and 1.754 µm, respectively). All burrs at the intersection between the tooth and end surface have been cleared, and the helical gear's surface quality improved. Kenda et al. [52] used AFM process for plastic gear injection mould polishing. A polished surface on plastic gear teeth improves geometry stability and lifespan, which was proved on the gear testing rig. AFM generates consistent surface quality. The achieved roughness is homogeneous on an entire machined surface; it is reduced from Ra = 0.68 µm to Ra = 0.08 µm in 120 minutes. Samples have been produced using the WEDM process. This WEDM produced gear surface have defects such as a white layer, microcracks, and craters. With the application of AFM, it is possible to remove this damaged surface. The application of plastic gear in the servo motor is shown in Fig. 1.17(a).

Kenda et al. [82] proposed novel AFMmm (AFM with movable mandrels). They performed an energy consumption analysis to prove its efficiency. Results show that novel AFMmm can efficiently remove WEDM damaged surfaces and induce compressive residual stresses. Finishing time in the case of AFMmm technology is reduced more than seven times than conventional AFM. By using AFMmm process, plastic gears' fatigue life improved by 125%. Venkatesh et al. [83] utilized the AFM process for steel bevel gear finishing. New tooling for fixing bevel gears has been designed and developed so that the abrasive media passage is thoroughly restricted to abrade the gear tooth surfaces. AFM tooling setup is shown in Fig. 1.17(b). The results indicated that the improvement in the surface finish was more than 50%. However, the enhancement in material removal was marginal.

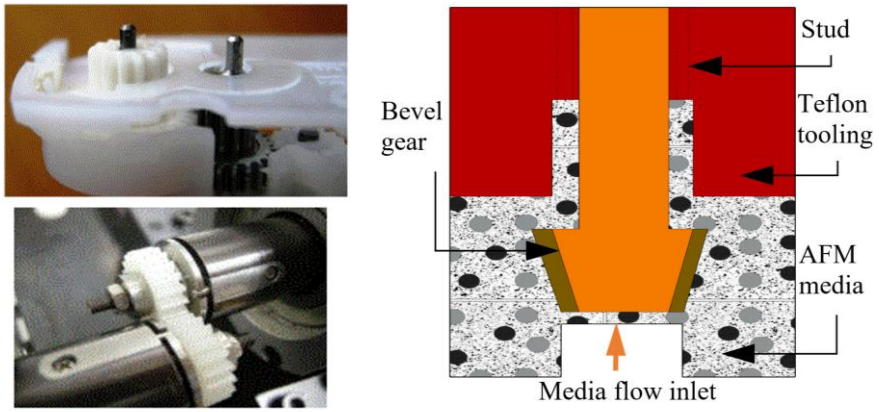


(a) (b)

**Fig. 1.17** (a) Application of plastic gear [52] and (b) tooling setup for bevel gear finishing by AFM [83]

Yadav et al. [84] have used the magnetorheological gear profile finishing (MRGPF) tool to finish a macro-sized EN-24 steel spur gear teeth profile with an addendum diameter of 47 mm. The MRGPF tool was made likely similar to the gear grinding profile wheel tool. Gear shaped tool with the electromagnetic core is shown in Fig. 1.18(b). The mechanism of polishing with this tool is shown in Fig. 1.18(a) and (b). This MR finishing has reduced the noise and vibrations of gears at high speed during its functional operation. Surface area roughness gets significantly reduced to 25.3 nm from its initial ground tooth profile of 242 nm. The surface texture also gets significantly improved.

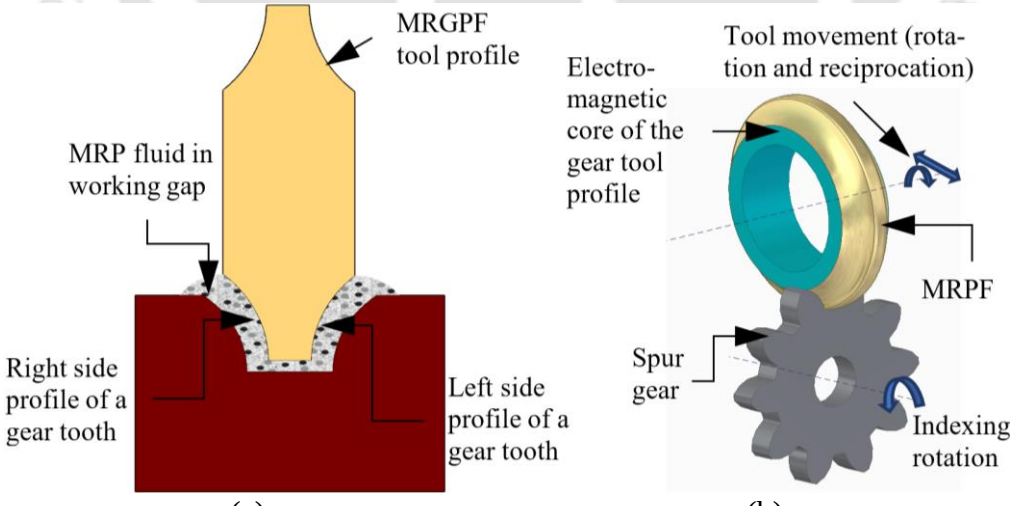


(a) (b)

**Fig. 1.18** (a) Finishing mechanism of MRGPF process, and (b) MRGPF tool movement similar to disk wheel gear grinding [84]

Based on the previous work on the gear finishing, it is found that no MR fluid-based finishing method has yet been applied on small-sized/miniature gears (pitch diameter < 15 mm). Almost

all techniques are used for conventional macro-sized gears. The uniform point-contact finishing on miniature gear tooth profiles is difficult to achieve due to constraints related to fixture material and fixture design. Also, the previous processes do not efficiently remove manufacturing defects from the miniature gear profiles.

### 1.3.3 Poppet valve

The poppet valve is used to leak-proof sealing high-pressure gases in aerospace gas propulsion engines or internal combustion (IC) engines. This poppet valve can also be used as relief valves, selectors and pressure regulators [85]. The poppet valve is one of the classes of seating valves. The poppet valve has some fundamental advantages over other valves because of its simple construction and self-centring capability. The poppet valve's sealing effectiveness can be maintained easily than other valves [86]. The intake and exhaust valves of the gas propulsion engine cylinder generally use a poppet design [87]. The word poppet is derived from the popping action of the valve. Poppet valves are commonly fabricated in four primary configurations: semi-tulip, tulip**,** mushroom and ridge. The valve configuration utilized in any engine relies on the leak-proof criteria and size of the combustion chamber [88]. Nanofinishing of ridge profiles of the new poppet valve is a challenging task due to its narrowness. Precise finishing of the narrow ridges will enable the poppet valve to properly fit on the valve seat surface in the aerospace gas propulsion engine to make it leak-proof. Also, precise uniform nano-finishing will make the poppet valve both wear and corrosion-resistant [89]. Poppet valve should also show inertness towards chemical reactions. Poppet valve should have high-temperature resistance, mainly used as inlet and exhaust valves. Nickel aluminium bronze (BS1400: Gr.AB2) is used as poppet valve material due to its corrosion resistance and bearing properties. Surface roughness is an essential element in the estimation of part performance in a real environment. The MRFF process can be used very efficiently to finish these kinds of complex surfaces.

Bruno et al. [90] first patented a simple poppet valve composed of a flexible poppet that fits towards a valve seat. A simple poppet valve is shown in Fig. 1.19(a). It consists primarily of a movable poppet that closes against a valve seat. Pressure from the inlet tends to hold the valve tightly closed. A slight force applied to the poppet stem opens the poppet. The action is similar to the valves of an automobile engine [91]. The poppet stem usually has an O-ring seal to prevent leakage. In some valves, the poppets are held in the seated position by springs. The number of poppets in a valve depends on the purpose of the valve. The construction of a simple

2/2 normally-closed valve, where the depression of the pushbutton lifts the disc off its seat and allows fluid to flow, is shown in Fig. 1.19(b). When the button is released, spring and fluid pressure force the disc to close the valve. Poppet valves are simple, cheap and robust [92].

The high-pressure hydraulic systems use poppet valves [92]. The engine performance depends specifically on the initiation and duration of injecting air, method of opening the valve, air injection pressure, valve design, and other control parameters [93]–[95]. The different types of the poppet valve are shown in Fig. 1.20. Construction and design considerations among these poppets are different for intake and exhaust valves. Intake valves are made of nickel-chromium alloy [88]**.** In contrast, exhaust valves are made from silichrome alloy**.** In certain heavy-duty and most air-cooled engines, the exhaust valves are sodium-filled. During engine operation, the sodium inside the hollow valve melts. When the valve opens, the sodium splashes down into the valve head and absorbs heat.

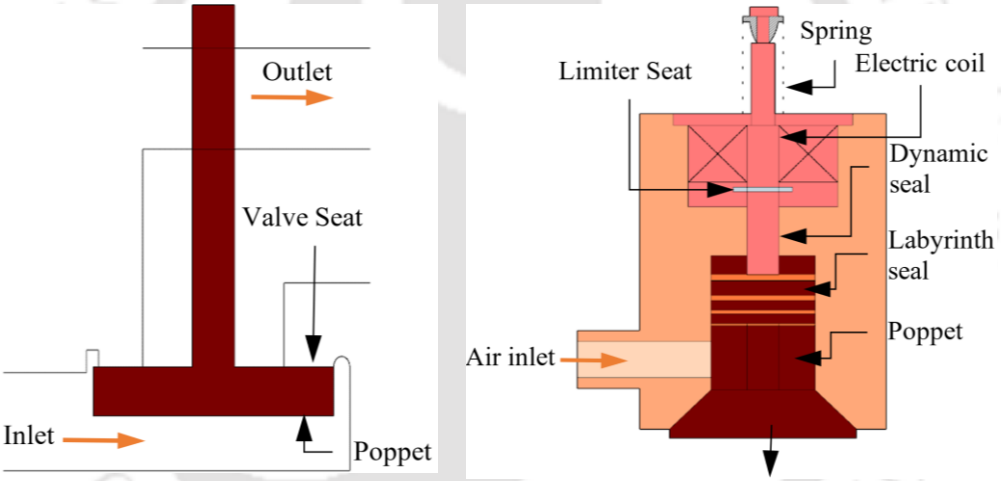


**Fig. 1.19** Schematic diagram of (a) simple poppet valve and (b) spring-loaded poppet valve

Poppet valves are the usual method for regulating air/fuel combination in the cylinder and exhaust gas flow from the IC engine [96]. More carbon film thickness on the valve prevents thermal shocks (due to developed thermal stress) by creating additional thermal resistance. Irregular carbon deposits on the valve face can cause the failure of the valve [97], [98]. Higher temperature and increased pressures produce seat wear, lower oxide films and higher head deformation. This may result in leakage in the combustion chamber, which decreases the engine's performance. The valve seats may be an integral part of the cylinder head, or an insert is pressed into the cylinder head. Valve seat inserts are commonly used in aluminium cylinder heads. Steel inserts are needed to withstand extreme heat. When a valve seat insert is badly worn from grinding or pitting, it must be replaced. The use of poppet valve in gas propulsion

engine, where the timing of inlet and exhaust opening depends upon the power requirements, is shown in Fig. 1.21. Valve seats are important, as they must match the face of the valve head to form a perfect seal. Most of them are now designed with a valve seat angle of 30° to 45°, as shown in Fig. 1.20. This angle helps in preventing excessive accumulation of carbon on the contact surface of the seat, a condition that allows the valve from closing properly.

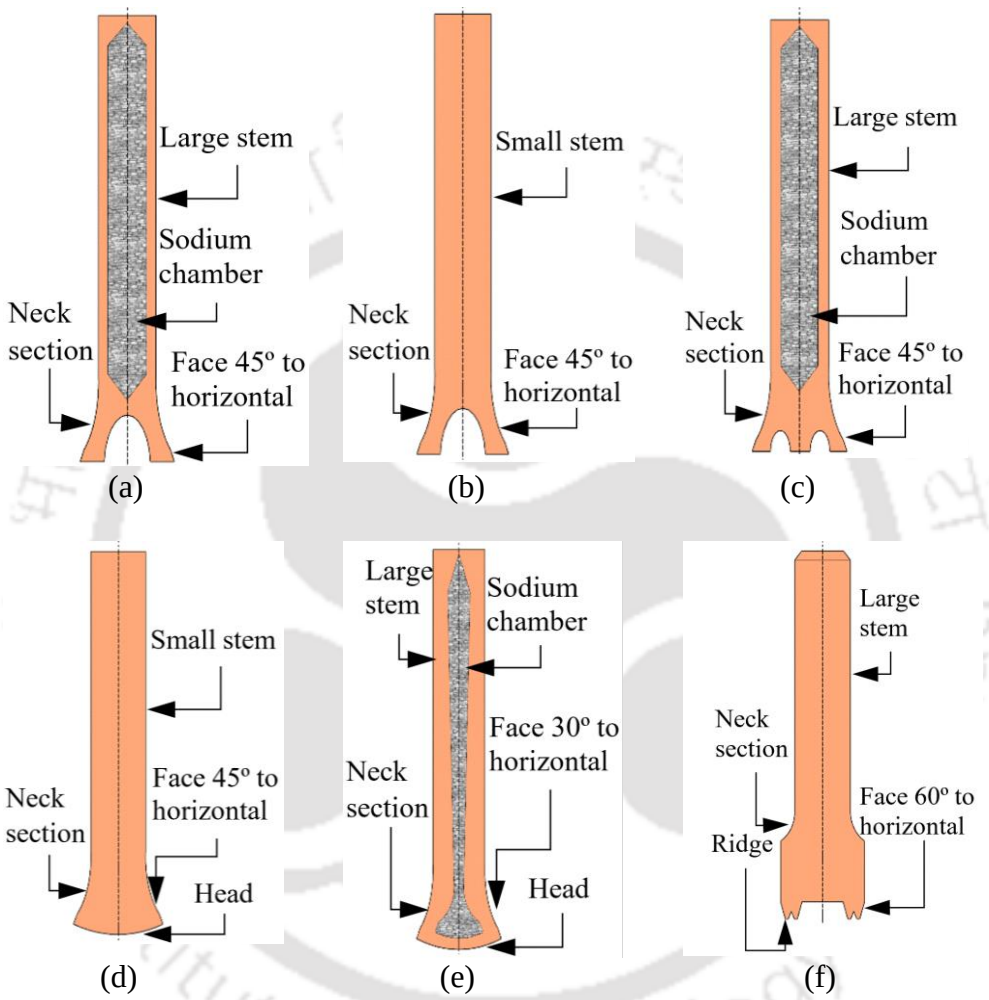


**Fig. 1.20** Schematic diagram of different types of poppet valves (a) full tulip type (usually exhaust), (b) tulip type (usually intake), (c) semi tulip type (usually exhaust), (d) mushroom type, (e) hollow head mushroom type (exhaust), and (f) ridge type (intake)

Adhesive and abrasive wear, shear strain, and material abrasion are the reasons for the seat wear of the intake valve/insert. Oxide film and tribo film can avoid direct metal connection. They decrease the friction coefficient on the sitting region, decreasing adhesive wear and wear regulated deformation [99]–[103]. Impact wear tests show that, at 400ºC (higher temperature), less acceleration of the wear rate was observed due to oxidation [104]. Residual fuel-burning deposits on valve seats cause rapid corrosion due to a molten phase presence [105]. The valves used in truck engines failed due to the formation of lamellar structure. The lamellar structure

reduces the strength, matrix loading capacity, durability and resistance to gas corrosion [106]. The valve seat leakage increases the percentage of more hydrocarbon emissions [107]. Poppet valves are affected by creep, fatigue, thermal stresses, wear, corrosion, resulting deposits, and valve burning from corrosion via exhaust surroundings, which leads to loss of properties of the material and engine efficiency [108], [109]. Due to the poorly finished surface, the poppet valve does not properly fit on the valve seat and can cause leakage problems [91], [110]. A good valve seat ensures the perfect mixture of air-fuel ratios. During compression and expansion strokes (power stroke), the valves work at high speed and withstand high temperatures, which leads the valve to undergo huge thermal stress, resulting in wear and tear of the valve. This wear and tear of the valve create the problem of exhaust gas leakage inside the chamber. To ensure a proper seal, generally, the valve lapping process is used. Hence, valve maintenance is a critical operation [91], [100]–[104], [110].

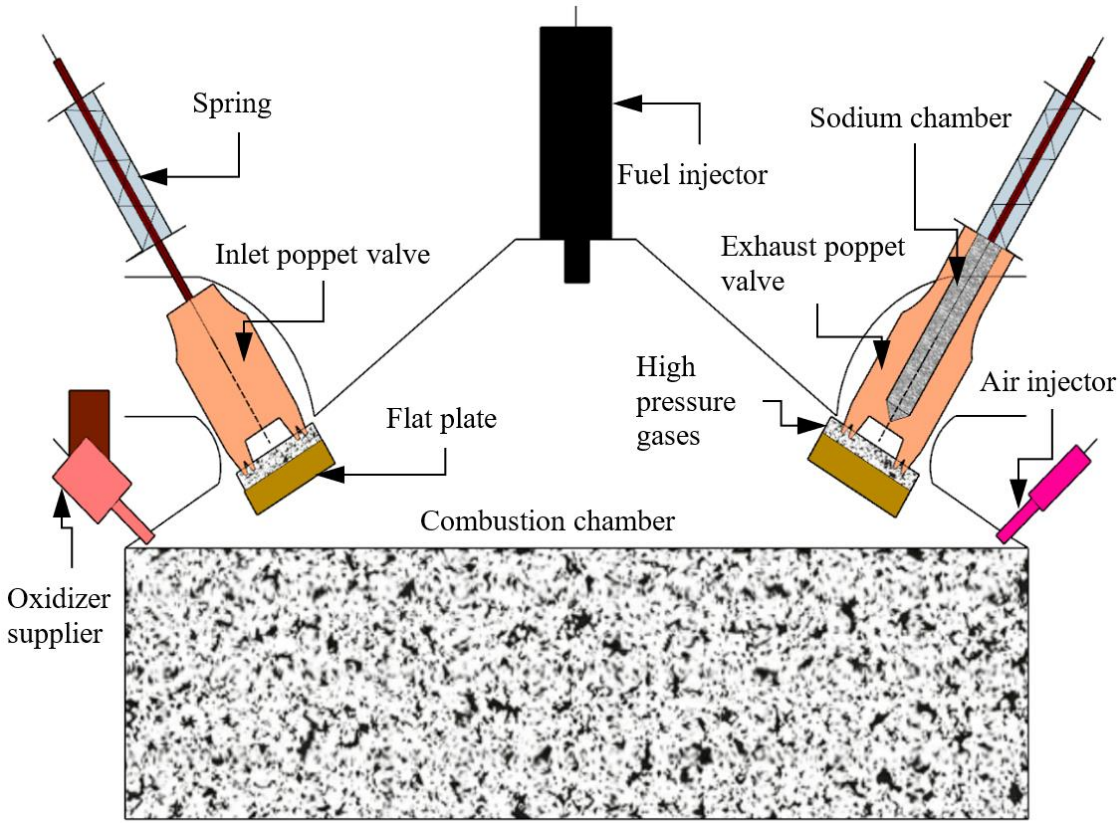


**Fig. 1.21** Poppets used as inlet and exhaust valve in gas propulsion engine

Initially, the lapping stick was used for performing the lapping operation of the valve by hand. The valve lapping paste was used for the lapping process [111]. A particular machine was made for spherical lap mating surfaces to form a perfect seal between a valve member and the seat against which it closes [112]. A valve seat lapping machine is made, more particularly for

lapping ball valves and seats in liquid-tightened insulating interaction [9], [113], [114]. A particular valve lapping machine is designed for internal combustion (IC) engine for overcoming certain issues by eliminating human intervention, reducing labour costs and taking less time in lapping valve and valve seats. Lapping is achieved by adding a synthetic paste (almost all oil and an adequate quality of sand) to the valve surfaces and rotating them on the head end in their respective seats/inserts. [99]. Electrochemical honing (ECH) and micro-grinding were used to get a higher degree of precise surface smoothness of the restoration surfaces of the engine valve face. ECH process was a better choice than micro-grinding for the finishing of recovered surfaces [115].

Mattsson et al. [89] have tested 28 different designs of poppet valves with different materials for corrosion resistance capacity with natural seawater. Poppet valve of aluminium bronze was partially affected after exposure due to its specific design considerations and surface finish [116]. The valve seat, badly worn from grinding or pitting, can cause the failure of the valve. When the contact area is reduced, the surface is highly finished uniformly, and the tension among the grouping sections strengthens, resulting in safer sealing [93]. The mirror-like finishing operation leads to good strength of the material even if any joints are formed [9]. The valve stem is mainly associated with tensile stress, and the shock causes circumferential scratches. Tool marks or scratches from the circumferential fatigue loci, in some cases during the use of the valve, causes complete failure of the valve. Elaborate lapping operations are used to remove tool marks or scratches caused by reaming tools or drills in the valve cavities. The valve's continuous smooth superior inner surface will enable it to resist the formation of fatigue cracks and increase the valve's strength [110], [117]. The reaming and polishing with abrasive paper form an amorphous layer (Beilby layer) over the surface of the internal wall of the valve. This amorphous layer causes a relatively low grade of heat transfer. Electropolishing of the internal surfaces of hollow metal valves can remove the objectionable amorphous layer [118].

Based on the previous work on the poppet valve finishing, it is found that no MR fluid-based finishing method has yet been used for poppet valve profile polishing. The precise finishing of the narrow ridge profiles of the new poppet valve is difficult to achieve by the conventional lapping process. Also, the uniform point-contact finishing on poppet valve profiles is difficult to achieve due to constraints related to fixture material and fixture design. The uniformly finished poppet valve will have improved wear and corrosion resistance and sealing effectiveness, further reducing hydrocarbon emissions.

## 1.3.4 Theoretical Investigation

### 1.3.4.1 Mathematical Modelling

In the MRFF process, the material removal rate is similar to the conventional polishing process. So, Preston's equation [119] is considered as the building block to understand and develop mathematical modelling for the process. Preston's equation for material removal rate is given as

$$MRR = C_P PV = C_P \frac{F_n}{A_c} V \tag{1.9}$$

Where $C_p$ is Preston's coefficient, $P$ is applied normal pressure, $V$ is the relative velocity between tool and workpiece, $F_n$ is the normal force, $A_c$ is the contact area between tool and workpiece.

Tricard et al. [50] modified Preston's equation for material removal analysis. The material removal rate is proportional to the product of local shear stress and fluid velocity. Their proposed model is simulated using a commercial CFD package, and the results are validated with the experiment. The parameters used in the calculation are jet radius, mesh area and mesh size. Their proposed model is

$$\dot{R}_r \sim \tau_r V_r \tag{1.10}$$

where $R_r$ is material removal rate, $V_r$ is the local fluid velocity, $\tau_r$ is local shear stress.

DeGroote et al. [120] also modified Preston's equation for calculating the material removal rate of optical glasses finished by the MRF process with nanodiamond abrasive particles. They observed that peak removal rate and drag force did not show the same relationship for different glasses due to their different chemical properties and compositions. Hence, they incorporated mechanical properties of the glass surface, drag force ($F_d$) or shear stress, polishing particle properties, chemical properties of the workpiece and polishing fluid into the modified Preston's equation for a better understanding of the process. The theoretical model is validated with experiments for six different types of glass workpieces. The other process parameters, i.e., wheel speed, magnetic field, viscosity, working gap, etc., are kept constant throughout the experiments. Their material removal model is given as

$$MRR_{peak} \propto \left[\frac{E_s}{K_c.H_s^{\,2}}\right]\left[\frac{F_d}{A}.V\right]\times\left[B_{nd}\phi_{nd}^{\,-1/3}.C_{nd}^{\,1/3}+B_{CI}\phi_{CI}^{\,4/3}.C_{CI}\right]\times\left[D_s\left(PH_{MRF}\right)^{3/10}\right]\left[e^{-\frac{sbs}{bRT}}\right] \quad (1.11)$$

where $E_s$ is Young's modulus, $K_c$ is fracture toughness of the bulk material, $H_s$ is nanohardness of the near surface layer, $A$ is contact area, $V$ is velocity of the wheel, $B_{nd}$ and $B_{CI}$ are coefficients, $\phi_{nd}$ and $C_{nd}$ are average particle size and concentration of nanodiamond abrasive particles, $\phi_{CI}$ and $C_{CI}$ are average particle size and concentration of CIPs, $D_s\left(PH_{MRF}\right)$ is percent weight loss of the glass in the MR fluid, $\left[e^{-\frac{sbs}{bRT}}\right]$ is glass average single bond strength.

Jung et al. [121] developed a theoretical model to calculate the total force exerted on the CIPs at the workpiece surface. The total force is composed of centrifugal force and magnetic force. The centrifugal force ( $F_{CEN}^{(r)}$ ) acting on a CIPs at a distance $r$ from the centre of the tool is calculated as

$$F_{CEN}^{(r)} = \left(\rho_p\left(4\pi r_p^3\right)/3\right)\left(\left(r_h-r\right)/\left(2r_p\right)\right)\left(\left(r_h+r\right)/2\right)\omega_T^2 \quad (1.12)$$

where $\rho_p$ and $r_p$ are the mass density and mean radius of the CIPs, respectively. $\omega_T$ is rotational speed of the wheel. The simplified form to calculate magnetic attraction force ( $F_{MAG}^{(r)}$ ) between two CIPs is given as

$$F_{MAG}^{(r)} = \frac{3m\left(\left|\vec{H}(r)\right|\right)^2}{4\pi\mu_0\mu_1\left(2r^p\right)^4} \quad (1.13)$$

where $\mu_0$ is permeability in free space, $\mu_1$ is relative permeability, $\vec{H}(r)$ is magnetic field intensity, and $m$ is magnetic dipole moment.

A material removal model for the MRF process was developed by Cheng et al. [24]. The model depends on normal pressure and carrier wheel velocity during finishing. The hydrodynamic pressure is more than magnetic pressure by six orders of magnitude. The material removal model proposed by them is based on Preston hypothesis, and it is given as

$$\text{Material removal} = K\int PVdt \quad (1.14)$$

where $K$ is a constant which depends on the workpiece material and the properties of MR fluid, $P$ is the normal pressure, and $V$ is the velocity of the wheel (tool) with respect to the workpiece surface. However, the validation of their derived model does not match their experimental

results. Further, the results obtained from the Preston equation does not accurately give the output result as the equation only deals with the basic parameters, i.e. pressure, velocity and time.

Miao et al. [122] modified Preston's coefficient for MRF process. Important parameters considered for material removal in the finishing process are hydrodynamic pressure, shear stress and a combination of the material figures of merit (FOM). Experimental results for a range of optical glasses are used for validation with the calculated model. Their predictive model is

$$MRR_{MRF} = C'_{(p,MRF(\tau,FOM))} E / \left(K_c H_V^2\right) \tau V \tag{1.15}$$

where $C'_{(p,MRF(\tau,FOM))}$ is modification of Preston's coefficient in terms of shear stress $\tau$ and material FOM, $E$ is Young's modulus, $K_c$ is fracture toughness of bulk material, $H_V$ is Vicker's hardness of workpiece, and $V$ is wheel velocity.

Miao et al. [123] further modified Eq. (1.15) to incorporate four other process parameters i.e. nanodiamond concentration, penetration depth, magnetic field strength and relative velocity due to their material removal contribution. The model is developed based on BK7 glass workpiece material, although the model can also be applied to other glasses by altering mechanical FOM for that specific material.

### 1.3.4.2 Force analysis

The knowledge of finishing forces is necessary for polishing any surface to control the process efficiently. Shorey et al. [35] showed that material removal significantly depends on shear stress rather than hydrodynamic pressure. Also, they associated normal force and drag force with the Preston coefficient. They reported that the abrasive particles are driven towards the workpiece surface due to the magnetic field gradient. The MRR increases with the addition of abrasive particles. A reduction in total drag force is observed with the increase in abrasive particle concentration. Kim et al. [124] found that levitation force also contributed to the material removal process by pushing the abrasive particles into the workpiece surface. Magnetic levitation force depends upon the volume of the non-magnetic particles, the intensity of magnetization and magnetic field gradient.

DeGroote et al. [120] found that with the increase in nanodiamond concentration, the drag force/shear stress increases; however, with further addition in nanodiamond abrasive particles, there is no increase in peak removal rate. It is also reported that with different glass

materials, the drag force required for material removal changes. Schinhaerl et al. [125] measured normal force in between workpiece surface and the finishing tool using a three-axis dynamometer for BK7 glass workpiece at different process parameters such as wheel speed, inductor current (magnetic field strength), pump speed (fluid flowrate) and immersion depth. The normal force primarily depends on immersion depth. They measured a maximum normal force of 20 N.

Miao et al. [122] measured normal force and drag force simultaneously using a dual force sensor. They found that the measured normal force is dependent on material hardness. Their study also demonstrates that shear stress dominates the material removal more than the drag force. It has also been reported that shear stress should be kept above certain critical value to remove material. Miao et al. [123] reported that shear stress does not depend on the nanodiamond concentration, penetration depth, magnetic field strength and relative velocity between the workpiece and the rotating MR fluid ribbon. Instead, it depends mainly on the mechanical properties of the material. Also, they reported that both drag force and normal force increase with the addition of nanodiamond particles and become steady with higher nanodiamond concentration.

Sidpara and Jain [126] carried out an experimental investigation to measure the normal and tangential forces on the workpiece surface. For this study, four parameters are selected, i.e. volume concentrations of CIPs, the volume concentration of abrasive particles, working gap and wheel speed. Among all parameters, the working gap and volume concentration of CIPs affect most significantly on the forces. Normal and tangential forces decrease with increasing working gap, while these forces increase with increasing CIP concentration. Both normal and tangential forces decrease beyond 3.5 % abrasive concentration.

Sidpara and Jain [127] conducted a theoretical study on the normal, tangential and squeezing force acting on the workpiece surface. They developed a normal squeeze force model. The theoretical models are validated with the experimental results for different working gaps, CIPs, abrasive concentration, and wheel speed. It is found that the theoretical normal and tangential force model matches well with the experimental results while considering squeeze force as compared to without squeeze force. Singh et al. [128] developed a model of finishing force acting on the workpiece surface. The finishing force is generated due to the bonding strength of MR polishing fluid and the rotation of the finishing tool. The finishing force is composed of normal force and shear force.

Sidpara and Jain [129] analyzed forces acting on the freeform surface by experimental as well as theoretical studies. They reported that mainly two types of forces, namely normal and

tangential forces, are involved during finishing. The normal force is applied on the abrasive particle through surrounding CIPs, and this force is responsible for indentation on the workpiece surface. Tangential force generates due to the rotation of the finishing tool which helps in removing tiny chips from the workpiece surface. Components of normal force and tangential forces are considered in the case of the freeform surface due to the different angles of curvatures. Normal force includes magnetic levitation force and centrifugal force, and on the other hand, the tangential force includes shear force and Coriolis force. The process parameters considered in this study are the angle of curvature of the workpiece, tool rotational speed and feed rate. Both the magnitude of normal force and tangential force decrease with increasing angle of curvature; however, with the increase in tool rotational speed and workpiece feed rate, these forces attain a maximum value and then decrease.

## 1.4 Objectives of the Present Thesis

The surface of a component plays a vital role in its performance and life span. To create a simple polishing setup for automatized uniform finishing of complex surfaces such as miniature gear and poppet valve, the rotational magnetorheological fluid-based finishing (R-MRFF) method is used. This process is capable of achieving the desired finishing at the nanoscale level. To explore the R-MRFF process with the developed polishing fixture following objectives are considered.

- To design and develop a polishing fixture for R-MRFF process to uniformly nano-finish the poppet valve and miniature gear component. The capability of R-MRFF setup to finish such complex surfaces is to be analyzed and explored.
- Simulation study to optimize the dimension and design of the polishing fixture. A preliminary experimental study to analyze the capability of the developed fixture to finish workpiece surfaces at the nanometer level.
- To develop a flow restrictor for controlling the flow of MR fluid to uniformly pass through each and every corner of miniature gear tooth profiles in the R-MRFF process.
- To synthesize different MR fluid compositions to obtain the required surface finish and surface topography on the miniature gear and poppet valve components made of SS316L and Ni-Al-Bronze alloy, respectively.
- Characterization of the finished surfaces to explore R-MRFF fixtures' capability to fabricate poppet valve and miniature gear worthy surfaces. Statistical analysis to

optimize the process parameters to achieve the best surface roughness and surface topography.

- Simulation study to explore the finishing forces in the R-MRFF process. Development of a mathematical model to predict the final surface roughness value and material removal rate for both miniature gear and poppet valve based on finishing force analysis and finite element analysis (FEA).

## 1.5 Organization of the Thesis

The thesis is organized into seven chapters with references. The introduction to the finishing processes and related literature review is discussed in **Chapter 1**. The literature review of different finishing processes for complex surfaces is thoroughly presented. Also, different advanced finishing processes and hybrid magnetic field-assisted finishing processes are discussed, along with previous studies on the processes reported by various researchers. The literature survey related to MR fluid, finishing of miniature gear and poppet valve components, mathematical modelling, and analysis of finishing forces using magnetorheological fluid-based finishing process is presented.

Design and development of workpiece fixture and novel uniform flow restrictor for miniature gear are discussed in **Chapter 2**. A magnetostatic fluid-flow simulation study is conducted to optimize the design of flow restrictor in R-MRFF setup. An experimental study is also conducted to explore the capability of R-MRFF setup to provide uniform nano finishing on SS316L miniature gear teeth profiles.

Design and development of novel magnet fixture for finishing poppet valve using R-MRFF process is discussed in **Chapter 3**. A magnetostatic simulation study is conducted to optimize the design of R-MRFF setup and to fix the dimension of magnet fixture. An experimental study is also conducted to explore the capability of R-MRFF setup to provide nano finishing on poppet valve profiles made of Ni-Al-Bronze alloy.

In **Chapter 4**, various compositions of MR fluid are discussed regarding SS316L miniature gear finishing. Different methods are used to analyze the surface characteristics of the steel gear profiles before and after finishing with the R-MRFF polishing setup. An optimization study is carried out to minimize surface roughness value and maximize material removal rate (MRR). A statistical analysis is conducted to evaluate the significance of each process parameter.

In **Chapter 5**, various compositions of MR fluid are discussed regarding Ni-Al-Bronze alloy poppet valve profile polishing. Different methods are used to analyze the surface characteristics of the poppet valve profile before and after finishing with R-MRFF finishing setup. An optimization study is carried out to minimize the surface roughness value. A statistical analysis is conducted to evaluate the significance of each process parameter.

In **Chapter 6**, finishing forces involved in the R-MRFF process while finishing poppet valve and miniature gear teeth profiles are discussed. Surface roughness simulation is performed based on the finishing force analysis and FEA findings for poppet valve and miniature gear teeth profiles. The simulation study is further corroborated with the validation experiments. Mathematical modelling for material removal rate (MRR) is also carried out to accurately predict the final MRR for poppet valve and miniature gear teeth profiles.

Discussion about the conclusions and critical findings of the present study with the future scope is presented in **Chapter 7**. The references are added at the end.

# Chapter 2 Design and Development of Novel Flow Restrictor for Miniature Gear Polishing

## 2.1 Introduction

Previous research shows that uniform finishing is tough to achieve due to the fixture design and fixture material constraints while finishing complex miniature gear surfaces. While solving this particular problem, a special type of novel flow restrictor (which is a negative replica of miniature SS316L steel gear) is designed and developed to achieve uniform finishing across miniature gear teeth profiles. From Fig. 2.1 (a), it is observed that, magnetic field lines are not uniformly passing across gear tooth profile that it is spatially varying. Due to these spatially varying magnetic field lines, the abrasive particles trapped in formed iron particles (IPs) chain will not always with in uniform point contact to miniature gear tooth profile. So, the flow of fluid in the simple cylindrical fixture setup separates. This separation of flow from the gear workpiece may result in the formation of dead zones (Fig. 2.1 (b)) that are the regions on the workpiece surface where the removal of material is very low (almost zero) due to the insufficient or ineffective flow of the medium. In order to address this specific issue and to ensure a more regulated flow along the gear profiles, a novel flow restrictor has been developed as a resolution. By utilizing this flow restrictor, a consistent constrained gap (Fig. 2.1 (c)) will always be present between the flow restrictor and miniature gear, forcing MRP fluid polishing particles to make uniform point contact to the each and every corner surface of the gear tooth profile even in non-uniform magnetic field distributions for finally achieving high shape consistency and uniform surface finish at the nano-scale level. A 3D view of the finishing mechanism along gear tooth profile without and with using flow restrictor is shown in Fig. 2.1 (d) and (e), respectively. Random movement of polishing particles along the gear tooth profile will be seen in the absence of a flow restrictor (Fig. 2.1 (d)). However, with using a flow restrictor, a confined movement of polishing particles occurs across gear tooth profile, although the magnetic field is non-uniform (Fig. 2.1 (e)) [130].

For designing the suggested uniform flow restrictor, first of all, the uniform magnetic flux density, normal stress, and shear stress distributions are calculated along the gear teeth profiles using a finite element (FE) based Comsol® Multiphysics software package. Further, based on FE analysis (FEA) results applied on different preliminary geometries of uniform flow restrictors, the final model of the uniform flow restrictor and workpiece fixture is planned.

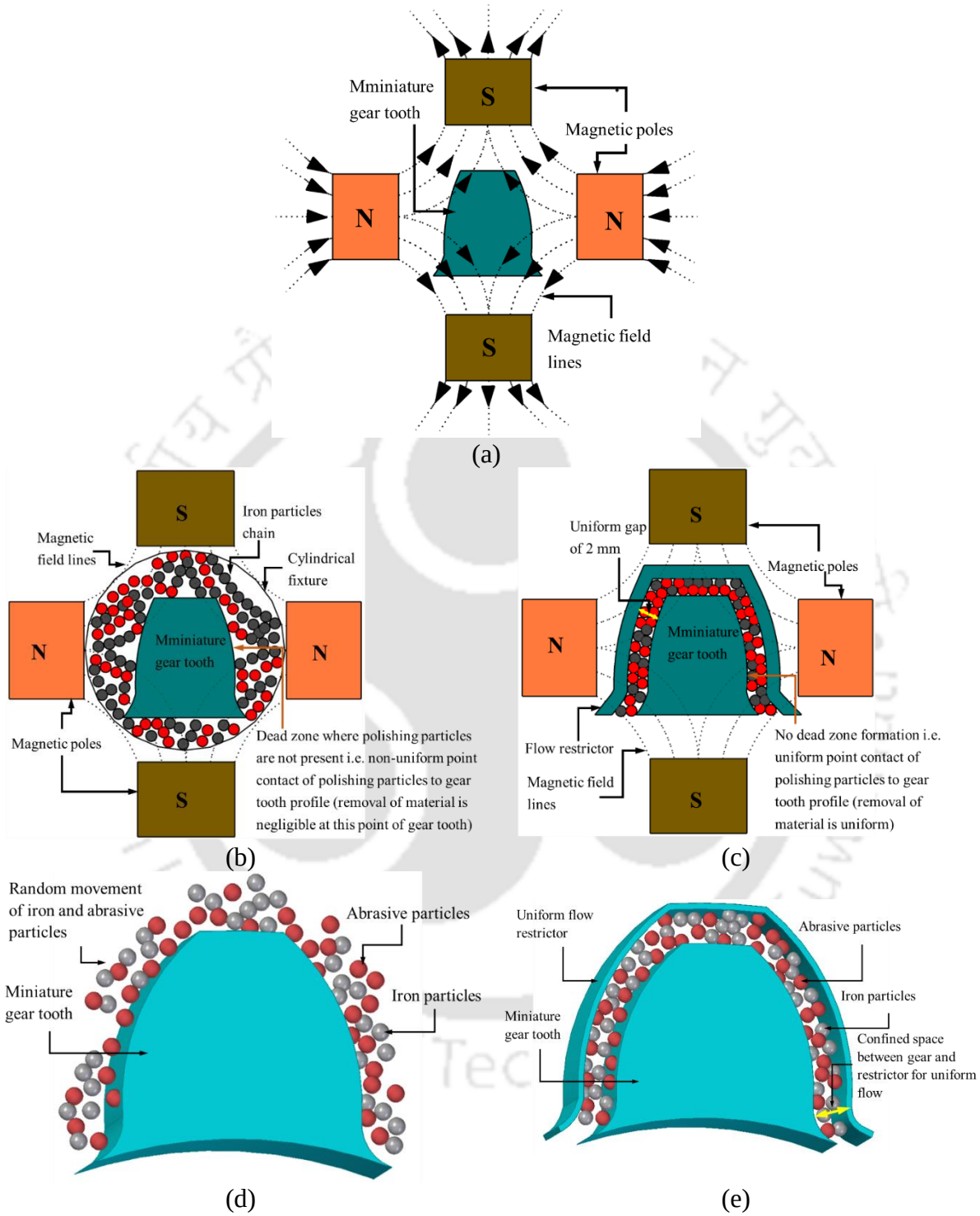


**Fig. 2.1** 2D schematic showing magnetic field line distributions during miniature gear MR polishing process; finishing mechanism at the gear tooth profile (b) without and (c) with using flow restrictor; 3D schematic showing (d) random and (e) confined movement of abrasive and iron particles across gear tooth profile without and with using flow restrictor

## 2.2 Magnetostatic Fluid Flow Analysis

To study the shear stress, normal stress, and magnetic field distributions on the gear profiles along with the MR polishing fluid without and with utilizing a uniform flow restrictor, the magnetostatic fluid flow was conducted using FEA-based Comsol® Multiphysics software package. The uniform flow restrictor is modeled as the exact negative replica of the gear teeth profiles to obtain uniformity in magnetic field, shear stress, and normal stress distributions on these profiles. Therefore, the gear tooth profile can be uniformly finished. MR polishing fluid is forced to flow in the gap between the uniform flow restrictor and gear. The input parameters used for the simulation study are provided in Table 2.1. Comsol® Multiphysics solves a fluid flow problem under a magnetic field by allocating materials, boundaries, and source conditions over a finite region space using Maxwell and Navier-Stokes equations. The magnetostatic fluid flow analysis for magnetic flux density, shear stress, and normal stress distributions is conducted with these specifications. Table 2.2 presents the boundary conditions used during the simulation study. The computational domain for fluid flow analysis with applied magnetic field without and with using uniform flow restrictor is shown in Fig. 2.2 (a) and (b), respectively.

Finishing forces are the main reason for the uniform material removal and excellent surface finish. These forces act on the workpiece through the abrasives. The magnetic force forms the cross-linked chains of magnetic particles under the magnetic field and helps indent the workpiece surface through trapped abrasives achieving desired surface roughness value. Literature survey reveals that two types of forces act on the workpiece surfaces, i.e., normal force and tangential force [131]–[133]. The tangential force is derived from the fluid structure interaction phenomenon. The normal force is modeled by considering magnetic levitation force and other normal forces depending upon the process, their impact on the workpiece at the time of fluid structure (workpiece) interaction. So, shear and normal stresses acting on the gear profiles can also be derived from the fluid surface interaction with an active magnetic field and applied pressure. The MR fluid behavior changes from Newtonian fluid (Zone-I, Fig. 2.2) to Bingham plastic fluid (Zone-II, Fig. 2.2) as the magnetic field is applied. In Zone-II (finishing zone), cylindrical workpiece fixture with eight incoming and outgoing holes are used for fluid flow. The inlet velocity ($U_s$ = 0.5 m/s) is uniform, calculated from piston movement and time to complete one stroke. At the outlet, a fully developed flow boundary condition is implemented. The walls have no-slip boundary condition. Table 2.2 represents the boundary conditions applied in Zone-I and Zone-II of the computational domain.

**Table 2.1** Input parameters used for simulation study

| Description | Value (unit) |
|---|---|
| Remnant flux density | 0.5 T |
| Volume fraction of magnetic particle | 0.22 |
| Density | 2594.3 kg/m$^3$ |
| Inlet velocity | 0.5 m/s |
| Pressure | 32.5 bar |
| Power law index | 0.3039 |
| Newtonian viscosity | 0.0358 Pa-s |
| Rotational velocity of magnet fixture | 100 rpm |

**Table 2.2** Boundary conditions

| Boundary type | Boundary conditions |
|---|---|
| Inlet | Uniform velocity ($U_s$ = 0.5 m/s) |
| Outlet | Fully developed flow (zero axial gradient) |
| Wall | No-slip |
| Interior wall (around workpiece fixture) | No-slip |

At the verge of Zone-I, the MR fluid transition gets started from Newtonian to non-Newtonian behavior. Zone-I remains unaffected from the magnetic field while Zone-II experiences change in fluid properties due to applied external magnetic field. Due to the uniform flow restrictor used in the fixture assembly, MR fluid is forced to flow as a uniform restricted movement. The following assumptions are considered to simplify fluid flow analysis:

- The flow is laminar, steady, and incompressible.
- The medium properties are considered independent of time and temperature. The temperature change with respect to time and location of the fluid is neglected.
- The medium is assumed homogeneous, although it contains solid particles.

For ensuring the uniform finishing along the involute, top, in-between, and face profiles (Fig. 2.3(a) and (b)) of gear tooth surfaces, a thorough study of magnetic flux density, shear stress, and normal stress distribution is conducted in the present study.

The fluid flows vertically with to & fro motions through the space between the steel gear tooth profiles and the fixture wall (Fig. 2.2). The area available for streaming MRP fluid is named as fluid channel. Hydraulic cylinders apply pressure to MRP media and force this media to pass across the gear tooth profiles through the workpiece fixture. Magnets kept in the magnet fixture rotate around the workpiece fixture for uniform gear finishing. During polishing, each distinct profile of a gear tooth is at different distance from the magnets and causes a varying magnetic field in the fluid flow area [134]. The rotation of magnets along with flow restrictor completely remove the inaccuracy caused by spatially varying magnetic field along the gear component surfaces, totally ensuring that each teeth profile polishes equally. Four Nd-Fe-B

permanent magnets are used for the current polishing operation (Fig. 2.2). The dimension of each magnet is 45×25×20 in mm. The fixture material for the gear component finishing is manufactured from brass since it is non-magnetic.

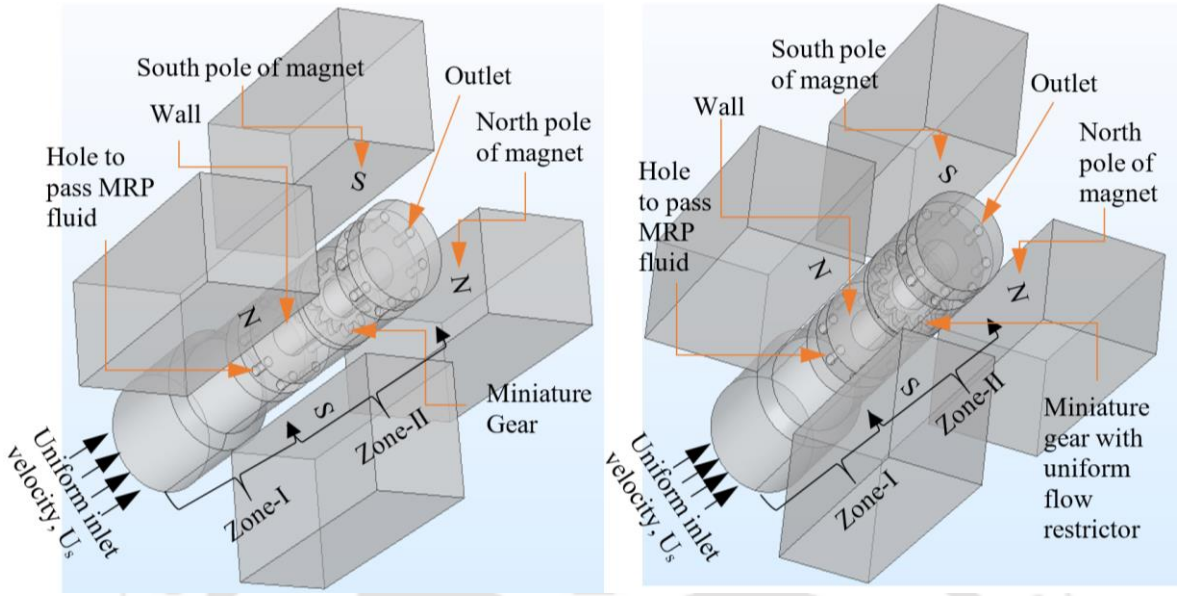


(a) (b)

**Fig. 2.2** Schematic diagram of 3D computational domain (a) without and (b) with using uniform flow restrictor for fluid flow analysis under applied magnetic field

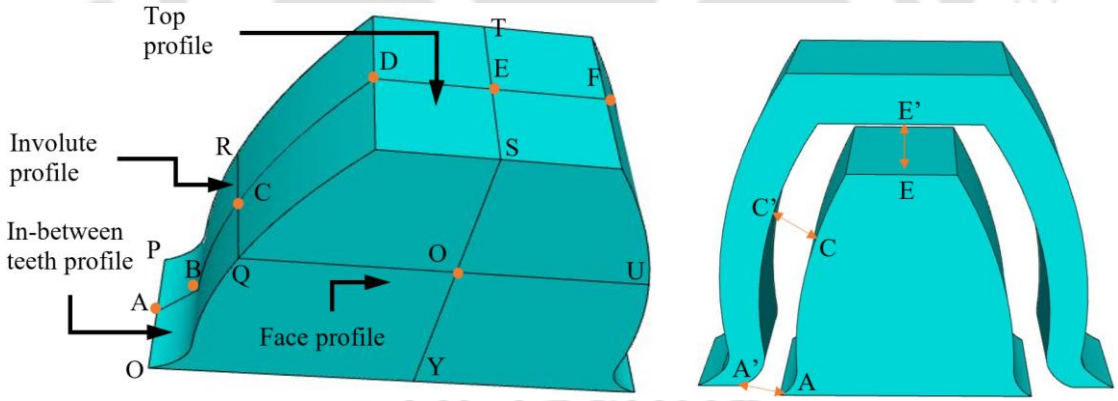


(a) (b)

**Fig. 2.3** Selected positions for comparing magnetic field, shear stress and normal stress distributions (a) along gear tooth in-between (AB), top (DF) & involute (BD) profiles and (b) in the gaps between miniature gear and uniform flow restrictor (AA', CC', EE')

Basic steps to perform simulation in the Comsol® Multiphysics software are to first import a geometry, add materials, add physics with their boundary conditions, mesh the computational domain, add study and compute the simulation process, finally get processed outputs. The rotation of magnets in simulation analysis is applied by considering identity boundary pairs in the computational domain, where source boundaries and destination boundaries are selected by

making a cylinder inside the computational domain. The moving mesh is considered for the rotational domain of magnets, and it is given as 100 rpm. This simulation model developed so far can be applied to any geometry and various parametric studies to find the optimum input parameters in the defined sets [135]. The outcome of this study would make the method more flexible and strengthen the mechanistic nature of this modern nano-finishing method.

## 2.2.1 Rheological Properties of MRP Fluid

MRP fluid flow is highly affected by modifications to external parameters rather than fluid channel design. Thus, to control the fluid's behaviour in the magnetic field, one must understand the fluid's magnetic properties. For this purpose, VSM analysis was conducted to obtain the M-B curve (Fig. 2.4(a)), and from that curve, the B-H curve is plotted. This B-H curve is used in simulation software to model the MRP media. The magnetic field strength can be evaluated as follows:

$$B = \mu_0 \left( H + M \right) \tag{2.1}$$

$$M = \rho M_m \tag{2.2}$$

Where $B$ is magnetic flux density (T) or (Wb/m$^2$), $\mu_0$ is the relative permeability of free space (Wb/A.m), $H$ is magnetic field strength (A/m), $M_m$ is mass magnetization (emu/g), $\rho$ is the density of MRP media (2.5943 g/cm$^3$). By putting the experimental values in Eq. (2.1), the B-H curve (Fig. 2.4(b)) is plotted.

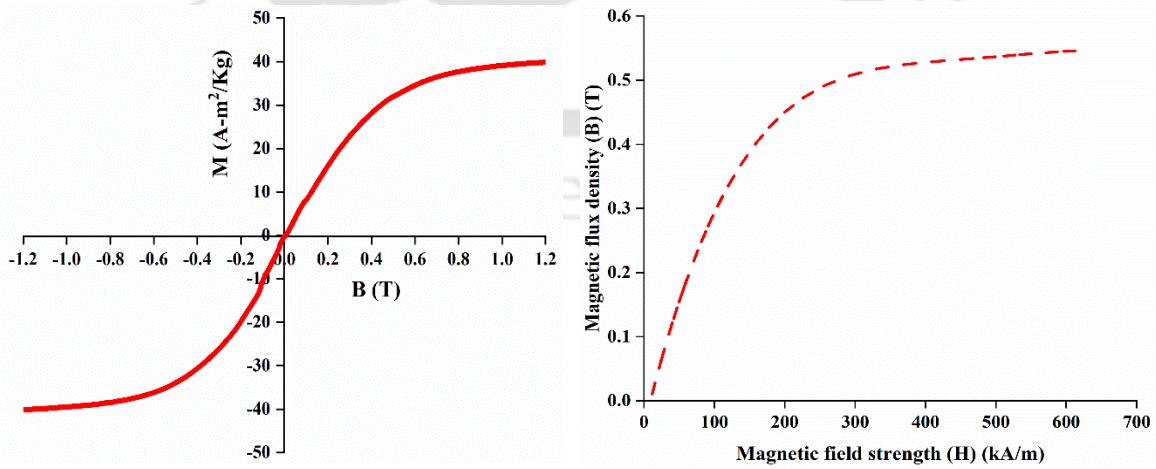


(a) (b)

**Fig. 2.4** (a) M-B and (b) B-H curves of MRP fluid

The MRP media viscosity varies in the fluid channel because of magnetic field and shear rate variation while flowing. The MRP media density, having a homogenous blend of all constituents, is evaluated by the following equation:

$$\rho_{MRP\ media} = V_{IP}\rho_{IP} + V_{AP}\rho_{AP} + V_G\rho_G + V_P\rho_P \tag{2.3}$$

where $V$ is volume fraction of each constituent, and $\rho$ is density of each constituent. As ($\rho_{ip}$ = 7.86 g/cm$^3$, $\rho_{AP}$ = 3.22 g/cm$^3$, $\rho_G$ = 0.825 g/cm$^3$ , $\rho_p$ = 0.875 g/cm$^3$), putting these values in Eq. (2.3), MRP media density is found to be 2.5943 g/cm$^3$. The Bingham plastic model is the best suited viscosity model of MRP media [136].

The Bingham plastic model is discontinuous in nature. So, it cannot be directly applied in simulation for computational purposes. Smoothing techniques are used to remove the point of discontinuity. The best approximate solution for an appropriate discontinuous model is given by the following equations [65].

$$\tau = \eta\dot{\gamma} \tag{2.4}$$

where $\tau$ is shear stress (kPa), $\dot{\gamma}$ is the shear rate (/s), $\eta$ is the non-Newtonian viscosity (Pa.s), can be obtained from Bingham–Papanastasiou model:

$$\eta = \mu + \frac{\tau_y}{|\dot{\gamma}|}\left[1 - e^{(-m|\dot{\gamma}|)}\right] \tag{2.5}$$

Where $\mu$ is Newtonian viscosity (Pa.s), $m$ is the consistency index, and $\tau_y$ is yield stress (kPa). Papanastasio's proposed equation is true for the entire shear stresses (both yielded and unyielded region) [137].

$\eta > 1$, shows a shear-thickening fluid, and a shear-thinning fluid is indicated by $\eta < 1$. Here "η" depends upon magnetic field strength (H). The Newtonian viscosity and yield stress underneath various shear rates are directly related to the magnetic field, as $\tau_y \propto B^3$ *and* $\mu \propto B^3$ [67], [138]. To study the rheological behaviour of MRP fluid, the study of viscosity is very important, so a magnetic field dependent shear stress equation is critical. As the magnetic field increases, yield stress increases accordingly. The yield stress is a function of the magnetic field [67].

$$\tau_y(H) = \sqrt{6}\phi\mu_0 M_s^{0.5} H_0^{1.5} \tag{2.6}$$

Where, $\phi$ is the volume fraction of IPs, $H_0$ is applied magnetic field strength (A/m), $M_s$ is saturation magnetization (A/m), $\mu_0$ is the magnetic permeability of free space ($4\pi\times10^{-7}$ N/A$^2$). Here, in simulation, shear stress can be modelled based on Eq. (2.4).

## 2.2.2 Governing Equations of Magnetic Field

A magnetic field module in Comsol® software is selected for simulating the magnetic field in the computational domain. The study is not dependent on time. Properties of MRP media is applied in the simulation software using a BH curve. In the computational domain, materials and magnetic fields are added. As per the alignment of poles of magnets, the remanent magnetic flux density of each magnet is specified. Maxwell's equations are generally used to govern the magnetic field equations. Those are as follows.

$$B = \nabla \times A \tag{2.7}$$

Where, $B$ is magnetic flux density or magnetic induction (T) and $A$ is magnetic vector potential (Tm or Wb/m). Divergence of the magnetic field must be zero because magnetic monopoles cannot exist

$$\nabla . B = 0 \tag{2.8}$$

With regards to magnetic insulation on boundaries, it implies that the field is zero at the boundary.

$$n \cdot B = 0 \tag{2.9}$$

Physics-controlled fine meshing is used as it refines the mesh at the corner and boundaries.

## 2.2.3 MRP Fluid Flow Modelling

The same computational domain is taken to model the MRP fluid, which has been mentioned in the previous section. The corner refinement mesh is modified to mesh the domain again. The fluid flow module is coupled with the magnetic field module to model the MRP fluid. The simple incompressible laminar fluid is considered for stationary study in the computational domain.

The magnetic force is produced by the magnetization of the MRP fluid particles during the use of the external magnetic field. Different body forces acts on MR fluid while finishing is gravitational force and magnetic force. The magnetic force is large, especially in comparison of gravitational force. So, the impact of gravity is disregarded. This magnetic force is generally termed as Kelvin force. This magnetic force/unit volume can be evaluated as follows:

$$F = \mu_0 \phi (M . \nabla) H \tag{2.10}$$

Where, $F$ is force/unit volume (N/m$^3$), $\phi$ is the volume fraction of IPs, and $M$ is magnetization (A-m$^2$/kg). After splitting the above equation into components and simplifying it, it can be written as follows:

$$F_x = \mu_0 \phi (M_x . \frac{\partial H_x}{\partial x} + M_y . \frac{\partial H_x}{\partial y} + M_z . \frac{\partial H_x}{\partial z}) \quad (2.11)$$

$$F_y = \mu_0 \phi (M_x . \frac{\partial H_y}{\partial x} + M_y . \frac{\partial H_y}{\partial y} + M_z . \frac{\partial H_y}{\partial z}) \quad (2.12)$$

$$F_z = \mu_0 \phi (M_x . \frac{\partial H_z}{\partial x} + M_y . \frac{\partial H_z}{\partial y} + M_z . \frac{\partial H_z}{\partial z}) \quad (2.13)$$

These volumetric forces are included in the Navier–Stokes equation to account for the effect of the magnetic field on the fluid flow. This body force (F) term in Eq. (2.15) is specified via Eq. (2.14). The resultant magnetic body force on the MRP fluid, can be further given by following equation

$$F = F_x \hat{x} + F_y \hat{y} + F_z \hat{z} \quad (2.14)$$

The Navier–Stokes equation uses the volume force to account for the influence of the magnetic field in the fluid flow.

$$\rho(\vec{u}.\nabla)\vec{u} = \nabla.\left[-pI + \eta\left(\nabla\vec{u} + (\nabla\vec{u})^T\right)\right] + F \quad (2.15)$$

where, $\eta$ is dynamic viscosity (kg/(m.s)), $u$ is the velocity (m /s), $p$ is the pressure (N/m$^2$). The same meshing for fluid flow simulation is also used as defined for magnetic field modelling with more corner and boundary refined mesh for the convergence of the solution. Fluid flow simulation is also assumed to be time-independent.

## 2.2.4 Magnetic Flux Density Distribution

The FE analysis results of the variation in magnetic flux density distributions in the working gap (A'A, C'C, E'E , Fig. 2.3 (b)) between the gear and flow restrictor, and along the arc length of in-between (AB), involute (BD), top (DF), face (QU & SY) (Fig. 2.3 (a)) surface of the gear tooth are shown in Fig. 2.5 (a), (b) (volume plot), (c) and (d) (volume plot), respectively. Further, without using a flow restrictor, these magnetic flux density distributions are compared with using a flow restrictor. The maximum magnetic flux density at the in-between, involute, top and face profile of gear tooth without and with flow restrictor is obtained almost similar as 0.17 T, 0.21 T, 0.22 T and 0.24 T, respectively, after magnetostatic FEA, which is good enough for polishing the gear tooth surfaces. The result of the FEA helps to develop a consistent flow-restricting profile as the precise negative replica of the gear profile. In turn, also the effective surface on the gear tooth was determined based on FE analysis of uniform shear and normal

stresses distributions. This helps to achieve the goal of the present work, such as enhancing surface finishing and eliminating any surface defects that may further minimize gearbox problems, noises, and vibrations during higher-speed applications.

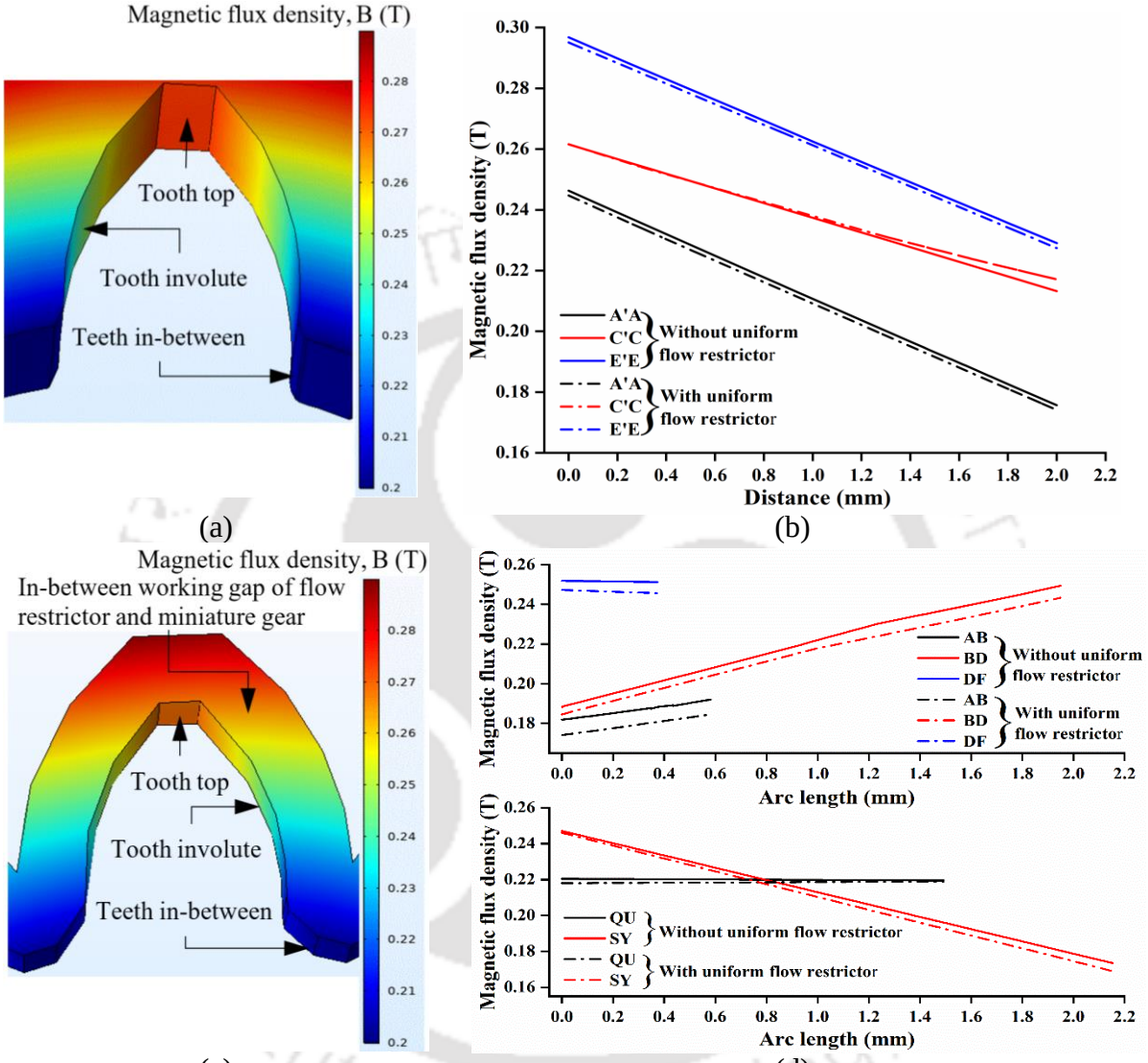


**Fig. 2.5** Magnetic flux density distribution along gear tooth (a) without (volume plot), (b) at working gaps A'A, C'C, E'E (Fig. 2.3(b)) without and with, (c) with (volume plot) and (d) along AB, BD, DF, QU & SY profiles (Fig. 2.3(a)) without and with, uniform flow restrictor

## 2.2.5 Shear Stress and Normal Stress Distribution

Compared to the result without and with using a uniform flow restrictor, the maximum shear stress obtained is 64 kPa and 58 kPa, respectively, for the 3D computational domain (Fig. 2.6). The amount of material removal that takes place in a finishing process mostly relies on the shear stresses response on the workpiece surfaces. So, in order to get an excellent surface finish,

the study of rheological properties (shear yield stress and viscosity) of MR polishing fluid is very important as they are the key design factors in the applications of MR fluids. The FEA obtained results for the variation in the shear stress distribution without and with using uniform flow restrictor along the arc length of in-between (AB), an involute (BD), top (DF), and face (QU & SY) (Fig. 2.3 (a)) profiles of the gear tooth are shown Fig. 2.6 (a), (b) (volume plot), (c) and (d) (volume plot), respectively. The more uniform shear stress is obtained when using a flow restrictor, and maximum variation (34 kPa to 58 kPa) of shear stress is obtained when not using a uniform flow restrictor (Fig. 2.6(b) and (d)). Maximum and uniform shear stress leads to faster, consistent material removal, thus uniform polishing.

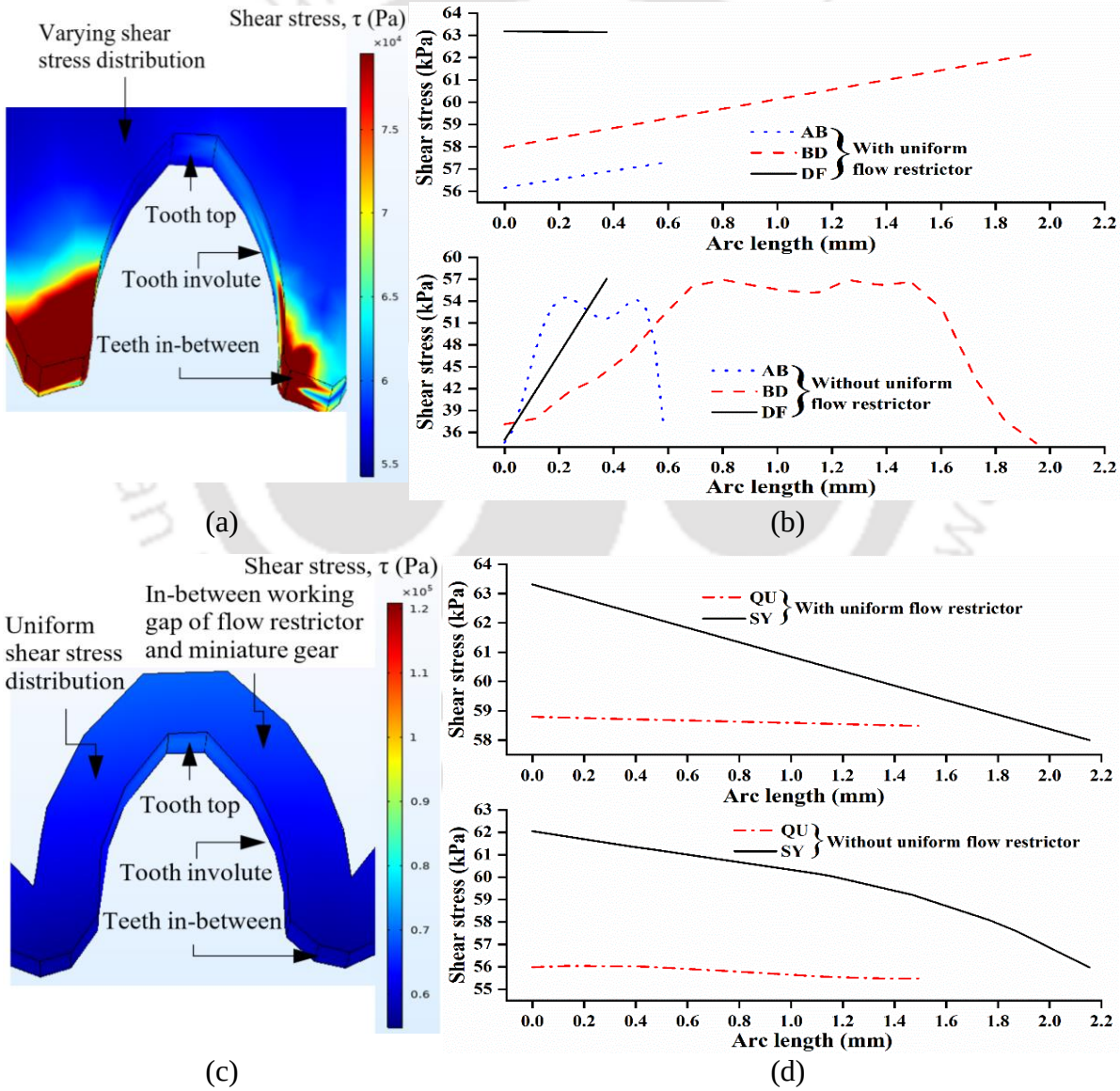


**Fig. 2.6** Shear stress distribution of gear tooth (a) without (volume plot), (b) along AB, BD, DE profiles (Fig. 2.3 (a)) without and with, (c) with (volume plot), (d) along QU & SY profiles (Fig. 2.3 (a)) without and with, uniform flow restrictor

Due to the fact that the MR fluid has an elastic modulus, it behaves in a manner similar to a non-linear elastic solid prior to yielding [67]. The elastic modulus could be transformed to a normal stress by multiplying by the average compressive strain ($\varepsilon_c$) [139]. The following equation gives the normal stress created by the applied magnetic field.

$$\sigma_n = 3\times\left(3\phi\mu_0 M_s H_0\right)\times\varepsilon_c \tag{2.16}$$

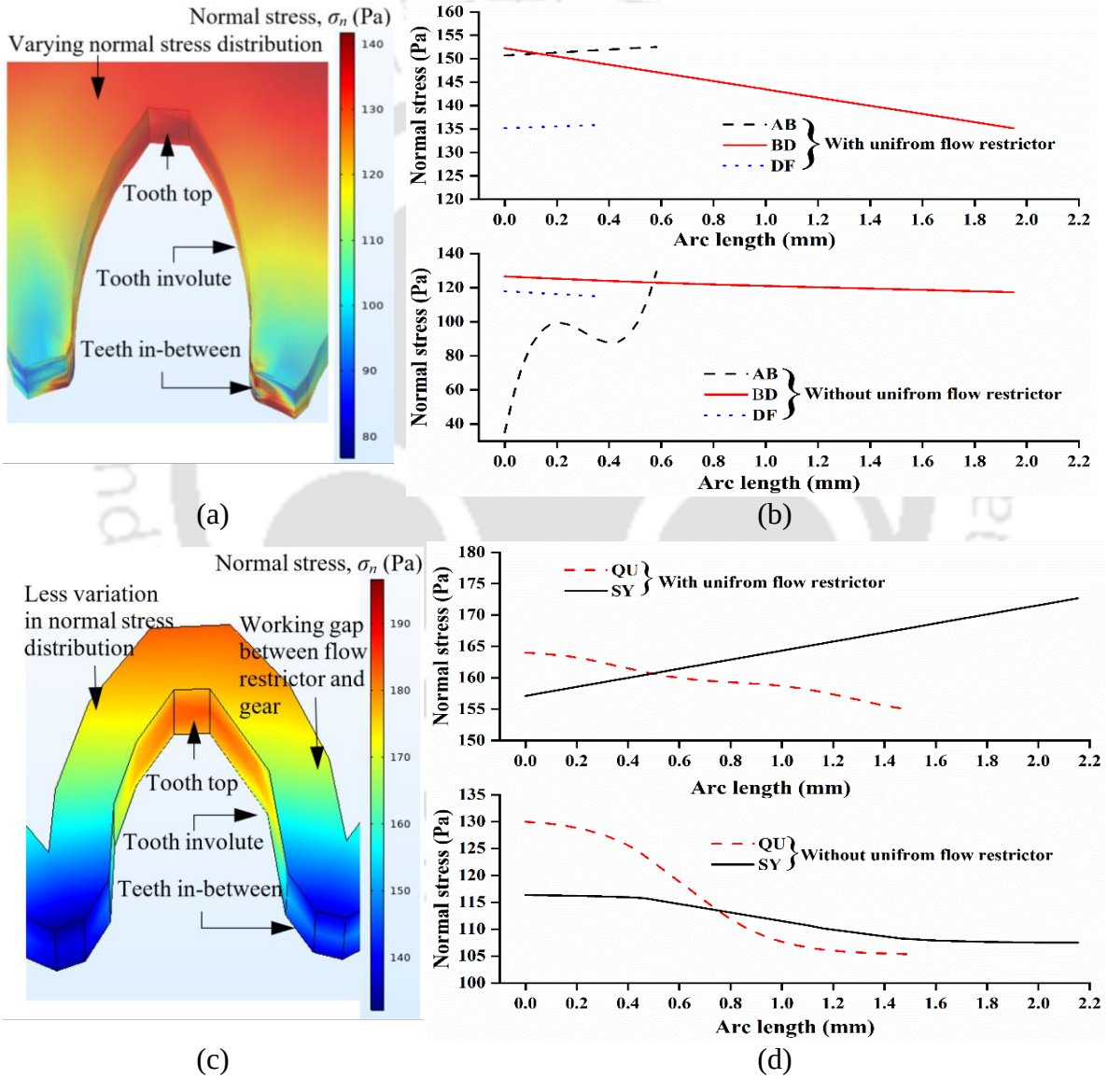


**Fig. 2.7** Normal stress distribution of gear tooth (a) without (volume plot), (b) along AB, BD, DE profiles (Fig. 2.3 (a)) without and with, (c) with (volume plot), (d) along QU & SY profiles (Fig. 2.3 (a)) without and with, uniform flow restrictor

The FEA obtained results for the variation in normal stress distribution without and with using uniform flow restrictor along the arc length of in-between (AB), an involute (BD), top (DE) and face (QU & SY) (Fig. 2.3 (a)) profiles of the gear tooth are shown in Fig. 2.7 (a), (b) (volume plot), (c) and (d) (volume plot), respectively.

The more uniform normal stress is obtained when using a flow restrictor, and maximum variation (30 Pa to 130 Pa) of normal stress is obtained when not using a uniform flow restrictor (Fig. 2.7 (b) and (d)). Uniform normal stress results in the consistent indentation of abrasive particles pertaining to an equal amount of indentation depth at each gear tooth profile, thus contributing to uniform material removal and fine surface finish.

The FEA results of shear and normal stresses distributions along the arc length of OP, QR, ST (Fig. 2.3 (a)) without and with using uniform flow restrictor at 100, 200 and 300 rpm of magnet fixture is shown in Fig. 2.8 (a) and (b), respectively. The results reveal that the almost same amount of variation is observed at 100 rpm and 200 rpm; however, values of the same type of variation increase (1.5 % increment) at 300 rpm. In the actual experiment working condition at 300 rpm, some amount of the leakage of MR polishing fluid from the tight setup is observed, so the 300 rpm is not considered in modelling surface finish, force analysis, and further experimentations.

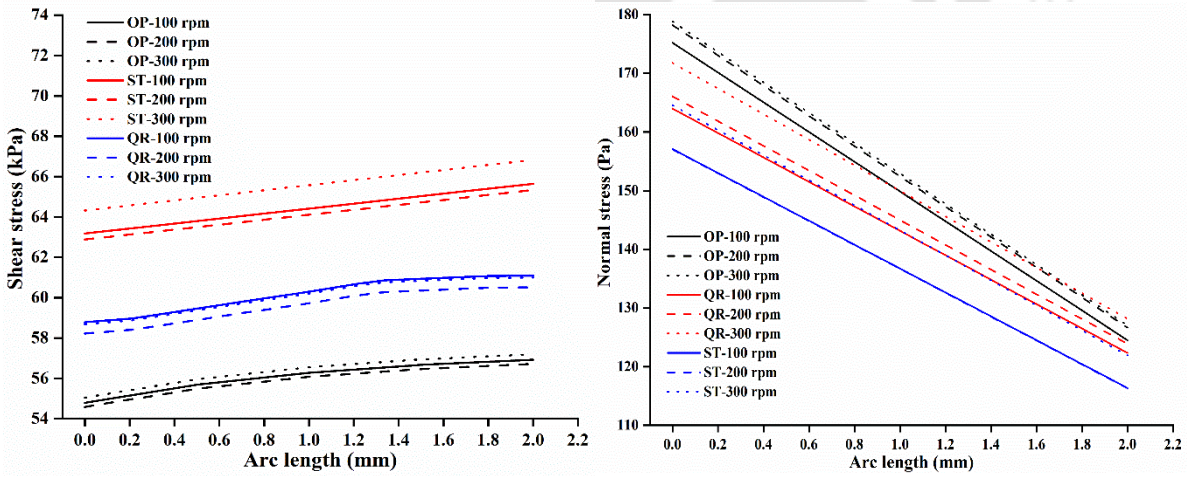


(a) (b)

**Fig. 2.8** (a) Shear stress and (b) normal stress distribution along OP, QR, ST (Fig. 2.3 (a)) on gear tooth profile at rpm (100−300) of magnetic fixture with uniform flow restrictor

# 2.3 Final Design of Flow Restrictor and Workpiece Fixture

By using FEA results of the magnetic flux density, shear stress, and normal stress distributions at the different gear surfaces necessary for the SS316L steel gear profiles finishing, the final

uniform flow restrictor and workpiece fixture is designed for the R-MRFF process. The outer diameter of the uniform flow restrictor and the workpiece fixture is 18 mm and 22 mm, respectively. The pitch diameter of the miniature gear is 12.5 mm. The total number of teeth is 10, and the thickness of the gear is 2 mm. Upon completing the final dimensions, all sections of the fixture are specifically produced.

The workpiece fixture holds the small gear workpiece and uniform flow restrictor. The workpiece fixture is surrounded by a magnet fixture which is given a rotational motion. The translational and rotational motion of the MRP fluid should have enough room to retain and flow through the workpiece fixture for finishing the gear workpiece. So the design of a workpiece fixture is a vital thing in the R-MRFF process. As magnets provide a strong magnetic field, any ferromagnetic materials for manufacturing the workpiece fixture is avoided. Otherwise, CIPs would get attached to the workpiece fixture wall and get clotted inside the fixture, which would have restricted the MRP media to pass through the workpiece fixture. Brass material is composed majorly of Copper and Zinc, which does not show any affinity to any provided magnetic field. So, Brass material is used to manufacture the workpiece fixture.

The workpiece fixture is fixed in between two polishing media cylinders along with the magnet fixture. Eight holes on the outer side of both the flanges of the workpiece fixture were made for allowing the MRP fluid to flow across the gear workpiece. The retention of more MRP fluid helps in the better finishing of the workpiece. A sufficient area was left in the workpiece fixture for retaining enough MRP fluid for gear finishing. The bottom flange is a male part having a shaft of 8 mm diameter and a 4 mm extruded part on the top to rest the gear workpiece (Fig. 2.9(a)).

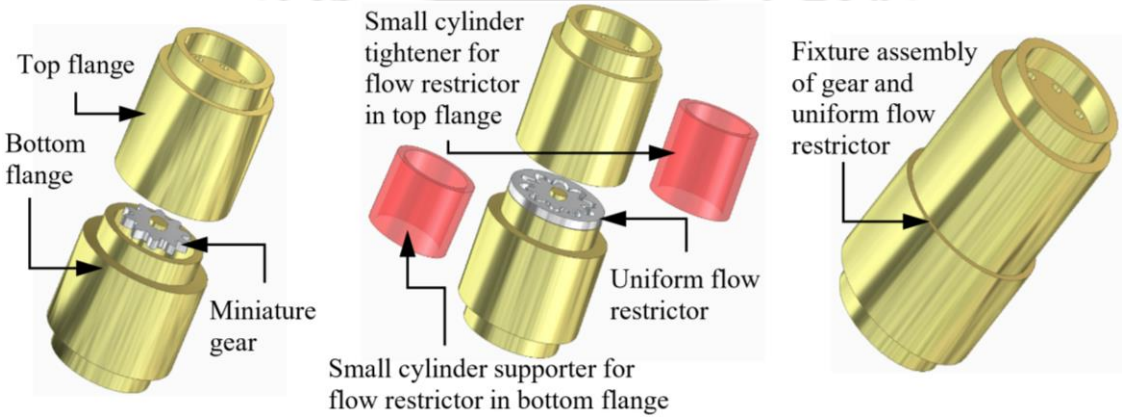


(a) (b) (c)

**Fig. 2.9** Detailed view of (a) gear fixture, (b) gear with uniform flow restrictor, and (c) complete workpiece fixture assembly

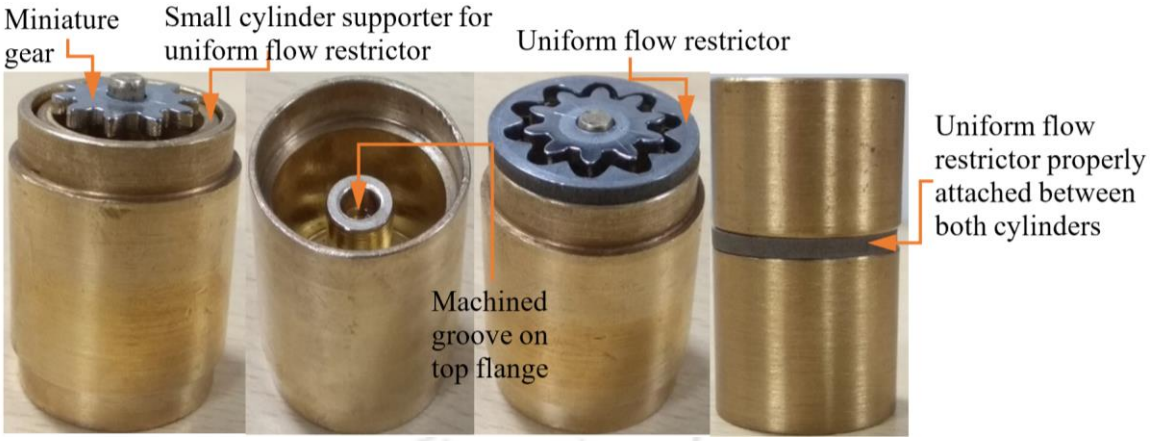


**Fig. 2.10** Gear, small cylinder support, uniform flow restrictor inside workpiece fixture assembly and uniform flow restrictor supported between two cylinders

The top flange of the workpiece fixture is the female part. A similar shaft of 8 mm diameter with a groove of 5 mm (Fig. 2.10) was machined to mesh the extruded part of the bottom flange (Fig. 2.9(a)). Both flange shafts are manufactured in such a way so that the miniature gear can rest in between them. The backside of both flanges was additionally stepped by 5 mm to make it compatible with the proposed R-MRFF fixture. Both flanges were designed so that they interlock properly with one another to prevent any leaking of the MRP fluid. The detailed CAD model of gear fixture with uniform flow restrictor is shown in Fig. 2.9 (b). Two small brass cylinders are used between the flanges to tightly fit the uniform flow restrictor with the gear workpiece (Fig. 2.9 (b)). The assembly of cylinders with a uniform flow restrictor makes the whole setup compact. The dimensions of the cylinders holding the uniform flow restrictor are such that the uniform flow restrictor is able to be placed parallelly around the miniature gear workpiece maintaining a uniform gap all around. As the experiment involves the use of a strong permanent magnet, the materials of these cylinders are chosen brass; as the brass is non-magnetic in nature, it does not promote clotting of iron particles (IPs) on the walls of cylinders. A schematic of fixture assembly of gear and uniform flow restrictor is shown in Fig. 2.9 (c). The manufactured workpiece fixture meshed perfectly with the experimental setup built for the R-MRFF process. The fixture assembly of gear and uniform flow restrictor is shown in Fig. 2.10.

## 2.4 Experimentation

A novel polishing workpiece fixture and uniform flow restrictor are designed and fabricated for the precision R-MRFF process to finish complex miniature gear profiles. A permanent Nd–Fe–B magnet supplies the magnetic field in the finishing area. All gear teeth profiles are

uniformly finished by the developed flow restrictor and gear fixture. The experimental setup includes two vertically symmetric hydraulic and polishing media cylinders [29]. The hydraulic cylinders are filled with liquid, for example, oil and the polishing media cylinders are filled with MR polishing fluid. Both the pistons of the hydraulic cylinder move to and fro together. In the first half cycle, the piston of the bottom hydraulic cylinder dispatches the MRP fluid through the workpiece fixture in the upward direction while simultaneously moving the piston of the top hydraulic cylinder in the upward direction and in the next half-cycle, the same process is reversing again to complete one cycle and finishes the gear profiles uniformly. The movement of the pistons of cylinders extrudes the pressure on the MRP fluid, which in result forces the MRP fluid through the workpiece fixture. The experimental setup of R-MRFF process is shown in Fig. 2.11.

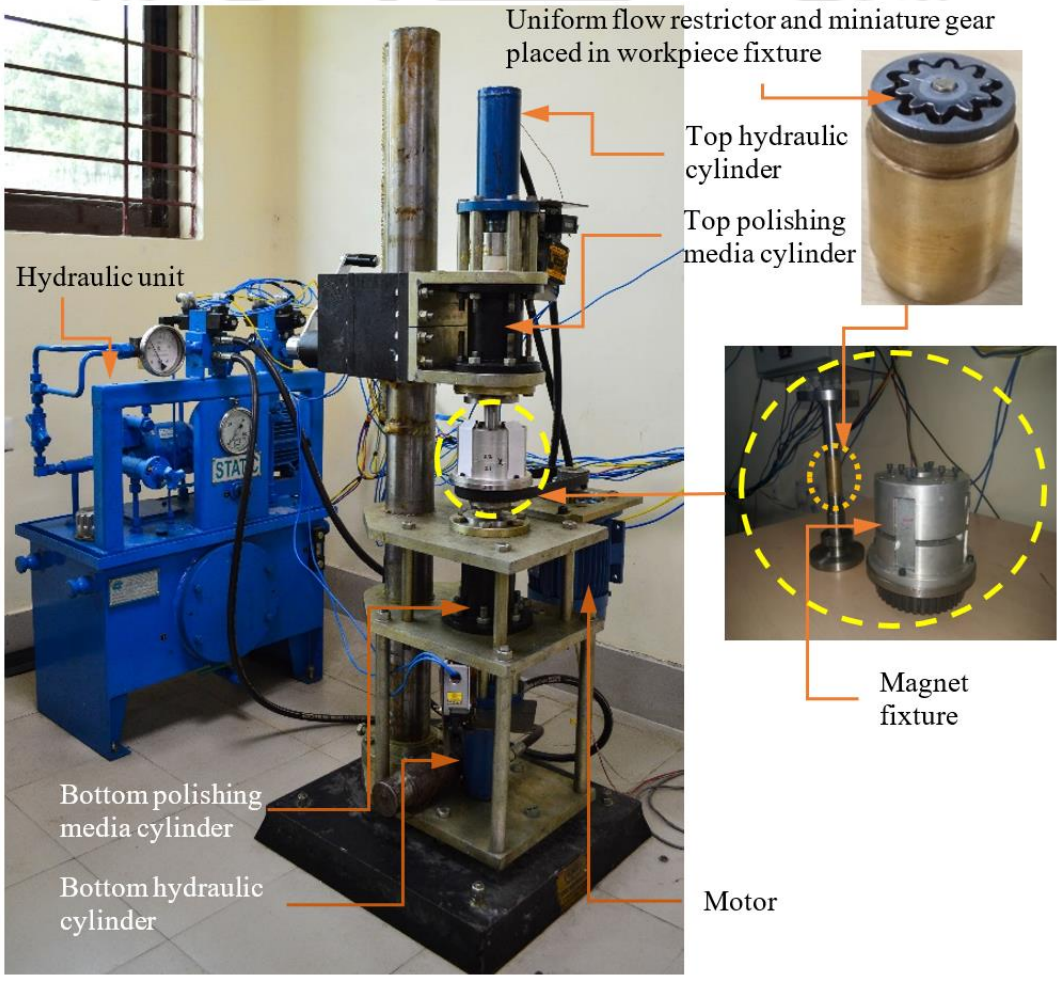


**Fig. 2.11** Experimental setup of R-MRFF process for miniature gear polishing

The magnet fixture rotates by a three-phase induction motor through an attached belt around the workpiece fixture. As magnets rotate, MRP fluid also rotates. The combination of

translational and rotational motion given to the MRP fluid produces a net helical motion that allows better finishing of any workpiece. The automatic limit switch is kept on for auto to & fro motion of the piston. The experimental conditions of MR finishing are summarized in Table 2.3. Numerous preliminary experiments chose such parametrical conditions.

**Table 2.3** Experimental conditions during R-MRFF

| **Parameter** | **Conditions** |
|---|---|
| Rotational speed of the magnet fixture | 100 rpm |
| Finishing time | 3hrs. 20 min |
| Number of finishing cycles | 800 |
| Applied extrusion pressure | 32.5 bar |

The MR polishing fluid compositions are listed in Table 2.4 [1], [13] to finish the SS316L miniature gear, which is chosen by numerous literature surveys. Initially, MR polishing fluid is formulated by mixing volume percentage of 15 % iron particle of 250 mesh size, 5 % SiC abrasive particles of 400 mesh size, 10 % grease and 70 % paraffin oil. Later after some preliminary experiments for fine finishing of gear, iron and SiC abrasive particles of 800 mesh size are used which compositions are shown in Table 2.4.

**Table 2.4** Compositions of MRP fluid for SS316L miniature gear polishing

| **Constituents** | **Volume concentration (%)** |
|---|---|
| Iron particles (mesh size 800) | 22 |
| SiC abrasive ( mesh size 800) | 15 |
| Grease | 10 |
| Paraffin oil | 53 |

The experiments are conducted to justify the current magnetorheological gear profile finishing method with the parametrical conditions listed in Table 2.3. Pre-and post-MR finishing, the surface roughness of the miniature gear teeth profiles is assessed using an Talysurf non-contact CCI (Coherence correlation interferometer) optical profilometer (make: Taylor Hobson) with the monochromatic light source (green LED light) according to ISO 4287:1997 standard. After the surface roughness measurements, the initial and the final finished gear teeth profiles were examined with the field emission scanning electron microscopy (FESEM), microscope and optical profilometer for characterizing the gear tooth surfaces during the finishing. These data are compared with each other for gear finished without and with using a uniform flow restrictor.

## 2.5 Results and Discussion

Experiments are executed to evaluate the functionality and performance of the novel uniform flow restrictor and workpiece fixture for standardized uniform polishing of the complex tooth profiles of miniature gear. On the teeth of a gear, there is an effective field of consistent and optimum distribution of magnetic flux density, shear stress, and normal stress is present. This helps in getting an excellent surface finish.

### 2.5.1 Surface Roughness

After using the novel uniform flow restrictor and workpiece fixture, the surface roughness parameters were evaluated for the gear teeth surfaces. Gear teeth surfaces were finished with MR polishing fluid, which composition is given in Table 2.4. The magnetic fixture is rotating, and extrusion pressure is applied to MR polishing media as a result, an abrasive particle will cut the peaks of roughness profile by sliding and rotating action as shown in Fig. 2.12 (c). The cutting force acting on active abrasives eliminates the roughness peaks. The roughness peaks have been adjusted to the flat smooth surface following the completion of several MR finishing cycles on the gear teeth profiles, as shown in Fig. 2.12 (d) and (e). At the beginning of the finishing process, the trapped active abrasives with iron particles hit the roughness peaks of initial gear teeth profiles, as shown in Fig. 2.12 (a) and (b). After finishing with novel workpiece fixture, without and with using a uniform flow restrictor, the minimum surface roughness ($R_a$) for the involute profile of gear tooth was decreased to 34.3 nm (Fig. 2.13 (b)) and 24.5 nm (Fig. 2.13 (c)) respectively from the original value of 265 nm (Fig. 2.13 (a)). For all other profiles of gear teeth, initial and final experimental roughness values with 800 finishing cycles obtained are presented in Table 2.5.

**Table 2.5** Measured surface roughness values along gear tooth profiles

| **Gear tooth profiles** | **Initial Ra (nm)** | **Final $R_a$ (nm)** | |
|---|---|---|---|
| | | Uniform flow restrictor | |
| | | Without | With |
| In-between | 264 | 22.1 | 24.3 |
| Involute | 265 | 34.3 | 24.5 |
| Top | 252 | 46.5 | 23.9 |
| Face | 259 | 19.6 | 25.2 |

The results demonstrate that nearly all parts of the teeth surfaces have shown the uniform value of surface roughness using a uniform flow restrictor. This significant uniform decrease of roughness values on the gear teeth profiles indicates that the novel uniform flow restrictor and workpiece fixture are capable of producing a uniform fine surface finish.

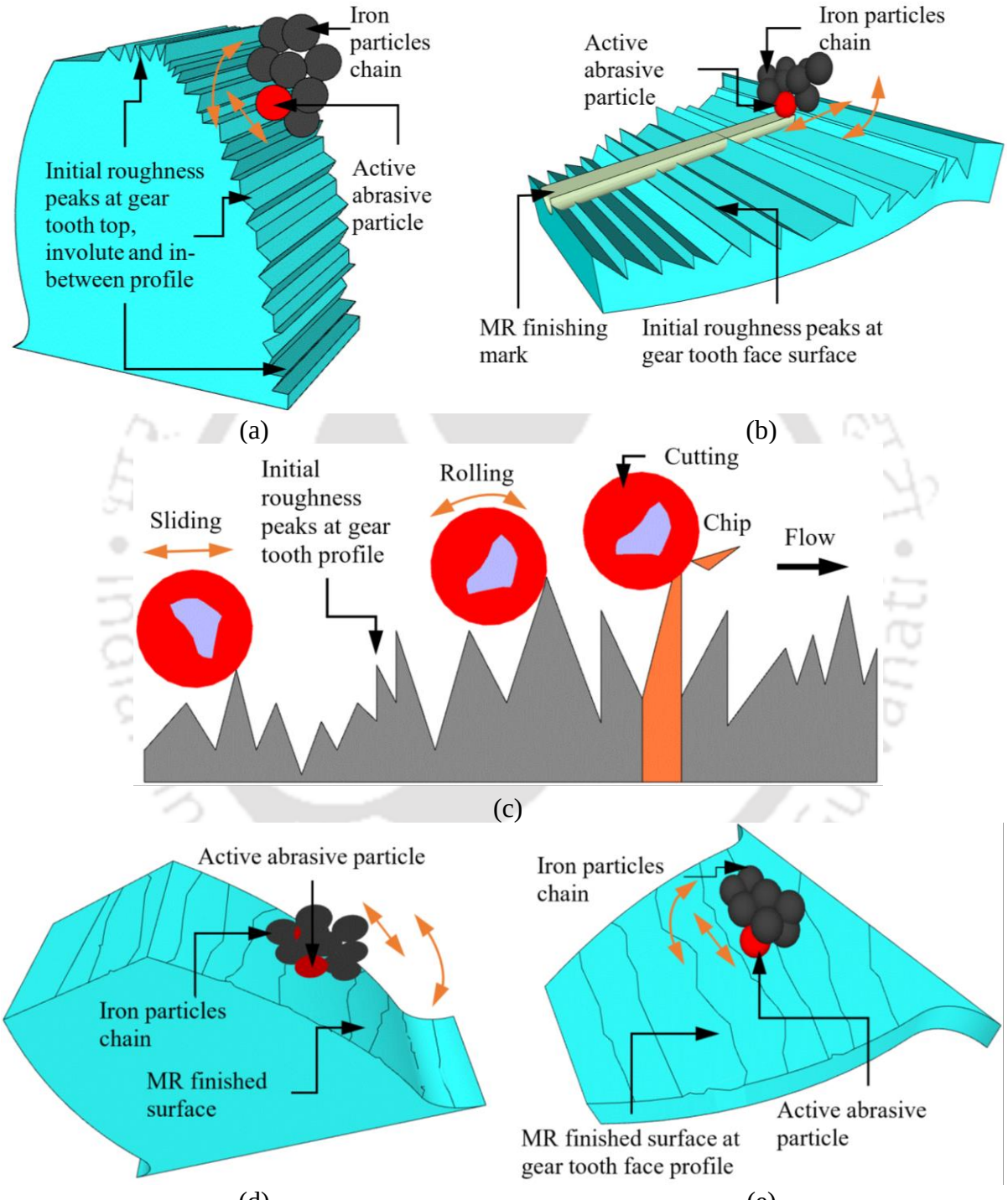


**Fig. 2.12** Surface roughness peaks at the tooth (a) top, involute, in-between and (b) face profile of miniature gear before finishing, (c) different states of a single abrasive particle on gear surface, final roughness profile after R-MRFF processing at tooth (d) top, involute, in-between and (e) face profiles of a miniature gear

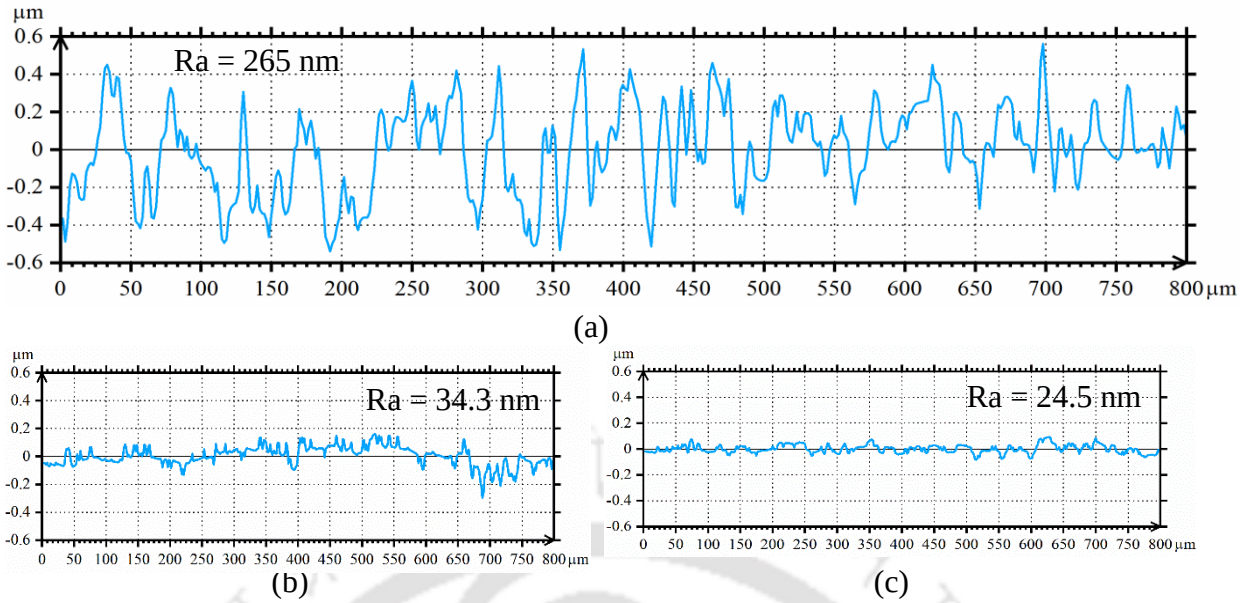


**Fig. 2.13** Surface roughness profiles of gear tooth on involute surface (a) before finishing, after finishing (b) without and (c) with using uniform flow restrictor

## 2.5.2 Surface Characterization

The gear workpiece is polished for 800 finishing cycles, and appreciable improvement in the finishing of the workpiece is observed. As the MR fluid rotates, the transverse length of active abrasive particles increases, and it gives a better MRR and surface finish. The MR polishing fluid prepared was thick so that no seepage of polishing media from the experimental setup takes place. The improvement in the finishing of the workpiece using this composition of MR polishing fluid can be reasoned that iron and abrasive particles used are of the same mesh sizes. Because of the same size of iron and abrasive particles, the trapped abrasives in between the chains of IPs could be in effective contact with the workpiece and thus could shear off the undulations of the workpiece. Thus, this composition of MR polishing fluid showed appreciable improvement in the finishing of the workpiece.

The comparative macrographs of tooth involute surface after finishing without and using uniform flow restrictor are shown in Fig. 2.14 (f) and (j), respectively. As shown in Fig. 2.14 (f), the tooth involute surface, without the use of a uniform flow restrictor, becomes smoother and shinier after finishing with MR polishing fluid. As expected, the involute surface becomes even smoother and shinier using a uniform flow restrictor (Fig. 2.14 (j)). No recast layer, pits or dents were observed. Recast layers on almost all the surfaces were completely removed.

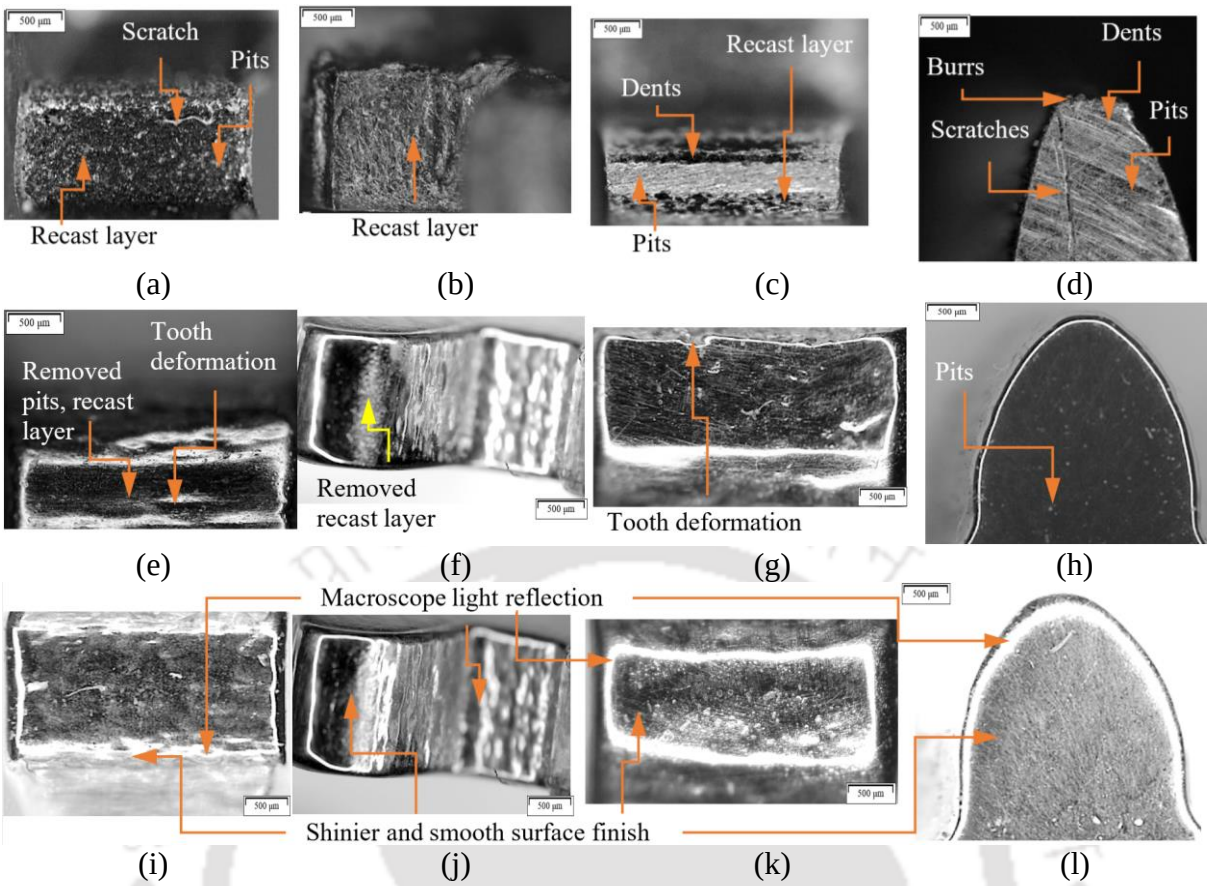


**Fig. 2.14** Macrographs of the tooth (a) in-between, (b) involute, (c) top and (d) face profiles of miniature gear before finishing, tooth (e) in-between, (f) involute, (g) top and (h) face profiles of miniature gear after finishing without using uniform flow restrictor, and tooth (i) in-between, (j) involute, (k) top and (l) face profiles of miniature gear after finishing with uniform flow restrictor

The surface became shinier and free from scratches. It is evident from the observation of macrographs that the surface finish on all the tooth profiles of miniature gear improved more with using a uniform flow restrictor. The initial, final macro-graphic image of all gear teeth profiles without and without using a uniform flow restrictor is shown in Fig. 2.14. A more amount of microscope light reflection is observed on miniature gear teeth profiles finished using uniform flow restrictor than without using uniform flow restrictor as shown in Fig. 2.14 (e)−(l). It concludes that a uniform flow restrictor produces a more smoother and shinier surface finish at miniature gear teeth profiles. Some tooth deformation is observed on gear tooth profile (Fig. 2.14 (e) and (g)) when flow restrictor is not used. However, the desired uniform surface finish with almost no tooth deformation was obtained using a uniform flow restrictor (Fig. 2.14 (i)−(l)).

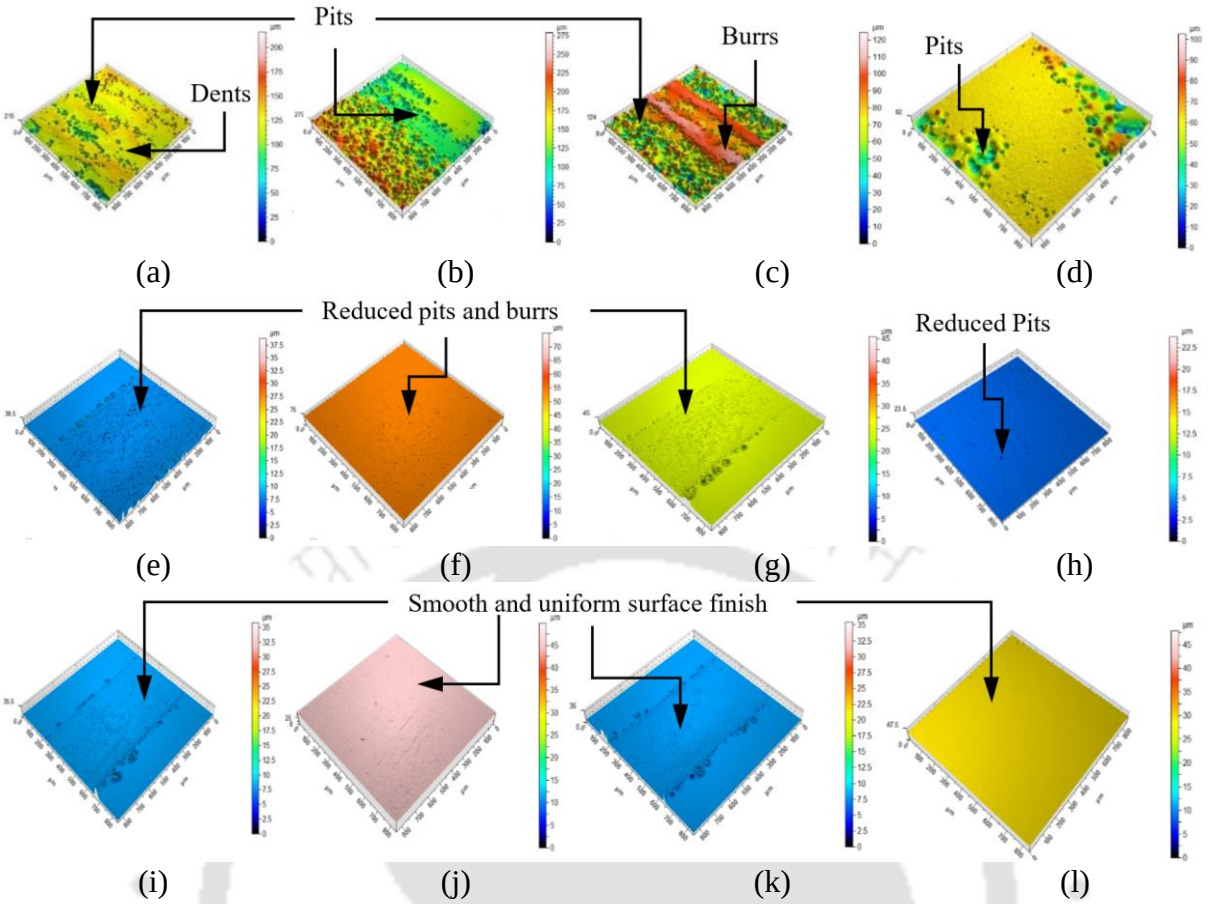


**Fig. 2.15** Surface topography of tooth (a) in-between, (b) involute, (c) top and (d) face profiles of miniature gear before finishing, tooth (e) in-between, (f) involute, (g) top, and (h) face profiles of miniature gear after finishing without using uniform flow restrictor, and tooth (i) in-between, (j) involute, (k) top and (l) face profiles of miniature gear after finishing with uniform flow restrictor

The comparative surface topography of gear tooth profiles with and without using a uniform flow restrictor is shown in Fig. 2.15. The comparative analysis of surface topography of gear tooth profile demonstrates that using uniform flow restrictor; the surface has shown uniform smoother finish than without using uniform flow restrictor. Apart from a good surface finish, also it removed the recast layer and all defects from entire gear tooth profiles. The field emission scanning electron microscope (FESEM) image of gear tooth profiles is studied to find the presence of the recast layer or any micro-defects on the gear profiles (Fig. 2.16). The loose materials and recast layer from the in-between profile of gear tooth got completely removed without using a uniform flow restrictor (Fig. 2.16 (e)). However, using a uniform flow restrictor surface became smoother and shinier (Fig. 2.16 (i)) with no surface defects. The presence of the recast layer was confirmed in the initial studies. The recast layer and the loose materials of the involute profile were completely removed.

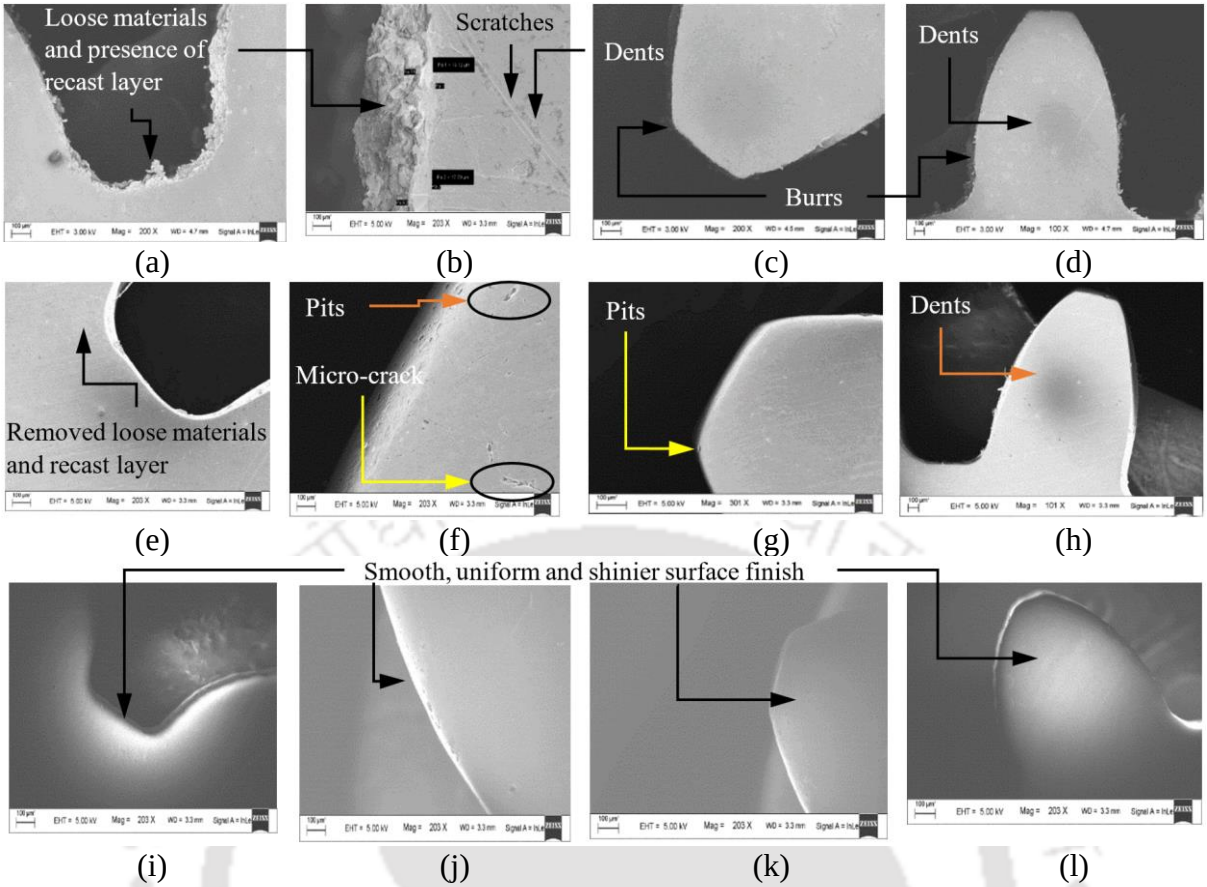


**Fig. 2.16** FESEM images of tooth (a) in-between, (b) involute, (c) top and (d) face profiles of miniature gear before finishing, tooth (e) in-between, (f) involute, (g) top, and (h) face profiles of miniature gear after finishing without using uniform flow restrictor, and tooth (i) in-between, (j) involute, (k) top and (l) face profiles of miniature gear after finishing with uniform flow restrictor

Additionally, the finished surface of the involute profile was completely free from dents, pits, cracks and scratches when used with a uniform flow restrictor, as shown in Fig. 2.16 (j). The tooth top and face profile of gear was polished nicely. The recast layer was gone, and the presence of scratch marks also reduced considerably. It was observed that the sides of the tooth were rounded a little bit. It was found from the literature survey that the rounding of the edges of the gear tooth helps to remove the burrs, pits and other undesired properties from the working surface [73]. As shown in Fig. 2.16 (k), a better surface finish and less form inaccuracy on the tooth top were obtained using a flow restrictor. From the results obtained from FESEM, it was found that the recast layer, loose materials, scratch marks, burrs, pits and dents were removed from the finished tooth profiles of the gear workpiece. The surface finish on different working surfaces was uniformly improved.

## 2.5.3 Uniform Finishing of Gear Teeth Profiles

After conducting the experiment without and with a uniform flow restrictor, the final roughness values obtained are plotted in a bar chart graph (Fig. 2.17) for observing the uniform finishing on gear profiles. The surface roughness (Ra) for each profile was measured five times, and finally, the average of measured Ra was considered. As shown in Fig. 2.17 (a), without using the uniform flow restrictor, more variation in surface roughness values are obtained at the different profiles of gear teeth, as compared to the surface roughness values obtained with using a uniform flow restrictor. After finishing using a uniform flow restrictor, almost the same surface roughness values are procured at each gear tooth surface, as shown in Fig. 2.17.

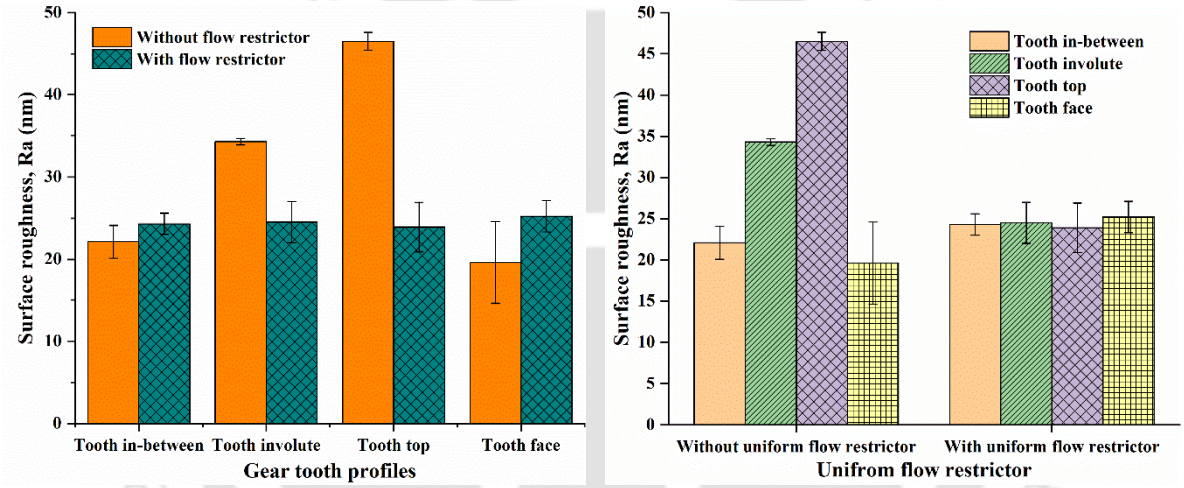


(a) (b)

**Fig. 2.17** Comparison of measured surface roughness values on different places of gear tooth profiles between (a) without and with using uniform flow restrictor, and (b) comparison of uniformity (i.e., surface roughness) on gear profiles without and with flow restrictor

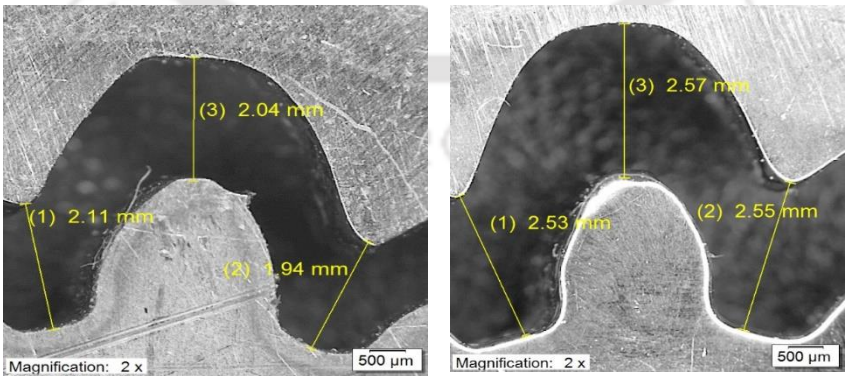


(a) (b)

**Fig. 2.18** Measured uniform gap between gear tooth and uniform flow restrictor profiles (a) before and (b) after finishing

It means that a uniform flow restrictor obtains more uniformity in surface roughness value at each surface. And also, after finishing with a uniform flow restrictor, the material removal rate (MRR) and finishing rate (FR) become higher and uniform. It is observed from the macroscopic image of miniature gear and uniform flow restrictor (Fig. 2.18 (a)) the uniform gap of about 2 mm is maintained at each surface of gear before finishing. It is again found from the macroscopic image of gear and uniform flow restrictor (Fig. 2.18 (b)) the uniform gap increases to about 2.54 mm at each surface of gear tooth after finishing.

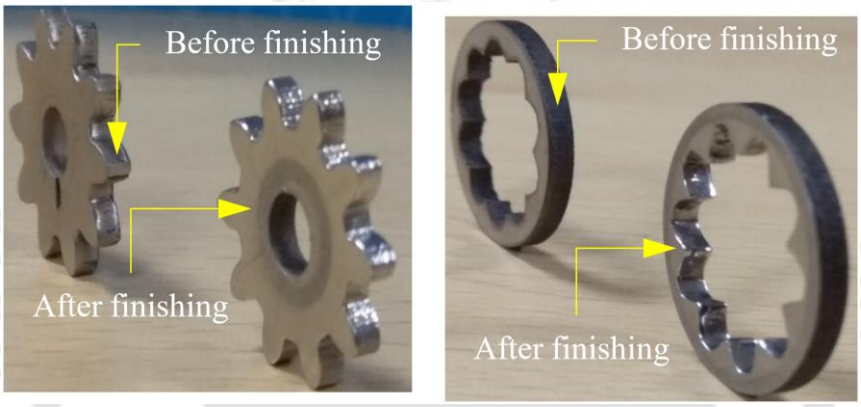


(a) (b)

**Fig. 2.19** (a) Miniature steel gear and (b) uniform flow restrictor before and after finishing

The increase in the uniform gap in the final arrangement is because of the loss of the same amount of material on the surfaces of both miniature gear and the internal surface of the uniform flow restrictor during the whole polishing process. The uniform gap is maintained between the gear workpiece and the uniform flow restrictor before and after finishing. This ensures that there is uniform material removal at each corner of the workpiece.

The Uniform flow restrictor, which is a negative replica of the gear workpiece, has finished the gear workpiece upto nano-scale level uniformly. The gear workpiece before and after finishing with the uniform flow restrictor is shown Fig. 2.19 (a), and the uniform flow restrictor before and after finishing is shown Fig. 2.19 (b).

## 2.6 Summary

In the present study, uniform flow restrictor and workpiece fixture are designed and developed for miniature gear finishing. Depending upon the uniform value of required magnetic flux density and shear stress distributions on gear teeth profiles, a novel uniform flow restrictor (a negative replica of miniature gear) and workpiece fixture are designed and developed for the R-MRFF process. The magnetostatic fluid flow FE analysis shows that the novel uniform flow

restrictor can finish the complex profiles of miniature gear teeth uniformly. For finishing complex miniature gear teeth profiles, the effectiveness of the designed uniform flow restrictor and workpiece fixture is confirmed experimentally using different surface characterization techniques, i.e., macrographic images, surface topography, and FESEM analysis. All manufacturing defects are almost removed after MR finishing of gear profiles when flow restrictor is used. Uniform magnetic flux density and shear stress distribution in the desired area helps the active abrasives to uniformly indent and cut the roughness peaks of the gear teeth profiles with reciprocating and rotating movements of MRPF. It allows smooth, high-geometrical accuracy finishing. The final roughness values on in-between, involute, top, and face profiles of miniature gear teeth are measured as 24.3 nm, 24.5 nm, 23.9 nm, and 25.2 nm, respectively, while using a uniform flow restrictor. The roughness values at the corresponding positions are measured as 22.1 nm, 34.3 nm, 46.5 nm, and 19.6 nm, respectively, without using a uniform flow restrictor. A small amount of tooth deformation is observed when a uniform flow restrictor is not used; however, while finishing using a uniform flow restrictor, no tooth deformation is found and a fine uniform surface finish is obtained on all teeth profiles of miniature gear after 800 finishing cycles. One of the exciting approaches for improved practical use of the miniature gear is the latest R-MRFF process with a novel uniform flow restrictor. The current study shows the reliability and effectiveness of the present uniform flow restrictor.

# Chapter 3 Design and Development of Novel Magnet Fixture for Poppet Valve Polishing

## 3.1 Introduction

The poppet valve has complex narrow ridge profiles, which is very tough to finish by conventional methods. To finish complex narrow surfaces, it is necessary that the MR fluid inside the workpiece fixture should make point contact with the complex narrow surfaces of the poppet ridges during finishing. However, from the literature survey, it was found that the uniform point contact finishing is tough to achieve due to constraints related to the fixture design and fixture material while finishing complex narrow surfaces of poppet ridges. While solving this particular problem, both simulation and experimental studies are carried out in the present study to design and develop a novel polishing fixture during MR finishing of the poppet valve. The poppet valve material is Nickel Al-Bronze alloy of AB2 grade.

A novel fixture is designed and developed for a precision R-MRFF process to polish complex narrow profiles of the poppet valve. A finite element (FE) based commercial software package Ansys® is used to determine the optimum fixture shape and its dimensions. Five permanent magnets are used to provide the required magnetic field in the finishing zone. The size of the permanent magnets is also determined using FE simulation. Later, an experimental study is carried out to ascertain the capability of the developed fixture. The fixture is designed to finish complex narrow surfaces of poppet ridges uniformly and precisely over the entire workpiece surface. The workpiece is attached to a three-axis CNC milling machine to impart a high degree of freedom for better finishing capability.

## 3.2 Design and Development of Magnet Fixture

The magnet fixture consists of five permanent magnets to be positioned at five specified places. It is required to design an ideal fixture to render enough magnetic field in the finishing region. Sm2Co17 (Samarium - Cobalt) of grade 30H is a sister rare earth permanent cobalt magnet to NdFeB. This magnet was chosen because of its good magnetic strength, having excellent corrosion resistance without any need for a protective coating. H versions of Sm2Co17 can operate up to +350°C without any loss of magnetic field. As described in the following sections, the best fixture configuration for the R-MRFF process is accomplished in three stages. In the 1st step, the poppet valve ridge profiles on the magnet fixture are established. In the 2nd step,

the size, number and locations of permanent magnets are established. Finally, in the 3rd step, all parts of the magnet fixture, including MRPF container, base (fixture for 5th magnet), and the final geometry of the magnet fixture, are determined. The schematic of the poppet valve with their finishing ridge profiles where polishing is required is shown in Fig. 3.1(a). Magnet fixture with all magnets placed at their respective locations is shown in Fig. 3.1(b).

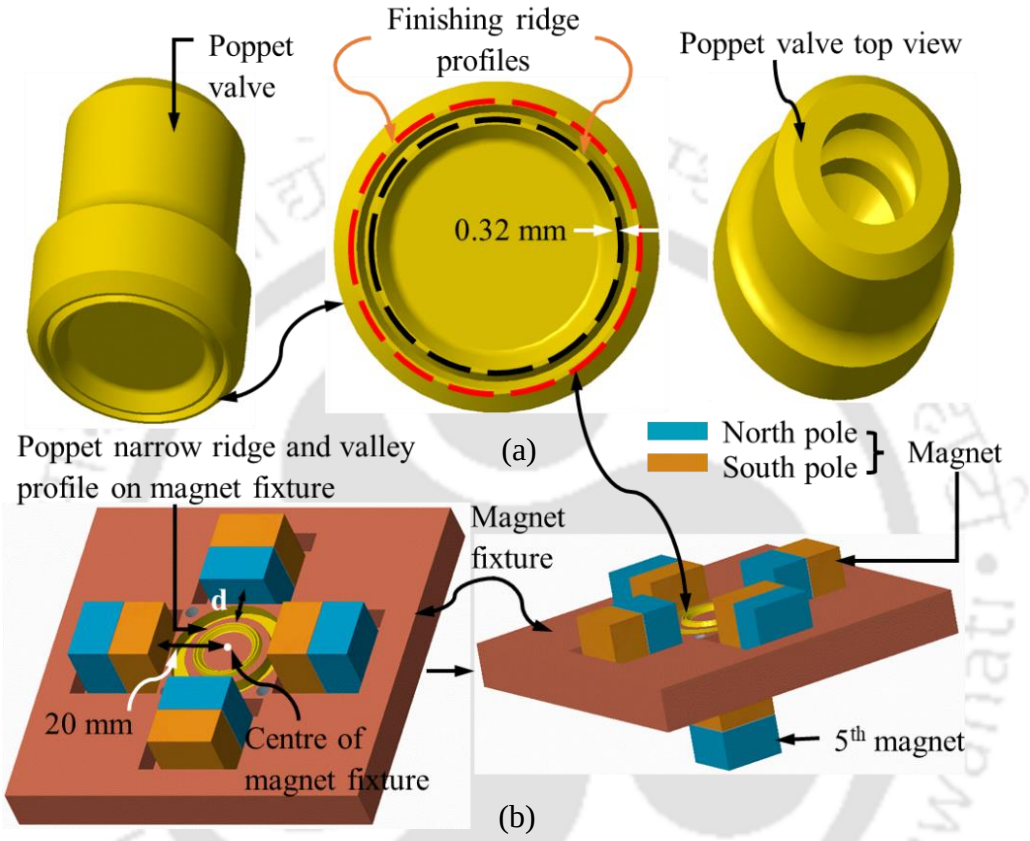


**Fig. 3.1** (a) Different views and finishing profiles of the poppet valve, (b) different views of magnet fixture with poppet valve ridge and valley profiles

## 3.2.1 Workpiece Ridge Profiles on Magnet Fixture

To polish the complex narrow ridge profiles of the poppet valve, a replica of the same is generated on the magnet fixture. It was challenging to polish ridge profiles with a narrow width of 0.32 mm on a circular periphery (Fig. 3.1 (a)). The major challenge was to polish only these complex narrow ridge profiles of the poppet valve (Fig. 3.2 (a)). Polishing on other parts is not necessary. For overcoming this challenge, the same ridge profiles (a replica) have been created on the magnet fixture to prevent MRPF from entering the valley region (in between ridges) during rotation of the poppet valve with a CNC machine (Fig. 3.2). During the rotation of the poppet valve, the relative angular motion between these two ridge profiles (one on the poppet and the other on the magnet fixture) will ensure that the other parts are not impacted by MRPF,

as shown in Fig. 3.2. The fine finishing only on the ridge profiles will provide better form accuracy to the poppet valve; thus, it will improve its sealing effectiveness.

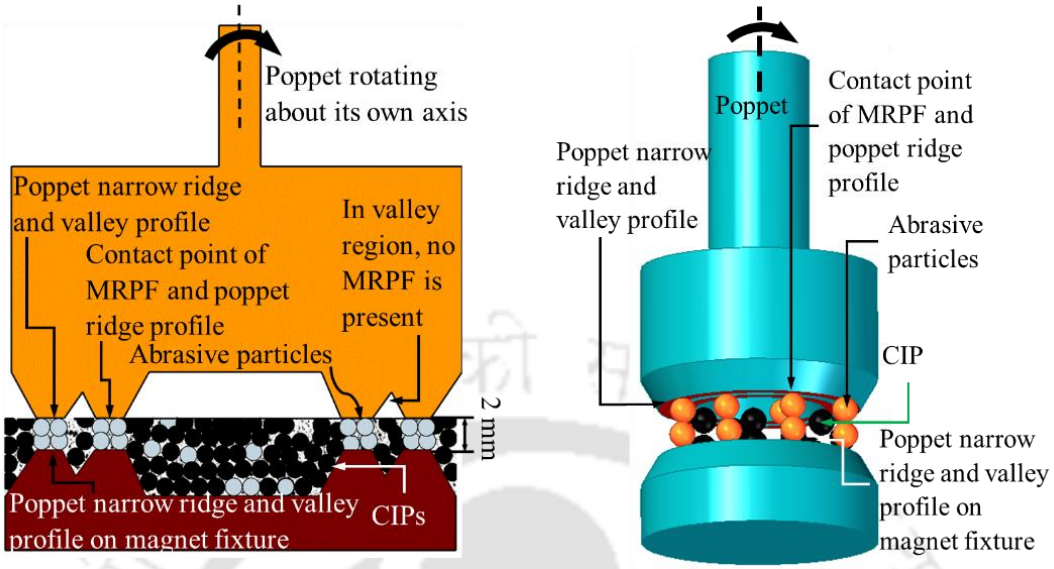


(a) (b)

**Fig. 3.2** (a) 2D and (b) 3D schematic of the finishing mechanism between ridges of poppet valve and magnet fixture

## 3.2.2 Size, Number and Locations of Permanent Magnets

Magnetostatic simulation is conducted to optimize permanent magnets' size, locations, and number. During the FE simulation, the following assumptions are considered:

- All the objects are at rest.
- The solver computes a static magnetic field.
- The permanent magnets are the source of the magnet field.

Maxwell's equations are generally used to govern the magnetic field equations (Eqs. (2.7) and (2.8)). The divergence of magnetic field (*B*) must be zero because magnetic monopoles cannot exist. Colloidal particles converge in the direction of a magnetic field, and each particle begins feeling an attractive force. Considering the uniform distribution of CIPs and other constituents, this force manifests itself as a body force analogous to gravity. The effect of magnetic force is more dominant than the gravitational force, so the effect of gravity is neglected.

Various magnet configurations with different lengths and cross-sections of the rectangular magnets are considered during simulation. Varying number of magnets are also tried to find the optimum magnetic field at the required finishing spots. Better uniform magnetic flux density distributions at the finishing spots are observed while considering five magnets having a dimension of 25×20×20 $mm^3$.

Since the experiments deal with a strong magnetic field, any ferromagnetic materials for fabricating the magnet fixture is avoided. Aluminium was used to manufacture the magnet fixture. The main factor for proper finishing of poppet ridge profiles is positioning the permanent magnets around the centre of the fixture. To generate uniform magnetic field distribution at poppet profiles, optimum distance (d, Fig. 3.1 (b)) between the finishing spots and the magnet face should be maintained. Another factor that should be considered during the positioning of magnets is the space to be occupied by the MRPF container (Fig. 3.3). By considering all these factors, magnets are placed at 20 mm from the centre of the magnet fixture (Fig. 3.1 (b)). The location of the $5^{th}$ magnet (Fig. 3.1 (a)), which is placed below the centre of the magnet fixture at an optimum minimum distance of 5 mm from the finishing spot on the magnet fixture. This optimum 5 mm gap of the $5^{th}$ magnet provides highly uniform magnetic flux density (MFD) both at the magnet fixture centre and finishing spots. The simulation setup is shown in Fig. 3.3. The 2 mm gap (Fig. 3.2 (a)) between the fixture ridge and poppet ridge profiles is loaded with MRPFs.

Three lines at (0º (AB), 45º (EF), and 90º (CD)) and two circles (cicle-1 and circle-2) are drawn along the finishing spots to check the required MFD distribution as shown in Fig. 3.3. The dynamic allocation of MFD is also seen at a certain height, starting from 0 to 33 mm (Fig. 3.3) at the centre, finishing spot–1 and finishing spot–2, respectively. All three lines, two finishing spots and height (OH) in the computational domain are shown in Fig. 3.3.

Several magnet configurations are tried to select optimum magnet fixture development. FEA based software package, Ansys® is used to evaluate MFD contour and vector plots to determine the optimal layout of magnet fixture. At various magnet fixture configurations considered in the present study, the following main goals are considered:

- The magnet fixture should securely hold the permanent magnets at their respective positions.
- The MFD lines should be oriented towards the finishing zone to avoid deviating from the finishing region.
- MFD lines should bound the MRPF at finishing spots and centre. So that fluid media should not segregate towards the MRPF container wall and should not impact the other parts rather than the finishing spots (i.e., ridges) during rotation of poppet at high speed.
- The fixture should protect the MRPF from the outside environment. Any foreign particle should not cling to the MRPF during polishing. Also, MRPF should not spill out of the container from the top or bottom.

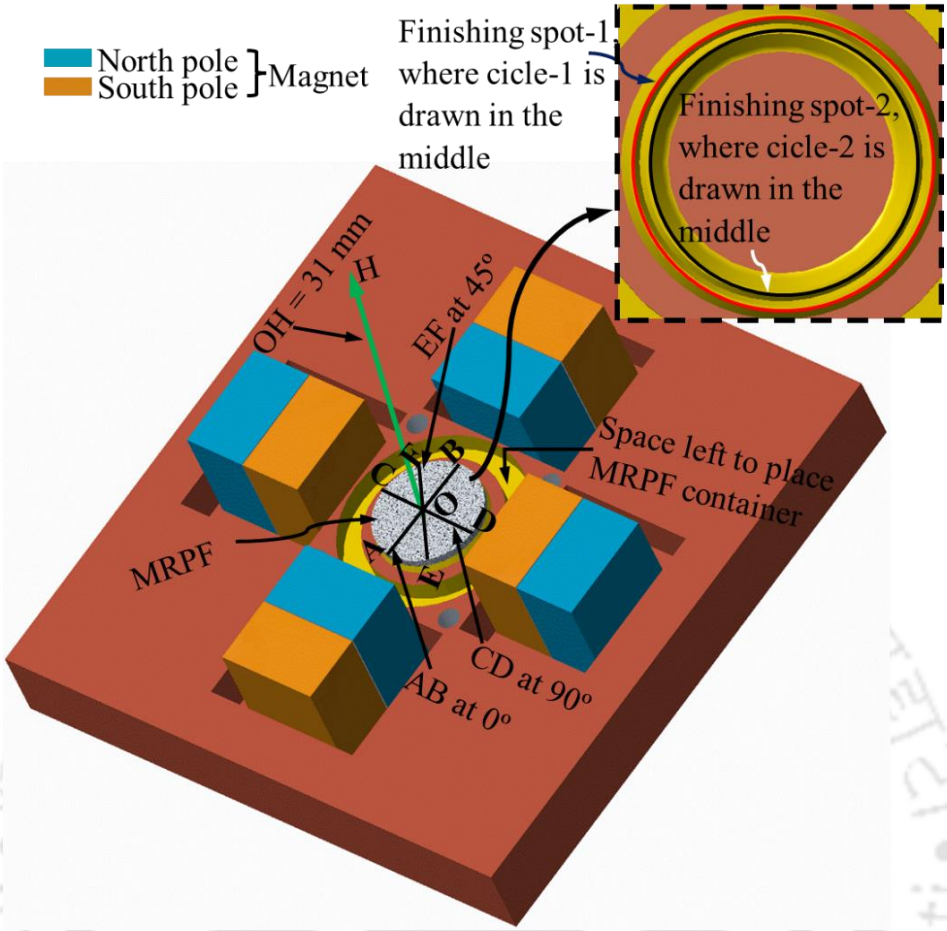


**Fig. 3.3** Schematic diagram of the computational domain for magnetic field simulation

All possible structures that allow for the best size and number of magnets have been tested for the magnetic field distributions. A parametric study to optimize the permanent magnet dimension during simulation is performed. Magnet proportions, i.e. length and cross-section, are known as two main characteristics. One parameter is held constant throughout the simulation while the others are varied. The rectangular magnet varies in length (20 to 25 mm) and cross-sections (between 15 mm × 15 mm to 20 mm × 20 mm). Among these, the maximum length and cross-section of the magnet have shown more uniform MFD values; it can be due to the less corner distance between the adjacent magnets. Generally, at the corner points, the maximum value of the magnetic field exists. Hence, the optimum magnet dimension for the rectangular magnet is chosen as 25 mm × 20 mm × 20 mm. Ansys® is used for magnetic field modelling in the fixture.

***1st configuration***

The magnetic field distribution with four permanent magnets is analyzed for 1st configuration of magnet fixture as shown in Fig. 3.4 (a) and (b). Afterwards, the magnetic field along the

lines AB, CD, & EF and finishing spots (1 & 2) are calculated as shown in Fig. 3.4 (c) and (d), respectively. It is found that the magnetic field distribution around the finishing spots is practically uniform; however, the magnetic field at the centre of the magnet fixture is almost negligible. A high magnetic field at the centre and at the finishing spots is essential to meet the finishing requirements. A high magnetic field at the centre of the magnet fixture will enforce MRPF to be bound at the centre. It should not impact any other parts rather than the finishing spots. Also, another requirement is that the MRPF should not segregate towards the wall of MRPF container during high-speed rotation of the poppet. These four magnets of 1st configuration cannot bound the MRPF towards the centre and finishing spots. Hence, it was discarded.

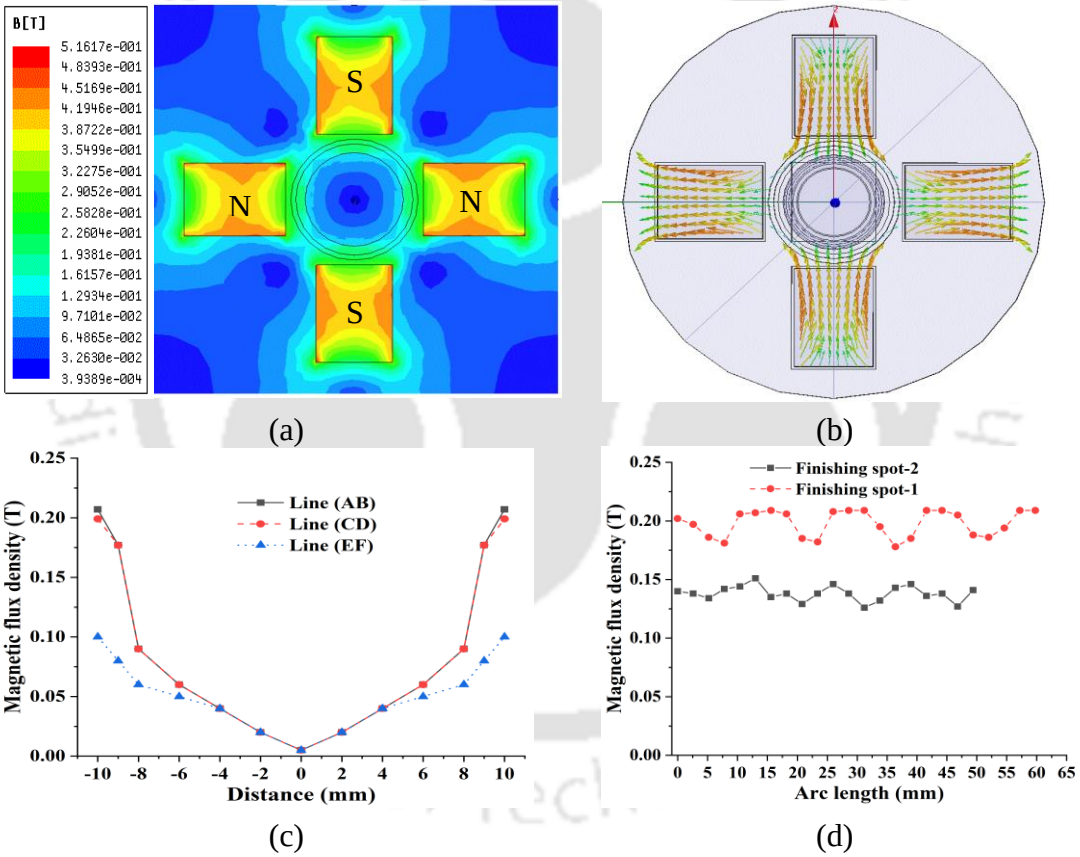


**Fig. 3.4** Magnetic flux density plot (a) contour, (b) vector, (c) along lines (AB, CD & EF, Fig. 3.3), and (d) around the periphery of finishing spots (1 & 2, Fig. 3.3) for 4 magnets

***2nd configuration***

In the present analysis, two more magnets (at different combinations) are also kept underneath the fixture's centre (unlike ***1st configuration***), like one magnet with the south pole and the other with the north pole facing upwards and vice-versa. The other combinations are the north poles of both the two magnets are either kept upward or vice-versa. After that, the MFD distribution

with six permanent magnets for 2nd configuration of the magnet fixture is ascertained. It is observed that the distribution of contour and vector plots of the magnetic field is not uniform in the finishing region, as shown in Fig. 3.5 (a) and (b), respectively. MFD along the lines AB, CD & EF and finishing spots 1 & 2 are shown in Fig. 3.5 (c) and (d), respectively. A maximum value of 0.21T MFD exists at the finishing spots, which is good enough to polish poppet profiles. However, there is a huge variation in the magnetic field (Fig. 3.5 (c) and (d)) both along the lines and finishing spots (1 & 2), respectively, which generates unwanted nonuniform finishing on ridges.

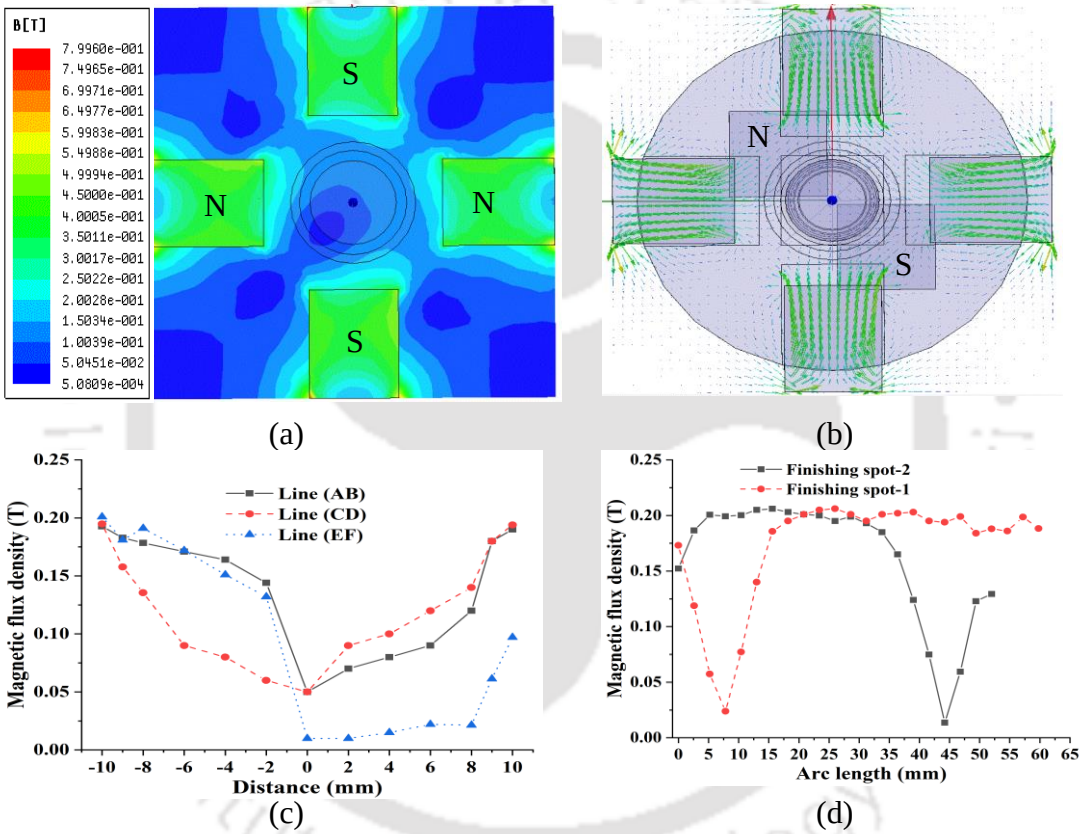


**Fig. 3.5** Magnetic flux density plot (a) contour, (b) vector, (c) along lines (AB, CD & EF, Fig. 3.3), and (d) around the periphery of finishing spots (1 & 2, Fig. 3.3) for 6 magnets

MFD distribution with two underneath magnets having one magnet with the south pole and another magnet with the north pole facing upward direction is shown in Fig. 3.5. Even though both magnets have the south pole or the north pole facing upwards, they show approximately a similar MFD variation. Uniform MFD distribution was not observed with 2nd configuration of the magnet fixture. Hence, it was discarded.

### *3rd configuration*

At the 3rd configuration, MFD distribution with eight permanent magnets is analysed (Fig. 3.6). The distribution of contour and vector plot of the magnetic field is almost uniform in the finishing region (like in 1st configuration), as shown in Fig. 3.6 (a) and (b), respectively. MFD distribution along the lines AB, CD & EF and finishing spots (1 & 2) is shown in Fig. 3.6 (c) and (d), respectively. Lesser variation in the magnetic field as compared to 2nd configuration along both the lines and finishing spots is observed. The maximum value of MFD 0.17 T is observed at the finishing spots. However, this configuration poses a major problem of reduced value MFD at the poppet surface compared with the previous 2nd configuration (Fig. 3.5). At the fixture centre, the MFD value is near zero, which is unacceptable. This may be due to MFD lines that cross each other because of different combinations of four magnets underneath the fixture centre.

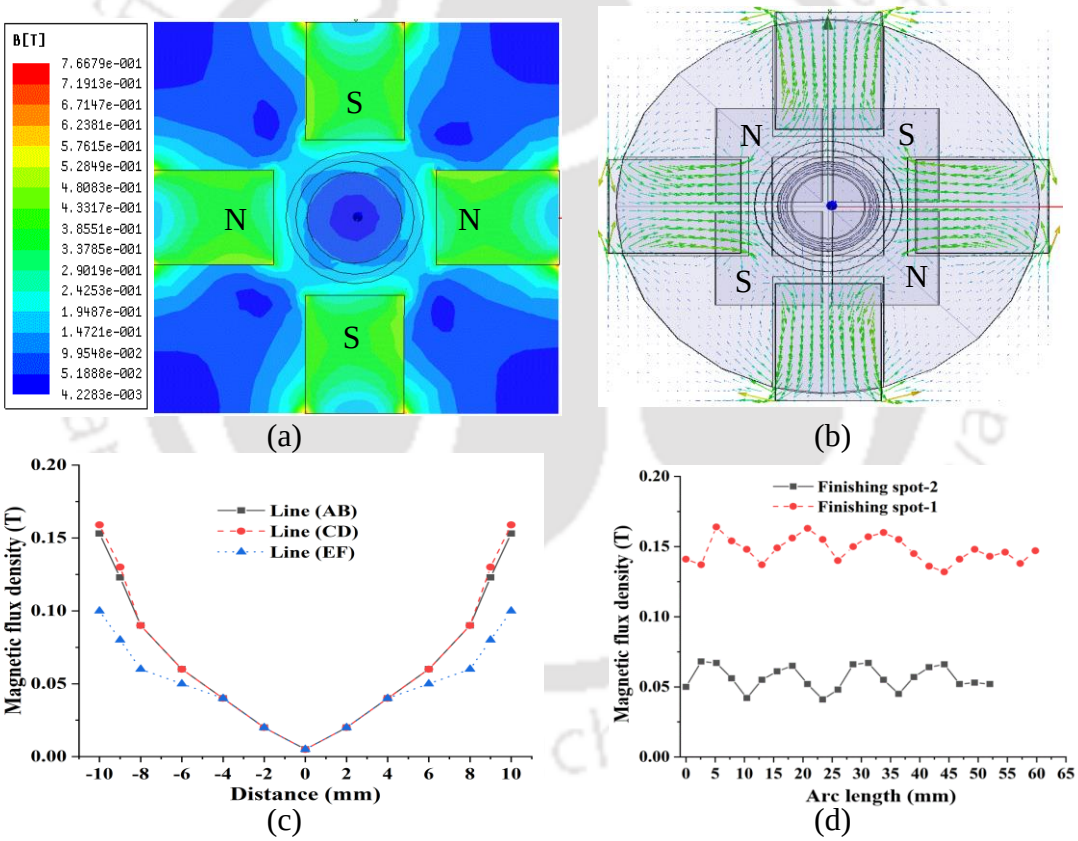


**Fig. 3.6** Magnetic flux density plot (a) contour, (b) vector, (c) along lines (AB, CD & EF, , Fig. 3.3), and (d) around the periphery of finishing spots (1 & 2, Fig. 3.3) for 8 magnets

Different combinations of underneath magnets are; Two magnets with the south pole facing up and the other two with the north pole facing up; all four magnets having the south poles facing up or vice-versa. The MFD distribution with four underneath magnets having two magnets with the south poles and another two with the north poles facing up is shown in Fig. 3.6. The

3rd configuration having different combinations of all four underneath magnets show approximately similar MFD variation. Here, the difference in MFD magnitude between finishing spots 1 and 2 is high (Fig. 3.6 (b)). Therefore, this configuration is also discarded.

Initially, only an even number of magnets were considered because previous literature deals with an even number of magnets. Also, the problem with an even number of magnets is that MFD lines cross each other due to the placement of magnets below and above the fixture. Later due to the requirement of a higher value of MFD at the centre and finishing spots, an odd number of magnets are also considered in the following configuration.

***4th configuration***

The magnetic field distribution with seven permanent magnets is considered for the 4th configuration of the magnet fixture. The distribution of contour and vector plots of the magnetic field is not so uniform in the finishing region, but it was good enough for polishing, as shown in Fig. 3.7 (a) and (b), respectively. MFD distribution along the line (AB, CD & EF) and finishing spots (1 & 2) is shown in Fig. 3.7 (c) and (d), respectively. These distributions show the higher variation of MFD along different lines, and finishing spots. The maximum value of MFD 0.15 T is measured at the finishing spots, which is sufficient enough for polishing poppet valve ridge profiles. At the centre, the maximum value of the calculated MFD is 0.13 T. Here, a total of six magnets on the fixture and one magnet underneath the fixture are placed. In this configuration, two combinations are tried; At 1st combination, the underneath magnet having south pole is facing up; In the 2nd combination, the north pole of the underneath magnet is facing up. After magnetic field simulation, it has been observed that the underneath magnet facing the south pole up (1st combination) shows less variation in MFD distribution at the finishing spots than the 2nd combination (Fig. 3.7 (c) and (d)). Also, the 1st combination provides enough magnetic field at the centre, as shown in (Fig. 3.7 (c)). Therefore, this design was reasonable enough to choose the magnet fixture. Still, a major problem remains as a 20 mm distance between the magnet face and the magnet's centre was not maintained due to the more number of the magnets (6 number). Hence, the space required to accommodate each magnet at an equal gap is not appropriately balanced side by side near the finishing spots. Because of these constraints, the magnets will be far away from the centre, although it was previously established that a maximum distance of 20 mm is to be maintained. The size of the fixture also became large. Here also, the maximum value of MFD was 0.15 T, which is less than all previous configurations. Due to these reasons, the proposed 4th configuration was not discarded entirely but given the thought for designing the next configuration with five magnets.

It is also understood that the underneath magnet having the south pole facing up gives enough magnetic field at the centre and finishing spots.

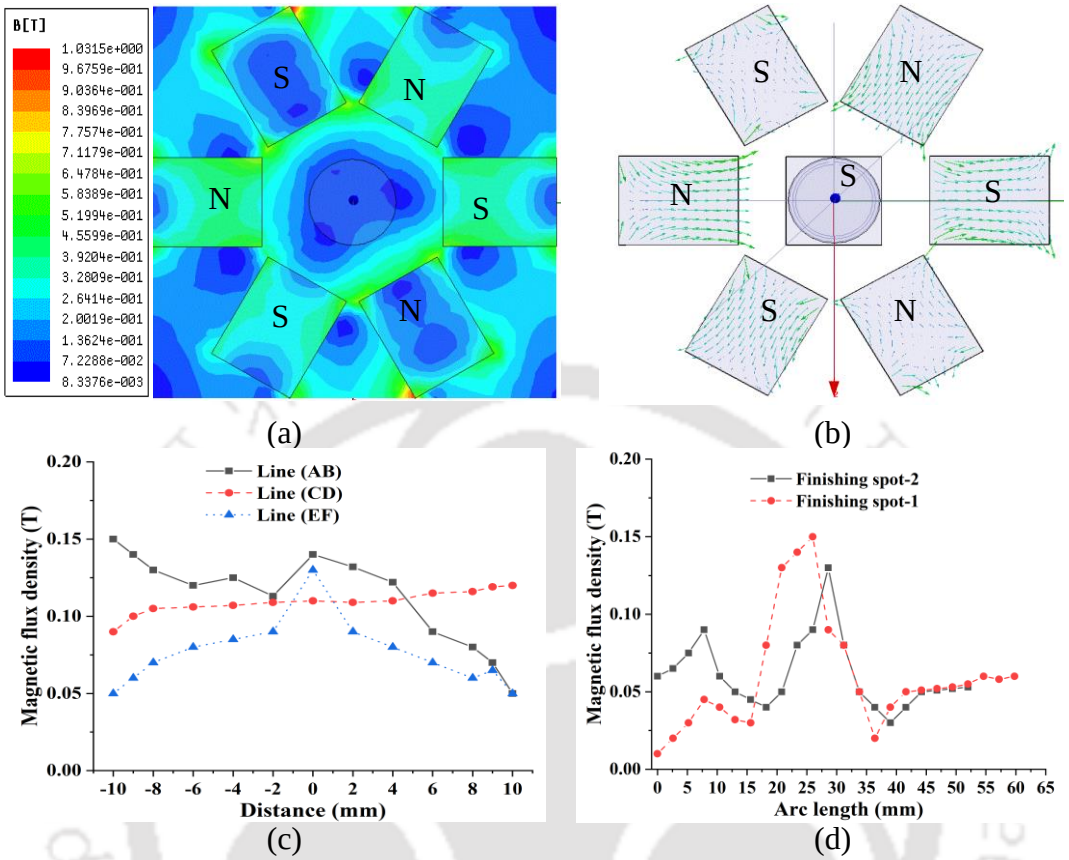


**Fig. 3.7** Magnetic flux density plot (a) contour, (b) vector, (c) along lines (AB, CD & EF, , Fig. 3.3), and (d) around the periphery of finishing spots (1 & 2, Fig. 3.3) for 7 magnets

### *5th configuration*

Finally, the 5th configuration with five magnets has been tried. The magnetic field distribution with five permanent magnets in the 5th configuration is determined. The distribution of contour and vector plots of the magnetic field is uniform and good enough for polishing in the finishing region, as shown in Fig. 3.8 (a) and (b), respectively. MFD distribution along the line (AB, CD & EF) and finishing spots (1 & 2) is shown in Fig. 3.8 (c) and (d), respectively. The variation in MFD distributions along lines and finishing spots is lesser than the 4th configuration having seven magnets. The maximum MFD value of 0.23T is observed at finishing spots, which is good enough for polishing poppet profiles and is higher than all previous configurations. Also, a higher value of MFD (0. 17T) exists at the centre.

Here four magnets on the fixture and one magnet underneath the fixture are placed. In this configuration, two combinations are tried; 1st combination with the underneath magnet having the south pole facing up and 2nd combination with the north pole facing up, even though

the knowledge of the south pole facing up showed the best result from the previous configurations. In between these two combinations, here also the underneath magnet facing south pole up shows the minimum variation of MFD distribution at finishing spots and enough magnetic field at the centre, as shown in Fig. 3.8 (d) and (c), respectively.

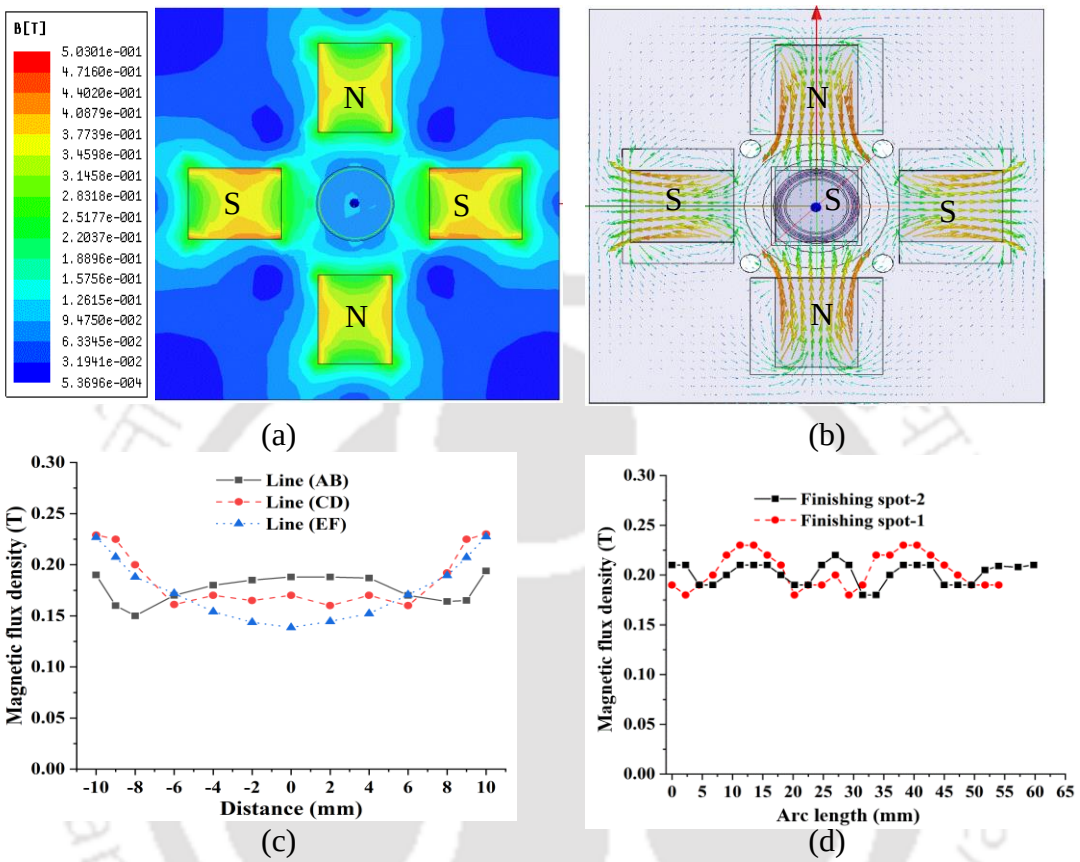


**Fig. 3.8** Magnetic flux density plot (a) contour, (b) vector, (c) along lines (AB, CD & EF, Fig. 3.3) and (d) around the periphery of finishing spots (1 & 2, Fig. 3.3) for 5 magnets

In this arrangement, the magnet dimension is correctly balanced side by side for close proximity to the finishing points, and there is also sufficient room to attach each magnet in an even space. Now four magnets are placed at a distance of 20 mm from the centre, at a distance of 11.19 mm from finishing spot-1 and at a distance of 10.17 mm from finishing spot-2 symmetrically. The 5$^{th}$ magnet is placed at 5 mm below the finishing spots (ridge) and 3.7 mm below from the fixture's centre. With this configuration, the magnet fixture satisfies all requirements for uniform polishing poppet profiles. Also, the best required MFD, 0.23T and 0.17T at finishing spots and centre, respectively, exist. Furthermore, the optimum size and location of the magnets have not been changed, enough space left for the MRPF container, and lastly, the size of the magnet fixture became compact and rigid. After testing all the five fixture configurations, the 5$^{th}$ configuration consisting of five magnets is chosen in the present study.

The five-magnet- configuration design will provide a standardized uniform nano-scale finishing at the appropriate positions of the poppet ridge profiles.

The other parts of the magnet fixture are designed accordingly as explained below in the following section. Finally, after fabricating the entire magnet fixture, the simulation results are validated with the experimental results as discussed below.

### 3.2.3 Other Parts and Geometry of Magnet Fixture

After selecting the 5$^{th}$ configuration, now the challenge was to design and fabricate other parts and decide the magnet fixture's final geometry. The total number of magnets and their optimum locations have been decided at 20 mm from the centre. Considering these constraints, the final dimension of the magnet fixture is designed as 110 mm × 110 mm × 20 mm. The maximum value of MFD exists at the centre of the magnet fixture. Hence, the magnets are placed accordingly on the aluminium plate. All four magnets are firmly fitted on the aluminium plate by perspex sheet (25 mm × 10 mm × 20 mm). Also, the magnets are covered with diamagnetic steel plates (32 mm × 27 mm × 1 mm). The steel plates covering the magnets are fixed on the aluminium plate using Allen bolts (M 3 x 20 mm) made of diamagnetic steel. Nonmagnetic Perspex, diamagnetic SS Allen bolt and SS plate are used to avoid any interference of the applied magnetic field.

Due to the complex design of poppet ridge profiles on the magnet fixture and MRPF container, these are manufactured as two separate parts. Also, it was challenging to fabricate these two components as a single rigid body. The container is made leak-proof from MR fluid using a gasket and rubber placed underneath the container in the magnet fixture at the specified slot. The magnet fixture also has a provision/space to attach the 5$^{th}$ magnet. The container has a dimension of 30 mm height, internal and external diameters of 26 mm and 32 mm, respectively. The MRPF container is shown in Fig. 3.9. There is also a need for a base to hold the whole magnet fixture and the 5$^{th}$ magnet. It was also necessary to make the entire fixture rigid and compact, easily fitting on a CNC table for uniform polishing of poppet valve profiles. The magnet fixture base is designed with a 110 mm diameter, as shown in Fig. 3.9.

The primary requirement was to finish only the ridge profiles of the poppet valve without disturbing other parts. Holding the poppet valve in the CNC spindle has been a challenging task since the upper part of the poppet is hollow (Fig. 3.1 (a)). Hence, ultimate care is taken while fixing it in the CNC spindle. After designing and fabricating all the parts of the magnet

fixture, the final assembly is made, as shown in Fig. 3.9. After that, the capability of the magnet fixture is checked with the experimental investigation.

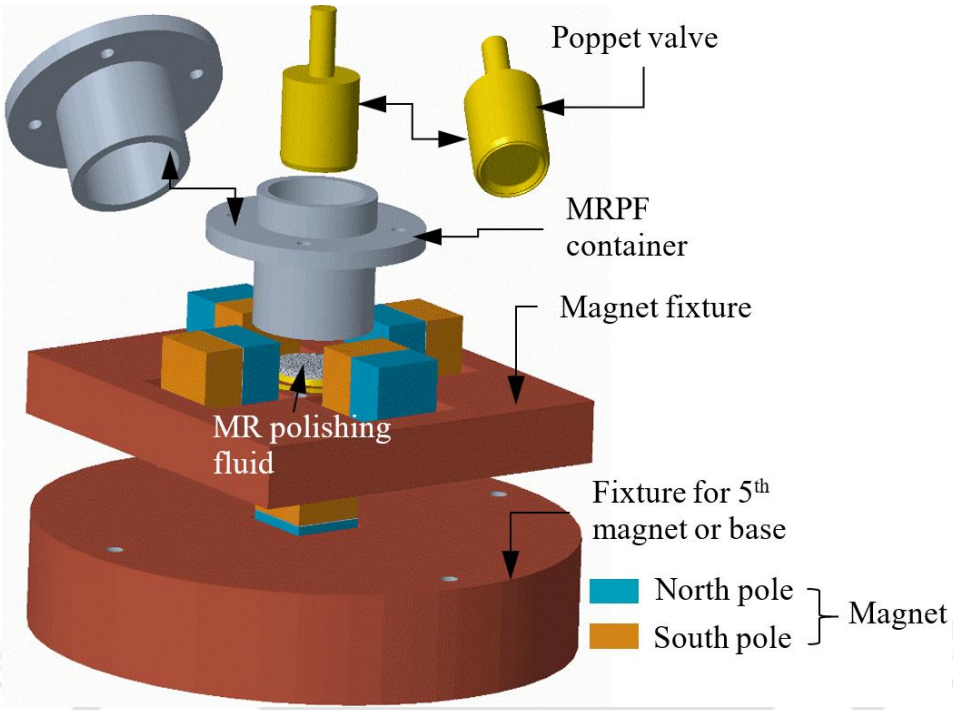


**Fig. 3.9** Schematic diagram of magnet fixture assembly for poppet valve polishing

## 3.3 Experimental Investigation

As discussed earlier, the final magnet fixture has been fabricated based on the 5th configuration. The values of MFD at different points is measured using a digital Gaussmeter. Further, the simulated MFD from Ansys is validated with the experimentally measured MFD to check the magnet fixture's capability.

Initially, the Gauss-meter probe is kept vertical for measuring the MFD at corresponding lines (AB, CD & EF) and finishing spots (1 & 2). The results obtained in the first experiment show a 75 % error with the simulated results. The measured results were almost similar for two more repeated experiments with the same vertically placed digital Gaussmeter probe, with a 75% error with simulated results. All the magnetic flux lines are not passing perpendicularly through the digital Gaussmeter probe due to the placement of the 5th magnet, which results in the inaccuracy of MFD measurement. Fig. 3.10 (a), (b) and (c) explain how the Hall probe of the digital Gaussmeter should be placed (at some angle) to pass the whole MFD lines perpendicular to the hall probe. However, it is unknown at what angle the magnetic probe is to be set. Hence, three more experiments are conducted to measure the MFD by placing the probe at 30º, 45º, and 60º angles, respectively. After completing all four experiments, it was found

that the probe placed at a 45º angle showed approximately less than 8% error with the simulated results.

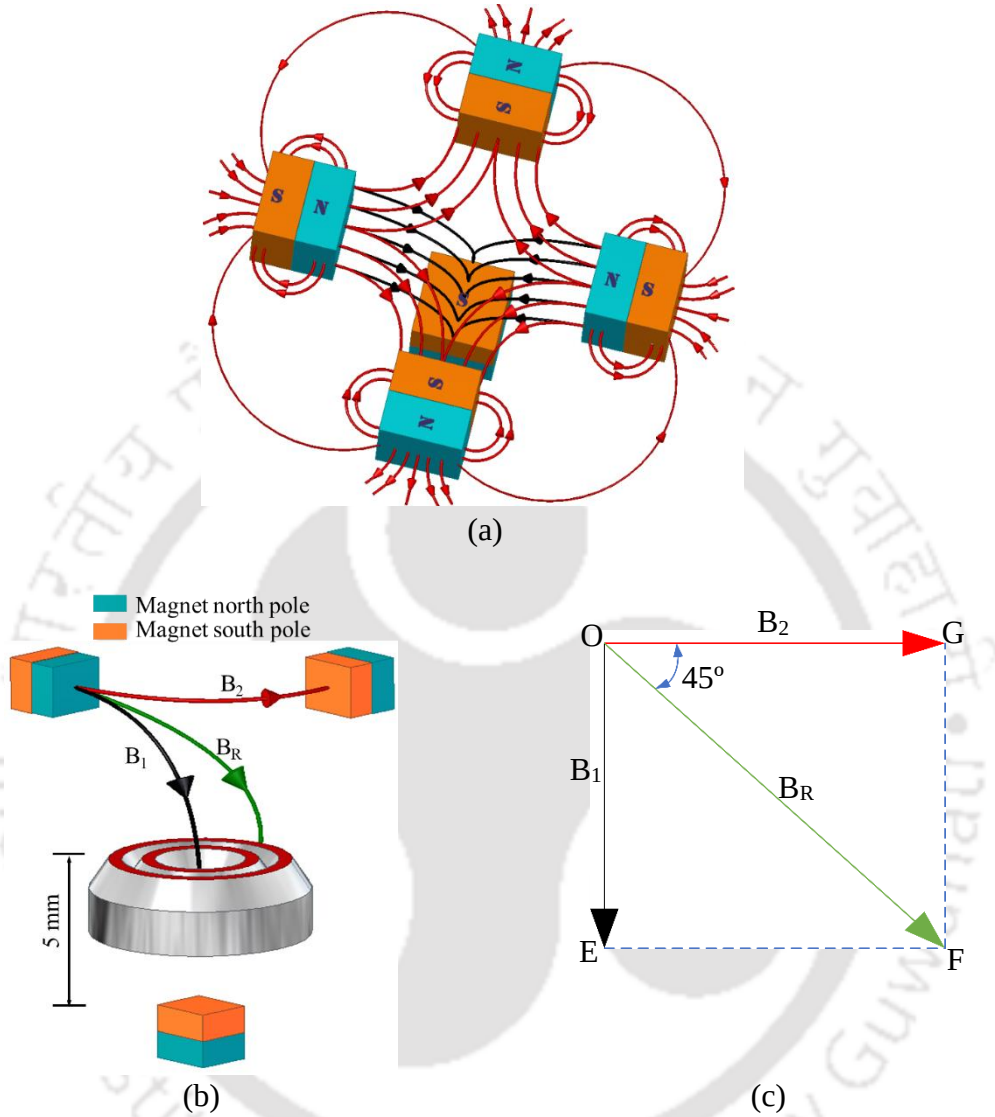


**Fig. 3.10** (a) Schematic illustration of overall 3D magnetic flux density (MFD) distribution by five magnets, net MFD line on finishing spots in (b) 3D and (c) 2D view

Here, the normal component of the magnetic field (which is most significant) is considered, neglecting other insignificant components. The resultant value of MFD on the poppet valve ridges can be obtained from Eq. (3.1). The probe placement at 45º is shown in Fig. 3.11. The MFD lines cross perpendicularly to the probe as shown in Fig. 3.11 (b) and (c), after placing the Hall probe at an angle of 45º. Hence, the measured MFD offers almost similar results as obtained through simulation. The total MFD can also be calculated analytically from Eq. (3.2). The total normal magnetic force acting on carbonyl iron particles can be calculated from Eq. (3.3) [140]–[142].

$$B_R = \sqrt{B_1^2 + B_2^2} \tag{3.1}$$

$$B_{TR} = B_R + \mu_0 \left( M_{CIP} \right) \tag{3.2}$$

$$F_m = \frac{m_{CIP} \chi_m B_R(s) \dfrac{dB_R(s)}{ds}}{\mu_0} \tag{3.3}$$

Here, $B_{TR}$ is the total resultant magnetic flux density or magnetic field in the working gap ($s$), which is filled with MRPF, $M_{CIP}$ is the magnetization of the CIPs, $\mu_0$ is the magnetic permeability of free space, $F_m$ is the normal magnetic force, $\chi_m$ is the magnetic susceptibility, and $B_R(s)$ is the variation of magnetic flux density along working gap ($s$). The distribution of magnetic lines of force (3D schematic view) by five magnets is shown in Fig. 3.10 (a). The resultant magnetic field in 3D and 2D schematic views is shown in Fig. 3.10 (b) and (c), respectively.

For accurate measurement of the MFD, 15º incremental interval of rotation angle along the periphery of the finishing spot (1 & 2), 2 mm incremental interval along the lines is considered. The probe is attached to a digital height gauge. The height gauge is placed on a small x-y-z table, as shown in Fig. 3.11.

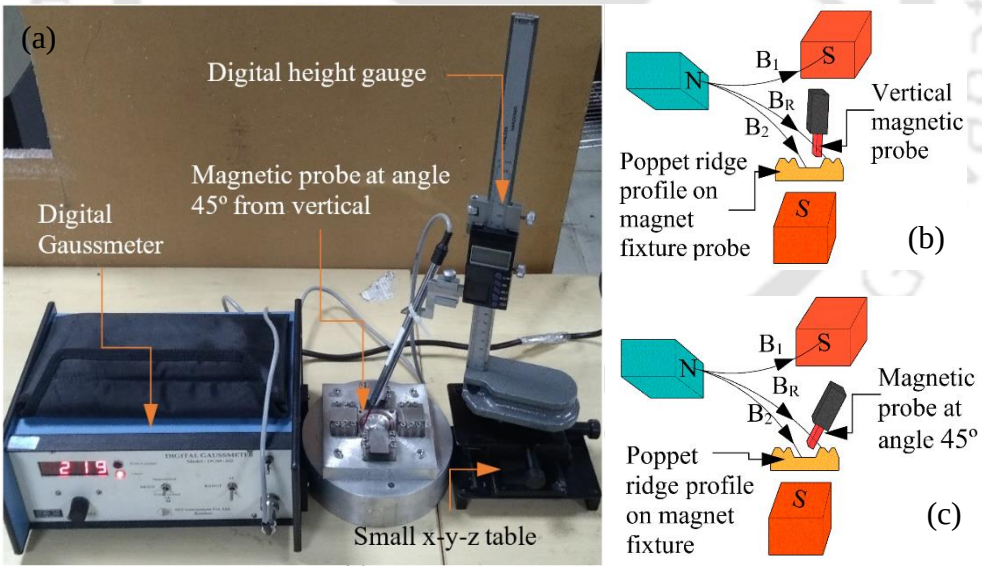


**Fig. 3.11** (a) Magnetic probe of digital Gaussmeter placed at a 45º angle from vertical, schematic of net MFD line passing through probe after placing the probe (b) vertically and (c) at an angle 45º

After fixing the Hall probe of the digital Gaussmeter at a 45º angle with the vertical axis, the final and accurate measurement of magnetic flux density is obtained along the lines (AB, CD & EF) and around the periphery of finishing spots (1 & 2). The comparison between the

experimental and simulated value of the magnetic flux density is shown in Fig. 3.12 and Fig. 3.13, respectively. Further, the measured magnetic flux density along three lines (AB, CD & EF) are plotted together in Fig. 3.14(a) to compare the magnetic field variation among these lines. Similarly, the measured MFD along finishing spots (1 & 2) are plotted together in Fig. 3.14(b). MFD values are measured three times at each position, and an average value is considered. Measured results show that placing the Hall probe of digital Gaussmeter at a 45º angle from the vertical axis reduces the error with simulated results to 8%. The magnetic probe is held at 45º and connected to the digital height gauge to see the variation in magnetic flux density along vertical direction (height 0 to 33 mm) at equal intervals of 1 mm starting from finishing spots (1 & 2) and centre (OH). The final plot of magnetic flux density along height is shown in Fig. 3.15. A comparison of the maximum value of magnetic flux density (from all measured and simulated results) at the centre and finishing spots 1 & 2 (Fig. 3.3) is made in Table 3.1.

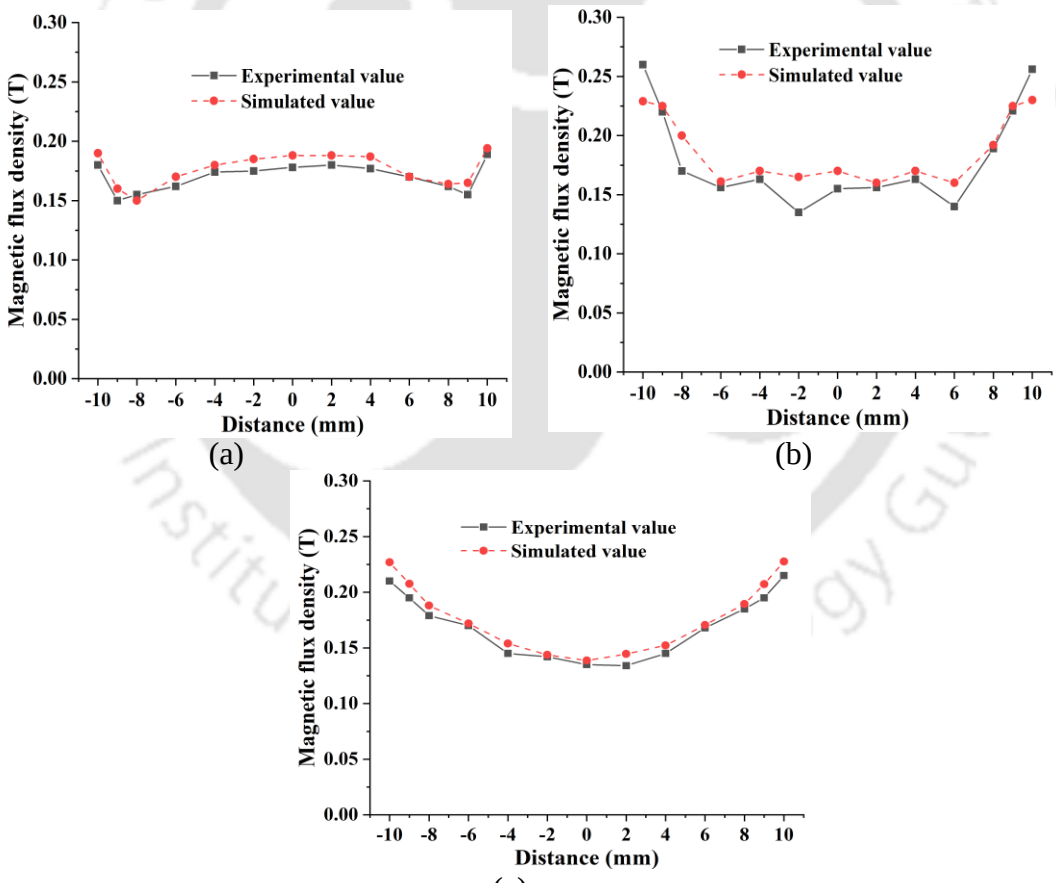


**Fig. 3.12** Experimental and simulated values of magnetic flux density along the lines (a) AB, (b) CD, and (c) EF

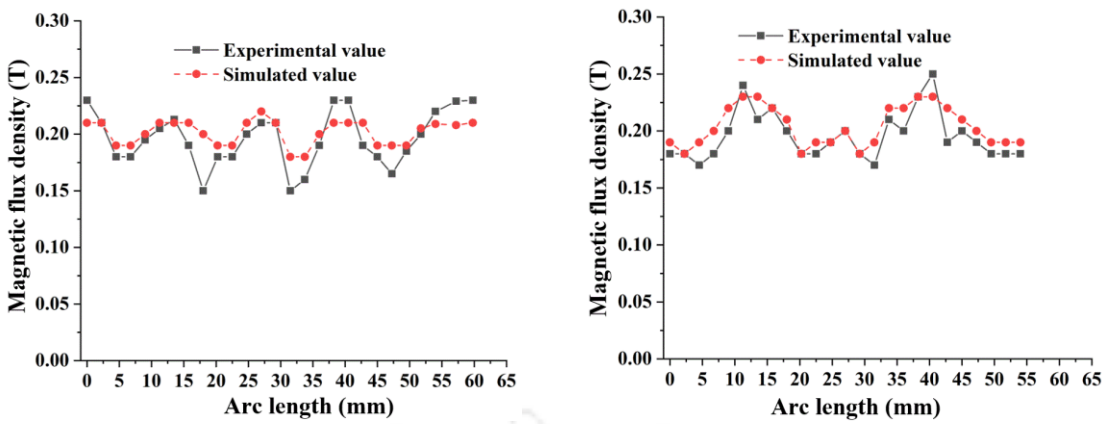


(a) (b)

**Fig. 3.13** Experimental and simulated values of magnetic flux density along the periphery of finishing spots (a) 1 and (b) 2

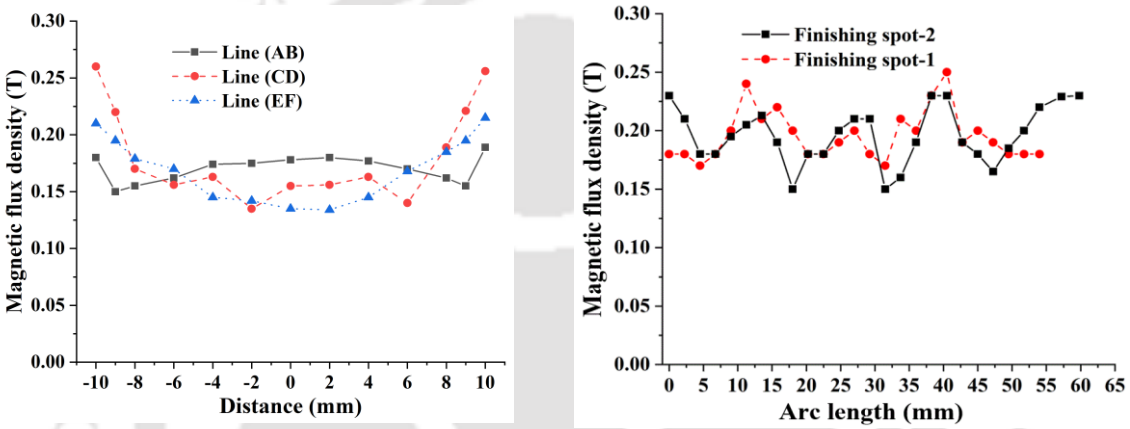


(a) (b)

**Fig. 3.14** Experimentally measured magnetic flux density plot along the (a) lines (AB, CD & EF, Fig. 3.3), and (b) periphery of finishing spots (1 & 2, Fig. 3.3)

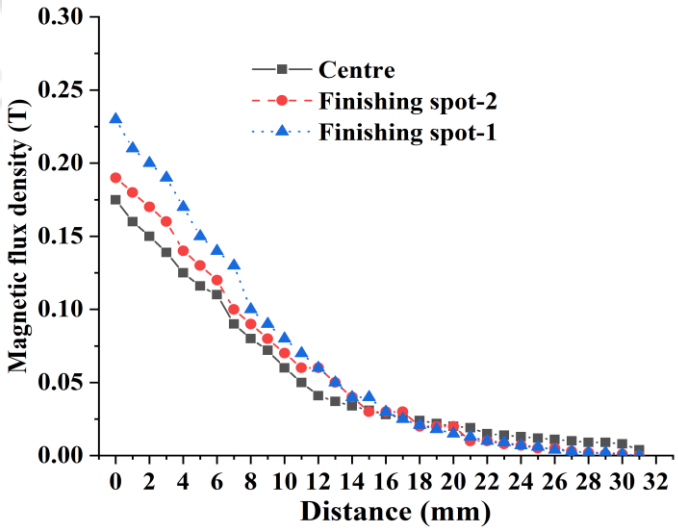


**Fig. 3.15** Magnetic flux density plots measured vertically along line OH (from magnet fixture centre, O) and along two lines parallel to OH (starting from finishing spots 1 and 2) (Fig. 3.3)

**Table 3.1** Maximum value of simulated and measured magnetic flux density at magnet fixture centre and finishing spots (1 & 2, Fig. 3.3)

| | Maximum magnetic Flux Density (T) | | |
|---|---|---|---|
| **Measured spots** | **From simulation** | **Experimentally measured** | **Error (%)** |
| Centre | 0.19 | 0.180 | 5.55 |
| Finishing spot-1 | 0.23 | 0.215 | 6.97 |
| Finishing spot-2 | 0.21 | 0.204 | 2.94 |

The experimental setup for the poppet valve is shown in Fig. 3.16. The magnet fixture has five permanent magnets (Sm2Co17 of grade 30H) of dimension 25×20×20 mm. The poppet valve is attached to a precision 3-axis CNC milling machine head. The magnet fixture is held with a precise vice during polishing, as shown in Fig. 3.16. At first, during starting of the finishing process, the CNC spindle is rotated at 1200 rpm. The initial working gap between the poppet ridge and the magnet fixture profiles is fixed at 2 mm. After that, the spindle is guided to move up to 1 mm downward (towards magnet fixture) with a feed rate of 0.01mm/min from its starting position to completely fine finish the poppet ridge profiles for 100 minutes. This vertical motion of the poppet valve is provided to make the process faster as with increased finishing time, the sharp cutting edges of the abrasives become blunt, and the abrasives require a higher normal force to polish the poppet ridge profiles further.

Table 3.2 provides the experimental conditions such as poppet rpm, finishing time and vertical feed rate. A CNC milling machine is used to adjust the rpm of the poppet valve. The surface topography and surface roughness of the workpiece before and after experimentation is measured using a non-contact type optical-type profilometer (Taylor Hobson Talysurf). The process mechanism is analyzed during preliminary experimental study, and the most significant process parameters are identified.

Indigenously made customized MRPF is prepared to finish the poppet valve profiles properly. Initially, the acid (HF and $HNO_3$) was used as a base medium with distilled water [143] because of the very high hardness (HRC 47) of the workpiece material. However, it was observed that some parts of the workpiece got damaged due to the chemical reaction between the workpiece and acid. The new compositions of MRPF are shown in

Table 3.3. Therefore, hydrofluoric acid (HF) has been removed from MRPF for further experimentations. However, $HNO_3$ remains, as it is used to brighten the surface. An extra agent, i.e., $H_2O_2$ is mixed with MRPF to dissolve the hard metallic surface to help abrasive particles indent easily. Copper (II) nitrate ($CuNO_3$), which forms due to the reaction of Cu, $HNO_3$ and $H_2O_2$, is also used as a polishing agent. So MRPF was formulated with a base medium of $H_2O_2$

and deionized water and further mixing with CIPs and abrasive particles. Further glycerol is added to the MRPF. This functions as a stabilizer to spread CIPs, consistently eliminating agglomeration. It also contributes to prevent sedimentation.

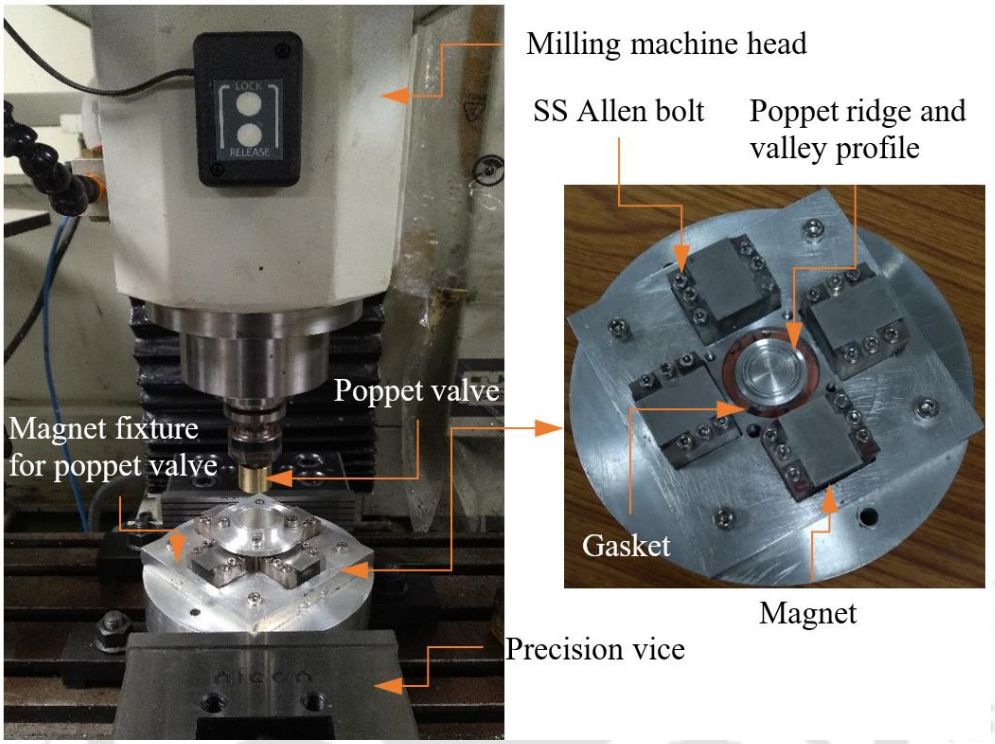


**Fig. 3.16** Experimental setup for poppet valve finishing with magnet fixture details

**Table 3.2** Experimental conditions during R-MRFF

| Parameter | Conditions |
|---|---|
| Finishing time | 1 hr. 40 min |
| Feed rate | 0.01 mm/min |
| Rotational speed of poppet | 1200 rpm |
| Working gap | 2 mm |

**Table 3.3** Composition of MR polishing fluid

| Constituents | Volume concentration (%) |
|---|---|
| CIPs | 30 |
| SiC abrasive (mesh size 800) | 7.1 |
| Glycerol | 8 |
| Nitric acid ($HNO_3$) | 1.17 |
| Hydrogen peroxide ($H_2O_2$) | 1.3 |
| Deionized water | 52.43 |

## 3.4 Results and Discussion

Experiments were conducted to evaluate the functionality and performance of the novel magnet fixture for standardized uniform polishing of the narrow ridge profiles of the poppet valve. On

the ridge profiles of the poppet, an effective, consistent and optimum distribution of magnetic flux density is present. This helps in getting a fine surface finishing. In order to understand the finishing surface characteristics, the influence of MRPF on surface topography, surface roughness, macrograph and the FESEM image is deduced.

### 3.4.1 Surface Roughness

The surface roughness parameters of the poppet valve profiles were evaluated while using the novel magnet fixture. Poppet valve profiles was finished with MRPF, and its composition is given in Table 3.3. At first, the polishing of the poppet was performed with just the rotary action of the poppet valve. Due to the only rotational movement given to the poppet valve, the sharp edges of abrasives got blunt and are unable to trim the roughness peaks [144]. Hence, the desired surface finish is not achieved. Hence, it becomes necessary to move poppet in the downward direction at a certain feed rate to increase further the applied normal force ($F_n$) (Eq. (6.26)) on abrasive particles. Also, due to the resulting magnetic force ($F_m$), the MRPF is bound to the periphery of poppet finishing spots, not segregating into the container, nor leaving the poppet valve profile. So the resultant indentation force ($F_{indentation}$) (Eq. (6.28)) will act on the abrasive particle (Fig. 3.17) to indent into the poppet ridge profiles, and due to resultant cutting force ($F_c$) (Eq. (6.27)), (Fig. 3.17) the abrasives easily remove material from poppet ridge surfaces. The resultant force ($F_R$), which acts on active abrasive grain to cut the roughness peak (Fig. 3.17(d)), is given in Eq. (3.4).

$$\vec{F}_R = \vec{F}_c + \vec{F}_{indentation} \tag{3.4}$$

After finishing, the minimum average surface roughness ($R_a$) on finishing ridge profiles were decreased to 20.1 nm (Fig. 3.18 (b)) from the initial value of 320 nm (Fig. 3.18 (a)).

Now to check the capability of novel magnet fixture for its intended requirements, different positions (on finishing ridge profiles and other areas) are selected as shown in Fig. 3.19. At these positions, the surface roughness values are measured. It was observed that the surface roughness values at finishing ridge profiles are decreased to minimum values as intended. However, an insignificant reduction in surface roughness values is observed in other positions as per the requirement to avoid any damages. These were the exact requirement of the present MR finishing operation of poppet valve ridges. Hence, the novel magnet fixture is capable of producing the required surface roughness values on poppet ridges.

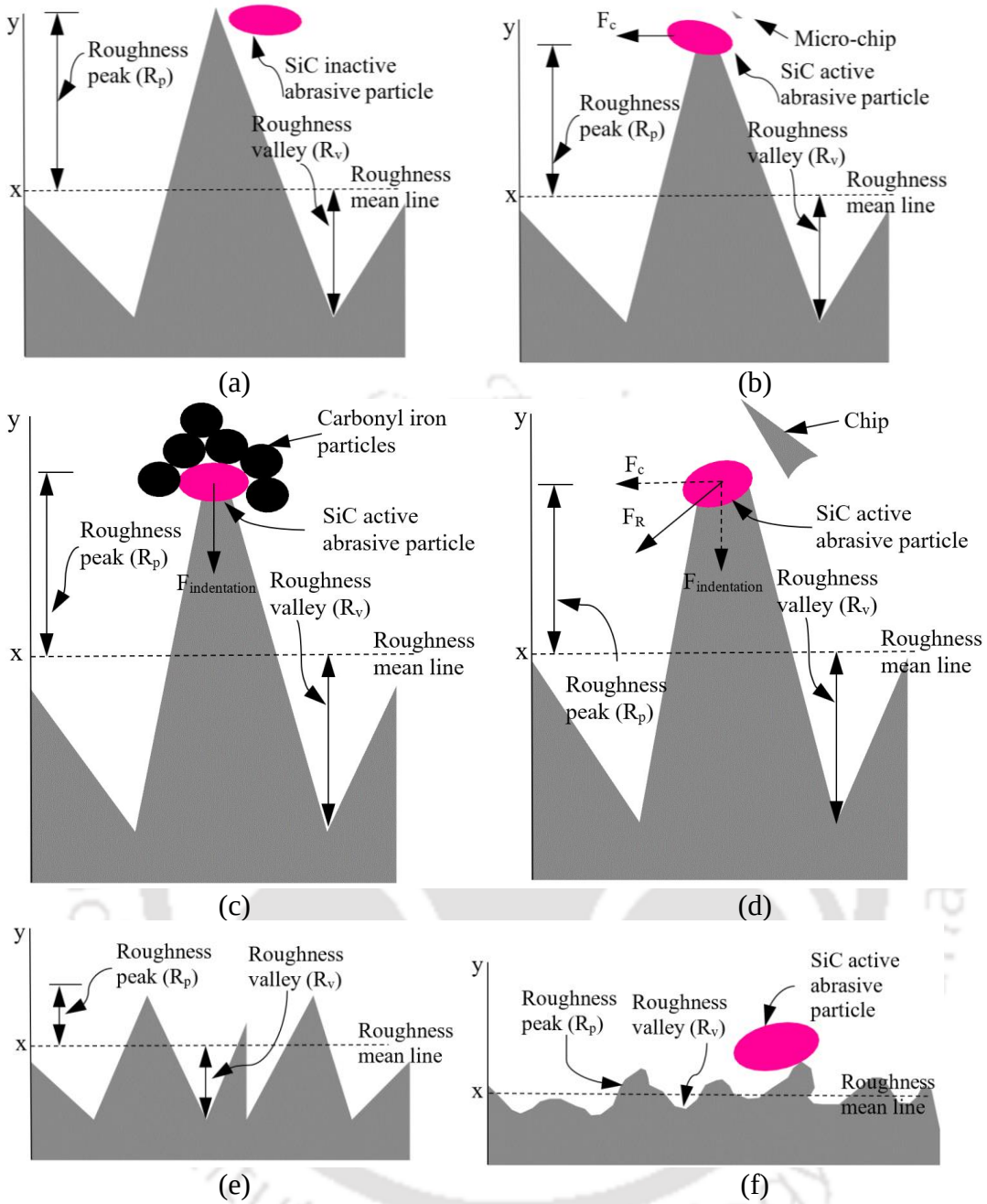


**Fig. 3.17** (a) Initail surface roughness peak; Roughness peak (b) micro-slicing by abrasive cutting force, (c) penetration by abrasive indentaion force (d) slicing by resultant of abrasive cutting force and indentation force, after (e) 60 minute and (f) 100 minute of finishing cycles

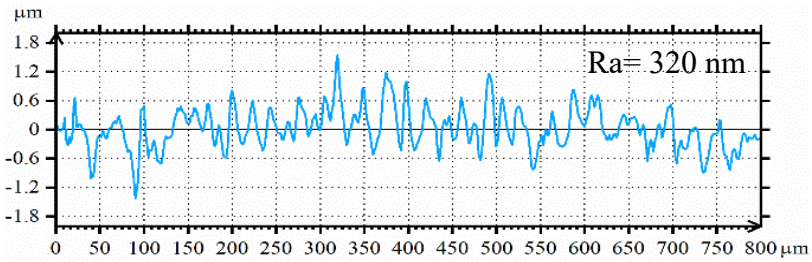


(a)

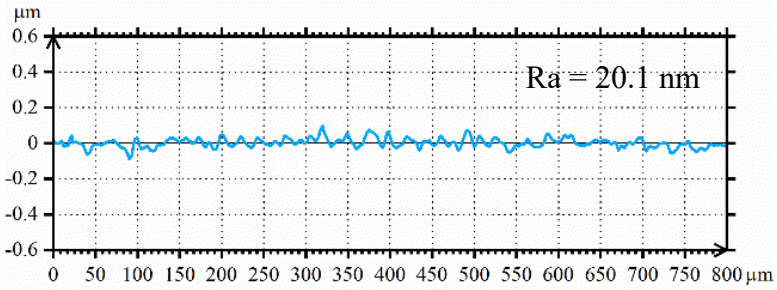


(b)

**Fig. 3.18** Surface roughness profiles of poppet valve (a) before and (b) after finishing

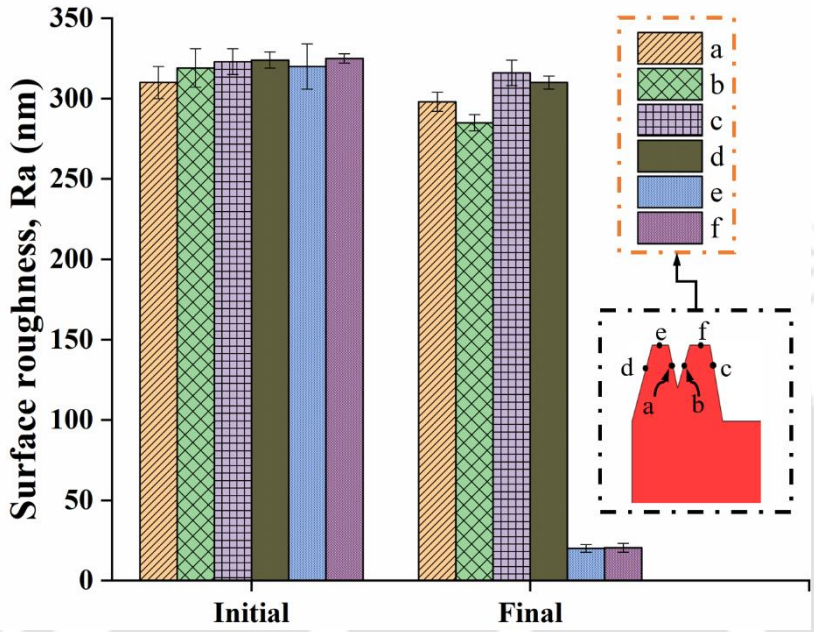


**Fig. 3.19** Initial and final surface roughness values at different selected positions on the poppet valve profiles

## 3.4.2 Surface Characterization

The surface topography of the poppet valve profile before and after finishing is shown in Fig. 3.20. Initial turning scratches, deep valleys and pits (Fig. 3.20 (a)) has been removed after final MR polishing (Fig. 3.20 (b)). These results demonstrate that nearly all parts of the poppet profile have the same reduced surface roughness value. The significant decrease of surface roughness values on the poppet valve profile indicates that the novel magnet fixture is capable of producing a good fine surface finish. This is attributed to the same degree to which the magnetic field is dispersed at the poppet profiles (Fig. 3.8 (c) and (d)). The surface finishing mechanism by the action of cutting force ($F_c$), and indentation force ($F_{indentation}$), is shown in Fig. 3.17.

The macro-graphs of the poppet valve profile before and after finishing are shown in Fig. 3.21. Before finishing, as shown in Fig. 3.21 (a), the continuous deep valleys and pits were

present, which have been removed after MR finishing. After finishing, a consistent and smooth surface is obtained, as shown in Fig. 3.21 (b).

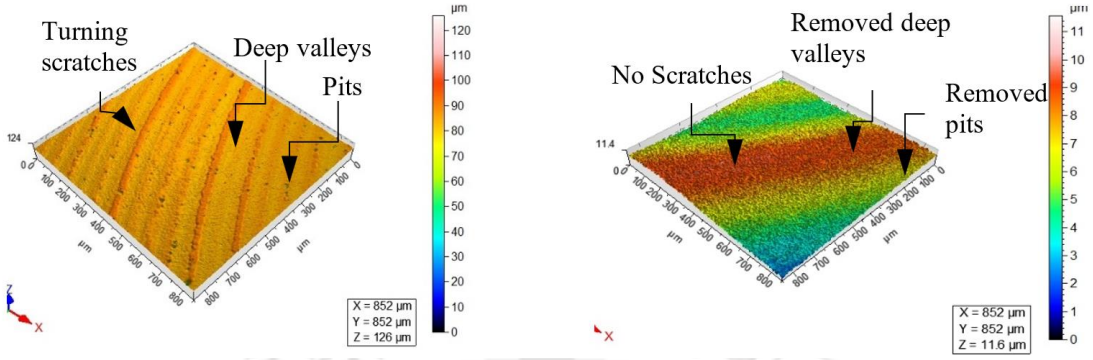


(a) (b)

**Fig. 3.20** Surface topography of poppet valve (a) before and (b) after finishing

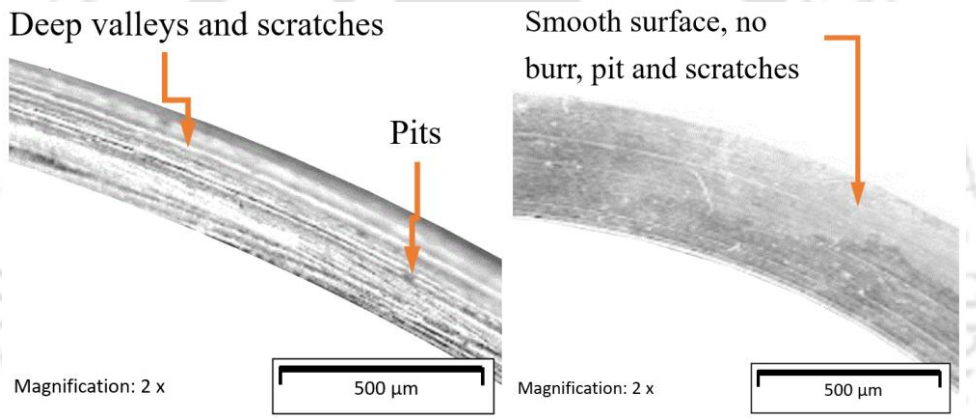


(a) (b)

**Fig. 3.21** Macrographic images of poppet valve profiles (a) before and (b) after finishing

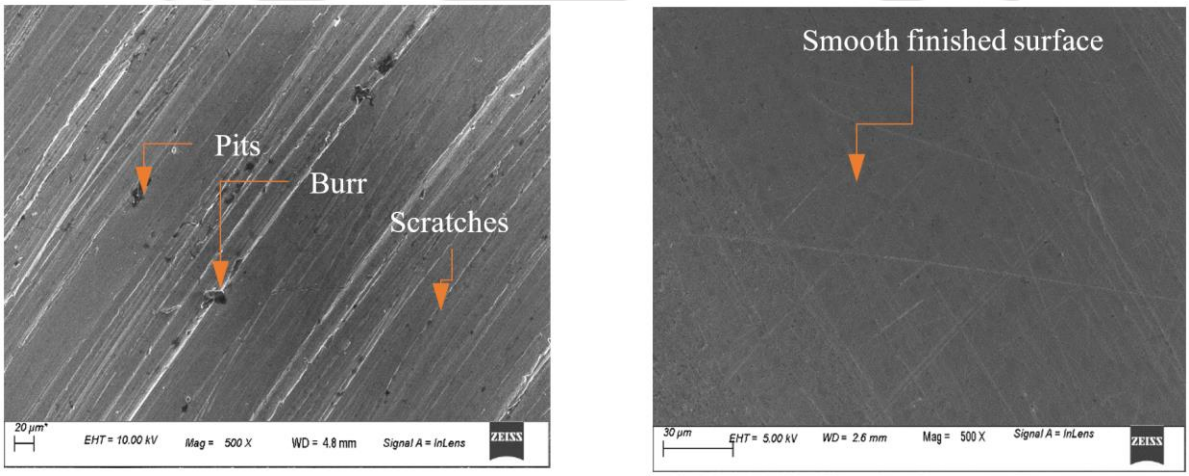


(a) (b)

**Fig. 3.22** FESEM images of poppet valve profiles (a) before and (b) after finishing

The FESEM images of the poppet valve profile before and after finishing are shown in Fig. 3.22 (b). FSEM image in Fig. 3.22 (a) show that initial scratches, burrs and pits are removed

after finishing (Fig. 3.22 (b)). The rotational motion of the poppet valve has left negligible rotational marks after finishing, as shown in Fig. 3.22 (b). In the present R-MRFF process, the material removal was performed by active abrasive particles in the direction of the cutting force on the poppet valve profile. All initial defects generated while fabricating the poppet by turning operation were removed. The final polished surface becomes very smooth with almost no surface defects, as shown in Fig. 3.22 (b). Therefore, the FESEM image of the finished surfaces of a poppet valve indicates that the surface structure is significantly improved in accordance with the ground surface. As illustrated in Fig. 3.22 (b), the final surface characteristics are the exact criterion for finishing the poppet ridge profile.

## 3.5 Summary

One of the exciting approaches for improved practical use of poppet valves is its ridge profile polishing using the latest R-MRFF technology with a novel magnet fixture. Depending upon the standardized uniform distribution of magnetic flux density obtained through magnetostatic FE analysis on the poppet valve profiles, a novel magnet fixture for the R-MRFF method is developed. For finishing the poppet valve profiles on required positions, the effectiveness of the designed fixture is confirmed experimentally. The current study shows the reliability and effectiveness of the current magnet fixture. The resultant magnetic field produced by five magnets is uniformly distributed along the poppet ridge profiles. Because of that, active abrasive particles will uniformly indent into the poppet surface, which results in a consistent cutting of the poppet surface asperities in the vertical and rotating directions with the poppet movement. It allows smooth finishing and high-geometrical accuracy of the poppet profiles. The surface roughness ($R_a$) value for poppet valve profiles is reduced significantly to 20.1 nm, from 320 nm. The quality of the poppet surface is improved considerably and uniformly. The error between the measured value of magnetic flux density by digital Gauss-meter and the simulated value obtained using Ansys® is less than 8%. The MR polishing fluid reacts with poppet valve material during the finishing process and forms a polishing agent, which helps in finishing the poppet valve precisely. The surface characterization of finishing ridge profiles shows that all defects (burrs, pits, scratches, etc.) are entirely removed. A finely finished poppet valve using a novel magnet fixture will improve its corrosion, wear resistance, and sealing effectiveness, further minimising hydrocarbon emissions at elevated pressure and temperature during its actual use.

# Chapter 4 Uniform Finishing of Miniature Gear

## 4.1 Introduction

Nano-finishing of miniature gear is a tough challenge due to the complexity of its geometry. Miniature gears are used in numerous complex applications, such as biomedical instruments for pumping, cutting, and various other works, even in small servo motors, commonly used in UAVs in different manufacturing, military, and research applications. The high material removal causes noise or vibration between the meshing teeth. The traditional method for finishing of miniature gears produces an error in miniature gear teeth profiles because of the transverse grinding lines, fine micro-cracks, burr, scratch marks, burns, pits and thermal distortion. Very few finishing processes are applied to miniature gears due to the narrow spacing between the miniature gear teeth.

In the current study, a novel uniform flow restrictor (a negative replica of the miniature gear profiles) is used in the R-MRFF process for precise finishing of the miniature gear teeth profiles. For this purpose, the effect of key parameters on the process's performance has been studied through response surface methodology (RSM). Analysis of variance (ANOVA) has been applied to identify significant parameters. Further, a model is also simulated using Comsol® Multiphysics software to determine the depth of indentation caused by a single abrasive particle on SS316L spur miniature gear teeth profile due to normal finishing force. The surface characteristics of the polished surfaces with distinct magnetorheological fluids are outlined for surface roughness and surface texture without and with the use of a novel flow restrictor. Ultrafine surface roughness (Ra = 23.9 nm) at miniature gear teeth profiles are obtained using a Type-III MR fluid and uniform flow restrictor. All manufacturing defects like burrs, dents, scratches and pits are also completely removed. MR fluid of Type-III is selected to polish miniature gear teeth profiles. From experimental results, it was observed that the combination of a high volumetric proportion of iron/abrasive particles and a higher rotational speed of magnets is more favourable to obtain a higher degree of surface finish, while the combination of the high extrusion pressure and a higher rotational speed of magnets causes higher material removal. The finishing results are compared without and with using a uniform flow restrictor. After using the R-MRFF process, the miniature gear may have better mechanical strength, longer service life, and minimum maintenance during its working performance.

## 4.2 Experimental Investigation

The uniform flow restrictor is a negative replica of the miniature steel gear. There is a random movement of ferromagnetic iron and abrasive grains, although the magnetic field is active, as demonstrated in Fig. 4.1 (b). However, with the introduced fixture and uniform flow restrictor, uniform confined space between flow restrictor and miniature gear is generated [140]. MR fluid is forced to pass with constant velocity through each and every profile of the miniature gear teeth, as demonstrated in Fig. 4.1 (a). The finishing mechanism of the R-MRFF process with and without uniform flow restrictor is presented in Fig. 4.1 (a) and (b), respectively.

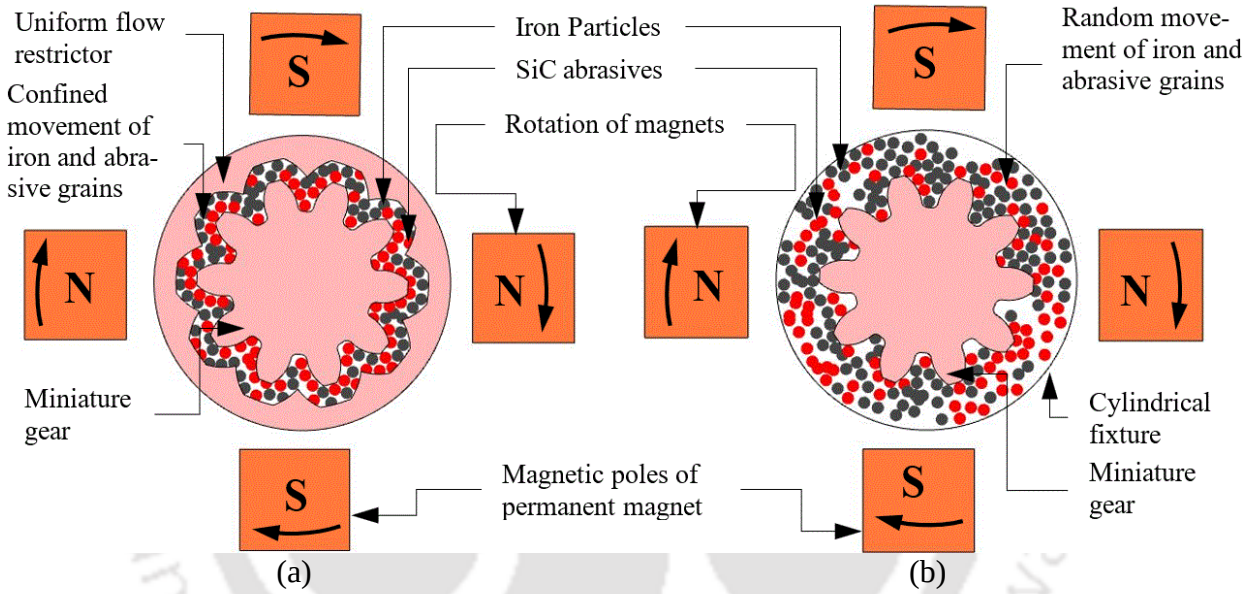


**Fig. 4.1** Finishing mechanism of R-MRAFF process for miniature gear teeth profiles (a) with and (b) without using uniform flow restrictor

Steel miniature gear and uniform flow restrictor are fabricated using wire electro-discharge machining (WEDM) process, which uses a slender wire. The wire is traced along the miniature gear profiles. The gear profile is manufactured by melting the material due to intense heat generation by electrical sparks in WEDM. The workpiece is exposed to high temperature along the machined surface, whose consequences reach to few millimetres deep inside the surface profiles. The material used to manufacture the miniature gear and uniform flow restrictor is SS316L. This steel grade is of lower carbon content than its SS316 variant, as the designation L means low here. SS316L grade steels are corrosion-resistant, durable, stronger at elevated temperatures, and unusually resistant to an acidic environment.

The miniature gear has a pitch diameter of 12.5 mm, outside diameter of 14 mm. The maximum outer diameter for uniform flow restrictor and workpiece fixture is 18 mm, and 22

mm, respectively. The miniature gear's involute profile is of 1.25 mm module, number of teeth is 10, and the thickness of the miniature gear is 2 mm. An Nd–Fe–B permanent magnet generates a magnetic field in the region where finishing is being performed. The workpiece fixture holds the miniature gear workpiece and uniform flow restrictor, and it is surrounded by a magnet fixture, which includes four permanent magnetic bars. Brass material is used to manufacture the workpiece fixture as it is non-magnetic. The workpiece fixture is fixed in between two polishing media cylinders along with the magnet fixture. Eight holes on the outer side of the workpiece fixture's flanges were made to allow the MRP media to flow across the miniature gear profiles. The retention of more MRP media helps in improved finishing of the workpiece. Uniform flow restrictor placement along with the miniature gear maintains a constant gap between all profiles of miniature gear teeth and uniform flow restrictor. A vertical two-way abrasive flow machining (AFM) setup, which has two hydraulic cylinders to flow the media up & down continuously, is used for the R-MRFF process for improved finishing capability. In the first half-cycle, MRP media of the bottom media cylinder passes through a workpiece fixture in an upward direction. In the next half-cycle, the same process reverses again to complete one cycle and uniformly finish the miniature gear profiles. The movement of the pistons of cylinders extrudes pressure on the MRP media, which forces the MRP media through the workpiece fixture. The experimental setup of the R-MRFF process with details of magnet fixture and workpiece fixture is demonstrated in Fig. 2.11. The attached limit switch helps in the piston's to and fro motion to automate the finishing process. Based on previous works on steel components, MRP media compositions are identified for the finishing of SS316L spur miniature gear, as demonstrated in Table 4.1 [84].

Three types of MR polishing media with varying sizes of iron particles and the concentration of abrasives have been prepared to check their gear profiles' consequences. The composition of different types of synthesized MR polishing media is demonstrated in Table 4.1. SiC abrasive having a mesh size of 800 is chosen, as it is best to finish steel miniature gear [84]. Hence, it is kept fixed for all experiments. Initially, paraffin oil's volume percentage is maintained at 63 % to make MR polishing media semi-thicker. The media quickly passes through a small gap of 2 mm between the miniature gear and the uniform flow restrictor. However, it was observed that, as MR polishing media is semi-thick, a small amount of MRP media started to seep out of the experimental setup. The grease is mixed as an additive to increase the viscosity of MR polishing media. Due to the frictional heat generation, the grease starts separating, weakening the adhesive bond between solid particles and liquid carrier of MR

polishing media. After using an extra rubber pad at the top and bottom media cylinders, this leakage was controlled.

The minimum amount of abrasive concentration in the MRP medium can't be less than 5 %. Also, the abrasive concentration cannot be much higher. Higher abrasive concentration causes their accumulation on the outside edges of the loop of MRP media, which is having iron particle chains, and many abrasives separate from this loop. This leads to the sliding and rolling of abrasives in the working gap without any polishing activity. Abrasives stuck in iron particle chains decrease magnetic force ($F$) in between two adjacent iron particles (IPs) [145] as described in Eq. (4.1).

$$F = \frac{\mu_0 \pi}{9}\left(\frac{r^2 CM}{R'}\right)^2 \tag{4.1}$$

Where $\mu_0$ is permeability for the free space, $r$ is the radius of an IP, $R'$ is the centre distance between two IPs, and $C$ is constant, $M$ is the magnetization of MRP media. The magnetic force ($F$) is inversely related to the gap between two adjacent iron particles ($R'$). So, whenever an abrasive particle arrives between iron particles, the gap between two adjoining iron particles rises, and $F$ reduces. Because of the lower value of magnetic force ($F$), the bonding strength between iron particles becomes weak, and consequently, they are unable to hold abrasives effectively. Thus, the final surface roughness value ($R_a$) rises, and MRR reduces with increased abrasive concentrations (Vol. %) beyond 5%.

**Table 4.1** Different types of synthesized MR polishing media

| Media types | Iron particles | | Abrasive grains | | Grease (Vol. (%)) | Paraffin oil (Vol. (%)) |
|---|---|---|---|---|---|---|
| | Mesh Size | Vol. (%) | Mesh Size | Vol. (%) | | |
| **Type-I** | 250 | 22 | 800 | 5 | 10 | 63 |
| **Type-II** | 400 | 22 | 800 | 8 | 10 | 60 |
| **Type-III** | 800 | 22 | 800 | 15 | 10 | 53 |

The parameters are taken in the present study that effects the reduction in surface roughness and improvement in MRR is the volumetric proportion of iron/abrasive particles (V), rotational speed of magnets (N) and extrusion pressure applied by hydraulic cylinder (P). On the basis of the preliminary experimentations done for % ΔRa, and available literature [30], [84], [131], MRP media is made by mixing IPs (mesh size 800), SiC abrasive powder (mesh size 800), grease, and paraffin oil. Grease is added to improve MRP media viscosity. This functions as a stabilizer to spread IPs, consistently eliminating agglomeration and preventing sedimentation.

In the present research, the % volume of the base fluid in MRP media varies from 53%– 63%. After selecting the MRP media composition, the no. of the finishing cycle is varied to find out the optimum no. of the finishing cycle. It was observed that up to 800 finishing cycles, the desired nanometer level surface finish are achieved. With further experimentation, surface finish improved; however, gear teeth profiles get deformed, and some amount of pitting is also observed. Hence, the 800 finishing cycle is the optimum cycle for the current study.

**Table 4.2** Preliminary experimentation for selecting a range of process parameters

| S. No. | V | N (rpm) | P (bar) | Initial Ra (nm) | Final Ra (nm) |
|---|---|---|---|---|---|
| 1. | 1 | 90 | 35 | 253 | 150.1 |
| 2. | 1. 5 | 90 | 35 | 256 | 112.9 |
| 3. | 2 | 90 | 35 | 257 | 116.3 |
| 4. | 2.5 | 90 | 35 | 260 | 124.1 |
| 5. | 3 | 90 | 35 | 261 | 148.1 |
| 6. | 4 | 90 | 35 | 254 | 159.4 |
| 7. | 1.5 | 30 | 35 | 254 | 128.5 |
| 8. | 1.5 | 60 | 35 | 250 | 126.3 |
| 9. | 1.5 | 90 | 35 | 259 | 111.5 |
| 10. | 1.5 | 120 | 35 | 256 | 127.9 |
| 11. | 1.5 | 150 | 35 | 265 | 152.1 |
| 12. | 1.5 | 90 | 30 | 262 | 130.2 |
| 13. | 1.5 | 90 | 32.5 | 258 | 124.9 |
| 14. | 1.5 | 90 | 35 | 259 | 112.1 |
| 15. | 1.5 | 90 | 37.5 | 259 | 136.1 |
| 16. | 1.5 | 90 | 40 | 262 | 150.1 |
| 17. | 1.75 | 90 | 35 | 255 | 115.9 |
| 18. | 2 | 90 | 35 | 257 | 119.6 |

V - Volumetric proportion of iron/abrasive particles, N - Rotational speed of magnets, and P - Extrusion pressure applied by the piston of hydraulic cylinder

**Table 4.3** Range of process parameters

| Levels | Process parameters | | |
|---|---|---|---|
| | V | N (rpm) | P (bar) |
| -2 | 0.31 | 39.5 | 30.7 |
| -1 | 1 | 60 | 32.5 |
| 0 | 2 | 90 | 35 |
| 1 | 3 | 120 | 37.5 |
| 2 | 3.6 | 140.4 | 39.2 |

To determine the variable range of the process parameters, preliminary experimentations were performed on the gear component. The initial average roughness values (Ra) of the gear workpiece ranges between 252–265 nm. To measure the surface roughness of the gear component before and after conducting experiments, a “Talysurf” non-contact optical

profilometer is used. The preliminary experimentations were conducted for the 40 minutes of the finishing cycle with the different range of the selected variable parameters. To vary the chosen variable, one parameter was varied at one time, and the other two were fixed, as shown in Table 4.2. The values of surface roughness (Ra) obtained after initial experiments are reported in Table 4.2 for the variable parameters like the volumetric proportion of iron/abrasive particles (V), the rotational speed of magnets (N) and extrusion pressure (P). The results obtained from the preliminary experimentations are used for selecting the range of the process parameters for effectively finishing the gear teeth profiles. The selected range for parameters is reported in Table 4.3.

**Table 4.4** Plan of experiments for statistical DOE

| S. No. | Factors | | | Response | |
|---|---|---|---|---|---|
| | V | N (rpm) | P (bar) | % ΔRa | MRR (g/min) |
| 1 | 1 | 60 | 32.5 | 48.71 | 0.00090 |
| 2 | 3.68 | 90 | 35 | 66.89 | 0.00020 |
| 3 | 2 | 90 | 35 | 90.78 | 0.00081 |
| 4 | 1 | 120 | 32.5 | 55.35 | 0.00099 |
| 5 | 2 | 90 | 30.79 | 42.37 | 0.00071 |
| 6 | 2 | 90 | 35 | 83.55 | 0.00093 |
| 7 | 1 | 120 | 37.5 | 73.66 | 0.00118 |
| 8 | 2 | 90 | 35 | 88.23 | 0.00092 |
| 9 | 2 | 39.54 | 35 | 63.95 | 0.00070 |
| 10 | 2 | 90 | 35 | 91.21 | 0.00090 |
| 11 | 0.31 | 90 | 35 | 59.29 | 0.00091 |
| 12 | 3 | 60 | 37.5 | 41.32 | 0.00055 |
| 13 | 3 | 60 | 32.5 | 48.78 | 0.00032 |
| 14 | 2 | 90 | 39.20 | 40.07 | 0.00078 |
| 15 | 2 | 140.45 | 35 | 85.60 | 0.00110 |
| 16 | 1 | 60 | 37.5 | 42.37 | 0.00061 |
| 17 | 3 | 120 | 32.5 | 60.20 | 0.00042 |
| 18 | 2 | 90 | 35 | 88.44 | 0.00091 |
| 19 | 3 | 120 | 37.5 | 56.62 | 0.00097 |
| 20 | 2 | 90 | 35 | 90.54 | 0.00083 |

% ΔRa – Percentage change in centre line average surface roughness value, MRR -Material removal rate

To analyze the parametric study for the fine finishing of poppet valve ridge profiles, the design of experiments (DOE) is used. Further, for analyzing the outcome of various parameters on the % change in surface roughness (% ΔRa) and material removal rate (MRR), response surface methodology (RSM) is used. The effect of the different process parameters and their combined effects are studied. From the analysis of variance (ANOVA), each process parameter's influence on % ΔRa and MRR are analyzed, and significant process parameters are selected.

The regression equation will help to explore the process parameter influence on % ΔRa and MRR. The plan of experiments along with their response are shown in Table 4.4 and the experiments are carried out randomly. Each experimentation is performed on the poppet gear workpiece for 3 hr. 20 minutes. The confidence level of the model is 95% to verify the effectiveness of the model. The F-level test from analysis of variance (ANOVA) is done to identify the implication of the regression equation for strengthening the relation amid the % ΔRa and controlled process parameters. The % change in the Ra value and final MRR after the experimentation is calculated using Eq. (4.2) and Eq. (4.3), respectively.

$$\% \Delta R_a = \frac{Initial\ R_a\ value - Final\ R_a\ value}{Initial\ R_a\ value} \tag{4.2}$$

$$MRR = \frac{Initial\ weight - Final\ weight}{Finishing\ time} \tag{4.3}$$

The gear workpiece's surface characterization is also observed with the help of a field emission scanning electron microscope (FESEM).

## 4.3 Region of Active Abrasive Particles

The effective magnetic field distribution on the miniature gear profiles without and with uniform flow restrictors is almost the same and uniform. However, the shear stress (primary cutting stress) distributions along the arc length of tooth profile (BD) is uniformly distributed when a flow restrictor is used, as compared when a flow restrictor is not used (Fig. 2.6). Without using a flow restrictor, a maximum variation of shear stress is obtained along the arc length of tooth profile BD (Fig. 2.6).

The working gap between the uniform flow restrictor and miniature gear teeth profiles is equal at every surface along the miniature gear teeth profiles. As demonstrated in Fig. 2.6, in the presence of a uniform flow restrictor, there is an almost static variation of shear stress is present. So, from FE analysis, it can be concluded that when the uniform flow restrictor is used around the miniature gear teeth profiles, constant shear stress is present at every profile of the miniature gear teeth. The average shear stress variation without using flow restrictor is almost half of the when using flow restrictor at miniature gear teeth involute, top and in-between surface profiles. Hence, at a single stroke total number of active abrasive grains/particles taking part in finishing action will also be almost half at miniature gear teeth involute (BD), top (DF) and in-between (AB) profiles and same for the face profiles of gear teeth when the flow restrictor is not used as compared to when flow restrictor is used. On the face profiles of miniature gear tooth, there will be almost no effect of the flow restrictor. So the effective

surface area of active abrasives at the miniature gear teeth involute (BD), top (DF) and in-between (AB) profiles becomes half and will remain the same for the face profiles of miniature gear teeth. As total active abrasive particles are more and uniform with a uniform flow restrictor, it will result in fast and uniform material removal and, thus, uniform surface finish at the miniature gear teeth profiles [84]. The development of active abrasives area on the miniature gear teeth in-between, involute, and top profiles are considered rectangular. And active abrasives region formation on the face profile of miniature gear teeth is assumed to be of trapezoidal shape. The following equation gives the total surface area for the active abrasive grains region without using a uniform flow restrictor per single tooth per stroke.

$$\begin{aligned}\left(Total\ active\ surafce\ area/tooth\right)_{without\ flow\ restrictor} &= \frac{1}{2}\times\left(S.A\right)_{top}+\left(\frac{1}{2}\times\left(S.A\right)_{in-between}\right)\times 2\\ &+\left(S.A\right)_{face}+\left(\frac{1}{2}\times\left(S.A\right)_{involute}\right)\times 2\end{aligned} \tag{4.4}$$

The following equation gives the total surface area for the active abrasive grains region with using a uniform flow restrictor per single tooth per stroke.

$$\begin{aligned}\left(Total\ active\ surafce\ area/tooth\right)_{with\ flow\ restrictor} &= \left(S.A\right)_{top}+2\times\left(S.A\right)_{in-between}\\ &+\left(S.A\right)_{face}+2\times\left(S.A\right)_{involute}\end{aligned} \tag{4.5}$$

Two is multiplied because there is two half in-between surface and two involute surfaces per single tooth are present, and one top and face profiles are present. The total number of active abrasive grains ($N_g$) per single stroke and tooth in the region is given as per the following Eq. (4.6) [146].

$$N_g = \frac{\%\ vol.\ fraction\ of\ \ SiC\ abrasive\ grain\times total\ active\ surafce\ area\times D_g}{Volume\ of\ \sin gle\ SiC\ abrasibe\ grain} \tag{4.6}$$

where $D_g$ is the diameter of the SiC abrasive grains is 19 µm. The volume of single SiC abrasive grain $=\frac{4}{3}\pi\left(\frac{D_g}{2}\right)^3=3.591\times10^{-15}m^3$. The total number of active abrasive grains is calculated for different MR polishing media compositions for all profiles of single miniature gear tooth without and with uniform flow restrictor is given in Table 4.5. At the time of finishing, the magnetic field's effective region is retained equally at every surface of miniature gear teeth profiles. Only active abrasives change location because of the rotation of the magnet fixture during finishing. The inactive abrasives get activated during the presence of the proper magnetic field. Thus, the rotation of the magnet fixture and its reciprocation speed of active abrasives in MRP media provided by piston extrusion pressure in the medium cylinder

determines the shearing zone of the active abrasive grains and also how long it contacts the miniature gear teeth profiles.

**Table 4.5** Calculation of active abrasive particles and indentation depth

| MR fluid types | Number of active abrasive grains ($N_g$) | | Simulated depth ($t_{total}$) of indentation/tooth ($t \times 10^{-13}$ m) | |
|---|---|---|---|---|
| | Uniform flow restrictor | | Uniform flow restrictor | |
| | Without | With | Without | With |
| Type-I | 2788 | 3946 | -3.241 | -4.135 |
| Type-II | 4460 | 6313 | -5.180 | -6.611 |
| Type-III | 8364 | 11838 | -9.712 | -12.41 |

The total normal indentation force per SiC abrasive particle causes indentation on the workpiece to remove the material. A solid mechanics simulation is done in the commercial software package Comsol® Multiphysics to simulate the normal indentation force by an active abrasive particle on the workpiece surface.

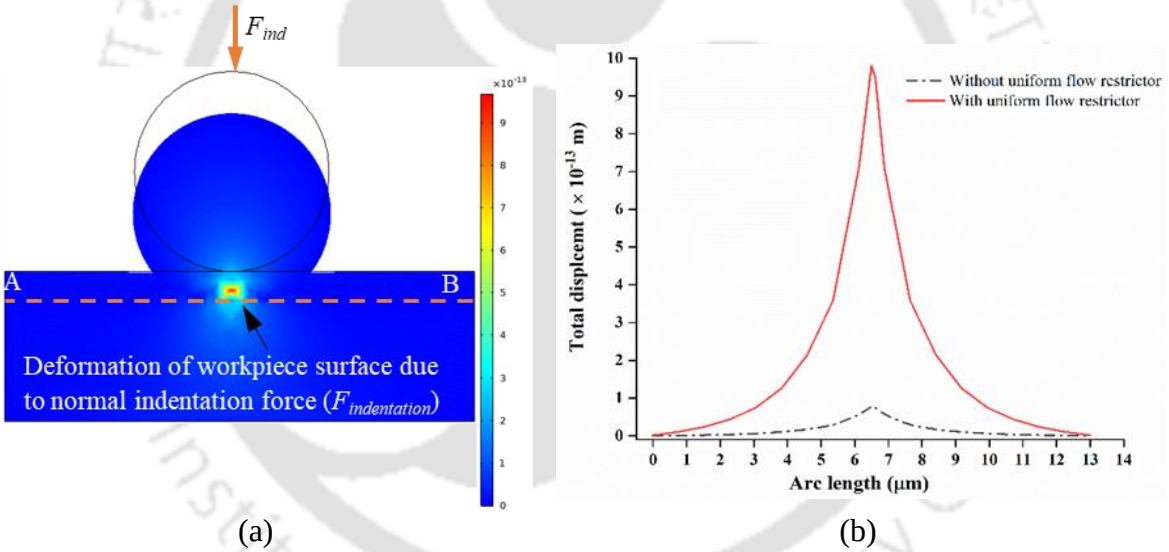


(a) (b)

**Fig. 4.2** (a) Deformation due to magnetic force and (b) total indentation by an abrasive particle on workpiece surface

The indentation force is used as the input force on the abrasive particles to simulate the material removal. At any point in time, a single point contact between abrasive particle and workpiece surface occurs. The deformation on the workpiece after applying the indentation force due to $N_g$ active abrasive particles/tooth is demonstrated in Fig. 4.2 (a). Now, the total displacement of the material due to $N_g$ active abrasive particles/tooth is demonstrated in Fig. 4.2 (b). An abrasive particle indentation on the workpiece surface propagates from that single contact point with maximum indentation force. The dislodgement of the workpiece by a single abrasive particle along line AB is plotted in Fig. 4.2 (b) without and with a flow restrictor. Maximum

material displacement due to $N_g$ active abrasive particles/tooth is $9.84 \times 10^{-13}$ m with using a uniform flow restrictor along the arc length of a workpiece (AB) (Fig. 4.2 (a)), and it is demonstrated in Fig. 4.2 (b) [147]. Material removal at any experimental condition is predicted from this simulation study of material dislodgement. During the simulation, it is assumed that the active abrasive particles move in a straight-line path.

## 4.4 Results and Discussion

An experimental investigation is executed to analyze the performance of different synthesized MR fluids on the miniature gear's complex teeth profiles. Further, the ANOVA method is used to find the optimum process parameters and their effect on the gear profiles. The surface roughness of the miniature gear tooth profiles before and after the MR finishing was measured by using a non-contact optical profilometer. After the surface roughness measurements, the initial and the MR finished miniature gear tooth profiles were investigated with the field emission scanning electron microscope (FESEM), microscope and optical profilometer for characterizing the tooth profiles of miniature gear during the finishing.

### 4.4.1 Surface Characterization

After finishing with Type-I and Type-II MRP media (Table 4.1), even after 800 finishing cycles (3 hrs. 20 min), no major improvement was seen in surface features and surface roughness values of miniature gear teeth profiles. This could be ascertained by the fact of the usage of the large size difference between the iron and abrasive particles. As the large size of iron particles forming chains along the magnetic field lines, with relatively much smaller sized abrasives being trapped in between them, could not come effectively in contact with the workpiece. And also, from Eq. (4.1), it is evident that as the distance between iron particles decreases due to the smaller size of abrasive particles, the interaction of magnetic force (F) increases. Due to the high value of F, the bonding strength between iron particles is strong. They will tightly grip the abrasive particles corresponding to which abrasive particles will not effectively contact the working surfaces, as demonstrated in Fig. 4.3 (a). Since effective contact could not occur between abrasive grains and the workpiece, no appreciable amount of finishing took place even after 800 cycles of finishing. A schematic diagram of a polishing mechanism having a difference of size between iron and abrasive particles and having the same size of iron and abrasive particles is demonstrated in Fig. 4.3 (a) and (b), respectively.

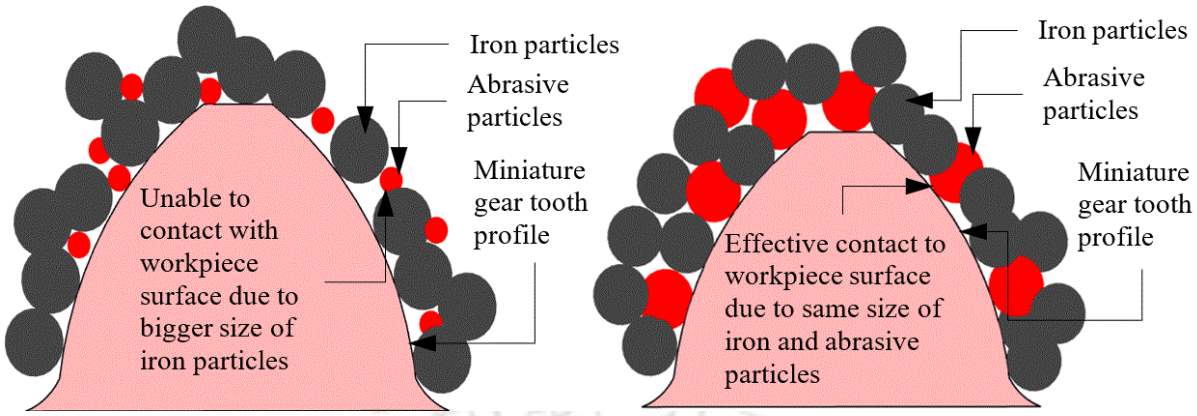


**Fig. 4.3** Schematic of R-MRFF polishing mechanism having size of iron particles (a) greater than and (b) same size of abrasive particles

### 4.4.1.1 MR Polishing Media of Type-I

An experiment with Type-I synthesized MR polishing media is carried out, which composition is given in Table 4.1. Type-I MR polishing media is relatively thinner than Type-II and Type-III MR polishing media. It was observed that no significant polishing of the workpiece took place after 800 finishing cycles. As displayed in the macrographic image and surface topography (Fig. 4.4(a) and (d)), initially, the recast layer, burrs, pits, and deep valleys are present on the involute profile of miniature gear teeth, which remains after finishing with MRP fluid of Type-I without and with using uniform flow restrictor (Fig. 4.4(b), (c), (e) and (f)). However, the surface roughness value (Table 4.6) at the involute teeth profile without and with using uniform flow restrictor reduced to 205.6 nm and 181.5 nm, respectively, from 265 nm. Hence, the MR polishing medium of Type-I is not suitable for finishing miniature gear teeth profiles.

### 4.4.1.2 MR Polishing Media of Type-II

As demonstrated in Table 4.1, Type-II MRP fluid comprises a volume percentage of 22 % iron particles with 400 mesh size, 8 % abrasive grains with 800 mesh size, 10 % grease, and 60 % paraffin oil. For Type-II MRP media, after 800 finishing cycles, there was little appreciable improvement in the surface features. Surface roughness values on miniature gear teeth profiles are observed compared with finished miniature gear teeth profiles using Type-I MR polishing media. The improvement in finishing the workpiece using this composition of MR polishing medium can be reasoned because the size difference between abrasive particles and iron particles used is lesser than Type-I MRP media. The surface roughness value (Table 4.6) at the

involute teeth profiles without and with using uniform flow restrictor reduced to 86.5 nm and 74.6 nm, respectively, from 265 nm. However, as demonstrated in the macrographic image (Fig. 4.5(a) and (b)), burrs are dislodged but still a minimum amount of recast layer is present on teeth profiles and also extra scratch mark has come on teeth profiles without using uniform flow restrictor. From the surface topography analysis (Fig. 4.5(c) and (d)) also it is observed that burrs have been eliminated, but pits remain on the teeth profile. Hence, the MR polishing medium of Type-II is not suitable for finishing miniature gear teeth profiles as required surface finish, and manufacturing defects of miniature gear teeth profiles has not been completely removed.

#### 4.4.1.3 MR Polishing Media of Type-III

As demonstrated in Table 4.1, Type-III MR polishing media comprises a volume percentage of 22 % iron particles with 800 mesh size, 15 % abrasive grains of 800 mesh size, 10 % grease, and 53 % paraffin oil. After little appreciable improvement in finishing miniature gear teeth profiles with Type-II MR polishing media, it was intended to obtain much finer smooth miniature gear teeth profiles. Type-III MRP media was synthesized to achieve more refined finishing while reducing iron particles' mesh size to abrasive particle mesh size. Finishing with this type of MR polishing media was also done for 800 finishing cycles. It was observed that there was a much higher significant amount of improvement in the surface finish and surface features have taken place. The fine finish obtained with this type of MRP media is due to the same size of iron and abrasive particles. Because of the similar size of iron and abrasive particles, the abrasives stuck in-between iron particle chains will be in effective contact with the miniature gear teeth profiles (Fig. 4.3 (b)). Thus, they could shear off the gear surfaces' undulations easily (Fig. 4.3(b)). Hence, this composition of MR polishing media showed appreciable improvement in finishing the miniature gear teeth profiles.

After final finishing with novel workpiece fixture, Type-III MRP media without and with using uniform flow restrictor the minimum surface roughness ($R_a$) for the involute profiles of miniature gear tooth was decreased to 34.3 nm and 24.5 nm, respectively from the original value of 265 nm.

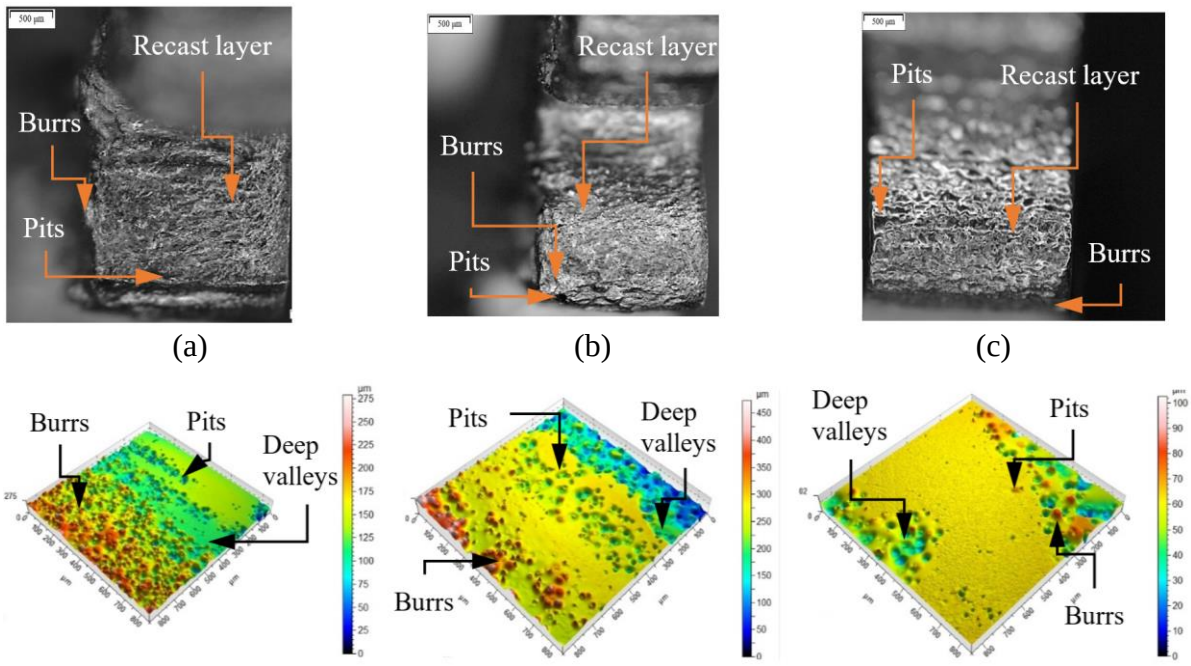


**Fig. 4.4** Macrographs of gear teeth involute profile (a) before finishing; After finishing (b) without and (c) with using uniform flow restrictor; Surface topography of involute profile (d) before finishing; After finishing (e) without and (f) with uniform flow restrictor by Type-I MRPF

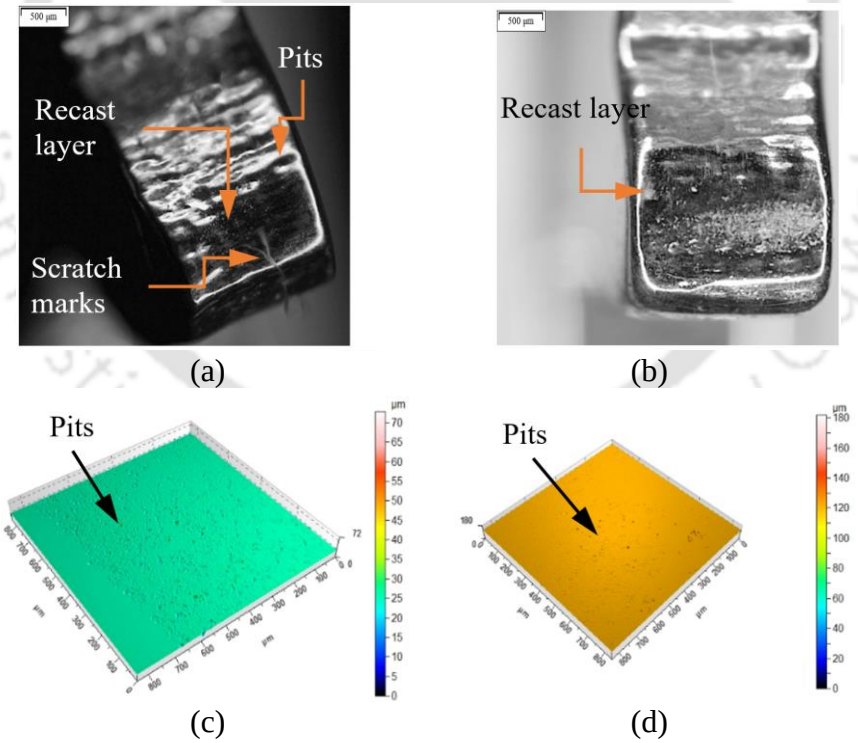


**Fig. 4.5** Macrographs of gear teeth involute profile after finishing (a) without and (b) with using uniform flow restrictor; Surface topography of involute profile after finishing (c) without and (d) with uniform flow restrictor by Type-II MRPF

For the top, involute, in-between, and face profiles of miniature gear teeth, initial and final experimental roughness values with 800 finishing cycles by each type of MR polishing media obtained are presented in Table 4.6.

This significant uniform decrease of final surface roughness ($R_a$) on the miniature gear teeth profiles with Type-III MRP media indicates that the novel uniform flow restrictor and workpiece fixture can produce a uniform fine surface finish on the miniature gear teeth profiles. Extrusion pressure is applied to MR polishing media; thus, abrasive grains will cut the peaks of roughness profiles by sliding and rotating action. The shear force acting on active abrasives eliminates the roughness peaks. After final finishing with MR polishing media of Type-III (Table 4.1), and by observing from the macrographic image (Fig. 4.6(a) and (b)) and surface topography analysis (Fig. 4.6(c) and (d)) of miniature gear teeth profiles, it is found that fine uniform smooth surface is obtained with using uniform flow restrictor. Still, some little amount of pits are observed without using a uniform flow restrictor. The comparative analysis of surface topography and macrographic image of miniature gear tooth profiles demonstrates that with using uniform flow restrictor surface has been shown uniform smoother finish compared to without using uniform flow restrictor. So, finally, FESEM analysis is done to see if any kind of recast layer or manufacturing micro-defects are present on the miniature gear teeth profiles (Fig. 4.6(e) and (f)). Initially recast layer was present on the WEDM fabricated miniature gear profiles. The recast layer and the loose materials from the miniature gear teeth profiles were entirely removed. Additionally, the finished involute profiles were completely free form pits, cracks and scratches when finishing with uniform flow restrictor as demonstrated in (Fig. 4.6(f)). However, little amount of micro-cracks and pits (Fig. 4.6(e)), were observed on miniature gear teeth profiles when finished without using a uniform flow restrictor. It was observed that the sides of the tooth were rounded a little bit. It was found from the literature survey that the rounding of the edges of the miniature gear tooth helps to dislodge the burrs, pits, and other undesired features from the working surface [73]. Improved surface finish and form accuracy on the miniature gear teeth profiles was obtained with using a uniform flow restrictor. The results obtained from FESEM found that all manufacturing defects were eliminated entirely from the finished tooth profiles of the miniature gear using a uniform flow restrictor. The surface finish on different working surfaces was uniformly improved. Hence, the MRP media of Type-III is best suitable for finishing SS316L miniature spur gear teeth profiles [140]. After experimenting with each type of MR polishing media without and with using a uniform flow restrictor, the final roughness value obtained is plotted in bar chart graph as demonstrated in Fig. 4.7, for observing the uniform polishing at miniature gear teeth profiles

at each stage of finishing. As shown in Fig. 4.7(a), without using the uniform flow restrictor, more variation in surface roughness is obtained at the different profiles of miniature gear teeth, as compared to the surface roughness values obtained with uniform flow restrictor (Fig. 4.7(b)) by finishing with each type of MRP media. After finishing with using a uniform flow restrictor, the almost same surface roughness value is obtained at each miniature gear tooth profile, as demonstrated in Fig. 4.7(b). It means that more uniformity in surface roughness value is obtained at each stage and each gear tooth profile by using a uniform flow restrictor.

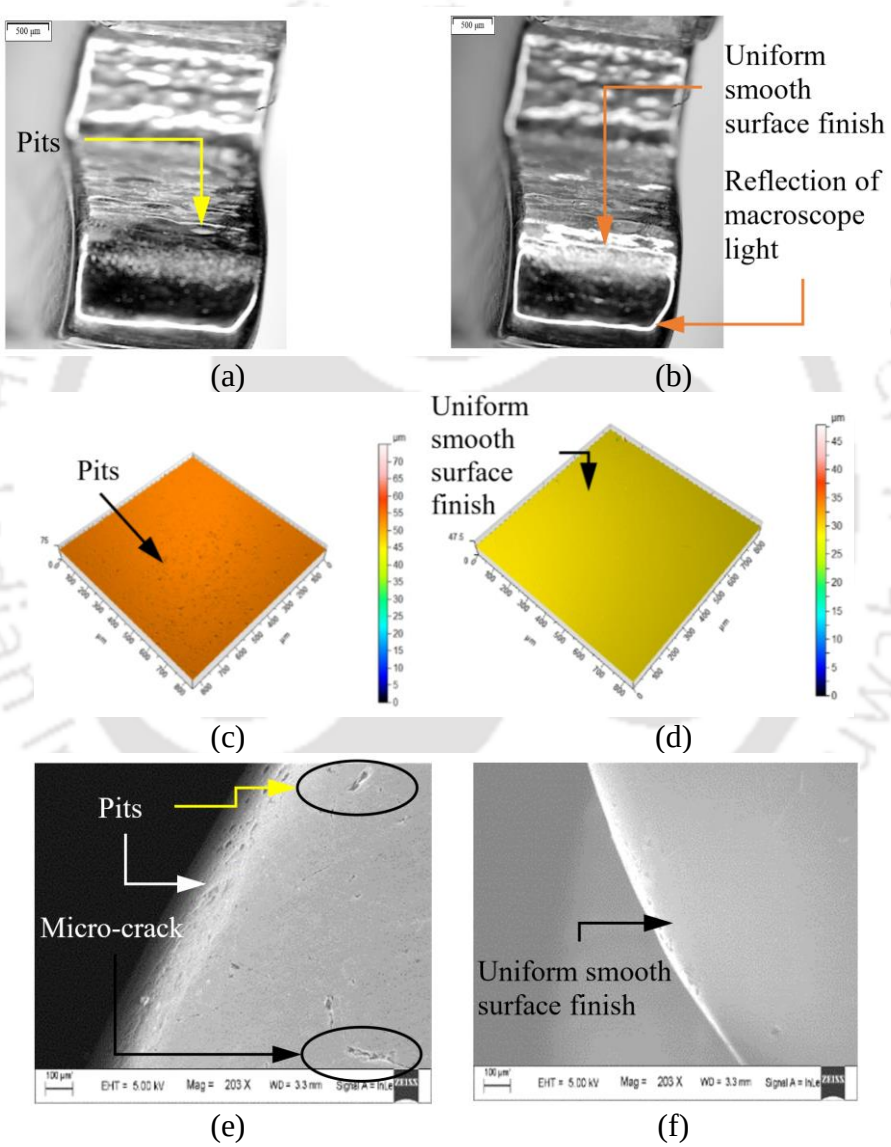


**Fig. 4.6** Macrographs of gear teeth involute profile after finishing (a) without and (b) with uniform flow restrictor; Surface topography of involute profile after finishing (c) without and (d) with uniform flow restrictor; FESEM images of involute profile after finishing (e) without and (f) with uniform flow restrictor by Type-III MRPF

The higher MRR can be achieved using a uniform flow restrictor, as the number of active abrasive particles is higher when using a uniform flow restrictor. Uniform flow restrictor,

which is an almost negative replica of the miniature gear workpiece, has finished the miniature gear workpiece up to a nano-scale level uniformly.

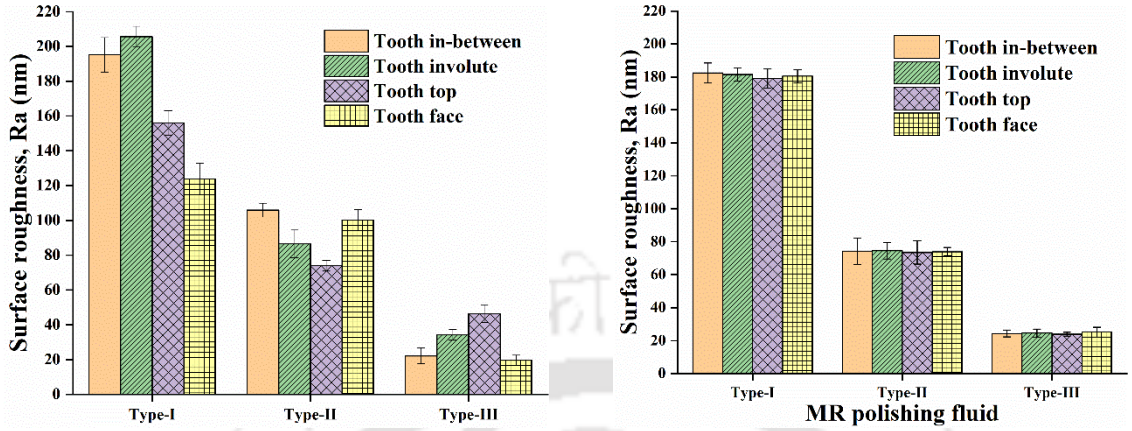


**Fig. 4.7** Surface roughness comparison at different positions of gear tooth profiles (a) without and (b) with uniform flow restrictor between Type-I, Type-II and Type-III MRPF

**Table 4.6** Comparison of measured surface roughness values at gear tooth profiles between three MR polishing medium for 800 finishing cycles

| Miniature gear tooth profiles | Initial Ra (nm) | $R_a$ (nm) with Type-I MRPF | | $R_a$ (nm) with Type-II MRPF | | $R_a$ (nm) with Type-III MRPF | |
|---|---|---|---|---|---|---|---|
| | | Uniform flow restrictor | | Uniform flow restrictor | | Uniform flow restrictor | |
| | | Without | With | Without | With | Without | With |
| In-between | 264 | 195.1 | 182.4 | 105.9 | 74.1 | 22.1 | 24.3 |
| Involute | 265 | 205.6 | 181.5 | 86.5 | 74.6 | 34.3 | 24.5 |
| Top | 252 | 156.1 | 179.1 | 74.1 | 73.5 | 46.5 | 23.9 |
| Face | 259 | 123.8 | 180.4 | 100.2 | 74.0 | 19.6 | 25.2 |

## 4.4.2 ANOVA Study

In the present research, 20 experiments are performed to assess the outcomes of the selected process parameters on the % ΔRa and MRR. The experimental response data is tabulated in Table 4.4. Further, an analysis of variance (ANOVA) is utilized to develop the quadratic theoretical statistical model. After performing ANOVA on the basis of the sequential model, the p-value of the model for % ΔRa and MRR is found to be less than 0.05 for 95% confidence interval, this shows that the model is significant. The p-value is 0.0634 and 0.0663 for % ΔRa and MRR, respectively, which is higher than 0.05, which signifies that the lack of fit is not significant. The experimental response data were used to perform ANOVA as reported in Table 4.7. The ANOVA table shows that the F-value of the developed quadratic model is 33.25 for % ΔRa and 25.78 for MRR, respectively. The model is significant, and the chance of the model

to be insignificant due to noise is only 0.01%. The obtained response surface quadratic equation for % ΔRa and MRR is given in Eqs. (4.7) and (4.8), respectively.

$$\%\Delta R_a = -3448.05 + 84.67V - 0.139N + 197.08P - 0.0467VN - 1.151VP + 0.047NP - 10.04V^2 - 0.006N^2 - 2.844P^2 \quad (4.7)$$

$$MRR = -0.0044 - 0.001V - 0.00005N + 0.0004P - 6.22\times10^{-7}VN + 0.00004VP + 1.32\times10^{-6}NP - 0.0001V^2 + 7.34\times10^{-8}N^2 - 9.49\times10^{-6}P^2 \quad (4.8)$$

Using Eqs. (4.7) and (4.8), the % ΔRa and MRR is calculated and compared with the experimental % ΔRa values and MRR. The variation in experimental and calculated value for % ΔRa values and MRR is shown in Fig. 4.8(a) and (b), respectively. From the Figure, it can be concluded that there is not much variation amid the experimental and the calculated values from the developed model.

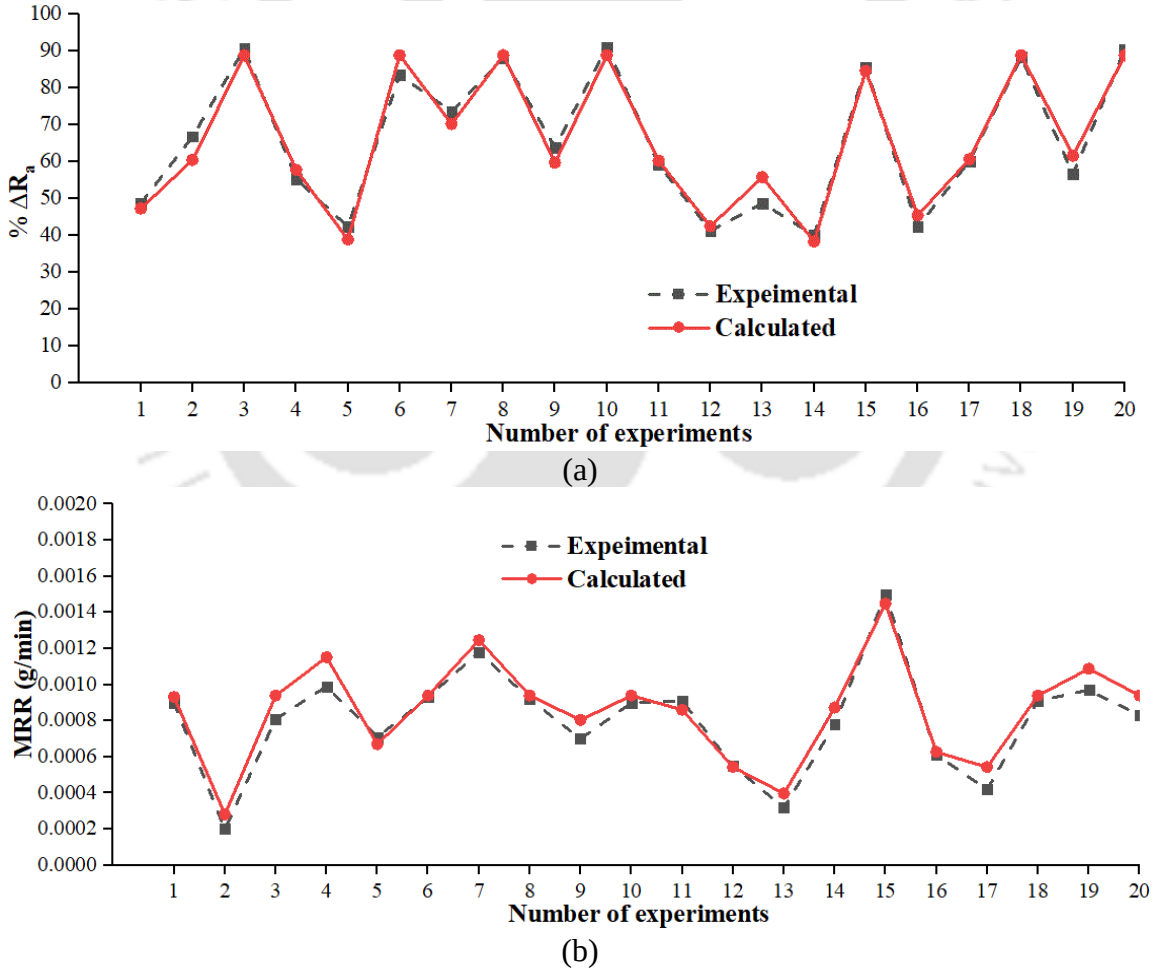


**Fig. 4.8** Comparison between experimental and predicted values of (a) % ΔRa and (b) MRR

It can also be validated from the model as the co-efficient of determination ($R^2$) value of regression equation of the model is 96.77% for % ΔRa and 95.87% for MRR, respectively,

which shows the accuracy of the model. A higher $R^2$ value (near 1) suggests that the model fits the data better. The percentage contribution (F/ΣF) of each significant factor (linear and non-linear) in Table 4.7, gives a rough but efficient guide for the percentage contribution of the factors [148]. After the regression analysis of the process parameters on the % ΔRa and MRR, the outcome of the significant parameters has been conferred in this section. The influence of each process parameters on % ΔRa and MRR is plotted with the help of regression Eqs. (4.7) and (4.8), respectively. The plots are analyzed and discussed to clarify the process mechanism.

**Table 4.7** ANOVA for % ΔRa and MRR

| Source | % ΔRa | | | MRR (g/min) | | |
|---|---|---|---|---|---|---|
| | F value | p-value Prob > F | Percent contribution | F value | p-value Prob > F | Percent contribution |
| Model | 33.25 | < 0.0001* | | 25.78 | < 0.0001* | |
| V | 0.0004 | 0.9838** | 0.0001 | 73.02 | < 0.0001* | 31.86 |
| N | 33.62 | 0.0002* | 10.04 | 69.05 | < 0.0001* | 30.12 |
| P | 0.0281 | 0.8702** | 0.008 | 6.84 | 0.0258* | 2.984 |
| VN | 0.7088 | 0.4195** | 0.211 | 0.4174 | 0.5328** | 0.1821 |
| VP | 2.98 | 0.1151** | 0.890 | 14.81 | 0.0032* | 6.4619 |
| NP | 4.57 | 0.0583** | 1.365 | 11.82 | 0.0064* | 5.1573 |
| $V^2$ | 65.41 | < 0.0001* | 19.53 | 36.25 | 0.0001* | 15.816 |
| $N^2$ | 22.67 | 0.0008* | 6.771 | 9.41 | 0.0119* | 4.1058 |
| $P^2$ | 204.79 | < 0.0001* | 61.17 | 7.57 | 0.0204* | 3.3029 |
| Lack of fit | 4.45 | 0.0634** | | 4.35 | 0.0663** | |

* Significant, ** Not Significant, $R^2$ = 0.97 for % ΔRa, 0.96 for MRR, % ΔRa – Percentage change in Ra (CLA), MRR – Material removal rate

### 4.4.2.1 Effect of Process Parameters on % ΔRa and MRR

The influence of the volumetric proportion of iron/abrasive particles, V on % ΔRa, is shown in Fig. 4.9 (a). Low IP/SiC proportion implies a higher concentration of abrasive particles, and a lower concentration of IPs and high IP/SiC proportion implies the other way around. The lower IP/SiC proportion results in lower % ΔRa because of the higher concentration of abrasives, which implies the formation of a weak chain structure resulting in the easy breaking of the chain. As the distance between the two CIPs (R') increases, which reduces the magnetic interaction force (F) as given in Eq. (4.1) [149]. This led to the reduction in the shear strength of the MR fluid [150]. Easily ruptured chains cannot provide enough polishing force, which in turn results in low % ΔRa [25]. With the increase in IP/SiC proportion, the volume concentration of IP in the polishing medium starts to increase, resulting in a strong polishing force on the abrasive particle, which increases % ΔRa. However, as observed from Fig. 4.9 (a),

after an optimum value of IP/SiC proportion, % ΔRa shows decreasing trend due to the decrease of abrasive particles in the polishing medium.

Fig. 4.9 (b) depicts the effect of magnet rpm on % ΔRa. % ΔRa increases with the increase in the magnet rpm due to the higher centrifugal force and tangential cutting force, which help in finishing. Also, abrasive particles cover more area on the workpiece surface due to the simultaneous reciprocating and rotational motion of the polishing medium, which results in a better finishing performance. However, beyond the optimum magnet rpm, % ΔRa goes down due to the shear-thinning nature of MRP fluid.

The effect of extrusion pressure on % ΔRa is shown in Fig. 4.9 (c). From Fig. 4.9 (c), it is observed that % ΔRa increases with increased extrusion pressure, and it reaches to an optimum value. With the increase in the extrusion pressure, both shear force and axial cutting force increase, which help in removing surface undulations from the workpiece surface. The increase in material removal helps to achieve a better surface finish. Increasing surface finish increases the percentage improvement in surface roughness. However, beyond the optimum extrusion pressure, % ΔRa reduces due to the shear-thinning nature of MRP fluid.

The influence of the volumetric proportion of iron/abrasive particles, V on MRR is shown in Fig. 4.9 (d). As the IP/SiC proportion increases, shear stress (depends upon magnetic field strength) increases and also volumetric magnetic body force increases [151]. Hence, the material removal increases. However, when the IP/SiC proportion goes beyond a limit, the trend of MRR decreases due to the decrease of abrasive particles in the polishing medium.

Fig. 4.9 (e) depicts the effect of magnet rpm on MRR. MRR increases with the increase in the magnet rpm due to the higher centrifugal force and tangential cutting force, which help in more removal of roughness peaks. Also, the gap (2 mm) between the flow restrictor and flow restrictor is very less and uniform, which increases the MRR with simultaneous reciprocating and rotational motion of the polishing medium.

The effect of extrusion pressure on MRR is shown in Fig. 4.9 (f). From Fig. 4.9 (f), it is observed that MRR increases with increased extrusion pressure, and it reaches to an optimum value. With the increase in the extrusion pressure, both shear force and axial cutting force increase, which help in removing more materials from the workpiece surface. The increase in material removal in minimum time improves MRR. However, beyond the optimum extrusion pressure, % ΔRa reduces due to the ineffectiveness of MRP fluid, as MRP fluid becomes less viscous, showing shear-thinning nature.

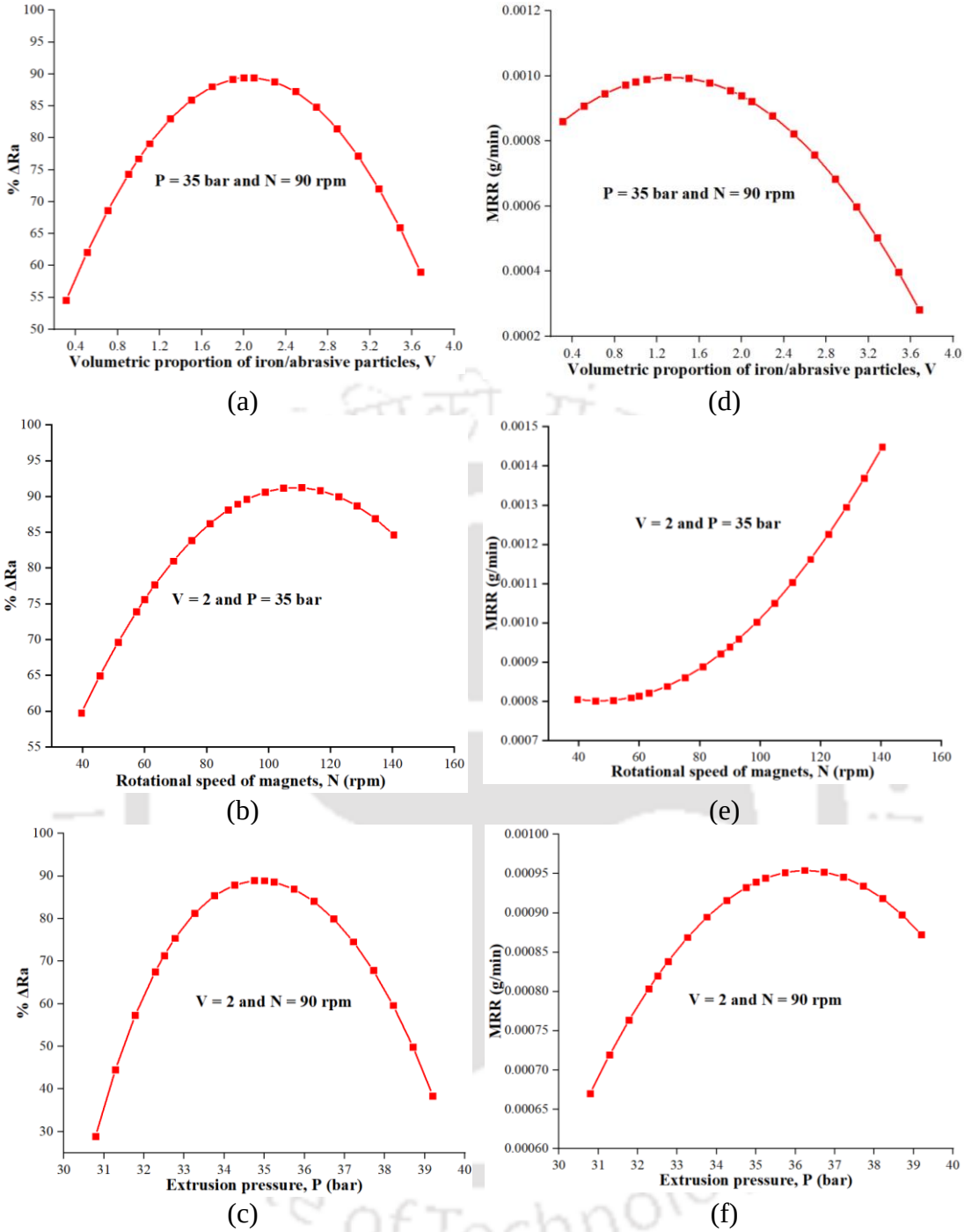


**Fig. 4.9** Effect of (a) volumetric proportion of iron/abrasive particles (V), (b) rotational speed of magnets (N), and (c) extrusion pressure (P) on %Δ Ra; Influence of (d) volumetric proportion of iron/abrasive particles (V), (e) rotational speed of magnets (N) and (f) extrusion pressure (P) on MRR

The 3D surface plot of the effect of both volumetric proportion of iron/abrasive particles, V and rotational speed of magnets, N on % ΔRa, with other parameters kept constant as (P = 35 bar) is shown in Fig. 4.10(a), which shows the similar effect explained earlier. Increasing both parameters simultaneously lead to the increment of cutting force and magnetic force (normal indentation force). Further increment of shear force and magnetic force leads to removal of

unwanted materials, which scratches already polished surfaces. Hence, it will result in a decreasing trend of the % ΔRa.

The 3D surface plot of the effect of both volumetric proportion of iron/abrasive particles, V and extrusion pressure, P on % ΔRa, with other parameters kept constant as (N = 90 rpm) is shown in Fig. 4.10(b), which shows the similar effect explained earlier. As the V and P increase simultaneously, the trend of the % ΔRa increases, then after it decreases. As the Vand P increases simultaneously, there is an increase in the normal force, which leads to an increase in the shearing of the surface asperities. Hence, the trend of % ΔRa increases. However, excessive increase in pressure results in loss of abrasives grip in the IPs chain, MRP fluid shows shear-thinning nature. There is also a decrease in the overall cutting edges of abrasives due to more IP aggregates outside the already existing IPs chains in which the abrasives are tightly gripped [25]. Owing to which there is improper chipping off surface asperities from the workpiece surface, which leads to a decrease in the trend % ΔRa.

The 3D surface plot of the effect of both volumetric proportion of iron/abrasive particles, V and rotational speed of magnets, N on MRR, with other parameters kept constant as (P = 35 bar), is shown in Fig. 4.10(c), which shows the similar effect explained earlier. Increasing V parameter leads to the enhancement in the MRP fluid shear strength due to an increment in yield stress. It will result in faster removal of material. However, with the maximum amount of IPs in MRP fluid, it will be hard to go beyond the yield strength of MRP fluid and breaks the IPs chain. These IPs chain bound the abrasives firmly will not let them effectively contact the workpiece surface. This leads to a reduction in the removal of material.

The 3D surface plot of the effect of both volumetric proportion of iron/abrasive particles, V and extrusion pressure, P on MRR, with other parameters kept constant as (N = 90 rpm), is shown in Fig. 4.10(d), which shows the similar effect explained earlier. As P, increases the trend of the MRR increases, then after it decreases. Pressure increases the indentation force of abrasives into the workpiece surface; as a result, MRR increases. Beyond a pressure limit, MRP fluid started to show shear-thinning nature, which decreases MRR. The regression equation (Eq. (4.7)) gives prediction of 89.21 % improvement in Ra, when N = 109 rpm, V = 1.5, and P = 35 bar. Experimentations were performed using the optimized parameters on the gear profiles for 200 minutes. After 200 minutes, there is no significant improvement observed on the gear profiles. The total improvement in % ΔRa after 200 minutes MR finishing on the gear involute profile was found as 90.75 % (Table 4.6). After the analysis, it was found that the error amid the experimental and theoretical values of % ΔRa and MRR lies in the range of −2.83% to 4.52%. This confirms the output reproducibility of the present work.

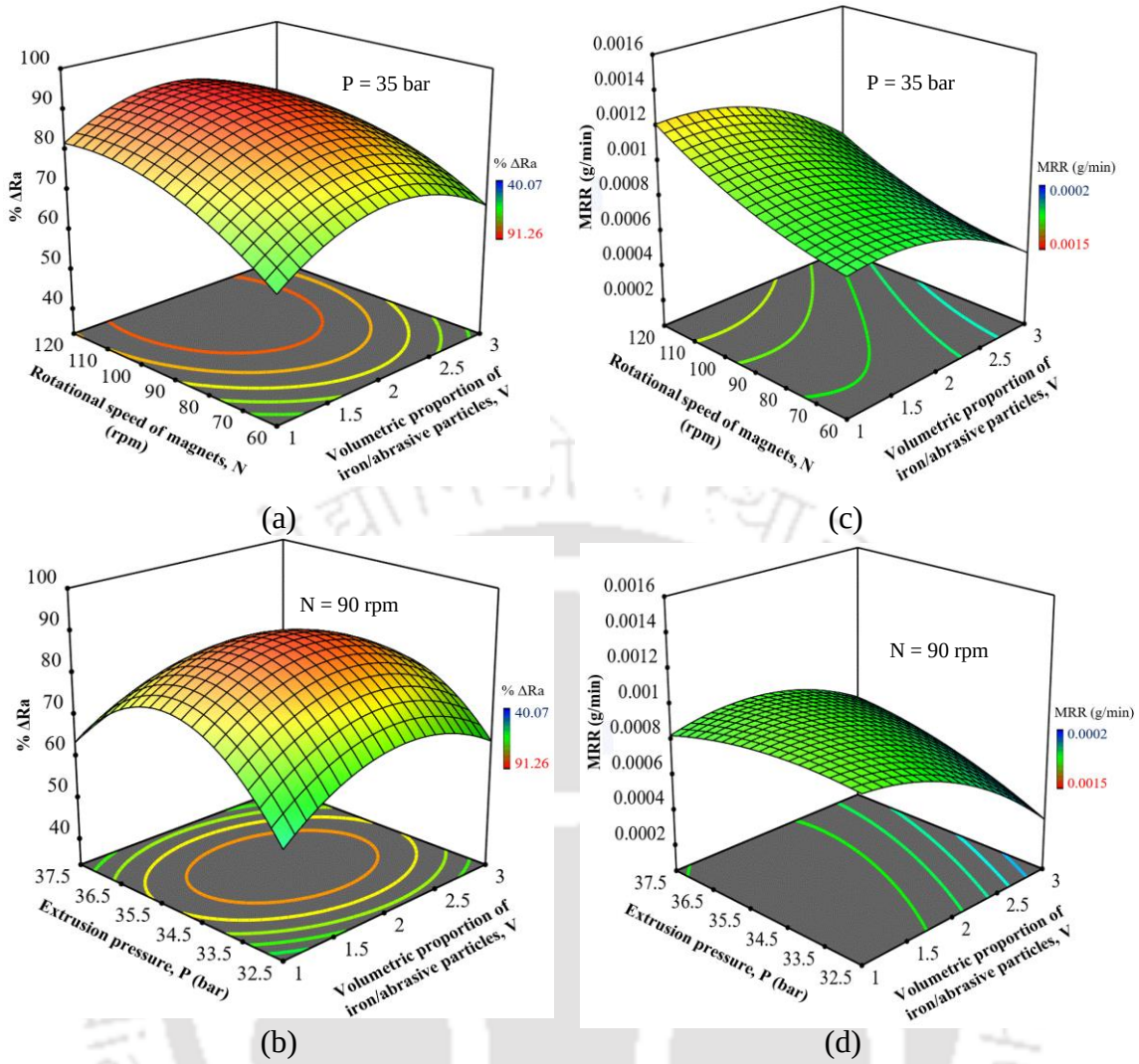


**Fig. 4.10** Combined effect of (a) Vol. proportion of iron/abrasive particles (V) and rotational speed of magnets (N), (b) Vol. proportion of iron/abrasive particles (V) and extrusion pressure (N), on %Δ Ra; Combined effect of (c) Vol. proportion of iron/abrasive particles (V) and rotational speed of magnets (N), (d) Vol. proportion of iron/abrasive particles (V) and extrusion pressure (N), on MRR

To validate the ANOVA model and further regression equation, three validation tests are carried out; Exp. I: at optimum experimental condition, followed by two more experiments (Exps. II and III) chosen randomly within the range of process parameters (Table 4.8). The initial surface roughness values of the workpieces are selected almost the same for all three experiments. The experimental value of % ΔRa and MRR is computed for all three validation tests using Eq. (4.2) and Eq. (4.3), respectively. These values are compared with the predicted values calculated using regression Eqs. (4.7) and (4.8), respectively. The comparison between the experimental and the predicted results as well as percentage error, is shown in Table 4.8. The observed maximum error for % ΔRa and MRR is less than 10 % among all three validation experiments, which describes the repeatability of the proposed model.

**Table 4.8** Validation tests for % ΔRa and MRR

| S.No. | V | N (rpm) | P (bar) | Exp. (% ΔRa) | Pred. (% ΔRa) | Error (%) | Exp. MRR (g/min) | Pred. MRR (g/min) | Error (%) |
|---|---|---|---|---|---|---|---|---|---|
| 1. | 1.5 | 109 | 35 | 90.75 | 89.21 | 1.70 | 0.00118 | 0.00114 | 4.13 |
| 2. | 2 | 85 | 36 | 80.51 | 84.39 | 4.82 | 0.00099 | 0.00091 | 8.57 |
| 3. | 2.5 | 100 | 33 | 82.11 | 76.99 | 6.24 | 0.00077 | 0.00073 | 5.86 |

Exp. – Experimental, Pred. – Predicted

# 4.5 Summary

In this chapter, uniform flow restrictor and workpiece fixture's effectiveness are confirmed experimentally and theoretically while finishing complex teeth profiles of miniature gear using R-MRFF process. Due to the large difference between iron and abrasive particles' size, expected finishing performance was not achieved using both Type-I and Type-II MRP medium even after 800 finishing cycles. The consistent restricted space between flow restrictor and gear teeth profiles creates a uniform flowing MRP media channel, leading to a super smooth uniform surface finish. The minimum roughness values in-between, involute, top, and face profiles of gear teeth are obtained as 24.3, 24.5, 23.9, and 25.2 nm, respectively, while using a uniform flow restrictor with Type-III MRP media. The corresponding surface roughness values without using the uniform flow restrictor are 22.1, 34.3, 46.5, and 19.6 nm, respectively with the same media. More active abrasive particles per stroke will result in faster material removal and a high finishing rate while using a uniform flow restrictor. Uniform surface roughness values are achieved at each tooth profile of miniature gear with different types of MR polishing media while using a uniform flow restrictor. Among all indigenously developed MRP fluid, The minimum value of surface roughness is achieved with Type-III MRP media. The rpm of magnets, extrusion pressure and volumetric proportion of iron/abrasive particles significantly affect both surface finish and MRR. The values of the optimized process parameters, i.e. the volumetric proportion of IP/SiC, extrusion pressure, and rotational speed of magnet fixture are 1.5, 35 bar, and 109 rpm, respectively, achieving 90.75% improvement in Ra. A combined effect of the moderate extrusion pressure and higher rpm of the magnet is more favourable to achieve higher MRR. In comparison, a combination of the lower volumetric proportion of iron/abrasive particles and higher rpm of the magnet causes a better improvement in surface finish. An increase in extrusion pressure and rpm of the magnet significantly increases the MRR. In contrast, only a marginal increase in MRR was observed with an increase in IP/SiC proportion up to 1.6; beyond that, MRR tends to decrease. The abrasion and ploughing action on the SS316L are the dominant mechanisms of material removal while finishing by the R-MRFF process.

# Chapter 5 Uniform Finishing of Poppet Valve

## 5.1 Introduction

Nano-finishing of poppet ridge profiles is a tough challenge due to the complexity in its geometry. This uniform finishing of the poppet valve in the actual application will reduce hydrocarbon emissions. Very few finishing processes can be applied to these complex narrow profiles. In the current study, a novel magnet fixture arrangement is used in the R-MRFF process to precisely finish the poppet ridge profiles. For this purpose, the effect of key parameters on the process's performance has been studied through response surface methodology (RSM). Analysis of variance (ANOVA) has been applied to identify significant parameters. The surface characteristics of the polished surfaces with distinct magnetorheological fluids are outlined for surface roughness and surface texture with the use of a novel polishing setup. Ultrafine surface roughness (Ra = 20.1 nm) at poppet profiles are obtained using an MR fluid of Type-III. All manufacturing defects like burrs, dents, scratches and pits are also completely removed. MR fluid of Type-III is selected to polish poppet ridge profiles. Experimental results showed that a combination of the lower feed rate and a high rpm of the poppet valve is more advantageous for obtaining a greater % ΔRa in minimum time. After using the R-MRFF process, the poppet valve will have high wear and corrosion resistance capability, longer service life, and minimum maintenance during its working performance. After final finishing, the maximum percentage improvement of surface roughness is obtained as 90.86%. It has high accuracy and reliability for specific applications.

## 5.2 Experimental Investigation

The magnet fixture consists of five Sm2Co17 (Samarium-Cobalt) of grade 30H permanent magnets at specified places. It was challenging to polish this kind of narrow ridge profile of the poppet valve, which has only a width of 0.32 mm and a circular periphery. For overcoming this challenge, the same ridge profile has been created on the magnet fixture. Due to relative angular motion between the ridge profiles of the poppet valve and magnet fixture, abrasives do effective contact mainly on the ridge profiles of the poppet valve. Precision 3-axis CNC vertical milling machine head is used to rotate the poppet valve. The experimental setup for poppet MR polishing is displayed in Fig. 3.16, mentioning all the main components. Fig. 3.16 shows the detailed view of magnet fixture, with same poppet valve ridge profiles and MR fluid container. MR fluid is filled in-between the working distance of magnet fixture and poppet profile in MR

fluid container. The spindle head is guided to move 0.1 mm below at every time interval of 10 minutes for excellent finishing of the poppet ridge profiles in 100 minutes. This vertical motion of the poppet valve is regarded to make the process faster by considering that at any time interval, the sharp cutting edge of abrasives does not leave the contact poppet ridge profiles.

Since there is no literature review available related to the MR finishing of the poppet valve, the parameters are taken in the present study that effects the reduction in surface roughness is the poppet valve rotation (N), vertical feed rate of the poppet valve (mm/min), % volume of CIPs (C) and % volume of SiC abrasives (A). On the basis of the preliminary experimentations done for % ΔRa and available literature, the MR fluid is made by mixing CIPs, SiC abrasive powder, glycerol, $HNO_3$, $H_2O_2$ and Deionized water [143]. Initially, the acid (HF and $HNO_3$) was used as a base medium with distilled water. It was done keeping that workpiece material was hard with hardness (HRC 47). However, acid has damaged the workpiece. Therefore, hydrofluoric acid (HF) has been removed, but $HNO_3$ remains, as it is used to brighten the surface, and an extra agent $H_2O_2$ is used for dissolving the metallic surface to help abrasive grains. So MR fluid was formulated in the base medium of $H_2O_2$ and deionized water, with CIPs and abrasive particles. To improve MR fluid viscosity, glycerol is added to the fluid. This functions as a stabilizer to spread CIPs, consistently eliminating agglomeration. Deionized water is used to prevent corrosion of the MR polishing fluid in place of the distilled water. The different compositions of MRP fluids are listed in Table 5.1. These MR fluids have been prepared to check the effects of different concentrations of abrasives, CIPs and various compositions of career media on the polished surfaces. A laboratory stirrer is being utilized for preparing MRP fluid by blending CIPs and SiC abrasive particles in the carrier media.

**Table 5.1** Different types of synthesized MRP fluids

| **Constituents** | **Volume concentration (%)** | | |
|---|---|---|---|
| | **Type-1** | **Type-2** | **Type-3** |
| CIPs | 30 | 30 | 40 |
| SiC abrasive (mesh size 800) | 7.1 | 7.1 | 7.1 |
| Glycerol | 8 | 8 | 8 |
| Hydrofluoric acid (HF) | 1.17 | ---- | ---- |
| Nitric acid ($HNO_3$) | 2.33 | 1.17 | ---- |
| Hydrogen peroxide ($H_2O_2$) | ---- | 1.3 | 1.3 |
| Deionized water | 51.4 | 52.43 | 43.6 |

In the present research, the % volume of the base fluid in MR polishing fluid varies from 52%–63% depending on the % volume of abrasives and % volume of CIPs selected for experimentation. To determine the variable range of the process parameters, preliminary

experimentations were performed on the poppet valve workpiece. The initial average roughness values (Ra) of the poppet valve workpieces (Nickel aluminium bronze (BS1400 Gr.AB2)) range between 298–330 nm after turning operation in Lathe for initial experimentation. To measure the surface roughness of the poppet ridge profiles before and after conducting experiments, a "Talysurf" non-contact optical profilometer is used, and the analysis of measured data is performed using a "TalyMap application" software. The preliminary experimentations were conducted for the 20 minutes of the finishing cycle with the different range of the selected variable parameters. The values of surface roughness obtained after preliminary experimentations are reported in Table 5.2 for the variable parameters poppet valve rotation (N), vertical feed rate of poppet valve (mm/min), % volume of CIPs (C) and % volume of abrasives (A). The results obtained from the preliminary experimentations are used for selecting the range of the process parameters for effectively fine finishing of the poppet valve profiles. The selected range for parameters is reported in Table 5.3.

**Table 5.2** Preliminary experimentations for selecting range of process parameters

| S. No. | A (vol %) | C (vol %) | N (rpm) | F (mm/min) | Initial Ra (nm) | Final Ra (nm) |
|---|---|---|---|---|---|---|
| 1. | 0.5 | 40 | 1200 | 0 | 330 | 230 |
| 2. | 3.5 | 40 | 1200 | 0 | 299 | 190 |
| 3. | 7 | 40 | 900 | 0 | 325 | 160 |
| 4. | 10.5 | 40 | 900 | 0.005 | 307 | 171 |
| 5. | 14 | 40 | 1200 | 0.005 | 315 | 225 |
| 6. | 7 | 30 | 1200 | 0.005 | 298 | 125 |
| 7. | 7 | 35 | 900 | 0.005 | 309 | 138 |
| 8. | 7 | 40 | 1200 | 0.010 | 308 | 141 |
| 9. | 7 | 45 | 1200 | 0.010 | 321 | 215 |
| 10. | 3.5 | 30 | 600 | 0.010 | 323 | 202 |
| 11. | 7 | 35 | 900 | 0.010 | 318 | 129 |
| 12. | 7 | 40 | 1200 | 0.005 | 327 | 140 |
| 13. | 7 | 45 | 1500 | 0.010 | 311 | 179 |
| 14. | 7 | 40 | 1200 | 0 | 313 | 187 |
| 15. | 10.5 | 40 | 1500 | 0.005 | 316 | 241 |
| 16. | 7 | 40 | 1200 | 0.010 | 322 | 118 |
| 17. | 10.5 | 30 | 1200 | 0.015 | 324 | 186 |
| 18. | 7 | 40 | 1200 | 0.02 | 320 | 198 |

C (vol%) – Percentage volume of CIPs concentration in MRP media, A (vol%) – Percentage volume of SiC abrasives concentration in MRP media, F – Vertical feed rate of the poppet valve, N – Poppet valve rotation

To analyze the parametric study for the fine finishing of the poppet valve ridge profiles, the design of experiments (DOE) is used. Further, for analyzing the outcome of various parameters on the % change in surface roughness (% ΔRa), response surface methodology (RSM) is used.

**Table 5.3** Process parameters and their range for DOE

| Levels | Process parameters | | | |
|---|---|---|---|---|
| | C (vol%) | A (vol%) | F (mm/min) | N (rpm) |
| -2 | 25 | 0 | 0 | 300 |
| -1 | 30 | 3.5 | 0.005 | 600 |
| 0 | 35 | 7 | 0.010 | 900 |
| 1 | 40 | 10.5 | 0.015 | 1200 |
| 2 | 45 | 14 | 0.02 | 1500 |

**Table 5.4** Plan of experiments for DOE

| S. No. | Factors | | | | Response |
|---|---|---|---|---|---|
| | C (vol%) | A (vol%) | F (mm/min) | N (rpm) | % ΔRa |
| 1 | 30 | 3.5 | 0.015 | 1200 | 68.73 |
| 2 | 35 | 7 | 0.01 | 900 | 91.88 |
| 3 | 30 | 3.5 | 0.005 | 600 | 53.94 |
| 4 | 25 | 7 | 0.01 | 900 | 66.28 |
| 5 | 30 | 10.5 | 0.015 | 1200 | 81.06 |
| 6 | 35 | 0 | 0.01 | 900 | 71.22 |
| 7 | 35 | 7 | 0.01 | 900 | 89.81 |
| 8 | 45 | 7 | 0.01 | 900 | 84.22 |
| 9 | 35 | 7 | 0.01 | 900 | 88.05 |
| 10 | 35 | 7 | 0.02 | 900 | 79.15 |
| 11 | 40 | 3.5 | 0.005 | 600 | 66.05 |
| 12 | 30 | 10.5 | 0.015 | 600 | 79.07 |
| 13 | 35 | 7 | 0.01 | 300 | 70.88 |
| 14 | 30 | 10.5 | 0.005 | 1200 | 76.01 |
| 15 | 35 | 7 | 0.01 | 1500 | 77.37 |
| 16 | 35 | 14 | 0.01 | 900 | 87.89 |
| 17 | 35 | 7 | 0.01 | 900 | 88.05 |
| 18 | 35 | 7 | 0.01 | 900 | 91.88 |
| 19 | 40 | 10.5 | 0.015 | 600 | 85.8 |
| 20 | 40 | 3.5 | 0.015 | 1200 | 79.85 |
| 21 | 40 | 10.5 | 0.005 | 1200 | 81.83 |
| 22 | 35 | 7 | 0.01 | 900 | 93.54 |
| 23 | 40 | 10.5 | 0.005 | 600 | 70.38 |
| 24 | 30 | 3.5 | 0.015 | 600 | 65.28 |
| 25 | 40 | 3.5 | 0.005 | 1200 | 78.96 |
| 26 | 40 | 10.5 | 0.015 | 1200 | 86.87 |
| 27 | 40 | 3.5 | 0.015 | 600 | 77.39 |
| 28 | 30 | 3.5 | 0.005 | 1200 | 67.83 |
| 29 | 30 | 10.5 | 0.005 | 600 | 63.56 |
| 30 | 35 | 7 | 0 | 900 | 62.76 |

% ΔRa – Percentage change in centre line average surface roughness value

The effect of the different process parameters and their combined effects are studied. From the analysis of variance (ANOVA), the influence of each process parameter on % ΔRa are analyzed, and significant process parameters are selected. The regression equation will help to explore the process parameter influence on % ΔRa. The plan of experiments along with their

response, are shown in Table 5.4, and the experiments are carried out randomly. Each experimentation is performed on the poppet valve workpiece for 1 hr. 40 minutes. The confidence level of the model is 95% to verify the effectiveness of the model. The F-level test from analysis of variance (ANOVA) is done to identify the implication of the regression equation for strengthening the relation amid the % ΔRa and controlled process parameters. The % change in the Ra value after the experimentation is calculated using Eq. (4.2). The surface roughness value (Ra) was measured five times during each experimental condition, and an average of five measured Ra is considered. Further, the study of the surface characteristics of the poppet valve is observed with the help of field emission scanning electron microscopy.

## 5.3 Active Abrasive Particles (AAPs)

Due to the effect of the magnetic field, an effective active abrasive particles surface area on the poppet ridge profiles will be formed. These particles are uniformly distributed due to uniform MFD distributions causing uniform surface finish at poppet ridge profiles. The area where the active abrasives indent into the workpiece surfaces by the effect of normal indentation force and execute polishing by shear force is regarded as an effective surface area [84]. During the polishing process of the poppet valve ridge profiles, the absolute amount of active abrasive particles usable for polishing is determined on the active surface area using the percentage volume fraction of abrasive particles and volume of single SiC abrasive particle of mesh size 800 [152]. The total surface area for active abrasive particles is "$\pi r \times w$", on the poppet ridge profiles, where "*r*" is the radius of finishing poppet ridge profiles, "*w*" is the width of poppet ridge profiles (Fig. 5.1). The total active abrasive particles acting on the poppet profiles are determined by the given below specific equation

$$N_g = \frac{\%\ vol.\ fraction\ of\ \ SiC\ abrasive\ particles \times \pi r \times w \times D_g}{Volume\ of\ \sin gle\ SiC\ abrasibe\ particle} \tag{5.1}$$

where, $D_g$ (19 µm) is the diameter of single active SiC abrasive grain. The volume of single SiC abrasive grain $= \frac{4}{3}\pi\left(\frac{D_g}{2}\right)^3 = 3.591\times10^{-15} m^3$, $N_g$ is the total amount of active abrasive particles on poppet ridge profiles. The total number of active abrasive grains is calculated for different compositions of MR polishing medium for both poppet ridge profiles is listed in Table 5.5. The effective surface area remains the same, only the location of active abrasive particles changes while polishing. As the poppet valve rotates, the inactive abrasives become active.

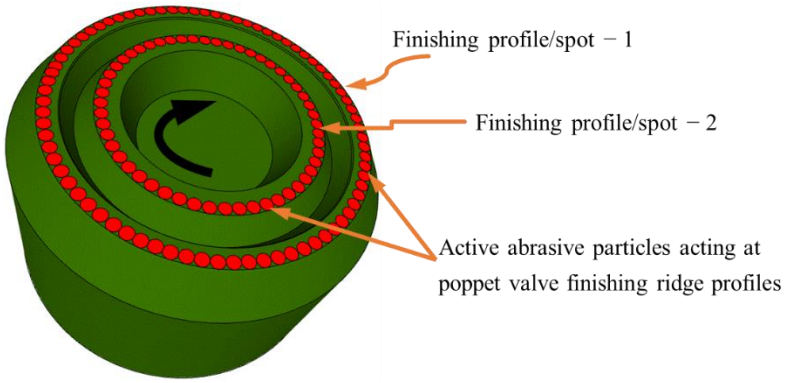


**Fig. 5.1** Active abrasive particles on poppet valve ridge profiles during finishing

The active abrasive particles of MRP fluid rotates with poppet valve rotation and shear-off the roughness peaks from the workpiece profiles due to the application of total cutting force. Thus, the number of AAPs on the workpiece surface has also played an important role in deciding the shearing rate of the roughness peaks. So, predicting the optimum % volume concentration of SiC abrasives in MRP fluid is important for effectively finishing the poppet valve surfaces with an optimum number of AAPs.

**Table 5.5** Number of active abrasive particles on poppet ridge profiles

| **Abrasive concentration (vol % )** | **Number of active abrasive particles ($N_g$)** | |
|---|---|---|
| | Finishing profile-1 | Finishing profile-2 |
| 3.5 | 1822 | 1631 |
| 7 | 3644 | 3262 |
| 10.5 | 5466 | 4894 |
| 14 | 7288 | 6525 |

# 5.4 Results and Discussion

Experiments were performed to evaluate the functionality and performance of the novel magnet fixture for standardized uniform polishing of the narrow ridges of the poppet valve. In order to understand the excellent surface characteristics, the influence of MR fluid on surface topography and surface roughness are analyzed using an optical profilometer. The material properties were checked using an EDX analysis, and also the presence of foreign materials was analyzed by means of a FESEM analysis.

## 5.4.1 Surface Characterization

Both surface roughness and surface topography are essential variables in the case of the poppet valve. Poppet valve efficiency and lifespan largely depend upon the poppet surface

morphology. Post using the novel magnet fixture; the surface roughness parameters were evaluated for the poppet ridge profiles. Poppet profiles were finished with MR polishing media, which composition is given in Table 5.1. After final finishing with the novel magnet fixture, the minimum surface roughness ($R_a$) for the poppet ridge profiles was decreased to 20.1 nm from the original value of 320 nm. Now, after finishing the poppet made of Nickel-Al-bronze alloy with these three types of MRP fluid, various surface roughness and surface characteristics are inspected.

This significant decrease of final surface roughness values on the poppet ridge profiles indicates that the novel magnet fixture is capable of producing a uniform fine surface finish. Extrusion pressure is applied to MR polishing media; as a result, abrasive particles will cut the peaks of roughness profiles by sliding and rotating action, as demonstrated in Fig. 5.2. The cutting force ($F_c$) acting on active abrasives eliminates the roughness peaks. After performing several MR rotations of the poppet valve, the roughness peaks have been adjusted into the flat smooth surface, as demonstrated in Fig. 5.2 (b). At the beginning of the finishing process, the trapped active abrasives with iron particles hit the roughness peaks of initial poppet ridge profiles, as demonstrated in Fig. 5.2 (a).

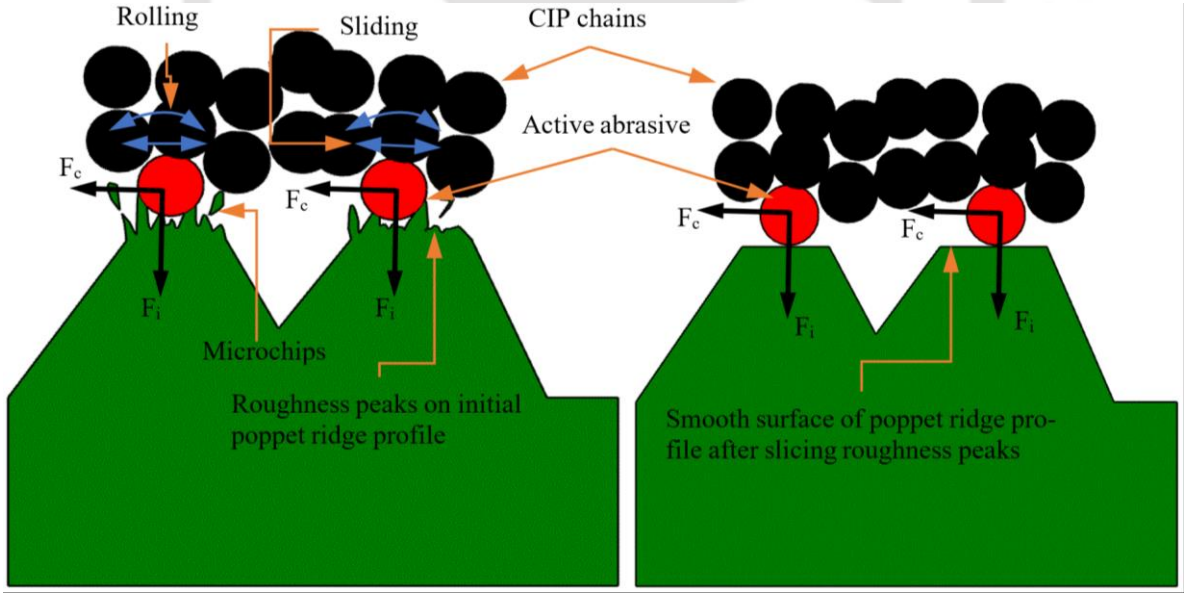


(a) (b)

**Fig. 5.2** Surface roughness peaks at the poppet profiles (a) before and (b) after finishing

### 5.4.1.1 MR Polishing Media of Type-1

Three types of magnetorheological polishing fluids have been prepared. Initially, EW grade CIPs with a mean diameter of 4 μm from BASF, Germany and SiC abrasive powder of size 19

μm is used to make the MR polishing fluid with the acid (HF and $HNO_3$) used as a base medium with deionized water [143]. It was done keeping in mind that workpiece material was hard with hardness (HRC 47). However, it was observed that the poppet workpiece gets damaged due to acid reaction, as shown in Fig. 5.3 (b). Hence, Type-1 MR fluid was discarded. Two more types of MR polishing fluid namely Type-2 and Type-3 as listed in Table 5.1. The first acid-base media comprises hydrofluoric acid (HF), nitric acid ($HNO_3$) and deionized water. Generally, HF supports in softening the surface while $HNO_3$ supports brightening the surface. The chemical reaction between copper and acid-base medium is presented in Eq. (5.2).

$$Cu+2HF+2HNO_3 \rightarrow CuF_2 + 2NO_2 + 2H_2O \quad (5.2)$$

The chemical reaction generates copper (II) fluoride, nitrogen oxide and water. Copper (II) fluoride is an inorganic compound with the chemical formula $CuF_2$. It is a white crystalline, hygroscopic solid with a rutile-type crystal structure.

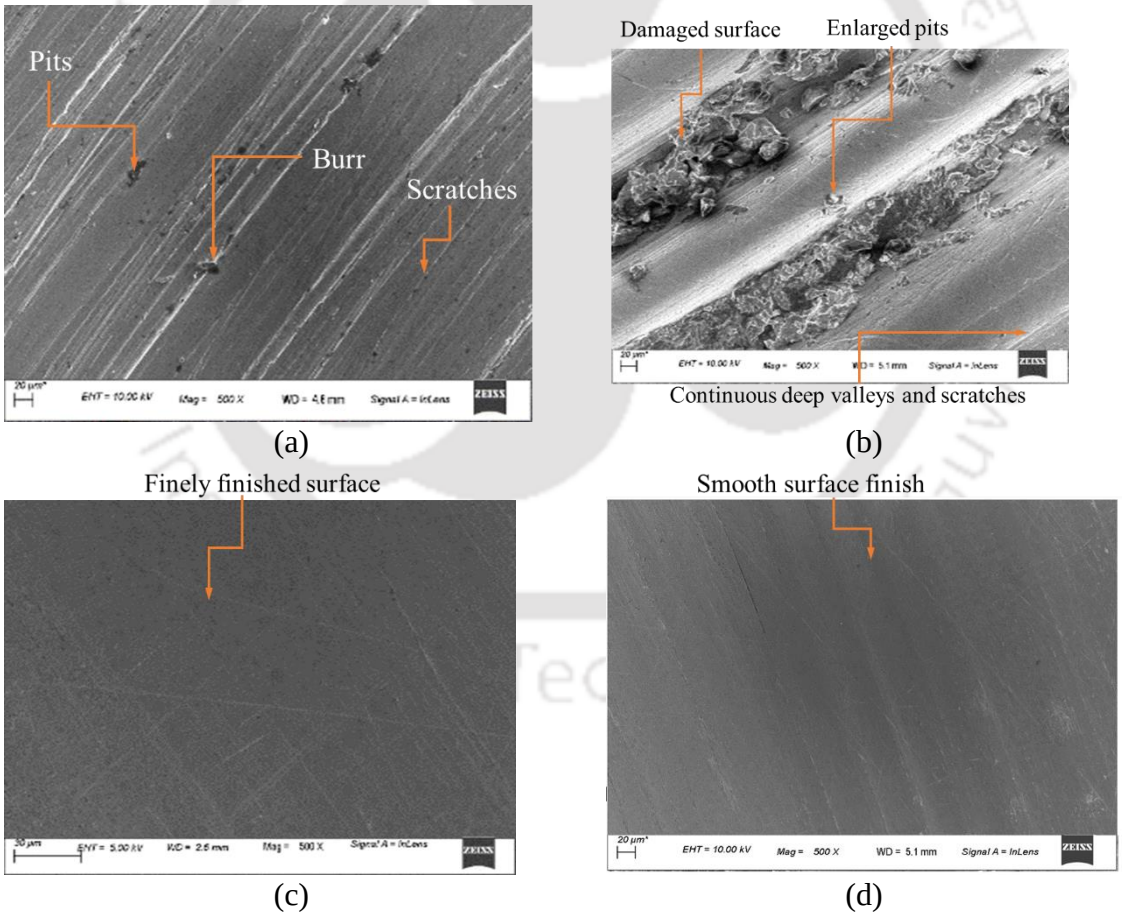


**Fig. 5.3** FESEM images of poppet valve (a) before finishing; After finishing with (b) Type-1, (c) Type-2, and (d) Type-3 MRP medium

After formation of copper (II) fluoride metal oxide fumes has occurred. $CuF_2$ forms rectangular prisms with a parallelogram base. This $CuF_2$ has changed the physical characteristic or property

of the poppet component. Hence, HF does not become stable during finishing. Fig. 5.4 represents the detailed descriptive image of reaction between MRP media of Type-1 and poppet material.

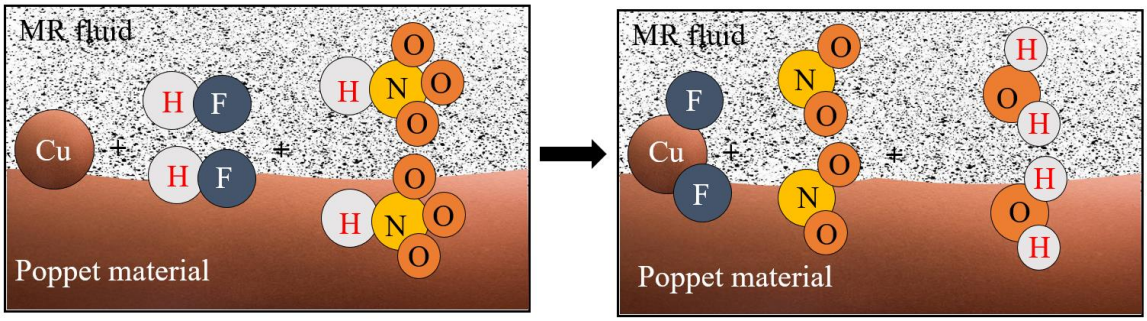


**Fig. 5.4** Schematic representation of chemical reactions that occur between Type-1 MRPF and poppet material

Fig. 5.5 (a) and (b) show surface topography of poppet workpiece before and after finishing with MR fluid of Type – I. In the final surface topography, after finishing with MR fluid of Type-1 (Fig. 5.5 (b)), the surface has more continuous deep valleys and scratches, increased number of pits are present than the initial surface. Initially, surface roughness value was 320 nm (Fig. 5.6), and it has increased to 1640 nm (Fig. 5.6) after finishing with MR fluid of Type-1.

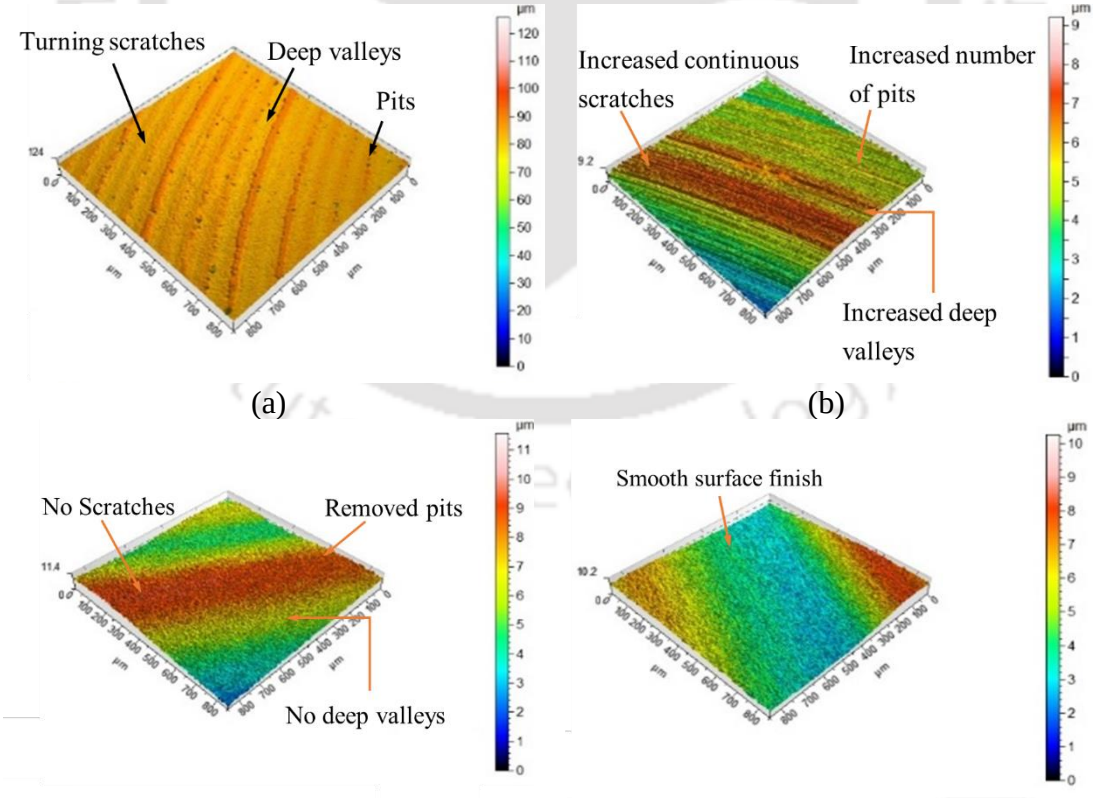


**Fig. 5.5** Surface topography of poppet valve (a) before finishing; After finishing with (b) Type-1, (c) Type-2, and (d) Type-3 MRP medium

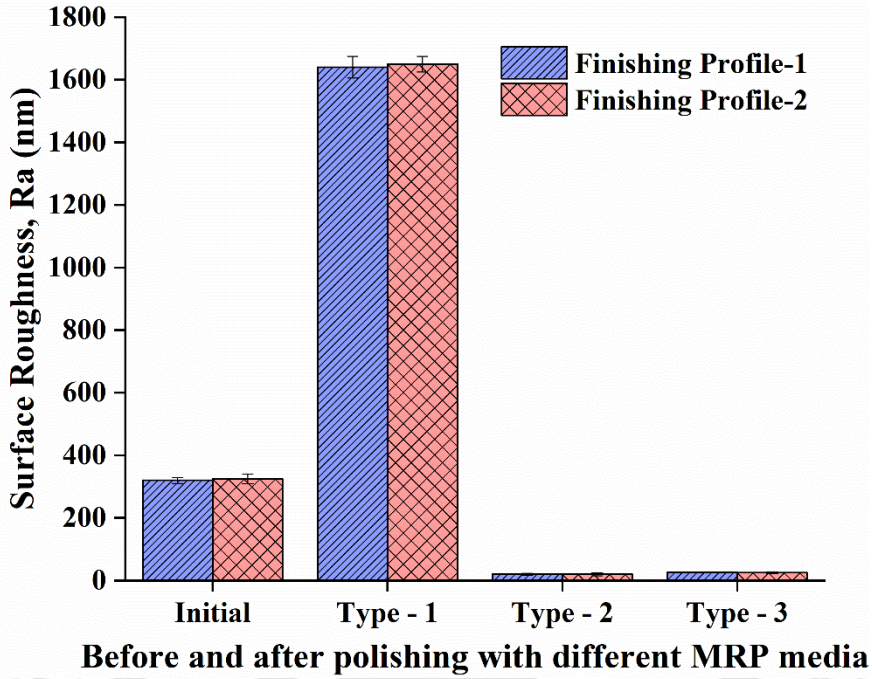


**Fig. 5.6** Comparison of surface roughness values on poppet ridge finishing profiles 1 and 2 (Fig. 5.1) before and after finishing with different MRP medium

Fig. 5.3 (a) and (b) show the FESEM images of initial and final surfaces of the poppet component at 500X magnification. Fig. 5.3 (a) shows that the initial surface is riddled with scratch marks, pits and burrs. However, the final surface (Fig. 5.3 (b)) shows more unwanted damaged particles, enlarged pits, continuous deep valleys, and scratches. Fig. 5.7 (a) and (b) show the EDX analysis for the composition of the workpiece before and after finishing using Type-I MRP media. The weight percentage of copper in the initial workpiece (Fig. 5.7 (a)) is 79.9 % making it the primary element. Fig. 5.7 (b) shows the wt. % of oxygen has increased to 7.5 % and copper wt. % of copper has reduced from 79.9 % to 75.3 % , due to the damaged workpiece surfaces.

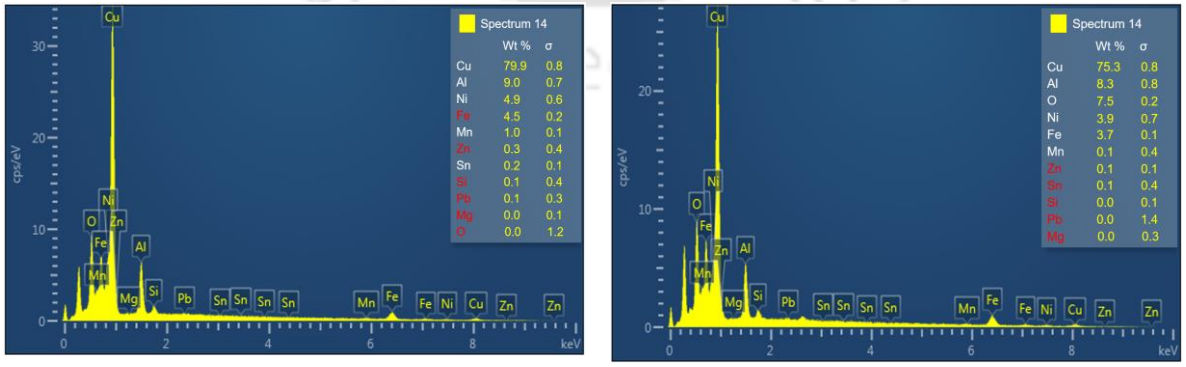


(a) (b)

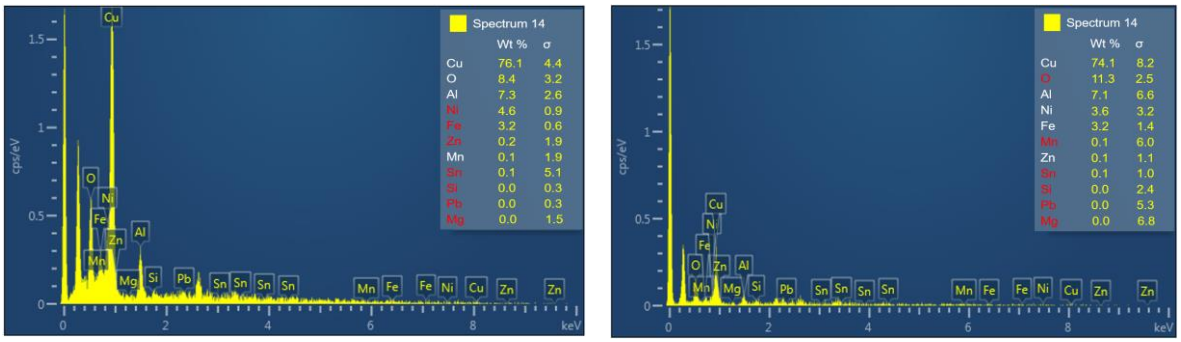


(c) (d)

**Fig. 5.7** EDX analysis of poppet valve (a) before finishing; After finishing with (b) Type-1, (c) Type-2, and (d) Type-3 MRP medium

After again reaction with hydrogen peroxide ($H_2O_2$), hydrofluoric acid (HF) and copper (Cu), Copper (II) fluoride ($CuF_2$) will be formed, as shown in Eq. (5.3).

$$Cu+2HF+H_2O_2 \rightarrow CuF_2 + 2H_2O \tag{5.3}$$

So hydrofluoric acid (HF) has been removed from the next preparation of MR fluid. Instead of HF, hydrochloric acid (HCL) is also not used because it will form $Cucl_2$, Which is mainly used in industry as a colouring agent and also used as a catalyst.

### 5.4.1.2 MR Polishing Media of Type-2

In the MR fluid of Type-2, HF has been removed, but $HNO_3$ remains as it is used to brighten the surface, and an extra agent $H_2O_2$ is used for dissolving the metallic surface to help abrasive particles.

$$2Cu+2HNO_3 + H_2O_2 \rightarrow 2CuNO_3 + 2H_2O \tag{5.4}$$

However, by the reaction of hydrogen peroxide ($H_2O_2$), nitric acid ($HNO_3$) and copper, as shown in Eq. (5.4), gives the Copper (II) nitrate ($CuNO_3$), which is also used as a polishing agent. It forms a simple blue crystalline solid. Fig. 5.8 represents the detailed descriptive image of reaction between MRP media of Type-2 and poppet material. The composition of the MR fluid of Type-2 is shown in Table 5.1.

Fig. 5.5 (c) show surface topography of poppet component after finishing with MR fluid of Type – 2. The surface roughness value has reduced from 320 nm (Fig. 5.6) to 20.1 nm (Fig. 5.6) after finishing with MR fluid of Type-2. The FESEM images of surfaces of the poppet workpiece at 500X magnification after finishing with MR fluid of Type-2 is demonstrated in Fig. 5.3 (c). The smooth surface without deep valleys, pits, burr and scratch marks is obtained on the poppet surfaces after finishing with MR fluid of Type-2. Fig. 5.7 (c) show the EDX analysis for the composition of the workpiece after finishing with MR fluid of Type-2. Fig. 5.7

(c) shows the wt. % of oxygen has increased to 8.4 % and copper wt. % of copper has reduced from 79.9 % to 76.1 %. After an experiment with MR fluid of Type-2, Type-3 is prepared with only $H_2O_2$ and deionized water as a base medium.

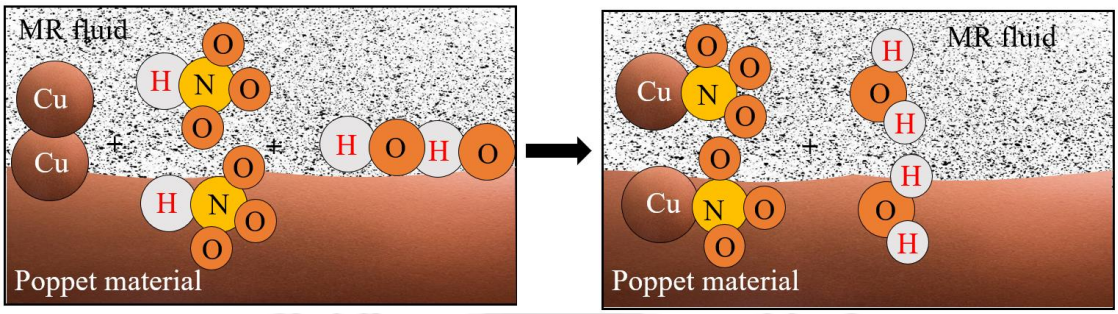


**Fig. 5.8** Schematic representation of chemical reactions that occur between Type-2 MRPF and poppet material

### 5.4.1.3 MR Polishing Media of Type-3

In this fluid, nitric acid ($HNO_3$) is removed. To only see the effect of weak acid hydrogen peroxide ($H_2O_2$) on the workpiece.

$$Cu+2H_2O_2 \rightarrow CuO_2 + 2H_2O \qquad (5.5)$$

Hydrogen peroxide ($H_2O_2$) acts as an oxidizing agent and helps the abrasive particles during finishing by dissolving the metallic surface of the workpiece. The chemical reaction generates Copper dioxide ($CuO_2$), which helps in promoting the oxide layer during finishing. Which is useful for not taking place any reaction on the surface during application and preventing further corrosion. Fig. 5.9 represents the detailed descriptive image of reaction between MRP media of Type-3 and poppet material.

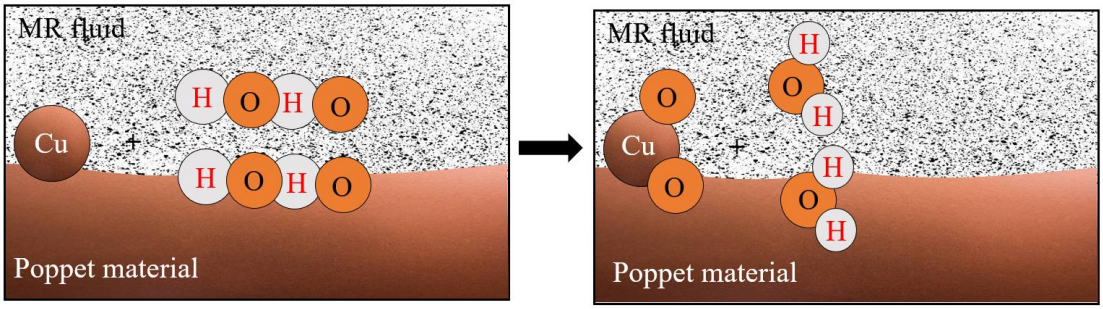


**Fig. 5.9** Schematic representation of chemical reactions that occur between Type-3 MRPF and poppet material

Fig. 5.5 (d) show surface topography of poppet component after finishing with MR fluid of Type - 3. As shown in Fig. 5.5 (d), a smooth surface without deep valleys, pits, burr and scratch

marks are also obtained on the poppet valve profile with MR fluid of Type-3. However, the surface roughness value has increased from 20.1 nm to 28.5 nm (Fig. 5.6). Fig. 5.3 (d) show the FESEM images of the poppet valve profile at 500X magnification after finishing with MR fluid of Type - 3.

A negligible amount of deep valleys remains at the surface of the workpiece. The EDX analysis for the composition of the poppet component after finishing with MR fluid of Type – 3 is demonstrated in Fig. 5.7 (d). Fig. 5.7 (d) shows the wt. % of oxygen has increased to 11.3 % and copper wt. % of copper has reduced from 79.9 % to 74.1 %, due to the formation of more layers of copper oxide ($CuO_2$).

Based on the above experiments, with Type-1, 2 and 3, Type-2 has given the best result with minimum surface roughness value. However, Type-3 has given more oxide layer formation to prevent corrosion and further reaction on the workpiece surfaces. If a poppet valve will be used in the application of seawater, then to prevent corrosion and surface reaction, more oxide formation on the surface is the best requirement, so MR fluid of Type-3 finished poppet is best suited for these types of application. It depends upon the application to select MR fluid of Type – 2 or Type – 3 finished poppet.

## 5.4.2 ANOVA Study

In the present research, a total of 30 experiments are performed to assess the outcomes of the selected process parameters on the % ΔRa. The experimental response data is tabulated in Table 5.4. Further, an analysis of variance (ANOVA) is utilized to develop the quadratic theoretical statistical model. After performing ANOVA on the basis of the sequential model, the p-value of the model for % ΔRa is found to be less than 0.05 for 95% confidence interval, this shows that the model is significant. For lack of fit, the p-value is higher than 0.05 (0.07851), which signifies that the lack of fit is not significant. The experimental response data were used to perform ANOVA as reported in Table 5.6. From the ANOVA table, it can be seen that the F-value of the developed quadratic model is 58.87. The model is significant, and the chance of the model being insignificant due to noise is only 0.01%. The obtained response surface quadratic equation for % ΔRa is given in Eq. (5.6).

$$\begin{aligned}\%\Delta R_a = & -270.23 + 12.76C + 6.89A + 6031.05F + 0.121N \\ & - 0.159C^2 - 0.238A^2 - 2.028\times10^5 F^2 - 4.8\times10^{-5} N^2 \\ & - 0.075CA - 0.066CF - 0.0001CN + 59.43AF - 0.0003AN \\ & - 1.7423FN\end{aligned} \tag{5.6}$$

Using Eq. (5.6), the % ΔRa is calculated and compared with the experimental % ΔRa values. The variation in experimental and calculated values is shown in Fig. 5.10. From the figure, it can be concluded that there is not much variation between the experimental and the calculated values from the developed model. It can also be validated from the model as the coefficient of determination ($R^2$) value of the regression equation of the model is 98.21%, which shows the accuracy of the model. A higher $R^2$ value (near 1) suggests that the model fits the data better.

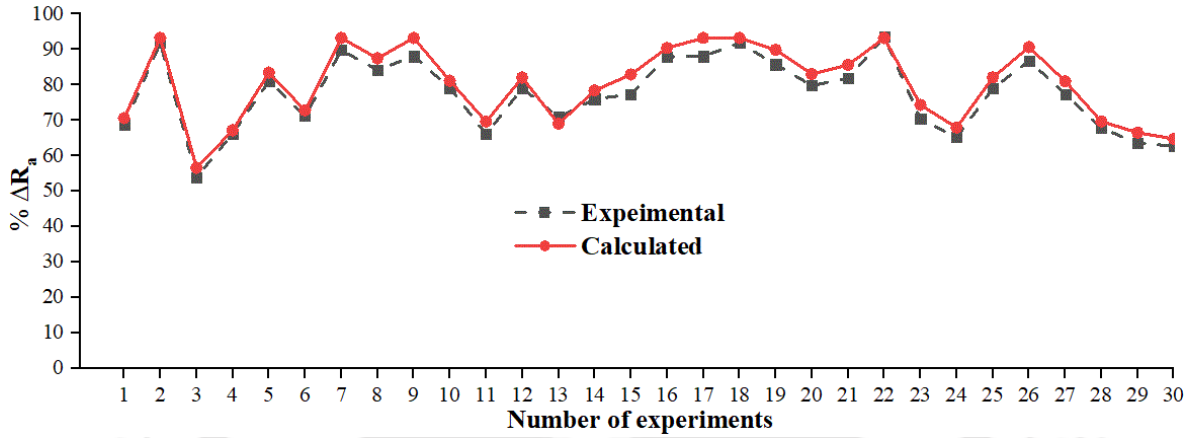


**Fig. 5.10** Comparison between experimental and predicted values of % ΔRa

**Table 5.6** ANOVA for % ΔRa

| Source | Sum of squares | DOF | Mean square | F value | p-value Prob > F | Percent Contribution |
|---|---|---|---|---|---|---|
| Model | 3025.48 | 14 | 216.11 | 58.87 | < 0.0001* | |
| C | 482.55 | 1 | 482.55 | 131.44 | < 0.0001* | 13.5581 |
| A | 416.52 | 1 | 416.52 | 113.45 | < 0.0001* | 11.7024 |
| F | 403.20 | 1 | 403.20 | 109.83 | < 0.0001* | 11.329 |
| N | 219.39 | 1 | 219.39 | 59.76 | < 0.0001* | 6.1643 |
| CA | 28.12 | 1 | 28.12 | 7.66 | 0.0144* | 0.7901 |
| CF | 1.003 | 1 | 1.003 | 0.04 | 0.9973** | 0.004 |
| CN | 0.9812 | 1 | 0.9812 | 0.2673 | 0.6127** | 0.0276 |
| AF | 17.31 | 1 | 17.31 | 4.71 | 0.0464* | 0.4858 |
| AN | 2.13 | 1 | 2.13 | 0.5802 | 0.4580** | 0.0598 |
| FN | 109.28 | 1 | 109.28 | 29.77 | < 0.0001* | 3.0708 |
| $C^2$ | 438.07 | 1 | 438.07 | 119.33 | < 0.0001* | 12.3089 |
| $A^2$ | 233.87 | 1 | 233.87 | 63.70 | < 0.0001* | 6.5707 |
| $F^2$ | 705.38 | 1 | 705.38 | 192.14 | < 0.0001* | 19.8193 |
| $N^2$ | 502.15 | 1 | 502.15 | 136.78 | < 0.0001* | 14.1089 |
| Lack of fit | 29.51 | 10 | 2.95 | 0.5774 | 0.7851** | |

* Significant, ** Not Significant, $R^2$ = 0.98 for % ΔRa, % ΔRa – Percentage change $R_a$ (CLA)

The percentage contribution (F/ΣF) of each significant factor (linear and non-linear) in Table 5.6 gives a rough but efficient guide for the percentage contribution of the factors [148]. After the regression analysis of the process parameters on the % ΔRa, the outcome of the significant

parameters has been conferred in this section. The influence of each process parameters on % ΔRa is plotted with the help of regression equations (Eq. (5.6)). The plots are analyzed and discussed to clarify the process mechanism.

### 5.4.2.1 Effect of Process Parameters on % ΔRa

The contribution of % volume of CIPs (C and $C^2$) is 25.85 % in the % ΔRa. The influence of (CIPs) concentration (vol %), C on % ΔRa is shown in Fig. 5.11 (a). The other parameters remain constant, as given in Fig. 5.11 (a). As the CIPs concentration increases up to the volume of 35%, the % ΔRa increases. Since the % volume concentration of CIPs increases, the normal stress, shear stress, and volumetric magnetic body force also increase [151]. Hence, the trend of % ΔRa increases with an increment in the removal of material. However, when the % volume concentration of CIPs goes beyond 35%, the trend of % ΔRa decreases. Further addition of CIPs, decreases the effectiveness of the active abrasive particles (AAPs) [25]. This leads to a reduction in material removal. Thus % ΔRa also decreases. The maximum value of the % ΔRa was achieved at 35% of the volume concentration of CIPs.

The contribution of % volume of abrasives (A and $A^2$) is 18.27 % in the % ΔRa. Fig. 5.11 (b) demonstrates the effect of abrasives concentration (vol %), A on % ΔRa. The other parameters remain constant, as given in Fig. 5.11 (b). Up to increment in abrasives concentration (vol%) up to 7 %, % ΔRa trend increases then after it decreases. It happens because, initially, the AAPs are firmly attached in between the CIPs and make fewer discontinuous chains. After increasing the concentration of the abrasive beyond 7% volume, the more number of AAPs gets twisted between the CIPs. The distance between the two CIPs (R') increases, which reduces the magnetic interaction force (F) as given in Eq. (4.1) [149], [126]. This led to the reduction in the shear strength of the MR fluid [150]. Many abrasives do sliding and rolling without any polishing activity in the working gap. Hence, the trend of % ΔRa decreases [145].

The contribution of the feed rate of poppet valve (F and $F^2$) is 31.14 % in the % ΔRa. The effect of the vertical feed rate of poppet valve (F) on % ΔRa is shown in Fig. 5.11 (c). The other parameters remain constant, as shown in Fig. 5.11 (c). Up to increment in F up to 0.01 mm/min, % ΔRa trend increases then after it decreases. As F increases up to the value of 0.01 mm/min, there is an increment in total indentation force, which is due to an increase in normal force on working parts by increasing the rate of average compressive strain [139]. This helps the AAPs penetrate the working surfaces rapidly, and thus shearing the surface asperities by

AAPs on the work part region also increases. This leads to an increase in % ΔRa. Beyond feed rate of 0.01 mm/min, total indentation force further increases, and hence it increases the interaction time of surface asperities and active abrasive particles (AAPs), which collide very rapidly and remove excess material [153]. The AAPs shear off the unwanted surface asperities in a short moment of time, leading to a decrease in % ΔRa. The maximum value of the % ΔRa was achieved at the feed rate of the poppet valve of 0.01 mm/min.

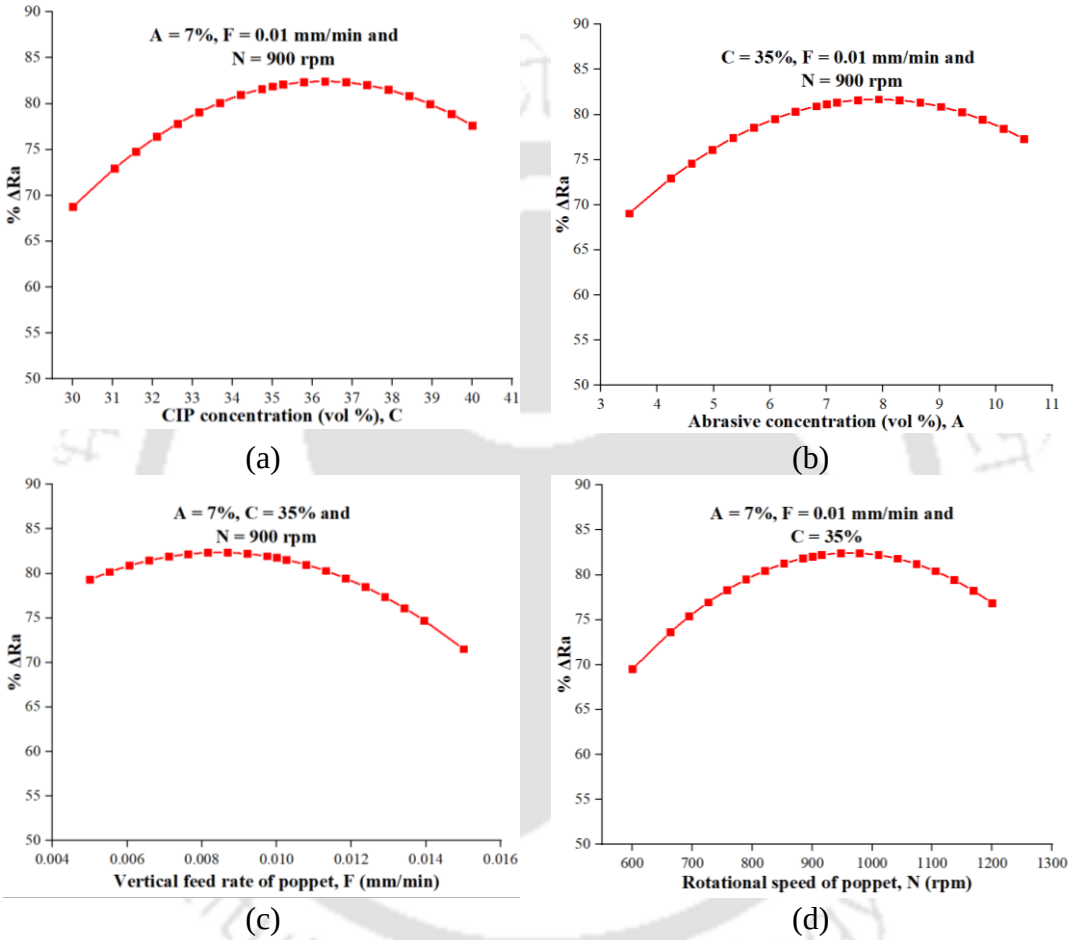


**Fig. 5.11** Effect of (a) CIPs concentration, (b) abrasives concentration, (c) vertical feed rate of poppet, and (d) poppet rotational speed on %Δ Ra

The contribution of poppet valve rotational speed (N and $N^2$) is 20.26 % in the % ΔRa. Fig. 5.11 (d) shows the effect of poppet valve rotation speed (N) on % ΔRa, with other parameters, are constant. With increasing in value of N, % ΔRa also increases up to a value of 900 rpm, and then the trend starts decreasing. It happens because, as the N increases, the rotational speed of the AAPs that rotates over the surface asperities of working surfaces also increases. It leads to an increase in the centrifugal force and tangential force. Thus there is an increment of total cutting force of AAPs, which shear off the surface asperities rapidly and precisely, which

provides an improvement in finishing. Hence, the trend of % ΔRa increases. Beyond the poppet valve rotation of 900 rpm, there is an excessive increase in centrifugal force. The active abrasive particles tend to loosen their grip in the CIPs chain during finishing. Hence, AAPs cannot shear-off the surface asperities properly from the work part surface, which decreases the trend of the % ΔRa. The maximum value of the % ΔRa was attained at the 900 rpm of poppet rotation.

Fig. 5.12 (a) shows the combined effect of poppet valve rotational speed (N), and feed rate of poppet valve (F) on the % ΔRa, with other parameters, kept constant as (A = 7% and C = 35%). As the N and F increases up to 900 rpm and 0.01 mm/min, respectively, the trend of the % ΔRa increases, then after it decreases. Increasing both the parameters simultaneously leads to the enhancement in the net relative motion of the AAPs that acts on the work part surface and also the indentation capability of AAPs to working surfaces. This enhances the surface finish of the workpiece, due to which there is an increase in the trend of the % ΔRa. However, beyond the N = 900 rpm and F = 0.01 mm/min, a significant centrifugal force destabilizes the CIPs columnar chain in the MRP fluid, affecting the finishing action. And also, at a high feed rate of the poppet valve, the rate of indentation force also increases, which creates unwanted valleys and peaks on working surfaces. Thus, overall % ΔRa decreases.

Fig. 5.12 (b) shows the combined effect of the feed rate of poppet valve (F) and % volume of abrasives (A) on the % ΔRa, with other parameters, kept constant as (C = 35% and N = 900 rpm). As the F and A increase up to 0.01 mm/min and 7 %, respectively, the trend of the % ΔRa increases, then after it decreases. Increasing both parameters simultaneously lead to the increment of shear force and indentation force. However, beyond F = 0.01 mm/min and A = 7 %, further, increase of shear force, and indentation force leads to removing unwanted materials. Hence, it will result in a decreasing trend of the % ΔRa.

Fig. 5.12 (c) shows the combined effect of % volume of (CIPs) C and poppet rotational speed (N) on the % ΔRa, with other parameters kept constant as (A = 7% and F = 0.01 mm/min). As the N and C up to 900 rpm and 35%, respectively, the trend of the % ΔRa increases, then after it decreases. As the N and C increase simultaneously, there is an increase in the centrifugal and normal force in MR polishing (MRP) fluid, leading to the increase in the shearing of the surface asperities. Hence, the trend of % ΔRa increases. However, beyond the N = 900 rpm and C = 35%, an excessive increase in centrifugal force results in loss of AAPs grip in the CIPs chain. Also, there is a decrease in the overall cutting edges of AAPs as more CIPs aggregates outside the already existing CIPs chains in which the AAPs are tightly gripped

[25]. Owing to which there is improper chipping off surface asperities from the workpiece surface, which leads to a decrease in the trend % ΔRa.

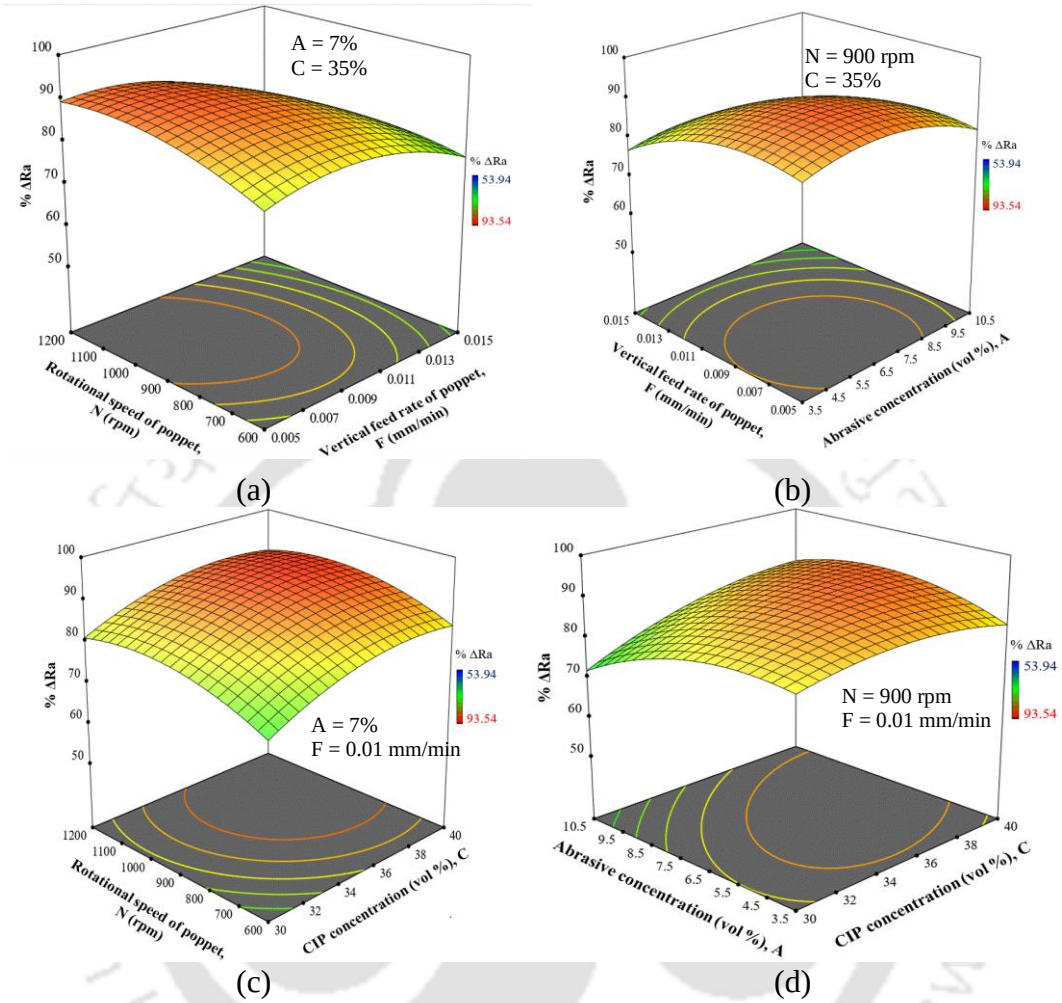


**Fig. 5.12** 3D plots showing combined effect of (a) rotational speed and feed rate of poppet, (b) feed rate and abrasive concentration, (c) rotational speed and CIPs concentration, and (d) abrasive and CIPs concentration on %Δ Ra

Fig. 5.12 (d) shows the combined effect of % volume concentration of abrasives (A) and % volume concentration of (CIPs) C on the % ΔRa, with other parameters kept constant as (N = 900 rpm and F = 0.01 mm/min). As the A and C up to 7 % and 35 %, respectively, the trend of the % ΔRa increases, then after it decreases. Increasing both the parameters simultaneously leads to the enhancement in the MRP fluid shear strength due to an increment in yield stress. It will result in faster removal of material. Hence, the trend of % ΔRa increases. However, beyond A = 7% and C = 35 %, decreases the shear strength of the MRP fluid. This is because the higher % volume concentration of abrasive increases the distance between the CIPs, which decreases the magnetic interaction force. This leads to the reduction in the removal of material, due to which % ΔRa decreases. In the present work, the main aim is to get maximum % ΔRa

for MR finishing of the poppet valve. To get the best possible outcome for the % ΔRa, the prediction of the optimum parameters was done after the regression analysis. The Eq. (5.6) was used to calculate the maximum % ΔRa.

The regression equation (Eq. (5.6)) gives prediction of 93.25 % improvement in $R_a$, when N = 900 rpm, F = 0.01 mm/min, C = 35% and A = 7%. The composition of MR polishing fluid for finishing the poppet valve with the present process is 35% volume concentration of CIPs, 7 % volume concentration of the abrasives and the remaining 58% volume concentration of water-based carrier fluid. Further, experiments are performed using the optimized parameters on the poppet valve profiles. The total improvement in % ΔRa after 100 minutes MR finishing on the poppet valve surface was found as 92.22%. After 100 minutes, there is no significant improvement observed on the poppet valve profiles.

To validate the ANOVA model and further regression equation, three validation tests are carried out; Exp. I: at optimum experimental condition, followed by two more experiments (Exps. II and III) chosen randomly within the range of process parameters (Table 5.7). The initial surface roughness values of the workpieces are selected almost the same for all three experiments. The experimental value of % ΔRa is computed for all three validation tests using Eq. (4.2). These values are compared with the predicted values calculated using regression equation (Eq. (5.6). The comparison between the experimental and the predicted results as well as percentage error, is shown in Table 5.7. A maximum error of 9.82 % is observed among all three validation experiments, which describes the repeatability of the proposed model.

**Table 5.7** Validation tests for % ΔRa

| S.No. | C (%) | A (%) | F (mm/min) | N (rpm) | Exp. (% ΔRa) | Pred. (% ΔRa) | Error (%) |
|---|---|---|---|---|---|---|---|
| 1. | 35 | 7 | 0.01 | 900 | 92.22 | 93.25 | 1.12 |
| 2. | 30 | 7 | 0.01 | 600 | 69.44 | 76.26 | 9.82 |
| 3. | 32 | 10.5 | 0.013 | 1100 | 87.97 | 91.51 | 4.02 |

Exp. – Experimental, Pred. – Predicted

# 5.5 Summary

The performance of the developed fixture is justified experimentally and theoretically while polishing poppet valve ridge profiles. Three types of MRP medium are prepared to check their effects on the finishing surfaces of poppet valve ridge profiles. The uniform distribution of magnetic flux density forms an effective surface area of active abrasives on the poppet valve ridge profiles. The surface roughness of the poppet profiles is reduced significantly to 20.1 nm

from its initial value of 320 nm using MR fluid of Type-2. The quality of the poppet profiles is improved considerably. Type-2 MR fluid achieved best result with minimum surface roughness value. However, using Type-3 MRPF more oxide layer is formed required to prevent corrosion and further reaction on workpiece surface. Depends upon the applications of the components, either MR fluid of Type – 2 or Type – 3 can be selected while finishing poppet valves. The value of the optimized process parameters, i.e. rotational speed of poppet (N = 900 rpm), vertical feed rate of poppet (F = 0.01 mm/min), CIPs volume fraction (C = 35%), and abrasives volume fraction (A = 7%), provided 93.25 % improvement in $R_a$. A combination of lower feed rate and higher poppet rpm is more advantageous for achieving higher % ΔRa with minimum finishing time. After using the R-MRFF process, the poppet valve will gain high wear and corrosion resistance capability, longer service life, and minimum maintenance during its working performance. It has high accuracy and reliability for specific applications.

# Chapter 6 Surface Roughness Simulation

## 6.1 Introduction

The uniform finishing of the poppet valve ridge and miniature gear profiles is analyzed using an FEA based software Comsol® Multiphysics, where outcomes are shear stress, normal stress and magnetic flux density distributions at workpiece profiles. Simulation of forces responsible for finishing in the R-MRFF method helps in regulating the process accurately. The forces which are responsible for finishing are normal forces (help in indenting the material), and shear forces (help in eliminating the indented materials). Surface roughness simulation is carried out using FEA findings and finishing force analysis. A mathematical model is also formulated to analyze the indention depth caused by a single active abrasive on workpiece material while finishing. The gap between the experimental and simulated results are marginal. It has high accuracy and reliability for specific applications.

## 6.2 Miniature Gear Finishing

The various finishing forces, acting on active abrasives during gear MR finishing, are responsible for eliminating the roughness peaks. These active abrasives cause the indentation into the workpiece surface, and this indentation depth is a function of the normal magnetic force ($F_m$) and other normal finishing forces. In order to determine the accurate predictive pattern of surface roughness, the mathematical model for the precise estimation of normal finishing forces, number of active abrasive particles and depth of indentation on the workpiece surfaces should be developed. The following assumptions can simplify the theoretical analysis of this mathematical model:

- Iron and SiC abrasive particles are spherically shaped and evenly spread in MRP fluid.
- The average diameter of the abrasive particles ($d_g$) is calculated from the mesh size number ($M_e$) as, $d_g = \frac{15200}{M_e}$ [154].
- Each abrasive has a single active cutting edge.
- The load on each abrasive is constant, and therefore the workpiece surface has the same indentation depth.
- Magnetic leaks and losses are ignored.
- The nano-chips of the workpiece do not alter MR polishing fluid.

- The tangential component of magnetic force is neglected.
- The induced magnetic field on the gear profiles is not used for magnetic force calculation.

Due to developed magnetic dipoles in iron particles of MRP fluid, these particles form a chain-like structure. The yield strength of this chain structure retains the active abrasive particles during its surface finish at the gear profiles [55]. The effectiveness of finishing depends on how tightly these chains bind the abrasive particles.

### 6.2.1 Analysis of Finishing Forces

The active forces (Fig. 6.1), which are responsible for material removal, depend upon gear teeth' profiles and motions given to the MRP fluid. The MRP fluid is given a continuous rotating and reciprocal motion through the R-MRFF process so that the approaching active abrasive particles uniformly remove the roughness peaks of the material. The magnetic force presses the abrasives, which are trapped by iron particles into the workpiece's surface (Fig. 6.1 (a) and (b)). The magnetic forces are assumed to be normal to each gear tooth profile. The magnetic force, $F_m$, works on one iron particle in a magnetic field is given as [155], [156]

$$F_m = m_{ip}\mu_0\chi_m H\nabla H \tag{6.1}$$

Where, $m_{ip}$ is the mass of iron particles (kg), $\chi_m$ is the magnetic susceptibility of IPs in ($m^3$/kg) inside the polishing medium, $H$ is the magnetic field strength in (A/m), $\nabla H$ is the gradient of the magnetic field strength, and $\mu_0$ is the magnetic permeability of free space ($4\pi\times10^{-7}$ N/$A^2$). This normal magnetic force $F_m$ helps the abrasives in indenting the workpiece surfaces. The relation between the magnetic field strength (H) and magnetic induction/magnetic flux density (B) may be regraded for practical use as shown in Eq. (6.2).

$$B = \mu_0 H \tag{6.2}$$

So, using Eq. (6.2), Eq. (6.1) can be rewritten as Eq. (6.3).

$$F_m = m_{ip}\frac{\chi_m}{\mu_0}B\nabla B \tag{6.3}$$

The variation of magnetic flux density (B) is only considered in the horizontal direction, and other directions are neglected. Thus, in the working gap (x) from the inner teeth profile of the uniform flow restrictor to the outer teeth profile of gear, Eq. (6.3) may be interpreted as Eq. (6.4).

$$F_m(x) = m_{ip} \frac{\chi_m}{\mu_0} B(x) \frac{dB(x)}{dx} \tag{6.4}$$

Here, *B (x)* is the magnetic flux density variation in the working gap (x) ranging from 0 to 2 mm. Mass of magnetic susceptibility $(\chi_m)$ of iron particles is presented in Eq. (6.5).

$$\chi_m = \frac{M}{H} = \frac{\mu_0 M}{B} \tag{6.5}$$

Where, *M* is iron particles magnetization (A-m$^2$/Kg), and magnitude is evaluated from the M-B curve of MRP media (Fig. 2.4(a)) [157]. B (x) is derived from the FE analysis using Comsol® Multiphysics in-between the working gap of A'A, C'C, E'E (Fig. 2.3 (b)) and along the arc length of SY of gear tooth face (Fig. 2.3 (a)). Eq. (6.6) and Eq. (6.7) represent the magnetic flux density variation in the working gap A'A with and without using a uniform flow restrictor, respectively.

$$B_{A'A}(x) = -0.0353x + 0.2461 \tag{6.6}$$

$$B_{A'A}(x) = -0.0352x + 0.2445 \tag{6.7}$$

In Eq. (6.6) and Eq. (6.7), "x" is in meters ranging from 0 to 0.002 m. Differentiating Eq. (6.6) and Eq. (6.7), with respect to x give Eqs. (6.8) and (6.9) as follows.

$$\frac{dB_{A'A}(x)}{dx} = -0.0353 \tag{6.8}$$

$$\frac{dB_{A'A}(x)}{dx} = -0.0352 \tag{6.9}$$

In a similar way, the FE analysis gives an equation of magnetic flux density variation in the working gap C'C, E'E and along SY of gear tooth face with and without uniform flow restrictor. Iron particles help the adjacent active abrasives in indenting the workpiece surfaces [158]. The magnetic force on the iron particles next to active abrasives is calculated using Eqs. (6.4)–(6.9). The calculated magnetic susceptibility $(\chi_m)$ and magnetic force ($F_m$) at positions A, C, E (Fig. 2.3 (b)) and O (Fig. 2.3 (a)) in the working gap of A'A, C'C, E'E and along SY of gear tooth face with and without uniform flow restrictor is given in Table 6.1.

Shear force ($F_s$) is responsible for shearing the material as microchips on the gear tooth profiles (Fig. 6.1(a) and (b)). Normal force ($F_n$) allows abrasives to penetrate into the gear tooth profiles (Fig. 6.1(a) and (b))) [159]. Normal force, $F_n$ is given as

$$F_n = \sigma_n \times A_p \tag{6.10}$$

where, $A_p$ is normal projected area of gear working profiles ($m^2$), $\sigma_n$ is normal stress variation along gear profiles (Pa). $\sigma_n$ is derived from FE analysis.

**Table 6.1** Calculated normal magnetic force at different positions of gear tooth profile using Eqs. (6.4)-(6.9)

| **Positions at gear tooth profile (mm)** | **Magnetic flux Density *B* (T)** | | **Mass of magnetic susceptibility** $(\chi_m) \times 10^{-4}$ **($m^3$/kg)** | | **Magnetic force** $(F_m) \times 10^{-10}$ **(N)** | |
|---|---|---|---|---|---|---|
| | Uniform flow restrictor | | Uniform flow restrictor | | Uniform flow restrictor | |
| | Without | With | Without | With | Without | With |
| A | 0.1755 | 0.1741 | 1.0468 | 1.046 | -0.1455 | -0.1440 |
| C | 0.2132 | 0.2172 | 1.030 | 1.027 | -0.1191 | -0.1102 |
| E | 0.2288 | 0.2273 | 1.021 | 1.022 | -0.1778 | -0.1741 |
| O | 0.2095 | 0.2075 | 1.032 | 1.032 | -0.1659 | -0.1719 |

In R-MRFF process (Fig. 6.1(a) and (b)), abrasive particles also rotate with the rotation of magnet fixture. Because of the rotation of abrasives, a centrifugal force will act (Fig. 6.1(a) and (b)).

$$F_{cen} = m_{AP} r \omega^2 \tag{6.11}$$

In Eq. (6.11), ($\omega = 2\pi N/60$) is the angular velocity (rad/s), $N$ is the rotational speed of the magnet fixture, "$r$" is the radial distance, and $m_{AP}$ is mass of the abrasive particle (kg). The total normal indentation force $(F_{indentation})_i$ on the active abrasives along the tooth top, involute and in-between profile of gear (Fig. 6.1(a)) is represented by,

$$\left(\vec{F}_{indentation}\right)_i = \vec{F}_m + \vec{F}_n - \vec{F}_{cen} \tag{6.12}$$

And the total normal indentation force $(F_{indentation})_f$ on the actives abrasives along the tooth face profile of gear (Fig. 6.1(b)) is represented by,

$$\left(\vec{F}_{indentation}\right)_f = \vec{F}_m + \vec{F}_n \tag{6.13}$$

A tangential force [160] & [161], will also act on the abrasives in the tangent direction of fluid rotation (Fig. 6.1 (a) and (b)).

$$\vec{F}_t = 2m\left(\vec{\omega} \times \vec{v}\right) \tag{6.14}$$

Here, $\omega$ and $v$ represent the abrasives' angular velocity and linear velocity (determined from FE analysis), respectively. By changing the rotational speed of the magnet ($N$), centrifugal

force ($F_{cen}$ in Eq. (6.11)) and tangential cutting force ($F_t$ in Eq. (6.14)) also change. The total cutting force $(F_c)_i$ acting on the active abrasives along the tooth top, involute and in-between profile of gear is the resultant of shear force ( $F_s$ ), and tangential force ($F_t$), (Fig. 6.1 (a)) and it is given as,

$$\left(\vec{F}_c\right)_i = \vec{F}_s + \vec{F}_t \tag{6.15}$$

And the total cutting force $(F_c)_f$ acting on the active abrasives along the tooth face profile of the gear is the resultant of shear force ($F_s$), tangential force ($F_t$) and centrifugal force ($F_{cen}$), (Fig. 6.1 (b)) and it is given as

$$\left(\vec{F}_c\right)_f = \vec{F}_s + \vec{F}_{cen} + \vec{F}_t \tag{6.16}$$

Here, frictional forces are considered as negligible.

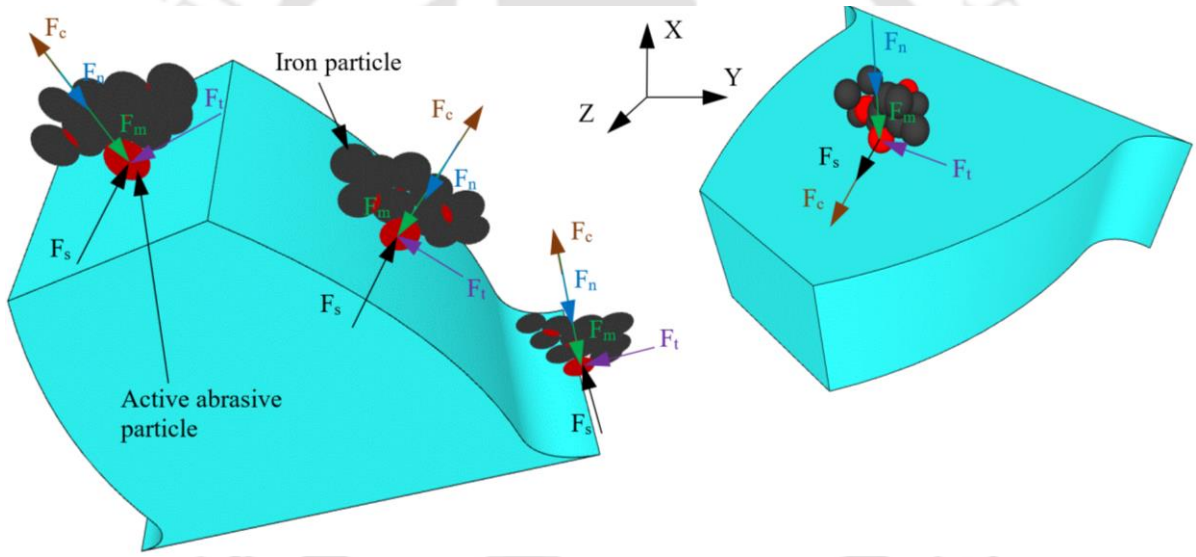


(a) (b)

**Fig. 6.1** Schematic representation showing forces acting during finishing at (a) tooth top, involute, in-between, and (b) face profiles gear tooth

## 6.2.2 Region of Active Abrasives on Gear Tooth Profiles

The external magnetic field developed shear, and normal stress from externally applied pressure forms an effective active abrasive particles surface area on the gear teeth profiles. The effective magnetic flux density without and with uniform flow restrictor along A'A, C'C, E'E, AB, BD, DF, and SY (Fig. 2.3 (a)) of gear tooth profile is almost uniformly distributed all over the surface (Fig. 2.5). However, the shear stress (primary cutting stress) distribution along AB, BD, DE profile of gear tooth (Fig. 2.3 (a)) show static variation, when flow restrictor is used as compared when flow restrictor is not used (Fig. 2.6). With and without using a flow

restrictor, shear stress variation is almost similar along the gear tooth face (SY) profile. There is no effect of flow restrictor on gear tooth face profile. The average shear stress variation without using flow restrictor is almost half of the when using flow restrictor at miniature gear teeth involute, top and in-between profiles.

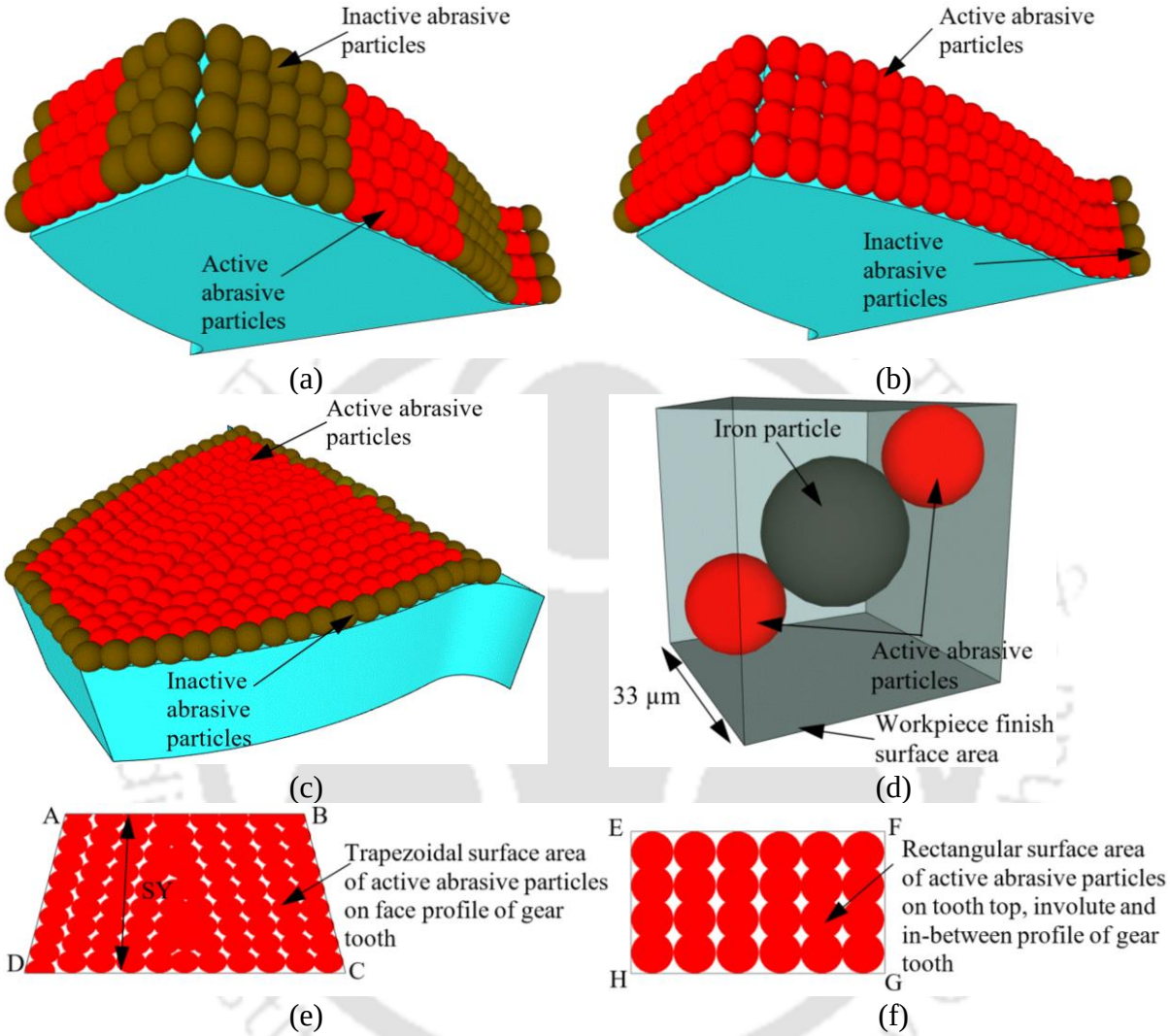


**Fig. 6.2** Region of active abrasive particles on gear tooth top, in-between, involute profiles during finishing (a) without, (b) with using uniform flow restrictor, (c) on tooth face surface both without and with using uniform flow restrictor, (d) placement of two active abrasive particles with a single iron particle in a cubic structure diagonally, inclined view of the active abrasive particles region at tooth (e) face and (f) top, involute and in-between profiles of miniature gear

**Table 6.2** Number of active abrasive particles on involute, top, in-between, and face profiles of miniature gear with and without using uniform flow restrictor

| **Number of active abrasive particles ($N_{active}$)** | | | | | | | |
|---|---|---|---|---|---|---|---|
| Tooth involute | | Tooth top | | Tooth in-between | | Tooth face | |
| Uniform flow restrictor | | Uniform flow restrictor | | Uniform flow restrictor | | Uniform flow restrictor | |
| Without | With | Without | With | Without | With | Without | With |
| 3485 | 6971 | 455 | 911 | 1067 | 2134 | 9951 | 9951 |

Hence, at a single stroke, the number of active abrasive particles taking part in finishing action will also become half at these profiles and will remain the same for the face profile. As total active abrasives are more when using flow restrictor so, it will result in fast material removal. The area where the active abrasives indent into the workpiece surfaces by the effect of normal magnetic force and perform finishing by cutting forces is regarded as an effective surface area [84]. The active abrasives area on gear tooth top, involute, in-between and face profile without and with uniform flow restrictor during its surface finishing with R-MRFF process is shown in Fig. 6.2 (a), (b) and (c), respectively. The configuration of active abrasives area on gear tooth in-between, involute and top profile is regarded as the rectangular shape (Fig. 6.2 (f)), and Eq. (6.17) determines it. The area (in $mm^2$) of active abrasive particles region (*EFGH*) is given as

$$EFGH = EF \times FG \tag{6.17}$$

The active abrasives area (*ABCD*, $mm^2$) on the face profile of gear teeth is regarded as the trapezoidal shape (Fig. 6.2 (e)), and it is given in Eq. (6.18).

$$ABCD = \frac{1}{2} \times \left( AB + CD \right) \times SY \tag{6.18}$$

In addition, the MR polishing fluid's abrasive and iron particles create a cube cell structure, and a single iron particle placed at the centre comes into contact with the two adjacent active abrasive particles diagonally in this cube (Fig. 6.2 (d)) [162]. These active abrasives of the cube participate in the finishing or can tell one face of the cube participates in the finishing process. Eq. (6.19) determines the total number of active abrasive particles ($N_g$) in the active region.

$$N_g = \frac{Area\ of\ \ the\ active\ abrasive\ particles\ region \times 2}{A_f} \tag{6.19}$$

Where '$A_f$' is an area of the cube face, and two is multiplied since two active abrasives participate in the finishing process at a time in a cubic structure. The total number of active abrasive particles is calculated for all gear tooth profiles with and without flow restrictor is given in Table 6.2. The effective surface area remains the same, only the location of active abrasive particles changes during finishing. As the magnet fixture rotates, the inactive abrasives become active.

## 6.3 Magnetostatic Fluid-Solid Interaction Analysis of Poppet during Finishing

Magnetostatic fluid-solid interaction simulation using software package Comsol® Multiphysics was conducted to study the magnetic field, shear stress and normal stress distribution along the

poppet valve ridge profiles. The input parameters used for the simulation study are listed in Table 6.3. Comsol® Multiphysics solve the permanent magnetic field with fluid flow and solid mechanics problems of a specified model by allocating materials, boundary criteria, and source conditions. Table 6.4 represents the boundary conditions used during simulation study. The computational domain for fluid-solid interaction analysis with the externally applied magnetic field is shown in Fig. 6.3. The rectangular permanent magnet, Sm2Co17 (Samarium-Cobalt) of grade 30H, is considered to give a continuous fine polishing of the poppet ridge profiles for the current analysis.

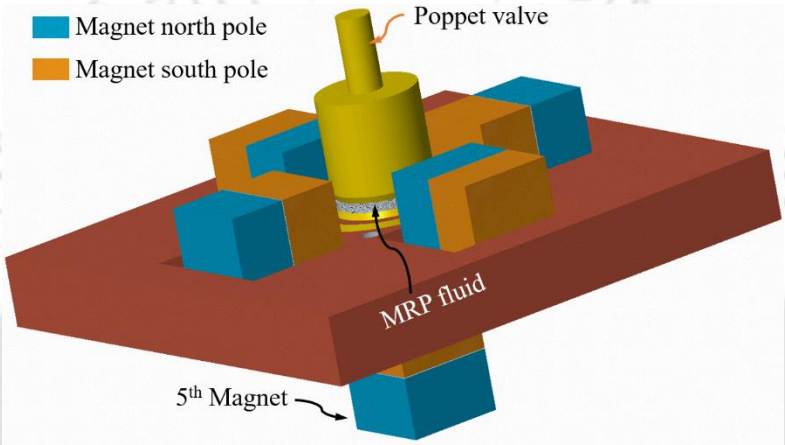


**Fig. 6.3** 3D computational domain for fluid-solid interaction analysis under magnetic field

In any finishing process, the forces exerted on the component profiles play a vital position in the surface integrity. The volume of material removal from the component profiles during finishing mostly relies on the forces responsible for finishing. These forces are exerted on the component surfaces via abrasive particles.

The normal force is modelled by assessing the magnetic excitation force on abrasives, spindle pressure on abrasives through poppet valve and their impact on the workpiece profiles at the time of fluid-solid (poppet profiles) interaction. Tangential force is derived from the fluid solid interaction phenomenon. Shear stress and normal stress working on the poppet profiles are derived from the fluid surface interaction with an active magnetic field and applied pressure. In the finishing region, due to the use of magnetic field, MRP fluid functions like a Bingham plastic fluid.

Zero velocity and displacement fields for every flow parameter are initially applied at the poppet profile and MRP fluid surface interaction. For ensuring the uniform finishing of the poppet valve profiles, magnetic flux density, shear stress and normal stress distributions are studied in detail (Fig. 6.4(a)). The various positions (A to H) (Fig. 6.4 (a))) on finishing spots

of poppet valve profile is taken to evaluate the various forces acting on abrasives, which can be used for simulating the final surface roughness values on these profiles. Only positions (A to H) (Fig. 6.4 (a)) is considered, and other parts of finishing spots are leftover because they are symmetric to these positions and give similar results. The working gap at positions A and B of finishing spots of the poppet valve, which is filled with MR fluid, is shown in Fig. 6.4(b).

**Table 6.3** Input parameters used for simulation study

| Variables | Value |
|---|---|
| Remnant MFD | 0.5 T |
| Consistency factor | 205.93 |
| Density | 2703 kg/m$^3$ |
| Magnetic particles vol. fraction | 0.30 |
| Power index law factor | 0.3039 |
| Feed rate of poppet valve | 0.01 mm/min |
| Rotational speed of poppet | 1200 rpm |
| Newtonian viscosity | 0.0358 Pa-s |

**Table 6.4** Boundary conditions used during the simulation study

| Boundary type | Boundary conditions |
|---|---|
| Interactive surface between poppet and MRP fluid | No slip and free elastic deformation |
| Initial relative interactive surface between poppet and MRP fluid | $U_{solid}$ (displacement field) = 0, $\partial U_{solid}/\partial t$ (structural velocity field) = 0 |

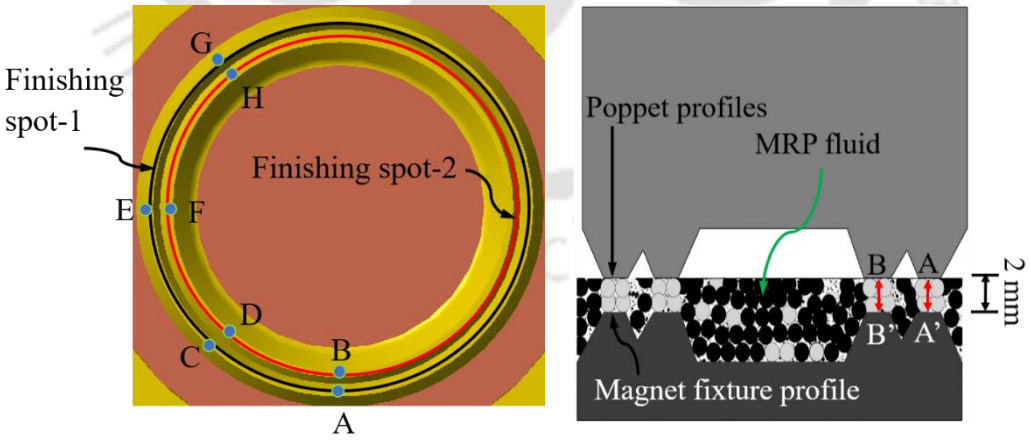


(a) (b)

**Fig. 6.4** Measuring points (a) on finishing spots of poppet ridge, (b) at the working gap between poppet and magnet fixture profiles for calculating magnetic flux density, shear stress, and normal stress distribution

Step one in Comsol® Multiphysics simulation is importing a geometric model in "igs" format, then combine three applicable physics into a single domain with their boundary conditions

and input parameters, then mesh the domain, after setting statistical study, finally compute the process outputs. To rotate the poppet valve in simulation analysis in Comsol software, identical boundaries pairs were used. Where two cylinders are made, one is selected as source boundary, and the other is selected as destination boundary within simulation domain. The vertical downward movement of the poppet valve inside the simulation domain is considered by prescribed mesh displacement in solid mechanics study. In the Multiphysics coupling interface, fixed geometry fully coupling is selected for fluid-structure interaction analysis. The mesh displacement in the normal direction to the boundary is limited by an equation such as ($u_p$ . $n$ = 0), where $n$ is the normal unit vector. In the frequency domain, a prescribed velocity ($v_p$) can be directly interpreted as a prescribed displacement up ($u_p = v_p / i\varphi$), where $\varphi$ is the angular frequency.

The simulations established so far may be applied to any shape and numerous parametric studies to identify the optimal input parameters in the stated set. MRPF's behavior in an external magnetic field is characterized by a B-H curve in the simulation domain. VSM analysis is used to plot M-B curve (Fig. 6.5 (a)), and the B-H curve (Fig. 6.5 (b)) is plotted from M-B curve.

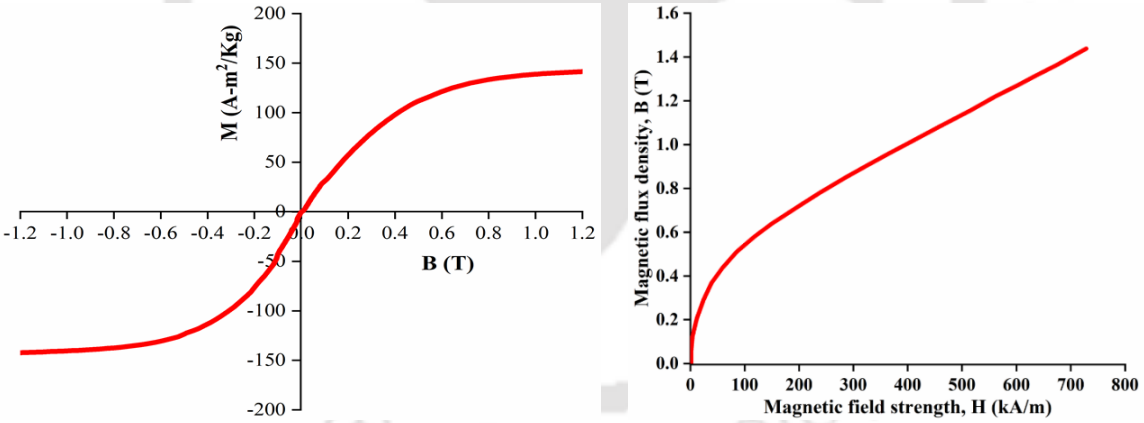


**Fig. 6.5** (a) MB and (b) BH curve of MRP fluid

## 6.3.1 Distribution of Magnetic Flux Density

FEA findings for the variation in the allocation of MFD between the working gap (B'B and A'A) (Fig. 6.4 (b)) of poppet and magnet fixture profiles at positions A, B (Fig. 6.4 (a)) on poppet surface and along the poppet finishing spots (Fig. 6.4 (a)) of the poppet ridge surfaces are demonstrated in Fig. 6.6 (c) and (d), respectively. The maximum MFD at finishing spot-1 and finishing spot-2 along the popper ridge profiles is obtained as 0.20 T and 0.21 T, respectively post magnetostatic FEA, that is good enough for finishing the poppet ridge

profiles. Magnetized CIPs exert forces on the abrasive particles against the poppet component in-between the working gap of magnet fixture and poppet profiles to depress them into the poppet surface consistently. The FEA findings help layout the magnet fixture profiles as the exact replica of the poppet valve ridge profiles, as MFD lines are exactly approaching at required positions along magnet fixture profiles (Fig. 6.6 (b)). These uniform MFD lines at exact desired finishing spots on the magnet fixture profile will bound the MRPF tightly during the rotation of the poppet valve in the CNC spindle so that polishing will take place precisely at the required poppet valve finishing ridge profiles. And also, MRPFs do not segregate towards the wall of the MRPF container. The MFD distributions in the complete domain setup along with MRP fluid using magnetostatic analysis is shown in Fig. 6.6 (a). Further, on the basis of magnetostatic coupled with fluid flow and solid mechanics FE analysis, the appropriate profile region on the poppet ridge surfaces was studied where consistent shear stress and normal stress is acting to finish poppet ridge profiles while the polishing process uniformly. This allows to accomplish the aim of the current investigation like enhancing the poppet profiles surface finish and removing all surface defects, which may further enhance the wear and corrosion resistance and reduce hydrocarbon emissions while the functional use of poppet valves at a maximum temperate.

## 6.3.2 Shear Stress and Normal Stress Distribution

The FEA obtained results for the variation in the distribution of shear stress along the finishing spots of poppet profiles (Fig. 6.4(a)) are shown in Fig. 6.7 (a) and (b), respectively. The maximum shear stress obtained at finishing spot-1 and finishing spot-2 is 47 kPa and 43 kPa, respectively. Maximum shear stress results in a faster material removal rate. Due to the applied field, MR fluid will behave like a Bingham-plastic fluid, and due to the rotation and free boundary surface of the fluid, it will flow and rotate. Because of these circumstances, shear stress will be generated due to the use of external magnetic field [67], [163] and rotation of poppet valve [164]. The viscosity of MR fluid will also depend upon the poppet valve rotation due to the effect of centrifugal force [165] as

$$\eta = \rho_{MRP}\omega^2 r \Big/ \left(\frac{\partial^2 v}{\partial z^2}\right) \tag{6.20}$$

Where, $v$ is the radial velocity of MR fluid, $r$ is radial distance, and $\omega$ is angular velocity. Hence, as the rotational velocity of the poppet valve changes, the viscosity will also change the value of shear stress will also change.

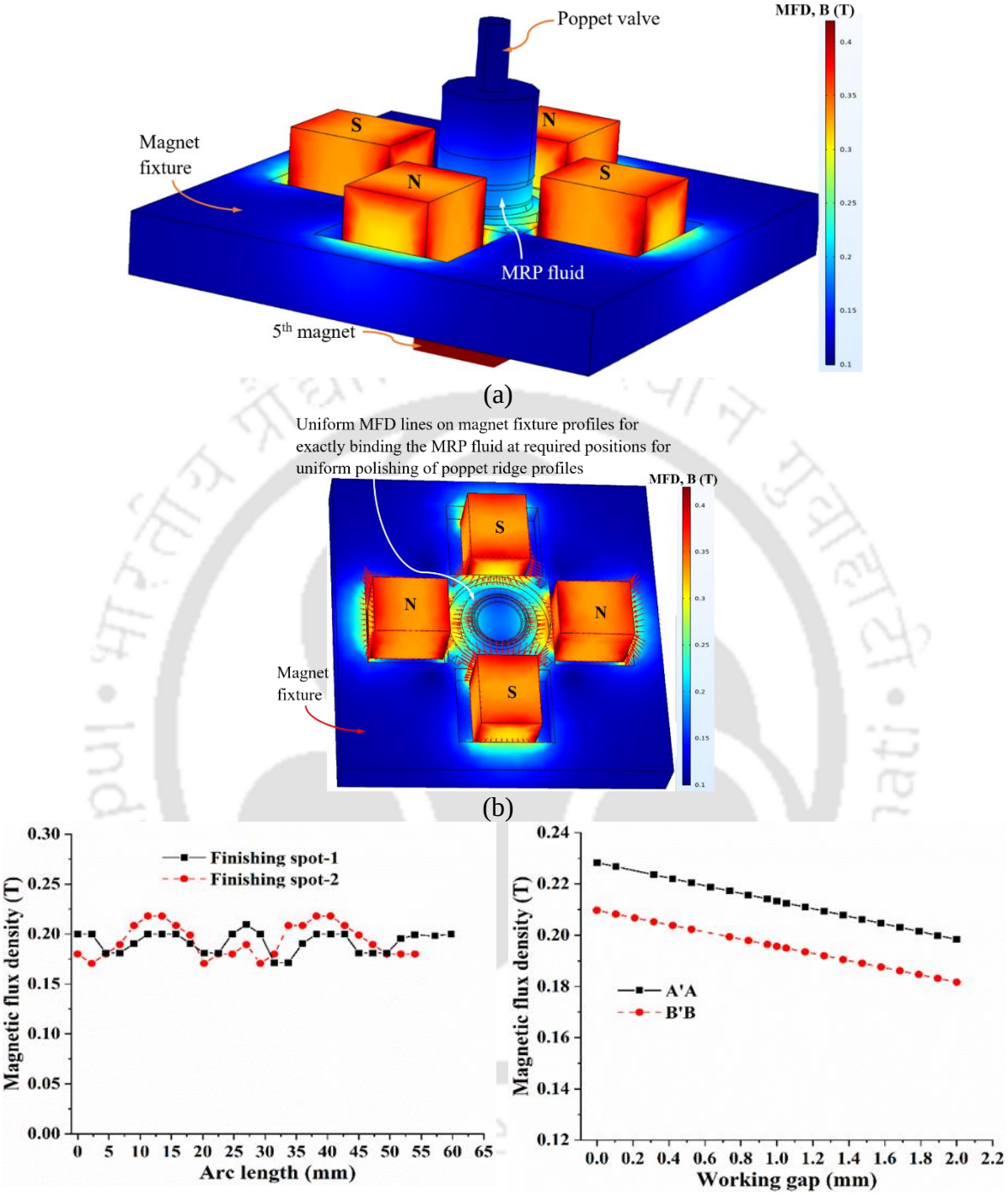


**Fig. 6.6** Distribution of magnetic flux density (a) volume plot at entire computational domain, (b) vector plot at desired finishing spots of magnet-fixture profiles, (c) at poppet ridge profiles along finishing spots-1 & 2 (Fig. 6.4 (a)) and (d) in working gaps B'B & A'A (Fig. 6.4 (b)) between poppet valve and magnet fixture profiles

The FEA obtained results for the variation in the distribution of normal stress along the finishing spots of poppet valve profiles (Fig. 6.4 (b)) are shown in Fig. 6.7 (c) and (d), respectively. The maximum normal stress obtained at finishing spot-1 and finishing spot-2 is

21 Pa and 23 Pa, respectively. The average compressive strain ($\varepsilon_c$) (Eq. (2.16)) increases as the prescribed feed rate of poppet increases; hence normal stress will also increase. Uniform normal stress results in the uniform indentation of abrasive particles pertaining to an equal amount of indentation depth at every poppet profile, thus resulting in uniform material removal from each surface of the poppet profile leading to a uniform surface finish. The study of shear stress on the component surface is most crucial to achieving the required good surface finish.

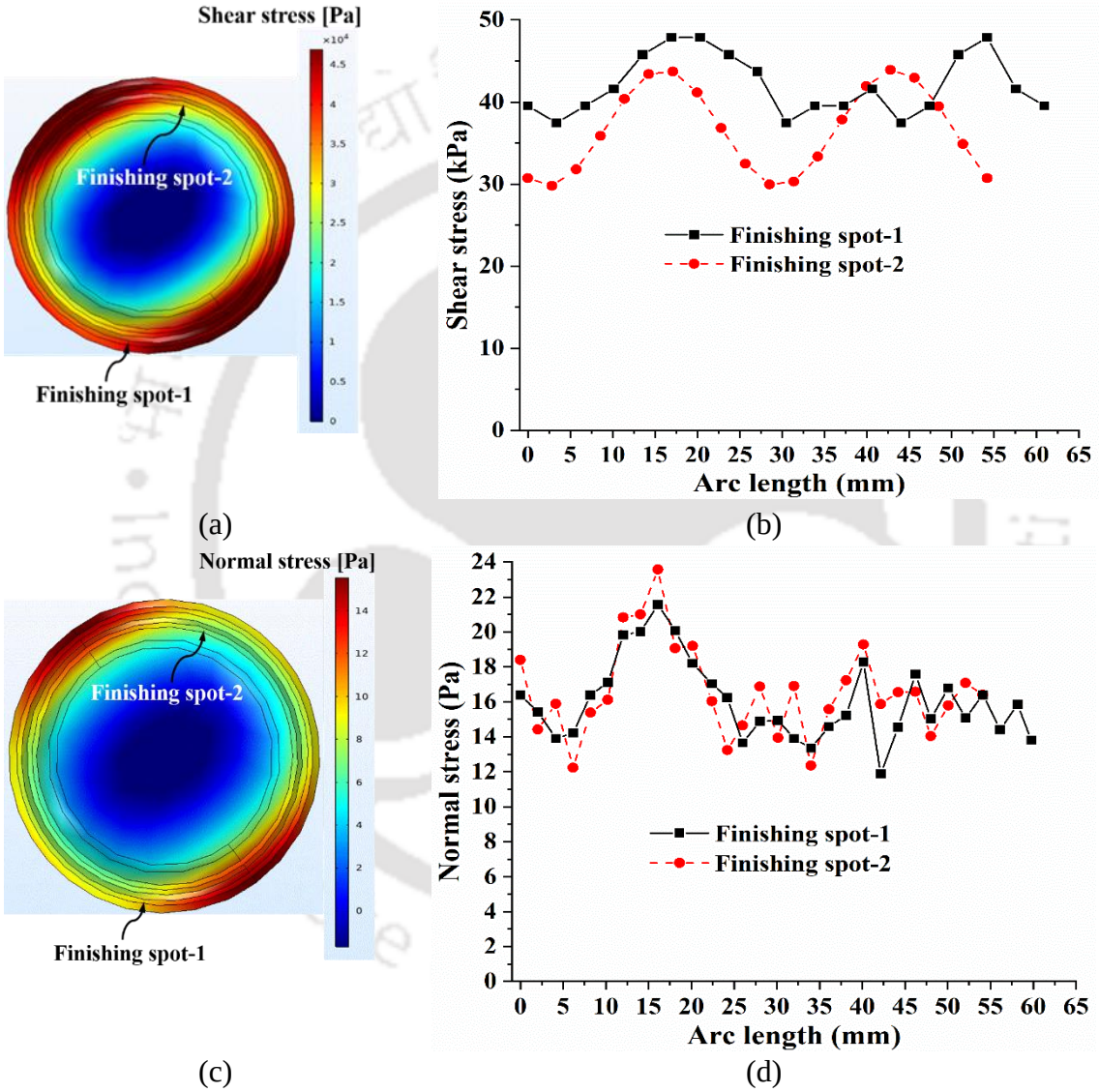


**Fig. 6.7** Volume plot of (a) shear stress and (c) normal stress distribution at ridge profiles; Calculated (b) shear and (d) normal stresses along finishing spots-1 and 2 (Fig. 6.4 (a))

The FEA obtained results for the variation in the distribution of shear stress and normal stress along the finishing spots of poppet valve profiles (Fig. 6.4 (a)) at 1200, 1300 and 1500 rpm of the poppet is demonstrated in Fig. 6.8 (a) and (b), respectively. From the results, it is found that there is the almost same amount of variation is shown at 1200 and 1350 rpm, and the values of

the same type of variation increase (1.8 % increment) at 1500 rpm. However, in actual experiment working condition at 1500 rpm, more vibration of the spindle is taking place, and contact of poppet ridge profiles to stiff MR fluid creates more friction and thus deteriorates the surface quality of poppet profiles, so this 1500 rpm is not considered in modelling of surface finish, force analysis and in the current experiment. And also, tightening the magnet fixture at the milling machining bed at such high speed is a somewhat difficult task even with certain faults; it can harm both poppet and magnet fixture profiles.

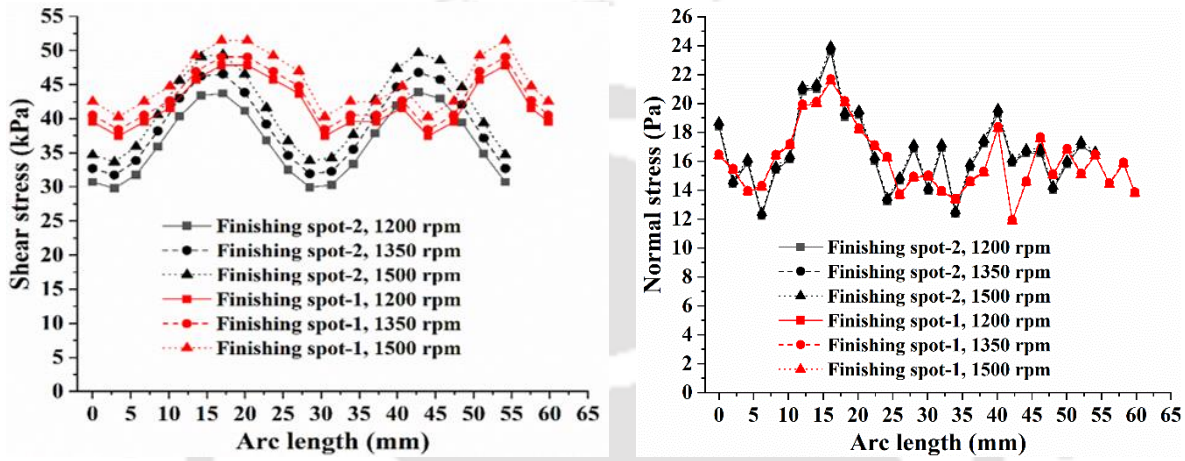


(a) (b)

**Fig. 6.8** (a) Shear stress and (b) normal stress distribution along finishing spots-1 & 2 (Fig. 6.4(a)) of poppet ridge profiles at different poppet rotations (1200, 1350 & 1500 rpm)

# 6.4 Mechanism of Poppet Valve Profile Polishing

The various finishing forces, acting on active abrasives during poppet valve MR finishing, are responsible for eliminating the roughness peaks. These active abrasives cause the indentation into the workpiece surface, and this indentation depth is a function of the normal magnetic force ($F_m$) and other finishing forces. In order to determine the accurate predictive pattern of surface roughness, the mathematical model for the precise estimation of normal finishing forces, total active abrasive particles and indentation depth on the workpiece profile should be developed.

## 6.4.1 Analysis of Finishing Forces

The active forces (Fig. 6.9), which are responsible for material removal, depend upon the ridge profiles of the poppet valve and motions transferred to the MR fluid by poppet. The MR fluid is given a continuous rotating motion through the poppet rotation in the R-MRFF process so

that the approaching active abrasive grains uniformly remove the roughness peaks of the material. The magnetic force presses the abrasives, which are trapped by iron particles into the poppet ridge profiles. The magnetic force, $F_m$, acts on CIPs in a magnetic field is represented by Eq. (6.1) [155].

The variation of magnetic induction or magnetic flux density (B) is only considered in the normal direction to the poppet profiles, and other directions are neglected. Thus, in the working gap (z) from the ridge profiles of poppet to the ridge profiles of magnet fixture, the relation between the magnetic force ($F_m$) and magnetic induction (B) may be regraded for practical use as shown in Eq. (6.21).

$$F_m(z) = m\frac{\chi_m}{\mu_0}B(z)\frac{dB(z)}{dz} \tag{6.21}$$

Here, *B (z)* is the magnetic flux density variation in the working gap (z) varying from 0 to 0.002 m. Mass of magnetic susceptibility $(\chi_m)$ of CIPs is presented in Eq. (6.5). *M* is iron particles magnetization in (A-m$^2$/Kg), and magnitude is evaluated through the M-B curve of MRPF (Fig. 6.5) [157]. B (z) is derived from the FE analysis in-between the working gap A'A (at finishing spot-1), B'B (at finishing spot-2) of poppet and magnet fixture profiles (Fig. 6.4 (b)) represent the magnetic flux density variation in-between the working gap.

$$B_{AA'}(z) = -0.015z + 0.2283 \tag{6.22}$$

$$B_{BB'}(z) = -0.014z + 0.2096 \tag{6.23}$$

In Eq. (6.22) and Eq. (6.23), "z" is in meters varying from 0 to 0.002 m. Differentiating Eq. (6.22) and Eq. (6.23), with respect to z give Eqs. (6.24) and (6.25) as follows.

$$\frac{dB_{AA'}(z)}{dz} = -0.015 \tag{6.24}$$

$$\frac{dB_{BB'}(z)}{dz} = -0.014 \tag{6.25}$$

The positions A and B is taken on poppet ridge profiles to show the calculation for normal magnetic force. In a similar way, at every working gap on the poppet ridge periphery, variation of magnetic flux density distribution can be evaluated to calculate normal magnetic force at different positions of poppet ridge profiles (Fig. 6.4(a)). CIPs help the adjacent active abrasives in indenting the workpiece surfaces [158]. The magnetic force on the CIPs next to active abrasives is calculated using Eqs. (6.21)-(6.25). The calculated magnetic susceptibility $(\chi_m)$ and magnetic force ($F_m$) at various positions on both finishing spots (A to H) (Fig. 6.4 (a)) of poppet ridge profiles is given in Table 6.5.

This magnetic force creates a repulsive levitation effect, which allows SiC abrasive to indent into the ridge profiles of the poppet and can perform better finishing on every surface of the poppet even with strongly bonded CIPs chains. Shear force ($F_s$) created by the poppet valve rotation through the CNC-milling machine spindle is responsible for shearing the material as microchips on the poppet ridge surfaces (Fig. 6.9). This shear force ($F_s$) can be derived from FE analysis.

**Table 6.5** Magnetic force at various positions on poppet valve ridge profiles calculated using Eqs. (6.21)-(6.25)

| **Positions at poppet ridge profiles** | **Magnetic flux Density *B* (T)** | **Mass of magnetic susceptibility** $(\chi_m) \times 10^{-4}$ **(m³/kg)** | **Magnetic force** $(F_m) \times 10^{-11}$ **(N)** |
|---|---|---|---|
| A | 0.1983 | 3.713 | -2.204 |
| B | 0.1816 | 3.635 | -2.019 |
| C | 0.1905 | 3.680 | -1.878 |
| D | 0.1989 | 3.543 | -1.970 |
| E | 0.2010 | 3.706 | -2.154 |
| F | 0.2178 | 3.619 | -2.127 |
| G | 0.1715 | 3.540 | -1.861 |
| H | 0.1850 | 3.541 | -1.994 |

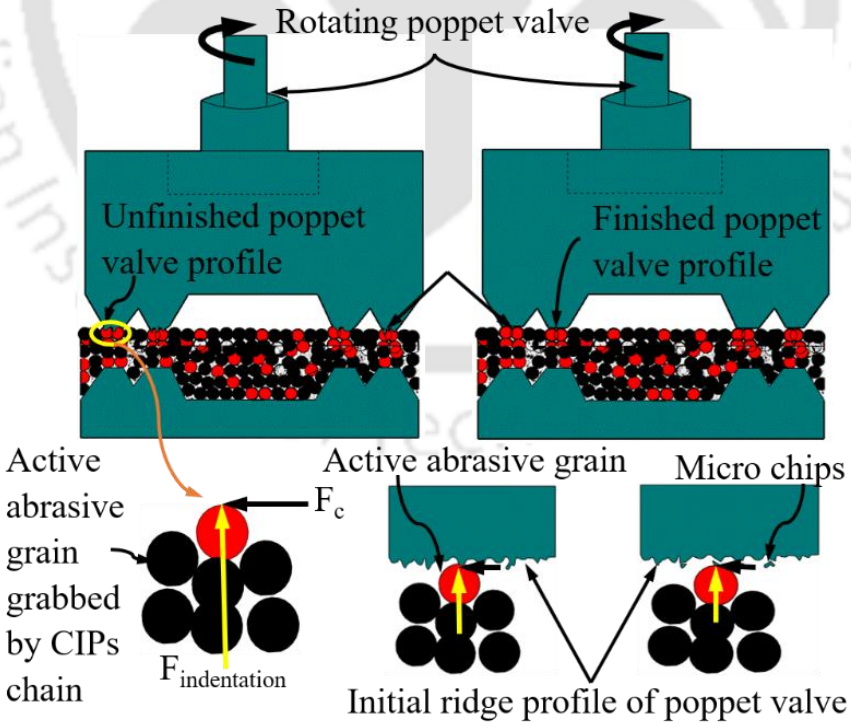


**Fig. 6.9** Forces acting at poppet ridge profiles during finishing

This poppet valve is compressed into MRP fluid ribbon by spindle pressure in an external magnetic field. Thus, the normal force ($F_n$) created by spindle pressure and elastic modulus of MR fluid, allows abrasives to penetrate into the poppet ridge surfaces. The normal force ($F_n$) on projected area ($\pi r \times w$) is given by

$$F_n = \sigma_n \times \pi r \times w \tag{6.26}$$

Where, $\sigma_n$ is normal stress (Pa) obtained using FEA, $r$ is the radius of poppet ridge profiles (m), and $w$ is the width of poppet ridge profiles (m). In this R-MRFF process (Fig. 6.9), abrasive particles also rotate with the rotation of the poppet valve. Because of the rotation of abrasives, a centrifugal force (Eq. (6.11)) will also act. Here, $\omega$ will be *the* rotational speed of the poppet valve. A tangential force (Eq. (6.14)) will also act on the abrasives in the tangent direction of fluid rotation. Where ω and $v$ represent the angular velocity and linear velocity of the abrasives, respectively. By changing the rotational speed of the poppet valve, centrifugal force ($F_{cen}$) and tangential cutting force ($F_t$) also change. The total cutting force, which is responsible for the cutting of asperities of roughness peaks is given by,

$$\vec{F}_c = \vec{F}_s + \vec{F}_{cen} + \vec{F}_t \tag{6.27}$$

The total normal indentation force $(F_{indentation})$ on the active abrasive grains along ridge profiles of poppet (Fig. 6.9) is represented by,

$$\left(\vec{F}_{indentation}\right) = \vec{F}_n + \vec{F}_m \tag{6.28}$$

Here, frictional forces are considered as negligible.

## 6.4.2 Area of Active Abrasive Particles on Poppet Profiles

Using magnet fixture profile (an exact replica of poppet valve profile) gives an almost uniform distribution of active abrasive particles along poppet ride profiles leading to uniform material removal and surface finish. The external magnetic field, developed shear and normal stress from externally applied pressure and rotation of poppet, forms an effective active abrasive particles surface area on the poppet ridge profiles. The effective magnetic flux density along finishing spots (Fig. 6.4(a)) of poppet profiles is almost uniformly distributed all over the surface is displayed in Fig. 6.6 (a). The shear stress and normal stress are also almost uniform and higher in magnitude at finishing spots, enabling smooth indentation of abrasive into poppet surfaces and shear off the materials from these surfaces easily. As total active abrasives are more and uniform so, it will result in fast material removal rate and uniform surface quality at poppet ridge profiles. The area where the active abrasives indent into the workpiece surfaces

by the effect of normal magnetic force and execute polishing by shear forces is regarded as an effective surface area [84]. The active abrasives area on poppet ridge profiles during its surface finishing with the R-MRFF process is shown in Fig. 5.1. During the polishing process of the ridge surfaces of the poppet, the absolute amount of active abrasive particles usable for polishing is determined where the maximum number of abrasive grains contacted to the poppet valve profiles [152]. The maximum abrasive grains touch the poppet profiles at the outermost diameter and are determined by the given below specific equation

$$N_g = \frac{Maximum\ length\ for\ which\ MRPF\ \ in\ contact\ with\ workpiece}{D_g} = \frac{2\pi r}{D_g} \qquad (6.29)$$

Where, $N_g$ is the total amount of active abrasive particles on poppet profiles, $r$ is the radius of poppet ridge profiles, $D_g$ (19 µm) is the diameter of a single active abrasive particle. The absolute amount of the active abrasive particle is calculated for both poppet ridge profiles is given in Table 6.6. The effective surface area remains the same, only the location of active abrasive grains changes while polishing. As the poppet rotates, the inactive abrasives become active.

**Table 6.6** Active abrasive particles on poppet valve ridge profiles

| **Number of active abrasive grains ($N_g$)** | |
|---|---|
| Poppet finishing spot-1 | Poppet finishing spot-2 |
| 3235 | 2898 |

# 6.5 Material Removal Modelling

The normal indentation force ($F_{indentation}$) is responsible for indenting the abrasives into the workpiece surface. The resultant cutting force on the abrasives removes the material from workpiece surfaces in the form of micro-chips. Constant load on each abrasive with a single cutting edge creates equal indentation depth on the workpiece surfaces. The indentation diameter ( $D_i$ ) and depth of indentation ($t$) [146] of an active abrasive particle into the workpiece surfaces is evaluated from the geometry of the Fig. 6.10 and the relation of Brinell hardness number ($H_{BHN}$ = 217 (for gear material) and $H_{BHN}$ = 445 (for poppet material)). The BHN of the machined workpiece is tested in the Brinell hardness tester. The BHN (kgf/mm$^2$) is reconfigured to compute the indentation diameter ($D_i$) is represented in (Eq. (6.30)) [146].

$$D_i = \sqrt{{D_g}^2 - \left( D_g - \frac{2\times10^{-6} F_{indentation}}{9.81 H_{BHN} \pi D_g} \right)^2} \qquad (6.30)$$

where, $D_g$ is the abrasive particle diameter in m and indentation force ($F_{indentation}$) is in N.

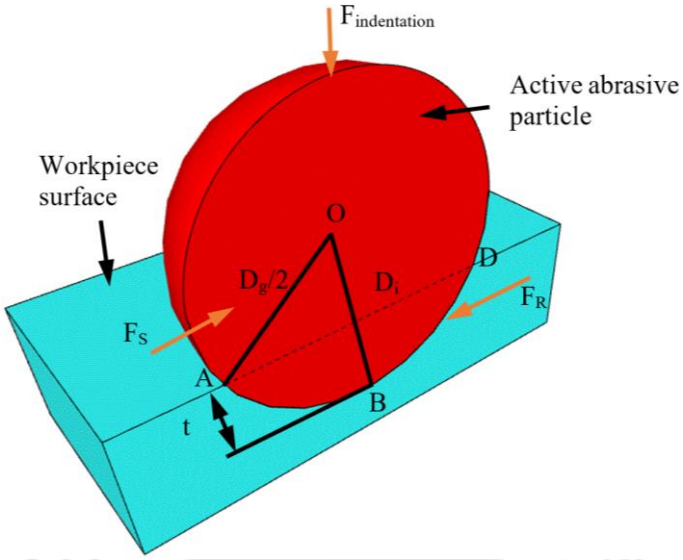


**Fig. 6.10** Cross-sectional view of an active abrasive particle indenting into workpiece surface and forces acting on it during R-MRFF process

**Table 6.7** Calculated normal, centrifugal and tangential forces at different positions of gear tooth profile

| **Positions at gear tooth profile** | **Normal force** $(F_n) \times 10^{-8}$ **(N)** | | **Centrifugal force** $(F_{cen}) \times 10^{-12}$ **(N)** | | **Tangential force** $(F_t) \times 10^{-12}$ **(N)** | |
|---|---|---|---|---|---|---|
| | Uniform flow restrictor | | Uniform flow restrictor | | Uniform flow restrictor | |
| | Without | With | Without | With | Without | With |
| A | 3.423 | 4.286 | 6.462 | 6.462 | 9.712 | 9.957 |
| C | 3.428 | 4.071 | 8.027 | 8.027 | 8.520 | 5.251 |
| E | 3.291 | 3.832 | 8.975 | 8.975 | 15.62 | 16.66 |
| O | 3.145 | 4.669 | 7.975 | 7.975 | 1.329 | 4.091 |

**Table 6.8** Calculated shear force, resistance force, indentation force, and depth of indentation at different positions of gear teeth profile

| **Positions at gear tooth profile** | **Shear force** $(F_s) \times 10^{-5}$ **(N)** | | **Resistance force** $(F_R) \times 10^{-15}$ **(N)** | | **Normal indentation force / SiC abrasive particle** $(F_{indentation}) \times 10^{-8}$ **(N)** | | **Depth of indentation** $(t) \times 10^{-13}$ **(m)** | |
|---|---|---|---|---|---|---|---|---|
| | Uniform flow restictor | | Uniform flow restictor | | Uniform flow restictor | | Uniform flow restictor | |
| | Without | With | Without | With | Without | With | Without | With |
| A | 1.528 | 1.607 | 2.482 | 3.582 | 3.420 | 4.280 | 2.693 | 3.370 |
| C | 1.597 | 1.743 | 2.456 | 3.314 | 3.419 | 4.072 | 2.692 | 3.206 |
| E | 1.761 | 1.821 | 2.346 | 2.976 | 3.290 | 3.834 | 2.590 | 3.019 |
| O | 1.705 | 1.746 | 2.219 | 4.040 | 3.140 | 4.664 | 2.472 | 3.673 |

$$t = \frac{D_g}{2} - \frac{1}{2}\sqrt{D_g{}^2 - D_i{}^2} \tag{6.31}$$

To allow the cutting operation to take place (Fig. 6.10) through the elimination of roughness peaks by an active abrasive on the workpiece surfaces, $F_S$ must be higher than $F_R$. Where, $F_s$ is the shear force applied by the polishing medium on the projected area of the embedded abrasive particle above the workpiece surface (*A-A'*). $F_R$ is the resistance/reaction force acting on the abrasive particle offered by the workpiece material at the embedded portion of the abrasive in the workpiece surface (*A'*). From Fig. 6.10, $F_s$ , $F_R$ and *A'* are given as

$$F_s = \left(A_c - A'\right) \times \tau_y \tag{6.32}$$

$$F_R = A' \times \sigma_y \tag{6.33}$$

$$A' = \frac{D_g{}^2}{4} \times \frac{\pi}{180} \cos^{-1}\left(1 - \frac{2t}{D_g}\right) - \left(\frac{D_g}{2} - t\right)\sqrt{D_g t - t^2} \tag{6.34}$$

Where, $A_c$ is the cross-section area of the spherical abrasive particle, $\sigma_y$ is yield stress of stainless steel (SS316L), and nickel aluminium bronze workpiece in shear 310.5 MPa and 290 MPa, respectively, $\tau_y$ is average MRP fluid shear stress at the workpiece profiles.

**Table 6.9** Calculated normal, centrifugal and tangential forces at different positions of poppet valve profiles

| **Positions at the poppet ridge profile** | **Normal force** $(F_n) \times 10^{-4}$ **(N)** | **Centrifugal force** $(F_{cen}) \times 10^{-9}$ **(N)** | **Tangential force** $(F_t) \times 10^{-7}$ **(N)** |
|---|---|---|---|
| A | 1.685 | 1.787 | 1.903 |
| B | 1.423 | 1.600 | 2.070 |
| C | 1.971 | 1.787 | 2.027 |
| D | 1.682 | 1.600 | 1.999 |
| E | 1.342 | 1.787 | 2.076 |
| F | 1.296 | 1.600 | 1.942 |
| G | 1.374 | 1.787 | 1.895 |
| H | 1.492 | 1.600 | 1.932 |

Table 6.7 represents the calculated values of normal, centrifugal and tangential forces at different positions of the gear profiles. Calculated shear force, resistance force, indentation force and depth of indentation at different positions of gear teeth profile is shown in Table 6.8. Table 6.9 represents the calculated values of normal, centrifugal and tangential forces at different positions of the poppet profiles. Calculated shear force, resistance force, indentation force and depth of indentation at different positions of poppet ridge is shown in Table 6.10.

From magnetostatic fluid flow analysis, the MRP fluid shear stress at the gear surface is calculated, and from magnetostatic fluid-solid interaction analysis, the MRP fluid shear stress at the poppet surface is calculated. Substituting these values into Eqs. (6.32)-(6.34), $F_s$ and $F_R$ are calculated for all gear and poppet ridge surfaces, listed in Table 6.8 and Table 6.10, respectively. Since the magnitude of $F_s$ is much greater than the magnitude of $F_R$, the active abrasive layer on the workpiece surface will easily shear off the roughness peaks. The condition for no cutting is $F_s<F_R$ [84], [166]. In such a condition, rotating abrasive particles adjusts the indentation depth until the necessary resistance ($F_R$) is equivalent to the usable shear force ($F_S$).

**Table 6.10** Calculated shear force, resistance force, indentation force, and depth of indentation at different positions of poppet ridge profiles

| **Positions at the poppet ridge profile** | **Shear force** $(F_s) \times 10^{-5}$ **(N)** | **Resistance force** $(F_R) \times 10^{-8}$ **(N)** | **Normal indentation force / SiC abrasive particle** $(F_{indentation}) \times 10^{-4}$ **(N)** | **Depth of indentation** $(t) \times 10^{-10}$ **(m)** |
|---|---|---|---|---|
| A | 1.181 | 2.771 | 1.681 | 6.461 |
| B | 1.141 | 2.145 | 1.429 | 5.452 |
| C | 1.362 | 3.529 | 1.975 | 7.589 |
| D | 1.245 | 2.768 | 1.685 | 6.452 |
| E | 1.301 | 1.979 | 1.342 | 5.167 |
| F | 1.209 | 1.865 | 1.296 | 4.968 |
| G | 1.124 | 2.036 | 1.371 | 5.252 |
| H | 1.147 | 2.304 | 1.492 | 5.714 |

## 6.6 Surface Roughness Modelling

An optical profilometer is used to take initial surface roughness data in the model. These datas are in the form of ordinates of all sampled points in the profile at equal intervals. After evaluating initial input roughness data, modelling of surface finish is performed. Cutting action will only take place on identified peak points, and each active abrasive particle crossing over the peaks penetrates equally to "*t*". Non-identified peak point will remain as it is for the next cycle.

Also, it is assumed that the cutting occurs from a particular peak with peak height ($h_i$) if the following condition is fulfilled i.e. $h_i > (h_{i,max}-t)$. Therefore, the new height of the $i^{th}$ roughness peak ($h_{i,new}$) will be $h_{i,new} = h_{i,\max} - t$. Where, $h_{i,max}$ is the highest peak height. It is explained schematically in Fig. 6.11 for a few peaks and valleys of the roughness profile. From Fig. 6.11 it can be seen that the new peak heights updated after cutting by one abrasive particle

is given as: $h_b' = h_{i,\max} - t$, $h_c$, $h_e' = h_{i,\max} - t$, $h_f' = h_{i,\max} - t$ and the valleys remain the same as $h_a$, $h_d$ without any update. Surface roughness is measured with respect to the mean line, the region above and below the mean line is identical. After each stroke or rotation, some material is withdrawn from the upper half of the mean line, so the location of the mean line would be changed by (Δh). Thus, the new mean line of roughness profile is estimated after each iteration and the data points are modified accordingly as, $h_{i,new} = h_i - \Delta h$. Where, $h_i$ is the magnitude of the i[th] data point considering all peaks and valleys. The new peak height $h_i'$ after one stroke or rotation with ($N_g$) active particle/stroke or rotation is given by

$$h_i' = h_{i,\max} - N_g t \tag{6.35}$$

If the point is not a peak point in the data file (for example, $h_c$ in Fig. 6.11), then it is transferred to the next profile as it is. New peak points were measured after each stroke or rotation to adjust the peak heights, and modified profile data were passed on for the next stroke or rotation analysis. Eq. (6.36) determines the centre-line-average (CLA) surface roughness value ($R_a$) from profile data points before and after each stroke or rotation.

$$R_a = \frac{\sum_{i=1}^{n} |h_i|}{n} \tag{6.36}$$

where "*n*" is number of data points and $h_i$ is roughness profile height at the data points.

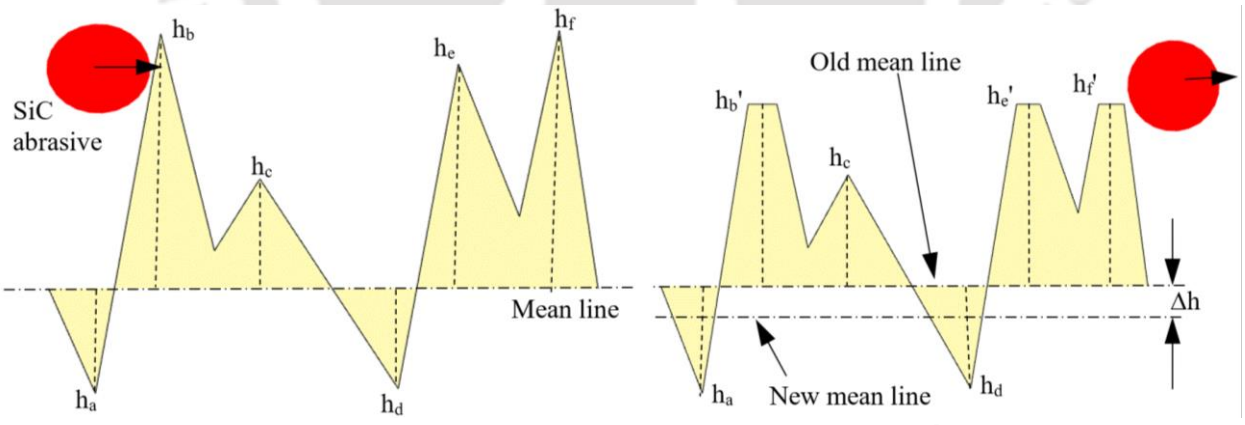


(a) (b)

**Fig. 6.11** (a) Abrasive particles approaching initial peaks/valleys, (b) new peak heights updated after one indentation depth (t). Δh is shifting the position of mean line after each stroke

Code was written as per the steps shown in Fig. 6.12 in "Phython" programming language to evaluate final $R_a$ value based on theoretical indentation values. During the evaluation of roughness values using software (JupyterLab) in the programming language "Phython,"

continuous material removal is assumed to occur until the profile height reaches zero or non-negative, after which no further material removal occurs at that point.

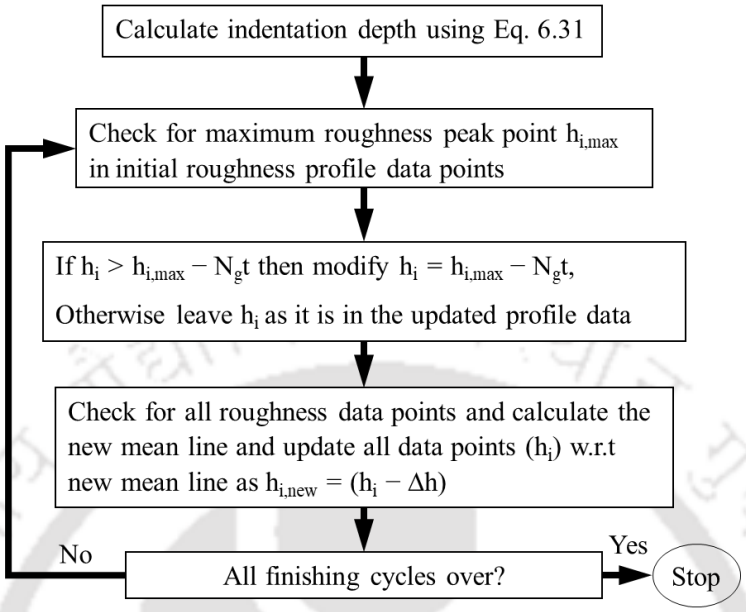


**Fig. 6.12** Algorithm for surface roughness simulation

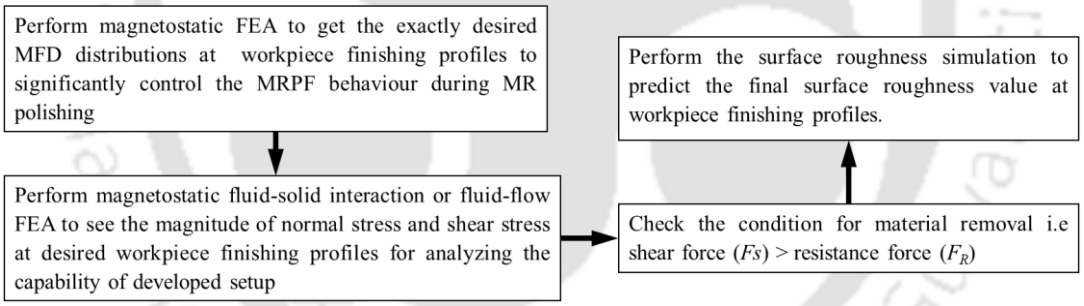


**Fig. 6.13** Steps to find the optimum value of output during R-MRFF simulation

The peak points of simulated roughness profile of miniature gear are plotted in red colour and valley points of roughness peak are plotted in blue colour to clearly identify the cutting of each maximum peak height ($h_{max}$) in reach rotation/stroke. The steps that should be followed to get optimum output in the R-MRFF method is shown in Fig. 6.13. These steps should be performed in the current R-MRFF process to predict the best surface roughness value before experimentation. It will make the process faster and better for MR polishing of poppet valve ridge and miniature gear teeth profiles.

## 6.7 Results and Discussion

Experiments are executed to evaluate the functionality and performance of the novel polishing setup for standardized uniform polishing of the complex miniature gear and poppet profiles. An optical profilometer is used to find the roughness profile of workpiece surfaces. The surface roughness values and material removal rate (MRR) are calculated and validated with the simulated results.

### 6.7.1 Validation of Material Removal Model

The normal magnetic indentation force acting on an active abrasive particle is determined from FE analysis. This force is used to calculate the indentation diameter ($D_i$) and depth of indentation ($t$) created by active abrasive particles into the workpiece surface. Material removal rate (MRR) obtained in the current process for workpiece profile will depend on this depth of indentation ($t$). Based on the magnetostatic fluid flow analysis, the variation of shear stress along the profiles of gear teeth is observed. Using this observation, the number of active abrasive particles impacting the different gear profiles during the finishing process is determined. Finally, based on these outcomes, MRR can be calculated using the Eqs. (6.37) and (6.38).

$$MRR_{theoretical} = \frac{Total\ Volume\ of\ \ material\ removed \times density}{finishing\ \ time} \tag{6.37}$$

And total volume of material dislodged is calculated from Eq. (6.38). The density of SS316L material is 8000000 g/m$^3$. The finishing time is 200 min.

$$Total\ Volume\ of\ \ material\ removed = N_g \times \pi(t^2 \times \frac{D_g}{2} - \frac{t^3}{3}) \times 10 \times 1600 \tag{6.38}$$

Ten is multiplied because there are ten teeth present on miniature gear. In one finishing cycle 2 strokes are present, and so for 800 finishing, 1600 strokes will be used for finishing the miniature gear teeth profiles. The theoretically calculated MRR without and with using flow restrictor is presented in Table 6.11. The material removal rate (MRR) is the absolute quantity of material that is removed per minute. The required time in completion of the desired number of finishing cycle is used to found the MRR. Experimentally, MRR is calculated using Eq. (6.39).

$$MRR_{experimental} = \frac{Initial\ weight - Final\ weight}{finishing\ \ time} \tag{6.39}$$

The experimental MRR obtained without and with using a flow restrictor is presented in Table 6.11. The higher MRR can be achieved using a uniform flow restrictor, as the number of active abrasive particles is higher when using a uniform flow restrictor.

**Table 6.11** Comparison between experimental and simulated MRR for gear finishing

| **MRR from theoretical analysis (g/min)** | | **Experimental MRR (g/min)** | | **% Error** | |
|---|---|---|---|---|---|
| Uniform flow restrictor | | Uniform flow restrictor | | Uniform flow restrictor | |
| Without | With | Without | With | Without | With |
| 0.00071 | 0.00104 | 0.00081 | 0.00118 | 12.3 | 11.5 |

Theoretically MRR can be calculated from using the Eqs. (6.37) and (6.40). Total volume of material dislodged is calculated from Eq. (6.40). Density of Nickel-Al-Bronze alloy material is 7600000 g/m$^3$. Finishing time is 100 min.

$$Total\ Volume\ of\ material\ removed = N_g \times \pi(t^2 \times \frac{D_g}{2} - \frac{t^3}{3}) \times 1200 \times 100 \qquad (6.40)$$

Here, 120000 is multiplied in the above equation because this much amount of revolution will poppet valve cover before completing the finishing cycle. The theoretically calculated MRR is presented in Table 6.12.

The material removal for Nickel-Al-Bronze poppet valve was determined depending on the mesh size of abrasive particle and total rotations of poppet valve. Material removal is amount of material that is dislodged per minute. The required time in completion of the desired number of finishing rotations is used to found the MRR experimentally (Table 6.12).

**Table 6.12** Comparison between experimental and simulated MRR for poppet valve finishing

| **Total MRR from theoretical analysis (g/min) for poppet finishing profiles** | **Experimental MRR (g/min) for poppet finishing profiles** | **% Error** |
|---|---|---|
| 0.0115 | 0.0132 | 12.87 |

## 6.7.2 Validation of Simulated Roughness Values

After using the novel uniform flow restrictor and workpiece fixture, the surface roughness parameters were evaluated for the gear teeth profiles. Gear teeth profiles were finished with MR polishing fluid. After finishing with the novel workpiece fixture, without and with using a

uniform flow restrictor, the minimum surface roughness ($R_a$) for the involute profile of gear tooth was decreased to 34.3 nm (Fig. 6.14 (a)) and 24.5 nm (Fig. 6.14 (c)) respectively from the original value of 265 nm. From the obtained experimental and simulated roughness value, 8.57 % error was observed on the tooth involute profile with using uniform flow restrictor. For all other profiles of gear teeth, similar initial and final simulated and experimental roughness values with 800 finishing cycles obtained are presented in Table 6.13. The results demonstrate that nearly all parts of the teeth profiles have shown the uniform value of surface roughness using a uniform flow restrictor. This significant uniform decrease of roughness values on the gear teeth profiles indicates that the novel uniform flow restrictor and workpiece fixture are capable of producing a uniform fine surface finish. The magnetic fixture is rotating, and extrusion pressure is applied to MR polishing media as a result abrasive particle will cut the peaks of roughness profile by sliding and rotating action.

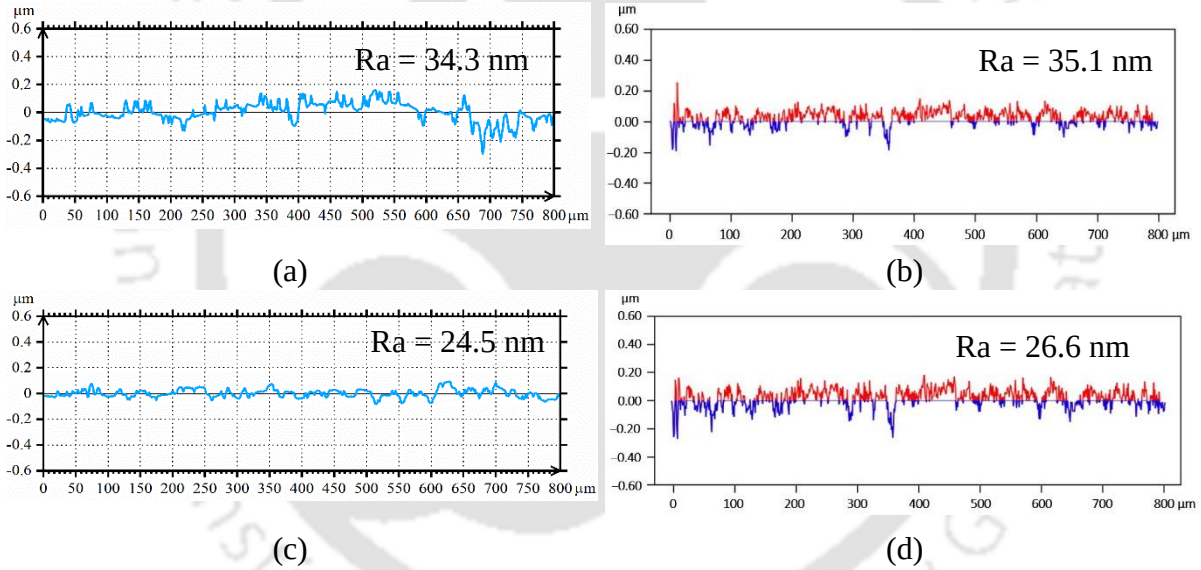


**Fig. 6.14** Surface roughness profiles of gear tooth involute profile from (a) experiment and (b) simulation after finishing without uniform flow restrictor; Roughness profiles with uniform flow restrictor from (c) experiment and (d) simulation

**Table 6.13** Comparison between simulated and experimental surface roughness values at different gear tooth profiles for 800 finishing cycles

| **Gear tooth profiles** | **Initial Ra (nm)** | **Experimental $R_a$ (nm)** | | **Simulated $R_a$ (nm)** | | **% Error** | |
|---|---|---|---|---|---|---|---|
| | | Uniform flow restrictor | | Uniform flow restrictor | | Uniform flow restrictor | |
| | | Without | With | Without | With | Without | With |
| In-between | 264 | 22.1 | 24.3 | 20.5 | 25.3 | 7.23 | 4.11 |
| Involute | 265 | 34.3 | 24.5 | 35.1 | 26.6 | 2.33 | 8.57 |
| Top | 252 | 46.5 | 23.9 | 40.2 | 24.71 | 13.54 | 3.38 |
| Face | 259 | 19.6 | 25.2 | 18.7 | 26.2 | 4.59 | 3.96 |

After using the novel magnet fixture, the surface roughness parameters were evaluated for the poppet profile. Poppet valve profiles were finished with MRP fluid. The surface roughness parameter (Ra) on both poppet ridge profiles before finishing was found almost equal as 320 nm, as shown in Fig. 6.15 (b). After finishing with the novel magnet fixture, the minimum surface roughness (Ra) for the poppet profile was decreased to 20.1 nm (Fig. 6.15 (a)) on finishing ridge profile-1 of the poppet valve from the original value of 320 nm.

From the obtained experimental and simulated roughness values, a maximum 11.5 % error (Fig. 6.15 (b)) was observed on the finishing spot-1 (Fig. 6.4 (a)) of the poppet valve profile. The results demonstrate that both poppet valve ridge profiles have shown the uniform value of surface roughness. This significant uniform decrease of roughness values on the poppet profiles indicates that the novel magnet fixture is capable of producing a uniform fine surface finish. The roughness peaks have been adjusted to the flat smooth surface following the completion of several MR finishing rotations on the poppet ridge profiles.

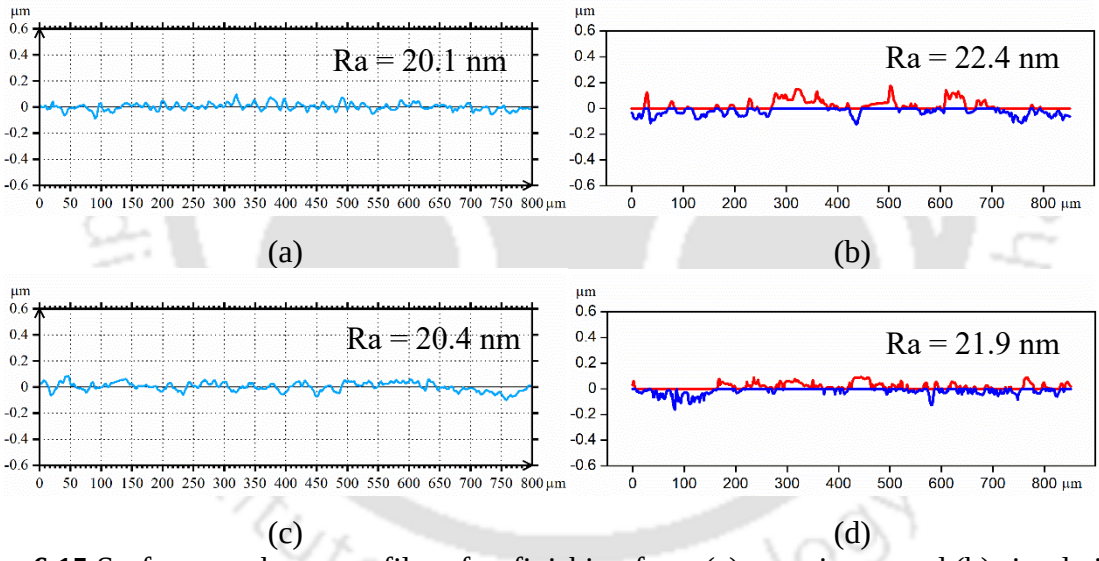


**Fig. 6.15** Surface roughness profiles after finishing from (a) experiment and (b) simulation at finishing spot-1, from (c) experiment and (d) simulation at finishing spot-2

## 6.8 Summary

The effectiveness of the novel R-MRFF setups is confirmed experimentally and theoretically while finishing complex profiles of poppet valve and miniature gear. The magnetostatic fluid flow FE analysis shows that a novel flow restrictor can polish the miniature gear profiles uniformly. The active abrasive particles become more uniformly distributed throughout the gear profiles while using a flow restrictor. The surface roughness of the involute gear profile

is reduced significantly to 24.5 nm from its initial surface roughness value of 265 nm using a flow restrictor in R-MRFF setup. An error of 8.57% was observed using a uniform flow restrictor between experimentally measured and simulated roughness values on gear tooth involute profile. The magnetostatic fluid-solid interaction using FE analysis shows that the novel magnet fixture can uniformly finish the poppet valve ridge profiles. The magnetic flux density and shear stress distributions are uniform and higher in magnitude at required finishing profiles. On these profiles, active abrasive particles become more effective. The surface roughness of the poppet valve profiles is reduced significantly to 20.1 nm from its initial value of 320 nm using R-MRFF process. An error of 11.5 % between experimentally measured and simulated Ra is obtained at the poppet ridge profiles. The number of active abrasives for each rotation of the poppet is uniform, resulting in faster material removal and uniform surface finish.

# Chapter 7 Conclusions and Scope for Future Work

## 7.1 Conclusions

In the present work, the rotational magnetorheological fluid-based finishing (R-MRFF) process is used to finish the complex profiles of miniature gear and poppet valve. For finishing miniature gear, a novel flow restrictor and workpiece fixture, and for finishing of poppet valve, a novel magnet fixture is designed and developed. Preliminary experimental investigations are carried out to explore the capability of the developed R-MRFF setups to find out appropriate MR fluid composition and process parameters while finishing both miniature gear teeth and poppet valve ridge profiles. Further, statistical design of experiments are performed to find the optimum process parameters and their contribution output responses for uniform nano-scale finishing. Also, surface roughness simulation is performed using analysis of finishing force and outcomes of finite element analysis. Following conclusions are drawn from the work reported in the thesis.

### 7.1.1 Miniature Gear

#### 7.1.1.1 Flow Restrictor and Workpiece Fixture Development

A novel flow restrictor and workpiece fixture are designed and developed to finish miniature gear teeth profiles. Magnetostatic fluid-flow finite element analysis (FEA) is performed to see the capability of developed flow restrictor for achieving better finishing characteristics. The conclusions drawn from this study are as follows:

- A novel uniform flow restrictor (exact negative replica of miniature gear) and gear workpiece fixture for the R-MRFF process are developed based on uniform magnetic flux density distribution, normal and shear stress values on gear teeth profiles.
- Uniform shear stress distributions help active abrasives to consistently cut the roughness peaks, with the MRP fluid having both rotating and reciprocating motions. Achieving uniform shear stress values on gear teeth profiles is crucial for uniform surface finishing.

- The magnetic flux density measured (from magnetostatic FEA) at in-between, involute, top, and face profiles of gear tooth are 0.17 T, 0.21 T, 0.22 T, and 0.24 T, respectively, after, which is sufficient enough to carry out the finishing operation.
- Maximum shear stress along gear profiles for magnetorheological finishing of gear component without and with using flow restrictor is 64 kPa and 58 kPa, respectively.
- Maximum normal stress along gear profiles for magnetorheological finishing of gear component without and with utilizing flow restrictor is 130 Pa and 155 Pa, respectively.
- The shear stress and normal stress variation along gear profiles are almost static when a flow restrictor is used. It helps in getting the uniform surface finishing across miniature gear profiles.
- The gap increment between each gear tooth and flow restrictor profiles after MR finishing is uniform, implying uniform material removal and surface finish.

#### 7.1.1.2 Synthesis of Optimum MR Fluid

Three types of MR fluids are synthesized to generate different types of surfaces. All three synthesized MR fluids consist of varying mesh sizes of iron particles (IPs) and SiC abrasive powder (mesh size 800) in an oil-based medium. Base medium has different concentrations of grease and paraffin oil. The generated surface morphologies are studied and analyzed. The conclusions drawn from this study are reported as follows:

- The IPs of mesh size 250 are used in MR fluid of Type – I. There was almost no improvement in observed surface characteristics. However, the improvement in surface roughness was observed as 31.50 % using a flow restrictor.
- In MR fluid of Type – I, iron particles size is much more than abrasive particles size. Hence, the abrasives cannot make effective contact with the gear profiles, which makes MR fluid of Type – I ineffective even after 800 finishing cycles.
- The IPs of mesh size 400 are used in MR fluid of Type – II. Some improvement in surface characteristics was observed. However, the recast layer and pits were still identified on gear teeth profiles. The improvement in surface roughness was observed as 71.84 % using flow restrictor after 800 finishing cycles.
- The IPs of mesh size 800 are used in MR fluid of Type – III. A fine, smooth, and uniform surface finish was observed with almost no surface defects when finished using flow restrictor. However, a small number of micro-cracks and pits were observed on miniature gear teeth profiles when finished without a uniform flow restrictor. It was

also observed that the sides of the tooth became little bit round, which helps in dislodging the burrs, pits, and other undesired features from the working surfaces.

- The improvement in surface roughness was observed as 90.75 % using flow restrictor and MR fluid of Type – III after 800 finishing cycles. Since, in MR fluid of Type – III, iron and abrasive particles are of the same size, which helps the abrasives to have effective contact with the gear profiles achieving highly uniform finishing.
- Uniform surface roughness values are achieved at each miniature gear tooth profile with different types of MR fluid at each stage while using a uniform flow restrictor. Also, a minimum value of surface roughness is achieved while using Type – III MR fluid.

### 7.1.1.3 Finishing of Miniature Gear Teeth Profiles

The capability of the R-MRFF process to deliver nano-scale surface finish for various gear teeth profiles is analyzed using different surface characterization techniques. An optimization study is carried out to minimize the value of surface roughness and maximize the material removal rate (MRR). A statistical analysis is conducted to evaluate the significance of each process parameter. Following conclusions are drawn from the present study.

- The final roughness values (Ra) measured at in-between, involute, top, and face profiles of miniature gear teeth using uniform flow restrictor are 24.3 nm, 24.5 nm, 23.9 nm, and 25.2 nm, respectively. These Ra values without using a uniform flow restrictor are 22.1 nm, 34.3 nm, 46.5 nm, and 19.6 nm, respectively.
- A small amount of tooth deformation was observed when finished without a uniform flow restrictor; however, no tooth deformation was observed while using a uniform flow restrictor.
- The value of the optimized process parameters, i.e., a volumetric proportion of IPs/SiC abrasives, extrusion pressure, and rotational speed of magnets, are 1.5, 35 bar, and 109 rpm, respectively, achieving 90.75 % improvement in Ra and 0.00118 g/min of MRR.
- The maximum error between predicted and validation-experimental results for % $\Delta$Ra and MRR are less than 10 %, which depicts the feasibility of the proposed model.
- A combination of low extrusion pressure and high rpm of the magnets is more favourable to achieve a higher MRR. In contrast, a combination of low volumetric proportion of iron/abrasive particles and higher rpm of magnets causes a higher improvement in surface finish.

- An increase in extrusion pressure and rpm of the magnets significantly increases the MRR. In contrast, only a marginal increase in MRR was observed with an increase in Vol. ratio of IP/SiC up to 1.6, beyond which MRR tends to decrease.
- The abrasion and ploughing action on the SS316L are the dominant mechanisms of material removal on gear teeth profiles while finishing by R-MRFF process.
- The consistent restricted space between flow restrictor and gear creates a uniform channel for flowing MRP media, which leads to a super smooth uniform surface finish.
- To achieve a surface finish below 30 nm on SS316L miniature gear profiles, the Vol. ratio of IPs/SiC, extrusion pressure, and rotational speed of magnets should be in the range of 1.5 – 2.5, 30 – 35 bar, and 90 – 120 rpm, respectively.
- The optimum number of finishing cycles is 800. Furthermore, after 800 finishing cycles, no improvement in surface roughness was observed, as the sharp edge of the abrasives became blunt and ineffective. Even in some cases, the surface roughness of the workpiece again increases due to the ploughing of abrasive particles on the already finished workpiece surface.

#### 7.1.1.4 Finishing Force and Surface Roughness Analysis

The finishing forces involved in the present R-MRFF process are analyzed to better understand and precisely control the process. Also, the surface roughness simulation study is carried out using finishing force analysis and FEA findings. Validation experiments are conducted to substantiate the simulation study. A material removal model using a single abrasive particle is formulated to predict material dislodgement during MR finishing. Following conclusions are drawn from the present study.

- Magnetic and shear forces are considered as the main component of normal indentation force ($F_{indentation}$) and cutting force ($F_c$), respectively. Normal indentation force is responsible for the indentation of abrasive particles on the workpiece surface. Cutting fore is responsible for shearing of the indented materials from the workpiece surface. Based on FE analysis, different values of normal indentation and cutting forces are observed on different teeth profiles.
- The normal indentation force $(F_{indentation})_i$ acting along the tooth top, involute, and in-between-teeth profiles is the resultant of normal force ($F_n$), magnetic force ($F_m$) and

centrifugal force ($F_{cen}$). The normal indentation force $(F_{indentation})_f$ acting along the tooth face profile of gear is the resultant of normal force ($F_n$) and magnetic force ($F_m$).

- The total cutting force $(F_c)_i$ acting along the tooth top, involute and in-between-teeth profiles is the resultant of shear force ($F_s$ ) and tangential force ($F_t$). The total cutting force $(F_c)_f$ acting along the tooth face profile of the gear is the resultant of shear force ($F_s$), tangential force ($F_t$), and centrifugal force ($F_{cen}$).
- The maximum percentage error between experimental and simulated MRR and surface roughness while using flow restrictor is 11.5% and 8.57%, respectively, which is marginal.
- From FEA analysis, it has been observed that the number of active abrasives that take part in the finishing action is more than those without flow restrictor. It results in high MRR and a higly uniform surface finish while using a flow restrictor.

## 7.1.2 Poppet Valve

### 7.1.2.1 Magnet Fixture Development

A novel magnet fixture is designed and developed to finish complex narrow ridge profiles of the poppet valve. Magnetostatic FEA is performed to observe the magnetic flux density distributions along finishing profiles for achieving better finishing characteristics. The conclusions drawn from this study are as follows:

- A novel magnet fixture for the R-MRFF process is developed based on the uniform magnetic flux distributions along the poppet's finishing profiles.
- The required magnetic flux density values at the centre and finishing spots bound the MR fluid in the finishing zone without segregating towards the MRPF wall container, also not leaving the finishing zone during poppet valve rotation. These conditions help uniform polishing across poppet valve profiles.
- The optimum magnetic flux density at the finishing spots and centre of the magnet fixture is obtained as 0.23 T and 0.17 T, respectively, sufficient for polishing the poppet ridges.
- Aluminium is considered to fabricate the magnet fixture due to its non-magnetic property, and it does not restrict / interfare with the movement of MRP fluid.

- The poppet valve is provided with a vertical feed in the downward direction to make the process faster. The optimum gap between the magnet fixture and poppet valve profile is 2 mm, and it is filled with MR fluid.
- The error between the simulated (Ansys®) and measured (digital Gauss-meter, probe placed at 45º angle) magnetic flux density is less than 8%, which is in a reasonable range.

### 7.1.2.2 Synthesis of Optimum MR Fluid

Three types of MR fluids are synthesized to generate different types of surfaces. The generated surface morphologies are studied and analyzed. For finishing the poppet valve profiles on required positions, the effectiveness of the designed fixture is confirmed experimentally. The conclusions drawn from the present study are as follows:

- In an acid-based medium, all three MR fluids consist of carbonyl iron particles (CIPs) and SiC abrasive powder. Base medium constituents of MR fluid of Type – 1 is hydrofluoric acid (HF), nitric acid ($HNO_3$) and deionized water. In the case of MR fluid of Type – 2, the base medium consists of nitric acid ($HNO_3$), hydrogen peroxide ($H_2O_2$) and deionized water. The base medium of MR fluid of Type – 3 consists of hydrogen peroxide ($H_2O_2$) and deionized water.
- Type – 1 MRP fluid damaged the surface due to the formation of Copper (II) fluoride ($CuF_2$). And the surface roughness (Ra) value is increased to 1640 nm from its initial 320 nm.
- After reaction of Type – 2 MR fluid with poppet valve material, Copper (II) nitrate ($CuNO_3$) forms, which is works as a polishing agent. Using Type – 2 MR fluid, the minimum surface roughness of 20.1 nm is achieved. The quality of the poppet surface has been improved considerably with no surface defects.
- A highly uniform surface finish on the poppet is achieved with both Type – 2 and Type – 3 of MRP fluids at each rotation cycle level using a novel magnet fixture.
- Type – 2 MRP fluid provides the best result with minimum surface roughness value; however, Type – 3 has promoted more oxide layer formation on poppet valve profiles. The oxide layer formation prevents corrosion avoiding further reaction of poppet valve profiles.

### 7.1.2.3 Finishing of Poppet Valve Ridge Profiles

The capability of the R-MRFF process to deliver nano-scale surface finish for poppet valve ridge profiles is analyzed using different surface characterization techniques. An optimization study is carried out to minimize the value of surface roughness. A stastical analysis is conducted to evaluate the significance of each process parameter. Following conclusions are drawn from the present study.

- The final roughness (Ra) value on finishing profiles -1 and -2 of the poppet valve is achieved as 20.1 nm and 20.4 nm, respectively.
- Uniform fine surface finish has been achieved after 1 hr. 40 minutes of finishing cycles.
- The optimized process parameters, i.e. rotational speed of poppet valve (N = 900 rpm), vertical feed rate of poppet valve (F = 0.01 mm/min), CIPs volume fraction (C = 35%), and abrasives volume fraction (A = 7%), respectively gives 93.25 % improvement in Ra.
- The observed error between validation experiments and predicted (from ANOVA) % ΔRa is less than 10 %, which shows the accuracy of the currently developed model.
- A combination of the lower feed rate and a high rpm of the poppet valve is more advantageous for obtaining higher % ΔRa in minimum time.
- To achieve a surface finish below 30 nm on Ni-Al-Bronze alloy poppet valve profiles, the rotational speed of poppet valve, vertical feed rate of the poppet valve, CIPs volume fraction, and abrasives volume fraction should be in the range of 800 – 1000 rpm, 0.005– 0.011 mm/min, 30 – 37 %, and 6 – 8 %, respectively.

### 7.1.2.4 Finishing Force and Surface Roughness Analysis

The finishing forces involved in the present R-MRFF process are analyzed to better understand and precisely control the process. The magnetostatic fluid-solid interaction is implemented FEA to see the capability of the developed fixture. The surface roughness simulation study is also carried out using finishing force analysis and FEA findings. Validation experiments are conducted to substantiate the simulation study. A material removal model is formulated to predict material dislodgement during MR finishing using a single abrasive particle. Following conclusions are drawn from the present study.

- Normal indentation force ($F_{indentation}$) is responsible for the indentation of abrasive particles on the workpiece surface. Cutting fore ($F_c$) is responsible for the shearing of the indented materials from the workpiece surface. Magnetic force is considered the

main component of normal indentation force, and shear force is considered the main component of cutting force.

- The normal indentation force $(F_{indentation})_i$ acting along the poppet valve profile is a resultant of normal force ($F_n$) and magnetic force ($F_m$).
- The total cutting force $(F_c)_i$ acting along the poppet valve profile is the resultant of shear force ($F_s$ ), tangential force ($F_t$), and centrifugal force ($F_{cen}$).
- The maximum shear stresses obtained from FEA at finishing spots 1 and 2 are 47 kPa and 43 kPa, respectively. Also, the maximum normal stress obtained at finishing spots 1 and 2 are 21 Pa and 23 Pa, respectively.
- The % error between experimental and simulated MRR and surface roughness values of poppet valve profiles are 12.87% and 11.5%, respectivel, which is marginal.
- Uniform magnetic flux density, normal stress and shear stress distributions in the target region make active abrasive particles uniformly distributed along the workpiece profile. These active abrasives uniformly indent into workpiece finishing profiles and shear off the undulations of the workpiece profile to get uniform finishing.

## 7.2 Scope for Future Work

- During experimentation on miniature gear teeth profiles, it was found that a sealing mechanism is required to prevent MR fluid leakage from R-MRFF setup. At higher rpm, the magnet fixture starts vibrating, decreasing finishing efficiency. So, a more robust R-MRFF setup can be further developed to avoid leakage and vibration associated with the existing setup.
- A new R-MRFF setup can be designed, where MR fluid will rest, and the gear will reciprocate and rotate inside MR fluid to make the process completely leak-proof and flexible.
- Further investigations with other types of flow restrictors can be studied to check the effect of MR fluid behaviour.
- The MR fluid delivery system can be further automated to make it precise and controllable at the finishing zone with in-situ MR fluid conditioning during poppet valve finishing.

- The MR fluid behaviour during the R-MRFF process can be further modelled considering turbulent flow medium and time-dependent study to understand the process mechanism better.
- The R-MRFF process can be further optimized and automated using artificial intelligence.
- An in-depth tribological study can be performed to analyze the performance of polished miniature gear and poppet valve profiles using R-MRFF process.
- The present poppet valve MR finishing method can also be further applied for other types of poppet valves (tulip, mushroom, rigid, etc.), spool and rotary valves, and any complex components with narrow profiles having a cylindrical head.

# References


[1] "What is Surface Finish and Surface Roughness?," *extrudesign.com*, 2018. [Online]. Available: https://extrudesign.com/.

[2] Y. Mizugaki, M. Sakamoto, K. Kamijo, and N. Taniguchi, "Development of Metal-Mold Polishing Robot System with Contact Pressure Control Using CAD/CAM Data," *CIRP Ann. - Manuf. Technol.*, vol. 39, no. 1, pp. 523–526, 1990.

[3] H. Huang, Z. M. Gong, X. Q. Chen, and L. Zhou, "Robotic grinding and polishing for turbine-vane overhaul," *J. Mater. Process. Technol.*, vol. 127, no. 2, pp. 140–145, 2002.

[4] F. J. Shiou, C. C. A. Chen, and W. T. Li, "Automated surface finishing of plastic injection mold steel with spherical grinding and ball burnishing processes," *Int. J. Adv. Manuf. Technol.*, vol. 28, no. 1–2, pp. 61–66, 2006.

[5] H. Weule, S. Timmermann, and W. Eversheim, "Automation of the Surface Finishing in the Manufacturing of Dies and Molds," *CIRP Ann. - Manuf. Technol.*, vol. 39, no. 1, pp. 299–303, 1990.

[6] B. Nowicki and M. Szafarczyk, "The new method of freeforms surface honing," *CIRP Ann. - Manuf. Technol.*, vol. 42, no. 1, pp. 425–428, Jan. 1993.

[7] L. Nagdeve, V. K. Jain, and J. Ramkumar, "Nanofinishing of freeform/sculptured surfaces: state-of-the-art," *J. Manuf. Rev.*, vol. 6, no. 3, pp. 1–20, 2018.

[8] J. Masseth and M. Kolivand, "Lapping and superfinishing effects on hypoid gears surface finish and transmission errors," *2007 Proc. ASME Int. Des. Eng. Tech. Conf. Comput. Inf. Eng. Conf.*, vol. 7, no. 4, pp. 759–765, 2008.

[9] S. M. Fulmali and R. B. Chadge, "Need of Lapping Machine for Valve Component: A Case Study," *Int. J. Mod. Eng. Res. www.ijmer.com*, vol. 2, no. 6, pp. 4609–4612, 2012.

[10] L. Rhoades, "Abrasive flow machining: a case study," *J. Mater. Process. Tech.*, vol. 28, no. 1–2, pp. 107–116, 1991.

[11] R. E. Williams, D. F. Walczyk, and H. T. Dang, "Using abrasive flow machining to seal and finish conformal channels in laminated tooling," *Rapid Prototyp. J.*, vol. 13, no. 2, pp. 64–75, 2007.

[12] T. R. Loveless, R. E. Williams, and K. P. Rajurkar, "A study of the effects of abrasive-flow finishing on various machined surfaces," *J. Mater. Process. Tech.*, vol. 47, no. 1–2, pp. 133–151, 1994.

[13] J. Kenda, F. Pušavec, and J. Kopac, "Modeling and energy efficiency of abrasive flow machining on tooling industry case study," *Procedia CIRP*, vol. 13, no. 5, pp. 13–18, 2014.

[14] G. W. Chang, B. H. Yan, and R. T. Hsu, "Study on cylindrical magnetic abrasive finishing using unbonded magnetic abrasives," *Int. J. Mach. Tools Manuf.*, vol. 42, no. 5, pp. 575–583, Apr. 2002.

[15] B. H. Yan, Y. C. Lin, and F. Y. Huang, "Development of magneto abrasive flow machining process," *Int. J. Mach. Tools Manuf.*, vol. 42, no. 8, pp. 953–959, Jun. 2002.

[16] S. Singh, H. S. Shan, and P. Kumar, "Wear behavior of materials in magnetically assisted abrasive flow machining," *J. Mater. Process. Technol.*, vol. 128, no. 1–3, pp. 155–161, Oct. 2002.

[17] P. Singh, L. Singh, and S. Singh, "Manufacturing and performance analysis of mechanically alloyed magnetic abrasives for magneto abrasive flow finishing," *J. Manuf. Process.*, vol. 50, pp. 161–169, Feb. 2020.

[18] N. Saka, T. Eusner, and J. H. Chun, "Nano-scale scratching in chemical-mechanical polishing," *CIRP Ann. - Manuf. Technol.*, vol. 57, no. 1, pp. 341–344, Jan. 2008.

[19] Y. Tani, K. Kawata, and K. Nakayama, "Development of High-Efficient Fine Finishing

Process Using Magnetic Fluid," *CIRP Ann. - Manuf. Technol.*, vol. 33, no. 1, pp. 217–220, Jan. 1984.
[20] S. Gao, H. Huang, X. Zhu, and R. Kang, "Surface integrity and removal mechanism of silicon wafers in chemo-mechanical grinding using a newly developed soft abrasive grinding wheel," *Mater. Sci. Semicond. Process.*, vol. 63, no. 2, pp. 97–106, 2017.
[21] S. D. Jacobs *et al.*, "Magnetorheological finishing: a deterministic process for optics manufacturing," *Int. Conf. Opt. Fabr. Test.*, vol. 2576, no. August 1995, pp. 372–382, 1995.
[22] D. Golini, S. D. Jacobs, W. I. Kordonski, and P. Dumas, "Precision optics fabrication using magnetorheological finishing," in *Advanced Materials for Optics and Precision Structures: A Critical Review*, 1997, vol. 10289, p. 102890H.
[23] M. Kumar, H. N. S. Yadav, A. Kumar, and M. Das, "An overview of magnetorheological polishing fluid applied in nano-finishing of components," *J. Micromanufacturing*, vol. 3, no. 5, pp. 1–19, 2021.
[24] H. B. Cheng, Y. Yam, and Y. T. Wang, "Experimentation on MR fluid using a 2-axis wheel tool," *J. Mater. Process. Technol.*, vol. 209, no. 12–13, pp. 5254–5261, 2009.
[25] D. A. Khan and S. Jha, "Synthesis of polishing fluid and novel approach for nanofinishing of copper using ball-end magnetorheological finishing process," *Mater. Manuf. Process.*, vol. 33, no. 11, pp. 1150–1159, 2018.
[26] A. Kumar Singh, S. Jha, and P. M. Pandey, "Design and development of nanofinishing process for 3D surfaces using ball end MR finishing tool," *Int. J. Mach. Tools Manuf.*, vol. 51, no. 2, pp. 142–151, 2011.
[27] W.-L. Song, S.-B. Choi, Q.-C. Cai, J.-Y. Choi, and C.-H. Lee, "Finishing performance of magnetorheological fluid under magnetic field," *Mech. Adv. Mater. Struct.*, vol. 20, no. 7, pp. 529–535, Aug. 2013.
[28] D. C. Harris, "History of magnetorheological finishing," in *Proceedings of SPIE - The International Society for Optical Engineering*, 2011, p. 801.
[29] S. Jha and V. K. Jain, "Design and development of the magnetorheological abrasive flow finishing (MRAFF) process," *Int. J. Mach. Tools Manuf.*, vol. 44, no. 10, pp. 1019–1029, 2004.
[30] M. Das, V. K. Jain, and P. S. Ghoshdastidar, "Nano-finishing of stainless-steel tubes using rotational magnetorheological abrasive flow finishing process," *Mach. Sci. Technol.*, vol. 14, no. 3, pp. 365–389, 2010.
[31] M. Das, V. K. Jain, and P. S. Ghoshdastidar, "Computational fluid dynamics simulation and experimental investigations into the magnetic-field-assisted nano-finishing process," *Proc. Inst. Mech. Eng. Part B J. Eng. Manuf.*, vol. 226, no. 7, pp. 1143–1158, 2012.
[32] A. Sidpara, M. Das, and V. K. Jain, "Rheological characterization of magnetorheological finishing fluid," *Mater. Manuf. Process.*, vol. 24, no. 12, pp. 1467–1478, 2009.
[33] M. Ashtiani and S. H. Hashemabadi, "An experimental study on the effect of fatty acid chain length on the magnetorheological fluid stabilization and rheological properties," *Colloids Surfaces A Physicochem. Eng. Asp.*, vol. 469, pp. 29–35, 2015.
[34] M. S. A. Rahim and I. Ismail, "Review of magnetorheological fluids and nanofluids thermal behaviour," *IOP Conf. Ser. Mater. Sci. Eng.*, vol. 100, no. 1, 2015.
[35] A. B. Shorey, S. D. Jacobs, W. I. Kordonski, and R. F. Gans, "Experiments and observations regarding the mechanisms of glass removal in magnetorheological finishing," *Appl. Opt.*, vol. 40, no. 1, p. 20, 2001.
[36] A. Sidpara and V. K. Jain, "Rheological properties and their correlation with surface finish quality in MR fluid-based finishing process," *Mach. Sci. Technol.*, vol. 18, no. 3,

pp. 367–385, 2014.
[37] J. Seok, J. J. Kyung-In, K. Doo-Yeon, and M. Sangjin, “Deburring microparts using a magnetorheological fluid,” *Int. J. Mach. Tools Manuf.*, vol. 53, no. 1, pp. 170--175, 2012.
[38] L. Nagdeve, A. Sidpara, V. K. Jain, and J. Ramkumar, “On the effect of relative size of magnetic particles and abrasive particles in MR fluid-based finishing process,” *Mach. Sci. Technol.*, vol. 22, no. 3, pp. 493–506, 2018.
[39] A. Sidpara and V. K. Jain, “Effect of fluid composition on nanofinishing of single-crystal silicon by magnetic field-assisted finishing process,” *Int. J. Adv. Manuf. Technol.*, vol. 55, no. 1–4, pp. 243–252, 2011.
[40] A. Sidpara and V. K. Jain, “Nano-level finishing of single crystal silicon blank using magnetorheological finishing process,” *Tribol. Int.*, vol. 47, no. 5, pp. 159–166, 2012.
[41] J. E. Kim, J. Ko, Y. D. Liu, I. G. Kim, and H. J. Choi, “Effect of Medium Oil on Magnetorheology of Soft Carbonyl Iron Particles,” *IEEE Trans. Magn.*, vol. 48, no. 11, pp. 3442–3445, 2012.
[42] S. Mantripragada, X. Wang, F. Gordaninejad, B. Hu, and A. Fuchs, “Rheological properties of novel magnetorheological fluids,” *Int. J. Mod. Phys. B*, vol. 21, no. 28–29, pp. 4849–4857, 2007.
[43] S. Genc and P. P. Phule, “Rheological properties of magnetorheological fluids,” *Smart Mater. Struct.*, vol. 11, no. 1, p. 140, Feb. 2002.
[44] S. N. Shafrir, J. C. Lambropoulos, and S. D. Jacobs, “Toward magnetorheological finishing of magnetic materials,” *J. Manuf. Sci. Eng. Trans. ASME*, vol. 129, no. 5, pp. 961–964, 2007.
[45] V. K. Jain, S. Kalia, and A. M. Sidpara, “Some aspects of fabrication of micro devices by electrochemical micromachining (ECMM) and its finishing by magnetorheological fluid,” *Int. J. Adv. Manuf. Technol.*, vol. 59, no. 9–12, pp. 987–996, 2012.
[46] M. Chen, H. Liu, Y. Su, B. Yu, and Z. Fang, “Design and fabrication of a novel magnetorheological finishing process for small concave surfaces using small ball-end permanent-magnet polishing head,” *Int. J. Adv. Manuf. Technol.*, vol. 83, no. 5–8, pp. 823–834, 2016.
[47] D. A. Khan and S. Jha, “Selection of optimum polishing fluid composition for ball end magnetorheological finishing ( BEMRF ) of copper,” *Int. J. Adv. Manuf. Technol.*, vol. 9, no. 3, pp. 11–32, 2017.
[48] G. Parameswari, V. K. Jain, J. Ramkumar, and L. Nagdeve, “Experimental investigations into nanofinishing of Ti6Al4V flat disc using magnetorheological finishing process,” *Int J Adv ManufTechnol*, vol. 33, no. 5, pp. 450–623, 2017.
[49] M. Kumar, A. Kumar, A. Alok, and M. Das, “Magnetorheological method applied to optics polishing: A review,” *IOP Conf. Ser. Mater. Sci. Eng.*, vol. 804, no. 01, pp. 12–13, 2020.
[50] M. Tricard, W. I. Kordonski, A. B. Shorey, and C. Evans, “Magnetorheological jet finishing of conformal, freeform and steep concave optics,” *CIRP Ann.*, vol. 55, no. 1, pp. 309–312, 2006.
[51] F. Shi, Y. Shu, Y. Dai, X. Peng, and S. Li, “Magnetorheological elastic super-smooth finishing for high-efficiency manufacturing of ultraviolet laser resistant optics,” *Opt. Eng.*, vol. 52, no. 7, p. 075104, 2013.
[52] J. Kenda, J. Duhovnik, J. Tavcar, and J. Kopac, “Abrasive flow machining applied to plastic gear matrix polishing,” *Int. J. Adv. Manuf. Technol.*, vol. 71, no. 4, pp. 141–151, 2014.
[53] V. K. Jain, “Abrasive-based nano-finishing techniques: An overview,” *Mach. Sci. Technol.*, vol. 12, no. 3, pp. 257–294, 2008.

[54] E. M. Furst and A. P. Gast, “Micromechanics of magnetorheological suspensions,” *Phys. Rev. E - Stat. Physics, Plasmas, Fluids, Relat. Interdiscip. Top.*, vol. 61, no. 6 B, pp. 6732–6739, 2000.
[55] H. Yamaguchi, X. D. Niu, X. J. Ye, M. Li, and Y. Iwamoto, “Dynamic rheological properties of viscoelastic magnetic fluids in uniform magnetic fields,” *J. Magn. Magn. Mater.*, vol. 324, no. 20, pp. 3238–3244, 2012.
[56] M. Ashtiani, S. H. Hashemabadi, and A. Ghaffari, “A review on the magnetorheological fluid preparation and stabilization,” *J. Magn. Magn. Mater.*, vol. 374, no. 10, pp. 711–715, 2015.
[57] J. H. Park, B. D. Chin, and O. O. Park, “Rheological properties and stabilization of magnetorheological fluids in a water-in-oil emulsion,” *J. Colloid Interface Sci.*, vol. 240, no. 1, pp. 349–354, 2001.
[58] C. W. Guo, F. Chen, Q. R. Meng, and Z. X. Dong, “Yield shear stress model of magnetorheological fluids based on exponential distribution,” *J. Magn. Magn. Mater.*, vol. 360, pp. 174–177, 2014.
[59] chhabra and rechardson, *Non-Newtonian Flow in the Process Industries*. Elsevier, 1999.
[60] J. D. Carlson and M. R. Jolly, “MR fluid, foam and elastomer devices,” *Mechatronics*, vol. 10, no. 4–5, pp. 555–569, Jun. 2000.
[61] Y. T. Choi, J. U. Cho, S. B. Choi, and N. M. Wereley, “Constitutive models of electrorheological and magnetorheological fluids using viscometers,” in *Smart Materials and Structures*, 2005, vol. 14, no. 5, pp. 1025–1036.
[62] N. A. Khan and F. Sultan, “Numerical Analysis for the Bingham—Papanastasiou Fluid Flow Over a Rotating Disk,” *J. Appl. Mech. Tech. Phys.*, vol. 59, no. 4, pp. 638–644, 2018.
[63] B. Herschel, “Consistency measurements of rubber-benzene solutions,” *INDUSTRIAL AND ENGINEERING CHEMISTRY*, 1924. .
[64] T. C. Papanastasiou, “Flows of Materials with Yield,” *J. Rheol. (N. Y. N. Y).*, vol. 31, no. 5, pp. 385–404, Jul. 1987.
[65] E. Mitsoulis, “Flows of viscoplastic materials: models and computations,” 2007.
[66] J. M. Ginder and L. C. Davis, “Shear stresses in magnetorheological fluids: Role of magnetic saturation,” *Appl. Phys. Lett.*, vol. 65, no. 26, pp. 3410–3412, 1994.
[67] J. M. Ginder, L. C. Davis, and L. D. Elie, “Rheology of magnetorheology fluids: models and measurements,” *Int. J. Mod. Phys.*, vol. 10, no. 23, p. 11, 1996.
[68] J. M. Ginder, “Behavior of magnetorheological fluids,” *MRS Bull.*, vol. 23, no. 8, pp. 26–29, 1998.
[69] R. R. Huilgol and Z. You, “Application of the augmented Lagrangian method to steady pipe flows of Bingham, Casson and Herschel-Bulkley fluids,” *J. Nonnewton. Fluid Mech.*, vol. 128, no. 2–3, pp. 126–143, Jul. 2005.
[70] R. D. Britton, C. D. Elcoate, M. P. Alanou, H. P. Evans, and R. W. Snidle, “Effect of Surface Finish on Gear Tooth Friction,” *J. Tribol.*, vol. 122, no. 1, p. 354, 2000.
[71] J. P. Misra, P. K. Jain, D. K. Dwivedi, and N. K. Merita, “Study of time dependent behaviour of ECH of bevel gears,” *Procedia Eng.*, vol. 64, no. 7, pp. 1259–1266, 2013.
[72] Y. Xu, K. Zhang, S. Lu, and Z. Liu, “Experimental investigations into abrasive flow machining of helical gear,” *Digit. Des. Manuf. Technol.*, vol. 546, no. 6, pp. 65–69, 2013.
[73] L. K. Gillespie, *Deburring and edge finishing handbook*. Society of Manufacturing Engineers, 1999.
[74] L. K. Gillespie and P. T. Blotter, “The formation and properties of machining burrs,” *J. Manuf. Sci. Eng. Trans. ASME*, vol. 98, no. 1, pp. 66–74, 1976.
[75] T. Miyake, A. Yamamoto, W. Kishimoto, K. Yamanaka, and K. Takano, “Study of Burr

Formation in Face Milling (1st Report)," *J. Japan Soc. Precis. Eng.*, vol. 53, no. 1, pp. 98–104, Jan. 1987.
[76] T. Miyake, A. Yamamoto, W. Kishimoto, K. Yamanaka, and K. Takano, "Study of Burr Formation in Face Milling (1st Report)," *J. Japan Soc. Precis. Eng.*, vol. 53, no. 1, pp. 98–104, 1987.
[77] Y. Fujisawa and M. Komori, "Method for removing burrs and pits from small gears using a gear-shaped tool composed of glass-fiber-reinforced plastic," *J. Mater. Process. Technol.*, vol. 210, no. 9, pp. 1159–1170, Jun. 2010.
[78] Y. Fujisawa and M. Komori, "Method for removing burrs and pits from small gears using a gear-shaped tool composed of glass-fiber-reinforced plastic," *J. Mater. Process. Technol.*, vol. 210, no. 9, pp. 1159–1170, Jun. 2010.
[79] M. H. I. B. Karpuschewski , H.-J. Knoche, "Gear finishing by abrasive processes," *CIRP Ann. - Manuf. Technol.*, vol. 57, no. 1–4, pp. 621–640, 2008.
[80] Y. C. Xu, K. H. Zhang, S. Lu, and Z. Q. Liu, "Experimental Investigations into Abrasive Flow Machining of Helical Gear," *Key Eng. Mater.*, vol. 546, no. 15, pp. 65–69, 2013.
[81] J. M. Allwood *et al.*, "Manufacturing at double the speed," *J. Mater. Process. Technol.*, vol. 229, pp. 729–757, Nov. 2015.
[82] J. Kenda, F. Pušavec, and J. Kopac, "Modeling and energy efficiency of abrasive flow machining on tooling industry case study," *Procedia CIRP*, vol. 13, no. 1–6, pp. 13–18, 2014.
[83] G. Venkatesh, A. K. Sharma, N. Singh, and P. Kumar, "Finishing of bevel gears using abrasive flow machining," *Procedia Eng.*, vol. 97, no. 1–5, pp. 320–328, 2014.
[84] A. K. S. Ravi Datt Yadav, "A novel magnetorheological gear profile finishing with high shape accuracy," *Int. J. Mach. Tools Manuf.*, vol. 139, no. 19, pp. 75–92, 2019.
[85] D. McCloy and R. H. McGuigan, "Some Static and Dynamic Characteristics of Poppet Valves," *Proc. Inst. Mech. Eng. Conf. Proc.*, vol. 179, no. 8, pp. 199–213, 1964.
[86] R. Zade, "Optimization of inlet valve of IC engine using FEA," *Int. Res. J. Eng. Technol.*, vol. 3, no. 10, p. 20, 2016.
[87] Watkings, "Automotive Systems," *SweetHaven Publishing Services*, 1995. .
[88] Integrated Publishing, "Valve and Valve Seats," *Integrated Publishing*, 2002. [Online]. Available: http://constructionmanuals.tpub.com/14264/css/Valve-and-Valve-Seats-92.htm. [Accessed: 15-Dec-2019].
[89] E. Mattsson and L. Svenssont, "Corrosion Investigation of Valves in Flowing Sea Water," *Br. Corros. J.*, vol. 7, no. 5, pp. 200–207, 1972.
[90] B. P. B. Lequesne and M. Royal Oak, "Variable Lift Operation of Bistable Electromechanical Poppet Valve Actuator," US4829947, 1988.
[91] R. O. Mich, *Electromagnetic Valves: Air Poppet Valve Controlled by ECU*. 1980.
[92] R. K. Johnson and Blaine, "Poppet Valve Member," US7708025 B2, 2010.
[93] J. Lei, J. Tao, C. Liu, and Y. Wu, "Flow Model and Dynamic Characteristics of a Direct Spring Loaded Poppet Relief Valve," *Proc. Inst. Mech. Eng. Part C J. Mech. Eng. Sci.*, vol. 232, no. 9, pp. 1657–1664, 2018.
[94] D. N. Johnston, K. A. Edge, and N. D. Vaughan, "Experimental Investigation of Flow and Force Characteristics of Hydraulic Poppet and Disc Valves," *Proc. Inst. Mech. Eng. Part A J. Power Energy*, vol. 205, no. 3, pp. 161–171, 1991.
[95] M. T. Muller and R. C. Fales, "Design and Analysis of a Two-Stage Poppet Valve for Flow Control," *Int. J. Fluid Power*, vol. 9, no. 1, pp. 17–26, 2008.
[96] F. Starr, "Development of the Poppet Type Exhaust Valve in the Internal Combustion Engine: Part I 1860–1930," *Int. J. Hist. Eng. Technol.*, vol. 82, no. 2, pp. 283–314, 2012.
[97] L. Witek, "Failure and Thermo-Mechanical Stress Analysis of the Exhaust Valve of Diesel Engine," *Eng. Fail. Anal.*, vol. 66, no. 15, pp. 154–165, 2016.

[98] M. I. Khan, M. A. Khan, and A. Shakoor, "A Failure Analysis of the Exhaust Valve From a Heavy Duty Natural Gas Engine," *Eng. Fail. Anal.*, vol. 85, no. 16, pp. 77–88, 2017.
[99] A. Abeysekara, C. Ag, and A. Abeysekara, "Valve Lapping Machine for Internal Combustion Engines," *Univ. Wolverhampt. Abstr.*, vol. 21, no. 12, pp. 0–57, 2015.
[100] S. V. S. Divya, R. Pavithran, "Engine Valve Lapping," *Int. J. Res. Eng. Sci. Manag.*, vol. 2, no. 5, pp. 2581–5792, 2019.
[101] Y. S. Wang, S. Narasimhan, J. M. Larson, J. E. Larson, and G. C. Barber, "The Effect of Operating Conditions on Heavy Duty Engine Valve Seat Wear," *Wear*, vol. 201, no. 1–2, pp. 15–25, 1996.
[102] P. Forsberg, P. Hollman, and S. Jacobson, "Wear Mechanism Study of Exhaust Valve System in Modern Heavy Duty Combustion Engines," *Wear*, vol. 271, no. 9–10, pp. 2477–2484, Jul. 2011.
[103] R. Zhao, G. C. Barber, Y. S. Wang, and J. E. Larson, "Wear Mechanism Analysis of Engine Exhaust Valve Seats With a Laboratory Simulator," *Tribol. Trans.*, vol. 40, no. 2, pp. 209–218, 1997.
[104] T. Ootani, N. Yahata, A. Fujiki, and A. Ehira, "Impact Wear Characteristics of Engine Valve and Valve Seat Insert Materials at High Temperature (Impact Wear Tests of Austenitic Heat-Resistant Steel SUH36 Against Fe-base Sintered Alloy Using Plane Specimens)," *Wear*, vol. 188, no. 1–2, pp. 175–184, 1995.
[105] T. Hejwowski, "Investigations of Corrosion Resistance of Fe-, Ni- and Co-Based Hardfacings," *Vacuum*, vol. 80, no. 11–12, pp. 1386–1390, 2006.
[106] Z. W. Yu and X. L. Xu, "Failure Analysis and Metallurgical Investigation of Diesel Engine Exhaust Valves," *Eng. Fail. Anal.*, vol. 13, no. 4, pp. 673–682, 2006.
[107] M. I. Karamangil, A. Avci, and H. Bilal, "Investigation of the Effect of Different Carbon Film Thickness on the Exhaust Valve," *Heat Mass Transf. und Stoffuebertragung*, vol. 44, no. 5, pp. 587–598, 2008.
[108] W. Mitianiec, "Modern Pneumatic and Combustion Hybrid Engines," *Improv. Trends Intern. Combust. Engines*, vol. 16, no. 333, pp. 15–16, Mar. 2018.
[109] Y. K. Lavhale and J. Salunke, "Overview of Failure Trend of Inlet & Exhaust Valve," *Int. J. Mech. Eng. Technol.*, vol. 5, no. 3, pp. 104–113, 2014.
[110] A. T. Colwell and C. Ohio, "Method of Polishing Hollow Stem Valves," US423716, 1945.
[111] K. M. Prasanth.P.S, "Optimal Selection of Valve Material for C I Engines Using ANSYS," *Int. J. Sci. Eng. Technol. Res.*, vol. 5, no. 6, p. 2076, 2016.
[112] J. H. Goulet, S. Lorenzo, S. G. Dawes, O. Land, A. J. Smith, and S. Leandro, "Valve Lapping Machine," US783214, 1960.
[113] V. Mancuso and L. Angeles, "Valve Seat Lapping Machine," US44836, 1935.
[114] A. E. Riggs, O. Sapulpa, and Oklahoma, "Valve Seat Lapping Machine," US451255, 1930.
[115] H. Singh and P. K. Jain, "A Comparative Study of Precision Finishing of Rebuild Engine Valve Faces Using Micro-grinding and ECH," *J. Remanufacturing*, vol. 5, no. 1, p. 20, 2015.
[116] D. N. J. and K. A. E. N D Vaughan, "Numerical Simulation of Fluid Flow in Poppet Valves," *Proc. Inst. Mech. Eng.*, vol. 206, no. 2, p. 119, 1992.
[117] james G. Sterling, C. Heights, and Ohio, "Process for Removal of Annular Scratches in Hollow Poppet Valve Stems," US525274, 1944.
[118] K. M. Bartlett, Cleveland, and Ohio, "Method of Electropolishing the Internal Surface of a Hollow Valve," US482378, 1949.
[119] F. W. Preston, "The Theory and Design of Plate Glass Polishing Machines. Part II. -

Society of Glass Technology," *J Soc Glas Technol*, vol. 13, no. 14, pp. 111–123, 1929.
[120] J. E. DeGroote, A. E. Marino, J. P. Wilson, A. L. Bishop, J. C. Lambropoulos, and S. D. Jacobs, "Removal rate model for magnetorheological finishing of glass," *Appl. Opt.*, vol. 46, no. 32, pp. 7927–7941, 2007.
[121] B. Jung, K. I. Jang, B. K. Min, S. J. Lee, and J. Seok, "Magnetorheological finishing process for hard materials using sintered iron-CNT compound abrasives," *Int. J. Mach. Tools Manuf.*, vol. 49, no. 5, pp. 407–418, 2009.
[122] C. Miao, S. N. Shafrir, J. C. Lambropoulos, J. Mici, and S. D. Jacobs, "Shear stress in magnetorheological finishing for glasses," *Appl. Opt.*, vol. 48, no. 13, pp. 2585–2594, 2009.
[123] C. Miao, J. C. Lambropoulos, and S. D. Jacobs, "Process parameter effects on material removal in magnetorheological finishing of borosilicate glass," *Appl. Opt.*, vol. 49, no. 10, pp. 1951--1963, 2010.
[124] W. B. Kim, S. H. Lee, and B. K. Min, "Surface finishing and evaluation of three-dimensional silicon microchannel using magnetorheological fluid," *J. Manuf. Sci. Eng. Trans. ASME*, vol. 126, no. 4, pp. 772–778, 2004.
[125] M. Schinhaerl *et al.*, "Forces acting between polishing tool and workpiece surface in magnetorheological finishing," *Curr. Dev. Lens Des. Opt. Eng. IX*, vol. 7060, no. 0, p. 706006, 2008.
[126] A. Sidpara and V. K. Jain, "Experimental investigations into forces during magnetorheological fluid based finishing process," *Int. J. Mach. Tools Manuf.*, vol. 51, no. 4, pp. 358–362, 2011.
[127] A. Sidpara and V. K. Jain, "Theoretical analysis of forces in magnetorheological fluid based finishing process," *Int. J. Mech. Sci.*, vol. 56, no. 1, pp. 50–59, 2012.
[128] A. K. Singh, S. Jha, and P. M. Pandey, "Mechanism of material removal in ball end magnetorheological finishing process," *Wear*, vol. 302, no. 1–2, pp. 1180–1191, 2013.
[129] A. Sidpara and V. K. Jain, "Analysis of forces on the freeform surface in magnetorheological fluid based finishing process," *Int. J. Mach. Tools Manuf.*, vol. 69, pp. 1–10, 2013.
[130] M. Kumar, R. K. Bharti, and M. Das, "Study of surface finishing mechanism in a rotational-magnetorheological miniature gear profile polishing using novel flow restrictor," *Wear*, vol. 487, no. 10, pp. 120–204, 2021.
[131] M. Das, V. K. Jain, and P. S. Ghoshdastidar, "Nanofinishing of flat workpieces using rotational–magnetorheological abrasive flow finishing (R-MRAFF) process," *Int. J. Adv. Manuf. Technol.*, vol. 62, no. 7, pp. 405–420, 2012.
[132] S. K. Paswan, T. S. Bedi, and A. K. Singh, "Modeling and simulation of surface roughness in magnetorheological fluid based honing process," *Wear*, vol. 376–377, no. 6, pp. 1207–1221, 2017.
[133] S. K. Paswan and A. K. Singh, "Analysis of surface finishing mechanism in a newly developed rotational magnetorheological honing process for its productivity improvement," *Wear*, vol. 426–427, no. 5, pp. 68–82, 2019.
[134] S. Jha and V. K. Jain, "Modeling and simulation of surface roughness in magnetorheological abrasive flow finishing (MRAFF) process," *Wear*, vol. 261, no. 7–8, pp. 856–866, Oct. 2006.
[135] N. K. Maurya, V. Rastogi, and P. Singh, "Experimental and computational analysis of mechanical properties of RGD840 material manufactured through PolyJet process," *Rapid Prototyp. J.*, vol. 27, no. 1, pp. 207–214, 2020.
[136] B. Gopinath *et al.*, "A systematic study of the impact of additives on structural and mechanical properties of Magnetorheological fluids," *Mater. Today Proc.*, Aug. 2020.
[137] N. A. Khan and F. Sultan, "Numerical Analysis for the Bingham—Papanastasiou Fluid

Flow Over a Rotating Disk," *J. Appl. Mech. Tech. Phys.*, vol. 59, no. 4, pp. 638–644, Jul. 2018.
[138] Jayant and V. K. Jain, "Analysis of finishing forces and surface finish during magnetorheological abrasive flow finishing of asymmetric workpieces," *J. Micromanufacturing*, vol. 2, no. 2, pp. 133–151, 2019.
[139] J. C. Lambropoulos, C. Miao, and S. D. Jacobs, "Magnetic field effects on shear and normal stresses in magnetorheological finishing," *Opt. Express*, vol. 18, no. 19, p. 19713, 2010.
[140] M. Kumar, S. Ahmad, and M. Das, "Magnetorheological-finishing of miniature gear teeth profiles using uniform flow restrictor," *Mater. Manuf. Process.*, vol. 36, no. 11, pp. 1–16, 2021.
[141] H. Kansal, A. K. Singh, and V. Grover, "Magnetorheological nano-finishing of diamagnetic material using permanent magnets tool," *Precis. Eng.*, vol. 51, pp. 30–39, 2018.
[142] K. Saraswathamma, S. Jha, and P. V. Rao, "Experimental investigation into Ball end Magnetorheological Finishing of silicon," *Precis. Eng.*, vol. 42, pp. 218–223, 2015.
[143] M. Das Anwesa Barman, "Nano-finishing of Bio-Titanium Alloy to Generate Different Surface Morphologies by Changing Magnetrheological Polishing Fluid Compositions," *Precis. Eng.*, vol. 101, no. 22, pp. 25–30, 2017.
[144] K. Arora and A. K. Singh, "Magnetorheological finishing of UHMWPE acetabular cup surface and its performance analysis," *Mater. Manuf. Process.*, vol. 35, no. 14, pp. 1631–1649, 2020.
[145] A. Sidpara and V. K. Jain, "Nano-level finishing of single crystal silicon blank using magnetorheological finishing process," *Tribol. Int.*, vol. 47, no. 5, pp. 159–166, 2012.
[146] S. K. Paswan, T. S. Bedi, and A. K. Singh, "Modeling and simulation of surface roughness in magnetorheological fluid based honing process," *Wear*, vol. 376–377, no. 6, pp. 1207–1221, 2017.
[147] M. Kumar and M. Das, "Improvement in surface characteristics of SS316L tiny gear profiles by magnetorheological-polishing fluid using flow restrictor," *Trans. Indian Inst. Met.*, vol. 74, no. 8, pp. 1–15, 2021.
[148] A. Barman and M. Das, "Simulation and experimental investigation of finishing forces in magnetic field assisted finishing process," *Mater. Manuf. Process.*, vol. 33, no. 11, pp. 1223–1232, 2018.
[149] A. Sidpara and V. K. Jain, "Rheological properties and their correlation with surface finish quality in MR fluid-based finishing process," *Mach. Sci. Technol.*, vol. 18, no. 3, pp. 367–385, 2014.
[150] A. Kumar, Z. Alam, D. A. Khan, and S. Jha, "Nanofinishing of FDM-fabricated components using ball end magnetorheological finishing process," *Mater. Manuf. Process.*, vol. 34, no. 2, pp. 232–242, Jan. 2019.
[151] J. Huang, J. Q. Zhang, and J. N. Liu, "Effect of magnetic field on properties of MR fluids," *Int. J. Mod. Phys. B*, vol. 19, no. 1, pp. 597–601, 2005.
[152] S. A. Sirwal and A. K. Singh, "Analysis of the surface roughness for novel magnetorheological finishing of a typical blind hole workpiece," *Proc. Inst. Mech. Eng. Part C J. Mech. Eng. Sci.*, vol. 233, no. 5, pp. 1541–1561, 2019.
[153] S. K. Paswan and A. K. Singh, "Theoretical and experimental investigations on nano-finishing of internal cylindrical surfaces with a newly developed rotational magnetorheological honing process," *Proc. Inst. Mech. Eng. Part C J. Mech. Eng. Sci.*, vol. 234, no. 2, pp. 363–383, 2020.
[154] M. C. Shaw, "A new theory of grinding," in *Proc. of the institution's conference on production science in industry*, 1971, pp. 5–4.

[155] A. W. Stradling, "The physics of open-gradient dry magnetic separation," *Int. J. Miner. Process.*, vol. 39, no. 1–2, pp. 1–18, 1993.
[156] M. Kumar, A. Alok, and M. Das, "Experimental and simulation study of magnetorheological miniature gear-profile polishing (MRMGPP) method using flow restrictor," *J. Mech. Sci. Technol.*, vol. 35, no. 11, pp. 120–125, 2021.
[157] S. Jha and V. K. Jain, "Modeling and simulation of surface roughness in magnetorheological abrasive flow finishing (MRAFF) process," *Wear*, vol. 261, no. 8, pp. 856–866, 2006.
[158] V. Grover and A. K. Singh, "Analysis of particles in magnetorheological polishing fluid for finishing of ferromagnetic cylindrical workpiece," *Part. Sci. Technol.*, vol. 36, no. 7, pp. 799–807, 2018.
[159] R. K. Jain, V. K. Jain, and P. M. Dixit, "Modeling of material removal and surface roughness in abrasive flow machining process," *Int. J. Mach. Tools Manuf.*, vol. 39, no. 1–2, pp. 1903–1923, 1999.
[160] S. Jha and V. Kumar Jain, "Parametric analysis of magnetorheological abrasive flow finishing process," *Int. J. Manuf. Technol. Manag.*, vol. 13, no. 2–4, pp. 308–323, 2008.
[161] R. Douglas Gregory, *Classical mechanics: An undergraduate text*. 2006.
[162] J. H. Shaikh and N. K. Jain, "Modeling of material removal rate and surface roughness in finishing of bevel gears by electrochemical honing process," *J. Mater. Process. Technol.*, vol. 214, no. 2, pp. 200–209, 2014.
[163] G. Daniel, C. Yoan, P. Zoltan, and P. Yves, "Bingham-papanastasiou and approximate parallel models comparison for the design of magneto-rheological valves," *IEEE/ASME Int. Conf. Adv. Intell. Mechatronics, AIM*, vol. 978, no. 1, pp. 168–173, 2014.
[164] N. J. Mourtos, "Rotating disk," 2008.
[165] A. G. Emslie, F. T. Bonner, and L. G. Peck, "Flow of a viscous liquid on a rotating disk," *J. Appl. Phys.*, vol. 29, no. 5, pp. 858–862, 1958.
[166] S. C. Jayswal, V. K. Jain, and P. M. Dixit, "Modeling and simulation of magnetic abrasive finishing process," *Int. J. Adv. Manuf. Technol.*, vol. 26, no. 5–6, pp. 477–490, Sep. 2005.

# List of Publications

## Journals:

1. **M. Kumar**, S. Ahmad, and M. Das, "Magnetorheological-finishing of miniature gear teeth profiles using uniform flow restrictor," Mater. Manuf. Process., vol. 36, no. 11, pp. 1–16, 2021.
2. **M. Kumar**, A. Alok, and M. Das, "Experimental and simulation study of magnetorheological miniature gear-profile polishing (MRMGPP) method using flow restrictor," J. Mech. Sci. Technol., vol. 35, no. 11, pp. 120–125, 2021.
3. **M. Kumar** and M. Das, "Improvement in surface characteristics of SS316L tiny gear profiles by magnetorheological-polishing fluid using flow restrictor," Trans. Indian Inst. Met., 2021. https://doi.org/10.1007/s12666-021-02339-x.
4. **M. Kumar**, R. K. Bharti, and M. Das, "Study of surface finishing mechanism in a rotational-magnetorheological miniature gear profile polishing using novel flow restrictor," Wear, vol. 487, no. 10, pp. 120–204, 2021.
5. **M. Kumar**, A. Kumar, A. Alok, and M. Das, "Magnetorheological finishing of small gear teeth profiles using novel workpiece fixture," J. Eng. Res., vol. 9, no. 3, pp. 1–15, 2021, doi: 10.36909/jer.ICCEMME.15759.
6. **M. Kumar**, H. N. S Yadav, A. Kumar, and M. Das, "An overview of magnetorheological polishing fluid applied in nano-finishing of components," J. Micromanufacturing, vol. 3, no. 5, pp. 1–19, 2021.
7. **M. Kumar,** A. Alok, V. Kumar, and M. Das, "Advanced abrasive-based nano-finishing processes: challenges, principles and recent applications," Mater. Manuf. Process., 2021, doi: 10.1080/10426914.2021.2001509.
8. **M. Kumar,** and M. Das, "Effect of optimum process parameters in rotational-magnetorheological poppet valve polishing", Mater. Manuf. Process, 2021, doi: 10.1080/10426914.2021.2016818.
9. **M. Kumar,** A. Alok, and M. Das**,** "Recent advancements in advanced abrasive-based nano-finishing processes for biomedical components", Trans. Indian Inst. Met., 2021. **(Accepted)**
10. **M. Kumar**, and M. Das, Impact of different magnetorheological fluid compositions on poppet valve profile polishing**,** Prec. Eng. **(Accepted)**

## Patents:

1. **Manjesh Kumar** and Manas Das, An arrangement for polishing poppet valve by magnetorheological fluid-based finishing process, Indian Patent, Application Number: 202131013271. | **Patent Published.**
2. **Manjesh Kumar**, Anwesa Barman and Manas Das, An arrangement for uniform polishing of narrow complex profiles of miniature gear, Indian Patent, Application Number: 202131049403. | **Patent Published.**

## Conference Proceedings:

1. **M. Kumar,** A. Kumar, H. N. S Yadav, A. Alok, and M. Das, "Abrasive based finishing method applied on biomedical implants: A review," Int. conf. on Comp. & Exp. Methods in Mechanical Engg., (ICCEMME), Mater. Today Proc., vol. 45, no. 5, pp. 60–70, 2021, https://doi.org/10.1016/j.matpr.2021.04.137**.**
2. **M. Kumar,** V. Kumar, A. Kumar, H. N. S Yadav, and M. Das, "CFD analysis of MR fluid applied for finishing of gear in MRAFF process," Int. Conf. on Aspects of Materials Science and Engineering, (ICAMSE), Mater. Today Proc., vol. 25, no. 3, pp. 1–7, 2021, https://doi.org/10.1016/j.matpr.2021.01.116.
3. **M. Kumar,** A. Kumar, A. Alok, and M. Das, "Magnetorheological method applied to optics polishing: A review," 8th Int. Symposium on Fusion of Science and Technology (ISFT), IOP Conf. Ser. Mater. Sci. Eng., vol. 804, no. 01, pp. 12–13, 2020, https://doi.org/10.1088/1757-899X/804/1/012012.
4. **M. Kumar**, A. Kumar, R.K Bharti, H.N.S Yadav and M. Das**,** "A review on rheological properties of magnetorheological fluid for engineering components polishing", ICAMEMS, Mater. Today Proc., 2021 https://doi.org/10.1016/j.matpr.2021.11.611.
5. **M. Kumar**, A. Kumar, H.N.S Yadav and M. Das**,** "Nanofinishing of tiny gear using magnetorheological abrasive flow finishing process", world congress on micro and nano manufacturing (WCMNM), IIT Bombay, J. Micromanufacturing, 2021.

## Book chapter:

1. **M. Kumar**, A. Kumar, H.N.S Yadav, and M. Das, "Gear profile polishing using rotational magnetorheological abrasive flow finishing process", Springer (Advances in Mechanical Engineering). **(Accepted)**